GAS ASSISTED THIN-FILM EVAPORATION FROM CONFINED SPACES

A Dissertation
Presented to
The Academic Faculty

by

Shankar Narayanan

In Partial Fulfillment
of the Requirements for the Degree
Doctor of Philosophy in the
School of Mechanical Engineering

Georgia Institute of Technology
December 2011

GAS ASSISTED THIN-FILM EVAPORATION FROM CONFINED SPACES

Approved by:

Dr. Andrei G. Fedorov, Advisor
School of Mechanical Engineering
Georgia Institute of Technology

Dr. Yogendra K. Joshi, Advisor
School of Mechanical Engineering
Georgia Institute of Technology

Dr. Mostafa S. Ghiaasiaan
School of Mechanical Engineering
Georgia Institute of Technology

Dr. Muhannad S. Bakir
School of Electrical and Computer Engineering
Georgia Institute of Technology

Dr. Seung Soon Jang
School of Materials Science and Engineering
Georgia Institute of Technology

Date Approved: August, 25, 2011

To my loving parents, for their encouragement and support

ACKNOWLEDGEMENTS

I am thankful to my parents for their unwavering loving support, which has always motivated me to pursue challenging tasks despite setbacks. It was their encouragement and tutelage that lay the foundation for my interest in engineering from a very young age. I would also like to thank my sisters for their encouragement and guidance, which has helped me take informed decisions at several occasions when my experience and foresight had fallen short. Special thanks are due to my brothers-in-law, nephew and nieces for being wonderful friends and a refreshingly joyful company.

I owe my most sincere gratitude to my advisors, Dr. Andrei Fedorov and Dr. Yogendra Joshi, for guiding me during the course of my doctoral studies. The joy and the enthusiasm they share for pursuing research have always been a constant source of motivation, especially during challenging times. I cannot thank them enough for providing this great opportunity and making sure that I had access to all the latest tools and equipments for pursuing scientific research. I have greatly benefitted from their vast experience and knowledge, which has always inspired me to strive harder in my pursuit of a PhD degree.

I would also like to express my gratitude to Dr. Fan Bill-Cheung for being my mentor at Pennsylvania State University and a constant support during my graduate studies. I am thankful to all my committee members at Georgia Tech, Dr. Mostafa S. Ghiaasiaan, Dr. Muhannad S. Bakir and Dr. Seung Soon Jang for reviewing my PhD thesis and providing their important feedback.

I am grateful to all the staff members at the Nanotechnology Research Center and Micro-electronics Research Center, who have always offered invaluable help and guidance with micro-fabrication tools and processes in the cleanroom. I would also like to thank the staff in the Electronic and Machine shops of George W. Woodruff School of Mechanical Engineering for assisting me in building the experimental test setup.

It is my pleasure to thank my friends and colleagues, who have contributed immensely to my personal and professional experience at Georgia Tech. They have truly made my stay at Tech quite enjoyable and it would have been impossible to complete my doctoral degree without their support and encouragement.

I'll like to acknowledge the financial support of the Interconnect Focus Center, one of five research centers funded under the Focus Center Research Program, a DARPA and Semiconductor Research Corporation program.

Thank you.

Shankar Narayanan

TABLE OF CONTENTS

LIST OF TABLES

LIST OF FIGURES

LIST OF SYMBOLS AND ABBREVIATIONS

Nomenclature for Chapters 2 and 3

A_{hs}	Area of hotspot (m^2)
C_p	Specific heat (J/kgK)
d	Diameter (m)
$D_{k,i}$	Knudsen diffusion coefficient for species I (m^2/s)
D_{memb}	Diffusion coefficient for transport of vapor across the membrane (m^2/s)
$D_{m,i}$	Molecular diffusion coefficient for species i in air-vapor mixture (m^2/s)
h_{fg}	Latent heat of evaporation of the coolant (J/kg)
$\overline{h}_m$	Average mass transfer coefficient of vapor at membrane outlet (m/s)
$\overline{h}_o$	Average heat transfer coefficient at membrane outlet (W/m^2K)
k	Thermal conductivity (W/mK)
K	Permeability of the membrane (m^2)
$\dot{m}$	Mass flow rate (kg/s)
$\overline{Nu}$	Average Nusselt number due to jet impingement at the outlet of membrane
$P(r)$	Fluid pressure in the film region as a function of radial coordinate r (Pa)
$\overline{\Delta P}$	Non-dimensional pressure drop, $\Delta\overline{P} = \left[P(r) - P_o\right] \Big/ \rho_{film} V_o^2$, (Pa)
P_o	Inlet pressure for radial in-flow in the film region, (Pa)
Pr	Prandtl number
Q_{1-7}	Heat conducted at the boundaries of film and membrane regions (W)

$\bar{r}$ Non-dimensional radial coordinate, $\bar{r} = 2r / d_{memb}$

R Resistances to heat and mass transfer

Re Reynolds number for flow in the film region, $\mathrm{Re} = V_o \delta_{film} / \left(2\nu_{film}\right)$

$\overline{\mathrm{Re}}$ Modified Reynolds number, $\bar{R}e = \mathrm{Re} \cdot \xi$

Re_{jet} Reynolds number for air flowing out of jet nozzle, $\mathrm{Re}_{jet} = {u_{jet} d_{jet}} / {\nu_{air}}$

s_{NM} Separation distance between the nozzle of the jet and the membrane (m)

T Temperature (K)

u_{jet} Average velocity of air from the jet nozzle (m/s)

$VFRAC$ Fraction of volume occupied by vapor phase in the membrane, δ_2 / δ_{memb}

V_o Velocity of fluid at the inlet of the film region (m/s)

V_r Radial component of velocity of flow in the film region (m/s)

$\bar{V}_r$ Non-dimensional radial velocity, $\bar{V}_r = {V_r} / {V_o}$ (m/s)

x_i Mole fraction of species i in a mixture of vapor and air

y A spatial coordinate used in cylindrical coordinate system, (m)

$\bar{y}$ Non-dimensional spatial coordinate in cylindrical coordinate system, $\bar{\mathrm{y}} = \mathrm{y} / \delta_{film}$

Greek Symbols

α_i A non-dimensional variable used to evaluate D_{memb}, $\alpha_i = 1 - \left(\frac{MW_i}{MW_\Sigma} \right)^{1/2}$

δ_1 Spacing between liquid vapor interface and the membrane inlet, (m)

δ_2 Spacing between liquid vapor interface and the membrane outlet, (m)

δ_{film} Film thickness, (m)

δ_{memb} Membrane thickness, $\delta_{memb} = \delta_1 + \delta_2$, (m)

ε Porosity of the membrane

λ A non-dimensional variable to denote $\sqrt{\frac{\overline{Re}\left(\overline{r}^2 - 1\right)}{2\overline{r}^2 \ln \overline{r}}}$

ν Kinematic viscosity, (m^2/s)

μ Dynamic viscosity, (kg/ms)

ρ Density, (kg/m^3)

Ψ A non-dimensional variable to denote the quantity $\frac{\dot{m} C_p \delta}{k A_{hs}}$

τ Tortuosity of the membrane

ξ A non-dimensional variable to denote δ_{film} / d_{memb}

Subscripts and Superscripts

amb Ambient conditions

film Film region $\left(0 \le y \le \delta_{film}\right)$

in, air Inlet condition for air

inl Inlet to the membrane

int Liquid-vapor interface

l Liquid phase

lm Effective thermal properties for liquid occupying the membrane region

memb Membrane region $\left(\delta_{film} \le y \le \delta_{film} + \delta_{memb}\right)$

out	Outlet of the membrane
out, air	Outlet conditions for air-vapor mixture
$surf$	Surface of the hot-spot
v	Vapor phase
vm	Effective thermal properties for vapor occupying the membrane region

Nomenclature for Chapter 6

A	Hamaker's Constant (J)
d	Diameter of water molecule (m)
e	Elementary charge (C)
G	Gibbs free energy (J)
h	Planck's constant (6.626068×10^{-34} m^2kg/s)
h_{fg}	Enthalpy of vaporization (J/kgK)
k_B	Boltzmann constant (1.3806503×10^{-23} $m^2kgs^{-2}K^{-1}$)
k_l	Thermal conductivity of the liquid (W/mK)
Kn	Knudsen number for vapor diffusion in a nano-capillary
M	Molecular weight (kg/kmole)
N	Number of moles of evaporating/condensing molecules (mole)
N_A	Avogadro's constant
$\dot{m}_o'', \dot{m}_o$	Mass flux and mass flow rate at reference conditions, respectively (kg/m^2s, kg/s)
n	Refractive index of a medium

p_{atm}	Atmospheric pressure (Pa)
p_l, p_v	Pressure of liquid and partial pressure of vapor phase, respectively (Pa)
$p_{vi}, p_{v,eq}$	Equilibrium vapor pressure of curved and flat interface, respectively (Pa)
$\dot{q}_a, \dot{q}_c$	Rate of heat advection and conduction, respectively (W)
R	Universal gas constant (J/kmolK)
r	Radial coordinate (m)
r_c	Radius of the capillary or pore (m)
r_i	Radial position of the interface (m)
t_e	Equilibrium thickness of the adsorbed film (m)
T_l, T_v	Temperature of the liquid and gas phase, respectively (K)
u_l, v_l	Axial and radial components of the liquid velocity inside the meniscus, respectively (m/s)
V_m	Molar volume of the evaporating liquid (m^3/kmol)
w_{li}	Velocity of the liquid phase normal to the interface (m/s)
x	Axial coordinate (m)
Z	Charge of a dissociated ion

Greek Symbols

ε	Dielectric constant
ε_o	Permittivity of free space
κ	Curvature of the meniscus (m^{-1})
μ_l	Absolute viscosity of the liquid (kg/ms)
$\hat{\mu}$	Chemical potential (J/kmol)

ν_e	Absorption frequency (s^{-1})
Π_d	Disjoining pressure (Pa)
ρ_l, ρ_v	Density of liquid and vapor phase, respectively (kg/m^3)
σ	Surface tension of liquid (N/m)
$\hat{\sigma}$	Accommodation coefficient
θ	Slope of the interface at any axial location

Nomenclature for Chapter 7

c_{pa}, c_{pl}	Specific heat of air and liquid phase, respectively (J/kgK)
d_h	Characteristic hydraulic diameter of the microchannel (m)
D_k	Diffusion coefficient for vapor transport in the membrane pores (m^2/s)
h_m	Mass transfer coefficient at the surface of the membrane due to air jet impingement (m/s)
h_{mem}	Heat transfer coefficient at the surface of the membrane due to air jet impingement (W/m^2K)
h_{si}	The average heat transfer coefficient on the side walls of silicon substrate (W/m^2K)
k_a, k_l	Thermal conductivity of air and liquid phase, respectively (W/mK)
k_{al}	Thermal conductivity of alumina (W/mK)
k_l	Thermal conductivity of the evaporating liquid (W/mK)
k_m	Average thermal conductivity of the membrane (W/mK)

k_s	Thermal conductivity of the substrate (Silicon and Pyrex) (W/mK)
k_v	Thermal conductivity of the vapor phase (W/mK)
L	Characteristic length of the microchannel (m)
$\dot{m}''$	Mass flux of the vapor phase due to evaporation at the interface (kg/m^{2}s)
M_l	Molecular weight of the evaporating liquid (kg/kmol)
p_a, p_l	Pressure of air and liquid phase, respectively (Pa)
p_{atm}	Atmospheric pressure (Pa)
Pr	Prandtl's number
$p_{v,eq}$, p_{vi}	Equilibrium vapor pressure of a flat and curved interface, respectively (Pa)
$\dot{q}''_{hs}$	Net heat flux dissipated at the hotspot (W/m^2)
$\dot{q}'''_m$	Volumetric heat sink in the membrane due to evaporation (W/m^3)
$\dot{q}'''_s$	Volumetric heat source in the Pyrex due to joule heating at the hotspot (W/m^3)
R	Universal gas constant (J/kmolK)
T_a,T_l	Temperature of the air and liquid phase, respectively (K)
T_m,T_s	Temperature of the membrane and substrate (Silicon and Pyrex), respectively (K)
T_{li},T_{vi}	Temperature of the liquid and vapor phase at the interface, respectively (K)
T_{ref}	Reference temperature, 300 K
T_{vo}	Temperature of the vapor phase at the outlet of the membrane (K)

u_{ax}, u_{ar}	Axial and radial components of air flow, respectively (m/s)
u_{lx}, u_{ly}	Velocity components of the liquid flow, respectively (m/s)
u_o	Average velocity of the air jet impingement (m/s)
Vi	Viscous number
$X_{v,eq}, X_{vi}$	The equilibrium and interfacial mole fractions of vapor phase, respectively
$X_{vo}, X_{v\infty}$	Mole fractions of vapor phase at the membrane outlet and in the ambient, respectively

Greek symbols

δ_l, δ_m	Thickness of the liquid film and membrane, respectively (m)
δ_v	The length of the vapor column inside a cylindrical pore of the membrane (m)
ε	Membrane porosity
μ_a, μ_l	Dynamic viscosity of air and liquid phase, respectively (kg/ms)
ρ_a, ρ_l	Density of air and liquid phase, respectively (kg/m^3)
$\hat{\sigma}$	Accommodation coefficient

SUMMARY

A novel cooling mechanism based on evaporation of thin liquid films is presented for thermal management of confined heat sources, such as microprocessor hotspots, high power light emitting diodes and RF packages with a high operational frequency. A thin nanoporous membrane (~1-5μm) is utilized to maintain microscopically thin liquid films (~1-5μm) by capillary action, while providing a pathway for the vapor generated due to evaporation at the liquid-vapor interface. The vapor generated by evaporation is continuously removed by using a dry sweeping gas, keeping the membrane outlet dry. This thesis presents a detailed theoretical, computational and experimental investigation of the heat and mass transfer mechanisms that result in cooling the confined heat sources.

Performance analysis of this cooling mechanism demonstrates heat fluxes over 600W/cm^2 for sufficiently thin membrane and film thicknesses (~1-5μm) and by using air jet impingement for advection of vapor from the membrane surface. Based on the results from this performance analysis, a monolithic micro-fluidic device is designed and fabricated incorporating micro and nanoscale features. This MEMS/NEMS device serves multiple functionalities of hotspot simulation, temperature sensing, and evaporative cooling. Subsequent experimental investigations using this microfluidic device demonstrate heat fluxes in excess of 600W/cm^2 at 90 ^{o}C using water as the evaporating coolant.

In order to further enhance the device performance, a comprehensive theoretical and computational analysis of heat and mass transfer at micro and nanoscales is carried out. Since the coolant is confined using a nanoporous membrane, a detailed study of

evaporation inside a nanoscale cylindrical pore is performed. The continuum analysis of water confined within a cylindrical nanopore determines the effect of electrostatic interaction and Van der Waals forces in addition to capillarity on the interfacial transport characteristics during evaporation. The detailed analysis demonstrates that the effective thermal resistance offered by the interface is negligible in comparison to the thermal resistance due to the thin film and vapor advection. In order to determine the factors limiting the performance of the MEMS device on a micro-scale, a device-level detailed computational analysis of heat and mass transfer is carried out, which is supported by experimental investigation. Identifying the contribution of various simultaneously occurring cooling mechanisms at different operating conditions, this analysis proposes utilization of hydrophilic membranes for maintaining very thin liquid films and further enhancement in vapor advection at the membrane outlet to achieve higher heat fluxes.

CHAPTER 1

INTRODUCTION

In order to sustain a remarkable reduction in the electronic product cost per function (~ 30% every year), the semiconductor industry pursues enhancement in equipment productivity, manufacturing yield, and most importantly, functionality (i.e., the number of bits, logic gates, transistors, etc. incorporated into a die). Consequently, an increase of merely 12% in chip area accommodates 40-60% more functionality per annum. At the same time, a continuous reduction of about 30% in feature sizes is observed every year [1]. While an overall increase in functionality has resulted in higher power dissipation, thermal management is further exacerbated by large leakage currents due to shrinking feature sizes. In addition, clustering of functional units on the microprocessor to enhance computational performance creates hotspots, requiring efficient heat dissipation from these confined areas. A failure to address hotspot thermal management can cause localized heating, resulting in substantial temperature gradients detrimental to chip performance and reliability [2]. Hence, a comprehensive chip-level thermal management solution requires an effective cooling mechanism that can dissipate large heat fluxes from hotspots and that can be seamlessly integrated with a suitable background cooling system.

Unlike air cooling, which is traditionally used for thermal management of microprocessors and has a fundamental limit on maximum heat flux that can be dissipated, liquid coolants have the advantage of utilizing the latent heat of vaporization by undergoing a change in phase, in addition to very efficient convective cooling; this

results in much greater power dissipation while maintaining a lower and uniform surface temperature. For instance, at chip (junction) temperatures close to 85 ^{o}C, pool boiling of dielectric fluorocarbon FC72 can dissipate heat fluxes of the order of 50 W/cm^2, while air-cooled heat sinks of an equivalent size can support only 0.1 W/cm^2 [3]. Though phase change has an appealing potential for heat transfer enhancement, limitations do exist to its implementation in applications with higher heat load. The highest heat flux achievable by boiling or evaporation depends on the thermo-physical properties of the coolant and hydrodynamics of two-phase flow. While boiling or phase change in the bulk of liquid near the heat source is a feasible option for hotspot thermal management, it requires the surface to exceed saturation temperature and is bounded by the Critical Heat Flux (CHF). At atmospheric pressure, CHF for saturated pool boiling is in the range of 15–25 W/cm^2 for FC72 and 100–120 W/cm^2 for water [4], which can be further enhanced by incorporating micro-textured surfaces (e.g., yielding 105 W/cm^2 for pool boiling of saturated FC72 [3]). A comparison of different cooling mechanisms currently in development for high heat dissipation is summarized by Agostini et al [5]. This study also lists the maximum heat flux corresponding to a junction temperature of 85 ^{o}C using jet impingement, single and two-phase flow in microchannel and porous media. Table 1.1 is a brief comparison of the highest performing cooling methods on the basis of heat flux dissipated for a particular junction temperature.

The dissipation of heat by evaporation of thin films has been previously demonstrated in various cooling systems. Evaporation from thin films in spray and mist cooling systems has been studied for thermal management of electronic devices. For example, Amon et al.[6] proposed a MEMS-based evaporative, spray cooling device for

high heat flux electronics, demonstrating the effect of incorporating microstructures to promote thinner films and consequently to enhance heat flux. Under certain conditions, while no boiling was observed, evaporation through the thin liquid film within the grooves of microstructures became significant. As the surface temperature increased, they observed that the thin film broke apart, leading to a dry spot. A uniform heat flux of 45 W/cm^2 was demonstrated at a mass flux of only 33.2 g/cm^2min using HFE-7200 dielectric coolant.

Table 1.1 Literature summary of maximum heat flux dissipated by different cooling mechanisms

Cooling Mechanism	Heat Flux
Single phase flow in microchannels (Pijnenberg et al.[7])	450 W/cm^2 (at T=85^oC with DI water and silicon microchannels)
Single phase flow in porous media (Hetsroni et al.[8])	416 W/cm^2 (at T=85^oC with stainless-steel sintered particles)
Single phase, multi-jet impingement cooling (Overholt et al. [9])	471 W/cm^2 (at T=85^oC with DI water)
Two-phase flow in microchannels with sub-cooling (Faulkner et al. [10])	275 W/cm^2 (at T=125 ^oC with water in horizontal, rectangular channels with inlet temperature of 10 ^oC)
Two-phase flow in microchannels with sub-cooling (Kosar et al. [11])	250 W/cm^2 (at T=160 ^oC with water in horizontal, rectangular channels with inlet temperature of 20 ^oC)
Two-phase flow in porous media (Chen et al. [12])	80 W/cm^2 (Water, Copper sintered particles)

Kim et al.[13] have experimentally demonstrated the effect of water evaporation and microporous coating on cooling. The heat transfer coefficient achieved for evaporative cooling with microstructures was approximately 0.05 W/cm^2K with a heat flux of almost 2 W/cm^2. The use of microstructures to maintain thin films and enhance cooling has also been explored by Li and Peterson [14, 15], who have demonstrated high heat fluxes (CHF ~ 370 W/cm^2) using boiling and evaporation as the mode of heat transfer for thin

capillary wicking structures. A theoretical study of cooling enhancement in finned heat exchangers using thin film evaporation was carried out by Ho Song et al.[16], and a performance investigation of evaporatively cooled, plain and finned tube heat exchangers was conducted by Hasan et al.[17]. In both cases a considerable increase in heat transfer was observed.

In the case of evaporation, phase change occurs at the free surface of the liquid film. The rate of heat transfer is controlled by two resistances – conduction/convective resistance across the film and mass transfer resistance for vapor transport from the evaporation interface to the ambient environment. The film conduction/convection resistance is primarily controlled by the film thickness, while the mass transfer resistance for removal of the vapor phase is controlled by three factors: the mass transfer coefficient, which depends upon the velocity and flow mode, the relative humidity or dryness of the sweeping gas blown over the film and the saturation density of the liquid that is being evaporated. Since these resistances act in series, it is important to minimize both of them to achieve the highest rate of heat transfer using evaporation.

The concept of gas assisted evaporative cooling (GAEC) for thermal management of high density electronic modules was first demonstrated with heat fluxes in the order of 20 W/cm^2 [4, 18]. The underlying idea in this case was to inject a gas stream into a channel to effectively disperse a liquid coolant flowing within the channel, thereby promoting its evaporation and increasing heat transfer. However, the formation of dry spots in thin films, where liquid is fully evaporated and not replenished, leads to a local decrease in the heat transfer coefficient, resulting in an increase of the surface temperature and eventually in failure of the cooling system. Thus, the main challenge associated with

developing an efficient and reliable evaporative cooling system is in maintaining a very thin and stable liquid film on the surface being cooled, which has not been successfully accomplished thus far.

Although considerable success with evaporative cooling has been reported, sustained evaporation with potentially higher heat fluxes from confined spaces has not yet been demonstrated. To address the issue of maintaining a stable liquid film with controllable thickness and at the same time maximizing mass transfer of the vapor phase for enhanced evaporation, a new cooling scheme (termed as "Perspiration Nanopatch") has been recently proposed, as shown schematically in Figure 1.1 [19]. A working fluid is pumped into a micro-fabricated cavity of desired dimensions so that the film thickness is imposed by the structure of the cavity, rather than by flow conditions which are not easily controllable. This allows for precise control of the liquid film, making it as thin as possible (~1 μm) to minimize thermal resistance, yet removing the possibility of local dry-out, as sufficient pressure head is provided for a constant coolant supply to maintain the cavity filled. To enable evaporation from the free surface of the cavity, the capping wall of the cavity (see Figure 1.1) is made of a highly porous membrane with a dense array of holes to provide a route for evaporating vapor, which is entrained by the dry sweeping gas. The use of a highly porous membrane with small pore sizes (~50-100 nm) imposes a significant capillary force on the liquid, which can support large pressure difference between the liquid inside the cavity and the ambient, confining fluid within the cavity. Since the capillary forces are inversely proportional to the pore size, the nano-porous membranes with 100 nm pores for instance, can support a pressure difference of the order of 0.2 MPa in the case of FC72 and 1.5 MPa in case of water at room

temperature. The capillary forces are controlled or enhanced by selective chemical functionalization of the membrane surface in contact with working fluid, e.g., by a hydrophobic coating inside of the perforated holes. At the same time, the overall mass transfer of vapor-phase is maximized by utilizing jet impingement of dry sweeping gas atop the membrane.

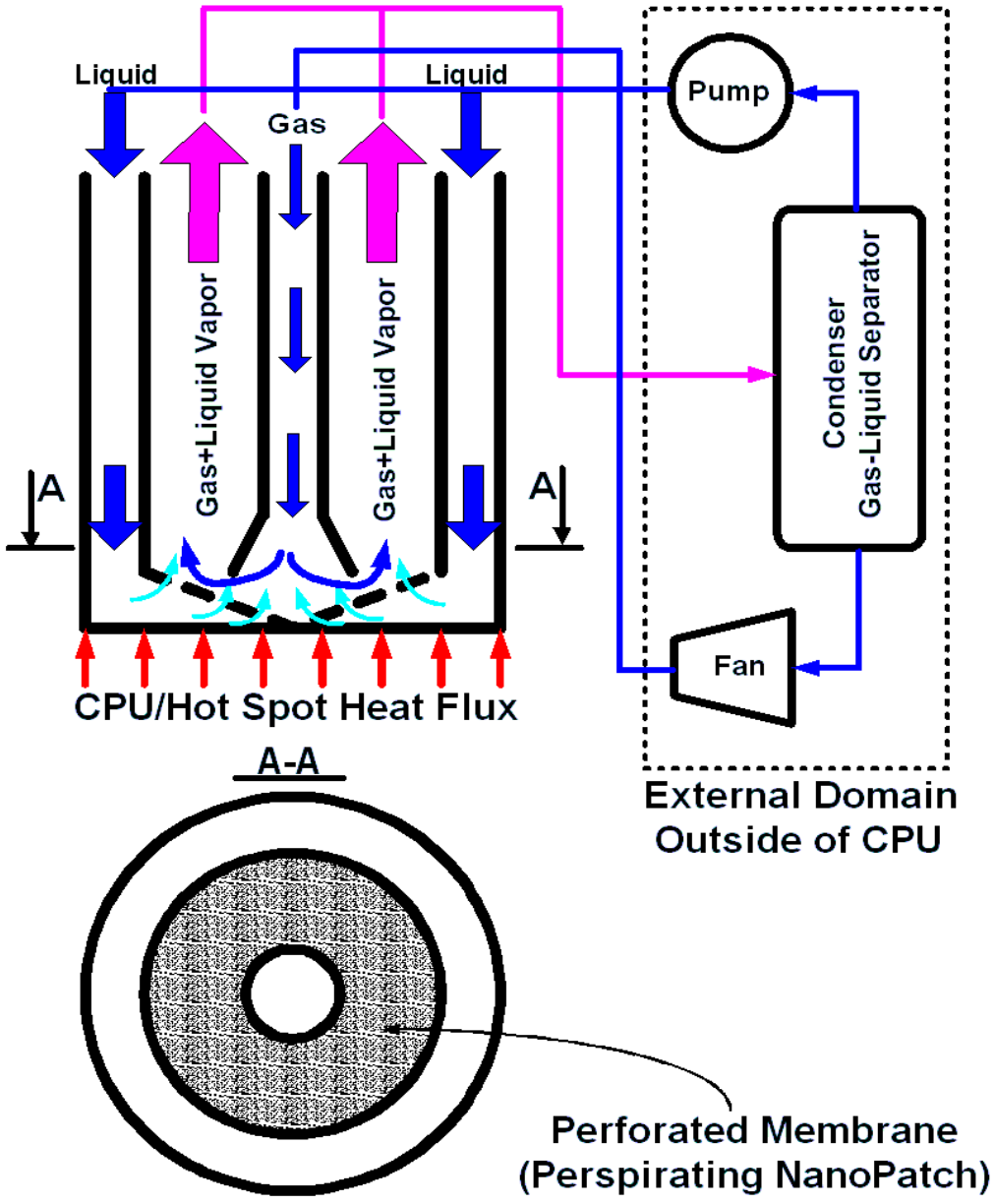

Figure 1.1 Schematic diagram describing the operation of Perspiration Nanopatch

CHAPTER 2

PRELIMINARY ANALYSIS OF GAS-ASSISTED THIN FILM EVAPORATION

A theoretical analysis of thin film evaporation is carried out with emphasis on determining the achievable cooling performance. The analysis uses classical models to couple heat and mass transfer processes in liquid and gas phases, including a semi-permeable membrane, to yield a physically-insightful yet mathematically-simple, closed-form expressions for dissipated heat flux as a function of key operating parameters. The computational results presented herein allow one to predict the performance of a micro-fabricated device under typical heat load conditions expected in electronics cooling applications. Interestingly, and contrary to popular belief, it is also demonstrated why volatile liquids such as fluorocarbons (e.g. FC72) should offer performance superior to water in gas-assisted evaporative cooling schemes, even though the thermo-physical properties of water (for e.g., thermal conductivity) are far superior. Dissipation of large heat fluxes with practical flow rates (of both coolant and sweep gas) and pumping requirements is demonstrated, establishing the suitability of this cooling mechanism for dissipation of heat from confined spaces.

2.1 Physical Arrangement and Model Development

2.1.1 Analysis of heat and mass transfer

To obtain the limits on performance and for the sake of simplicity, the tapered structure of the nano-patch, as shown in Figure 1.1, is replaced by a uniform thickness

layer and all the interfacial resistances in this analysis are neglected. The model assumes one-dimensional heat and mass transfer, thermal equilibrium between the coolant and the membrane structure, and saturation condition at the liquid vapor interface. Analysis of heat and mass transfer through porous membrane modules was carried out using simplifying assumptions, as described in membrane distillation (MD) and thermal management applications [20-25]. The heat transfer coefficient due to air jet impingement at the outlet of the membrane is obtained using Martin's correlation [26, 27], and analogy between heat and mass transfer (Chilton and Colburn Analogy [28, 29]) is utilized to obtain the mass transfer coefficient.

One of the variables essential for carrying out the performance analysis is the position of the liquid vapor (LV) interface in the membrane. The position of the LV interface inside the membrane is taken as an input parameter in carrying out the performance analysis. With water as the coolant, the LV interface coincides with the entrance of the pores in a hydrophobic membrane (as described in MD applications [22-25]). On the other hand, the location of the interface cannot be readily ascertained in the case of a partially hydrophobic or hydrophilic membrane, as the membrane could either be partially or completely flooded with the working fluid. Hence, the performance analysis is conducted by providing the position of the interface as an input depending on the type of membrane used.

In order to obtain the temperature distribution of the working fluid inside the liquid film and the membrane region, the steady-state one-dimensional conservation of energy is applied to a differential control volume (Figure 2.1):

$$0 = kA_{hs}\left(d^2T/dy^2\right) - \dot{m}C_p\left(dT/dy\right) \tag{2.1}$$

where k and C_p are the temperature dependent effective thermal conductivity and the specific heat of the coolant occupying the differential control volume, respectively, A_{hs} is the area of the hotspot, and $\dot{m}$ is the mass flow rate of the coolant.

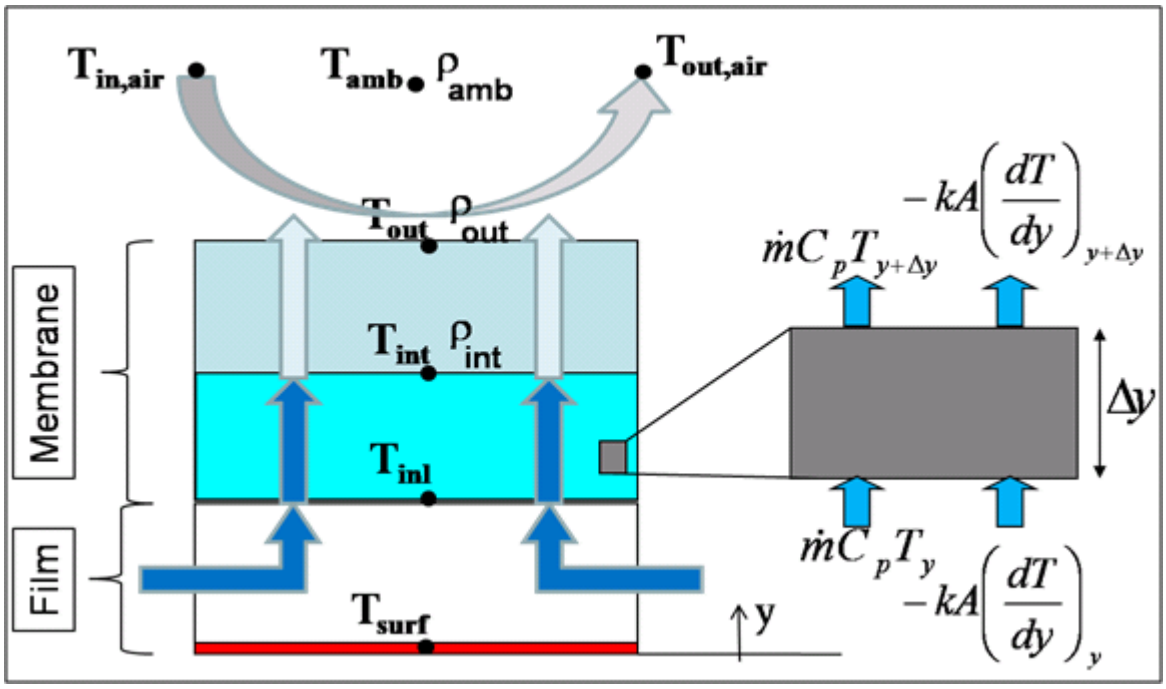

Figure 2.1 Schematic diagram illustrating a differential control volume and the temperature and density evaluated at various interfaces

The governing equation, given by equation (2.1), is applicable to both the liquid and vapor phases occupying the film and membrane regions, but with appropriate values for effective thermal conductivity and specific heat. The effective thermal conductivity of the film and the membrane regions are obtained using the porosity of the metallic mesh and the membrane, respectively, as corroborated by the analysis of heat and mass transfer in MD applications [26]. The boundary conditions applicable (Figure 2.1) are:

$$T\big|_{y=0} = T_{surf} \tag{2.2}$$

$$-k_{vm}\left(dT/dy\right)\Big|_{y=\delta_{memb}+\delta_{film}} = \bar{h}_o\left(T_{out} - T_{in,air}\right) \tag{2.3}$$

where $\bar{h}_o$ is the heat transfer coefficient at the outlet of the membrane, while T_{out} is the temperature at the surface of the membrane. Applying the governing equation (2.1) to different domains shown in Figure 2.1, for any given surface temperature T_{surf}, inlet temperature of air $T_{in,air}$, position of LV interface within a membrane and convective heat transfer coefficient $\bar{h}_o$ due to air impingement, the temperature distribution can be obtained in the film and membrane regions in terms of unknown junction temperatures, namely T_{inl}, T_{int} and T_{out}. For instance, the temperature distribution in the fluid film region ($y = 0$ to $y = \delta_{film}$, with boundaries maintained at T_{surf} and T_{inl}, respectively) is given by:

$$T = T_{surf}\left[\frac{\exp\left(\frac{\dot{m}C_{p,film}\delta_{film}}{k_{film}A_{hs}}\right) - \exp\left(\frac{\dot{m}C_{p,film}y}{k_{film}A_{hs}}\right)}{\exp\left(\frac{\dot{m}C_{p,film}\delta_{film}}{k_{film}A_{hs}}\right) - 1}\right] - T_{inl}\left[\frac{1 - \exp\left(\frac{\dot{m}C_{p,film}y}{k_{film}A_{hs}}\right)}{\exp\left(\frac{\dot{m}C_{p,film}\delta_{film}}{k_{film}A_{hs}}\right) - 1}\right] \tag{2.4}$$

Using the temperature distributions in different regions, the rates of heat conduction at the boundaries of these regions, Q_i's (where i = 1 to 7 as shown in Figure 2.2) can be evaluated. For example, it can be shown that Q_1 is given by the following equation:

$$Q_1 = -k_{film}A_{hs}\left.\frac{dT}{dy}\right|_{y=0} = \dot{m}C_{p,film}\left(T_{surf} - T_{inl}\right)\frac{\exp\left(\frac{\dot{m}C_{p,film}\delta_{film}}{k_{film}A_{hs}}\right)}{\exp\left(\frac{\dot{m}C_{p,film}\delta_{film}}{k_{film}A_{hs}}\right) - 1} \tag{2.5}$$

It is to be noted that the formulation presented herein differs from the stagnant film theory, wherein the mass transfer across a membrane is assumed to take place across a

stagnant film. With diffusion being the principal mode of solute transport in the stagnant film theory, the rate of mass transfer depends only on the diffusivity and the thickness of the membrane [30]. In our case, the net rate of heat transfer is obtained considering both convection and diffusion. As a result the final expression derived for the rate of heat transferred across the fluid membrane differs from the stagnant film model. The equations that relate heat transferred at the junction of adjacent regions namely, $Q_2 = Q_3$, $Q_4 - Q_5 = \dot{m} h_{fg,\text{int}}$, $Q_6 = Q_7$ and $Q_7 = Q_8$ (see Figure 2.2), provide information necessary for evaluating the unknown temperatures. These equations are sequentially listed as follows:

$$\dot{m} C_{p,film} \left(T_{surf} - T_{inl} \right) \frac{\exp \Psi_1}{\exp \Psi_1 - 1} = \dot{m} C_{p,lm} \left(T_{inl} - T_{\text{int}} \right) \frac{1}{\exp \Psi_2 - 1} \tag{2.6}$$

$$\dot{m} C_{p,lm} \left(T_{inl} - T_{\text{int}} \right) \frac{\exp \Psi_2}{\exp \Psi_2 - 1} - \dot{m} C_{p,vm} \left(T_{\text{int}} - T_{out} \right) \frac{1}{\exp \Psi_3 - 1} = \dot{m} h_{fg,\text{int}} \tag{2.7}$$

$$\dot{m} C_{p,vm} \left(T_{\text{int}} - T_{out} \right) \frac{\exp \Psi_3}{\exp \Psi_3 - 1} = \bar{h}_o A_{hs} \left(T_{out} - T_{in,air} \right) \tag{2.8}$$

$$\bar{h}_o A_{hs} \left(T_{out} - T_{in,air} \right) = \dot{m}_{air} C_{p,air} \left(T_{out,air} - T_{in,air} \right) \tag{2.9}$$

where $\Psi_1 = \left(\frac{\dot{m} C_{p,film} \delta_{film}}{k_{film} A_{hs}} \right)$, $\Psi_2 = \left(\frac{\dot{m} C_{p,lm} \delta_1}{k_{lm} A_{hs}} \right)$, $\Psi_3 = \left(\frac{\dot{m} C_{p,vm} \delta_2}{k_{vm} A_{hs}} \right)$, are nondimensional numbers relating the rate of advection to diffusion (Peclet Number). δ_1 and δ_2 are the spacing between membrane inlet and outlet from the LV interface, respectively.

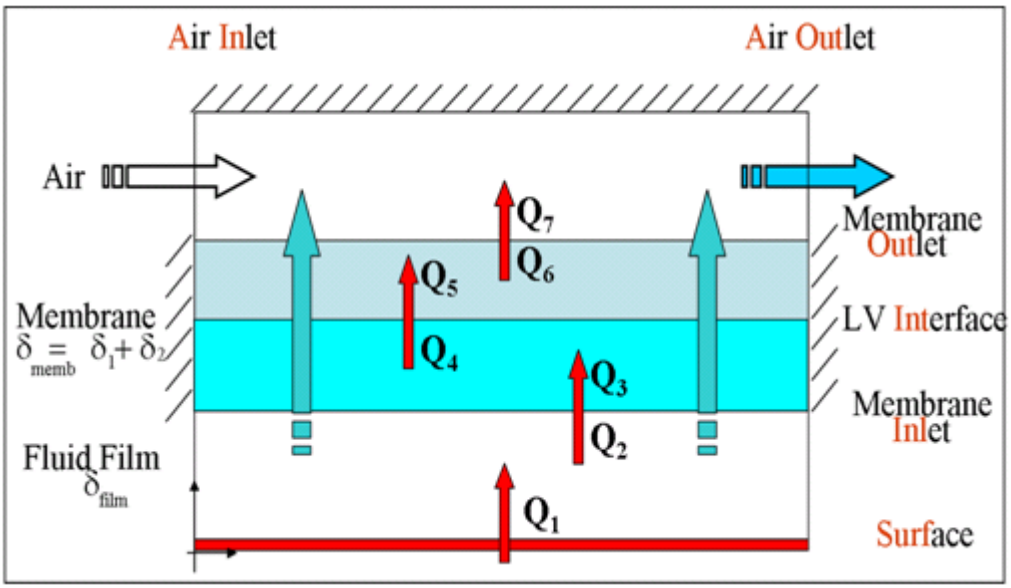

Figure 2.2 Schematic diagram illustrating heat and mass transfer between adjacent regions

It is important to note that equations (2.6)-(2.9) can be solved to obtain the temperature distribution only if mass flow rate of the coolant $\dot{m}$ is known. The overall mass transfer resistance R_{total} being dominated by transport of vapor phase, the mass flow rate is given by analyzing diffusion of vapor phase through the membrane and advection by the dry sweep gas. The mass flow rate is hence obtained by the following expression:

$$\dot{m} = \frac{\rho_{v,\text{int}} - \rho_{v,amb}}{R_{total}} = \frac{\rho_{v,\text{int}} - \rho_{v,amb}}{1/\left(\bar{h}_m A_{hs}\right) + \delta_2/\left(D_{memb} A_{hs}\right)} \tag{2.10}$$

where $\rho_{v,\text{int}}$ and $\rho_{v,amb}$ are the density of vapor phase at the LV interface and the ambient, respectively, $\bar{h}_m$ is the average mass transfer coefficient at the membrane outlet, and D_{memb} is the diffusion coefficient for the vapor phase through the membrane. The diffusion coefficient for vapor transport inside the membrane D_{memb} (corresponding to

Knudsen number lying between 0.01 and 10), is obtained from the Knudsen ($D_{k,i}$) and molecular ($D_{m,i}$) diffusion coefficients as:

$$D_{memb} = \frac{\varepsilon}{\tau}\left(\frac{1 - \alpha_i x_i}{D_{m,i}} + \frac{1}{D_{k,i}} \right)^{-1} \tag{2.11}$$

where $\alpha_i = 1 - \left(\frac{MW_i}{MW_\Sigma} \right)^{1/2}$, ε is the porosity of the membrane and τ is the tortuosity of the membrane, x_i is the mole fraction of species 'i' (vapor in this case) in a mixture of vapor and air, and MW_i and MW_Σ are the molecular masses of species 'i' and the mixture.

At the outlet of the membrane, jet impingement offers an efficient means for heat and mass transfer. One of the most widely used correlations for evaluating the heat transfer coefficient in a single-jet air impingement is due to Martin[26], who recommends the following equation after compiling data from several sources (e.g.[26, 27]).

$$\frac{\overline{Nu}}{\mathrm{Pr}^{0.42}} = G\left(A_r, {s_{NM}}/{d_{jet}} \right)\left[2\,\mathrm{Re}_{jet}^{0.5}\left(1 + 0.005\,\mathrm{Re}_{jet}^{0.55}\right)^{0.5} \right] \tag{2.12}$$

where $\overline{Nu} \equiv \frac{\bar{h}_o d_{jet}}{k_{air}}$, $\mathrm{Re}_{jet} = {u_{jet} d_{jet}}/{\nu_{air}}$, $A_r = d_{jet}^2 / d_{hs}^2$, s_{NM} is the separation between the nozzle and membrane, and the function $G = 2A_r \frac{1 - 2.2A_r^{0.5}}{1 + 0.2\left({s_{NM}}/{d_{jet}} - 6 \right)A_r^{0.5}}$. The range of validity for this correlation is defined by $2000 \le \mathrm{Re}_{jet} \le 400{,}000$, $2 \le {s_{NM}}/{d_{jet}} \le 12$ and $0.004 \le A_r \le 0.04$.

Equation (2.12) is used for evaluating the heat transfer coefficient, $\overline{h}_o$ at the outlet of the membrane. Using the correlation for evaluating average Nusselt number and Chilton-Colburn's analogy between heat and mass transfer[28, 29], one can predict the average mass transfer coefficient over a wide range of Pr and Sc numbers. Hence, equations (2.6)-(2.10) yield a set of five equations which are simultaneously solved for five unknown variables T_{inl}, T_{int}, T_{out}, $T_{out,air}$ and $\dot{m}$ for a given set of input parameters, taking into account the variation of thermophysical properties with temperature. Since the equations are rendered non-linear due to presence of temperature dependent thermophysical properties, they were solved using the method of successive approximations. The temperature dependence of property values of air, FC72 [31] and water used for obtaining simulation results are listed in Table 2.1 and Table 2.2.

Table 2.1 Thermophysical properties of Air as a function of temperature.

$$C_5 \cdot T^{5.0} + C_4 \cdot T^{4.0} + C_3 \cdot T^{3.0} + C_2 \cdot T^{2.0} + C_1 \cdot T + C_0$$

	Property	Function
1	ρ	$C_5 = -3.07\times10^{-13}, C_4 = 5.99\times10^{-10}, C_3 = -4.86\times10^{-7}$ $C_2 = 2.1\times10^{-4}, C_1 = -5.1\times10^{-2}, C_0 = 6.58\times10^{0}$
2	ν	$C_5 = -7.91\times10^{-20}, C_4 = 1.81\times10^{-16}, C_3 = -2.01\times10^{-13}$ $C_2 = 2.05\times10^{-10}, C_1 = 7.05\times10^{-9}, C_0 = -6.47\times10^{-7}$
3	k	$C_5 = -7.69\times10^{-22}, C_4 = 1.25\times10^{-18}, C_3 = 4.64\times10^{-12}$ $C_2 = -2.9\times10^{-8}, C_1 = 9.04\times10^{-5}, C_0 = 1.0\times10^{-3}$
4	Pr	$C_5 = 2.36\times10^{-14}, C_4 = -4.57\times10^{-11}, C_3 = 3.56\times10^{-8}$ $C_2 = -1.35\times10^{-5}, C_1 = 2.2\times10^{-3}, C_0 = 6.31\times10^{-1}$

Table 2.2 Thermophysical properties of FC72 and Water as a function of temperature.

$$C_6 \cdot T^{6.0} + C_5 \cdot T^{5.0} + C_4 \cdot T^{4.0} + C_3 \cdot T^{3.0} + C_2 \cdot T^{2.0} + C_1 \cdot T + C_0$$

	Fluid Properties	FC72 ($C_i = 0$ unless a value is specified)	Water ($C_i = 0$ unless a value is specified)
1	ρ_l (kg/m3)	$C_1 = 2.61, C_0 = 1.03\times10^3$	$C_0 = 9.98\times10^2$
2	ρ_v (kg/m3)	$C_6 = 2.81\times10^{-10}, C_5 = -6.19\times10^{-7},$ $C_4 = 5.68\times10^{-4}, C_3 = -2.78\times10^{-1},$ $C_2 = 7.66\times10^{1}, C_1 = -1.13\times10^{4}$ $C_0 = 6.9\times10^{5}$	$C_5 = 8.79\times10^{-12}, C_4 = -1.02\times10^{-8}$ $C_3 = 4.82\times10^{-6}, C_2 = -1.17\times10^{-3}$ $C_1 = 1.49\times10^{-1}, C_0 = -8.08\times10^{0}$
3	μ_l (kg/ms)	$C_0 = 0.38\times10^{-6}$	$C_0 = 8.94\times10^{-7}$
4	k_l (W/mK)	$C_1 = -0.00011$ $C_0 = 0.03$	$C_5 = -6.46\times10^{-13}, C_4 = 1.16\times10^{-9}$ $C_3 = -8.07\times10^{-7}, C_2 = 2.62\times10^{-4}$ $C_1 = -3.71\times10^{-2}, C_0 = 2.08\times10^{0}$
5	k_v (W/mK)	$C_2 = 3.76\times10^{-8}, C_1 = 6.53\times10^{-5}$ $C_0 = -2.0\times10^{-3}$	$C_5 = -5.37\times10^{-15}, C_4 = 9.19\times10^{-12}$ $C_3 = -5.82\times10^{-9}, C_2 = 1.98\times10^{-6}$ $C_1 = -3.24\times10^{-4}, C_0 = 3.36\times10^{-2}$
6	h_v (J/kg)	$C_5 = -1.57\times10^{-6}, C_4 = 2.58\times10^{-3}$ $C_3 = -1.69\times10^{0}, C_2 = 5.5\times10^{2}$ $C_1 = -8.8\times10^{4}, C_0 = 5.63\times10^{6}$	$C_5 = 2.25\times10^{-8}, C_4 = -6.12\times10^{-5}$ $C_3 = 4.76\times10^{-2}, C_2 = -1.65\times10^{1}$ $C_1 = 4.57\times10^{3}, C_0 = 1.82\times10^{6}$
7	h_{lv} (J/kg)	Row (6) – Row (8)	$C_5 = 4.63\times10^{-9}, C_4 = -3.04\times10^{-5}$ $C_3 = 2.23\times10^{-2}, C_2 = -5.41\times10^{0}$ $C_1 = -2.05\times10^{3}, C_0 = 3.17\times10^{6}$
8	h_f (J/kg)	$C_5 = 1.07\times10^{-6}, C_4 = -1.76\times10^{-3}$ $C_3 = 1.15\times10^{0}, C_2 = -3.73\times10^{2}$ $C_1 = 6.07\times10^{4}, C_0 = -4.03\times10^{6}$	Row (6) – Row (7)

2.2 Pressure Drop in the Thin-film Region

In order to evaluate the pressure drop associated with steady, laminar, axisymmetric, nonswirling inflow (from periphery towards the center) of liquid between two narrowly placed parallel disks (see Figure 2.3), the equations describing fluid motion, in particular the continuity, given by equation (2.13) and radial component of momentum, given by equation (2.14) are solved.

$$\frac{1}{\bar{r}}\frac{\partial}{\partial r}\left(\bar{V}_r \cdot \bar{r}\right) = 0 \tag{2.13}$$

$$\bar{V}_r \frac{\partial \bar{V}_r}{\partial \bar{r}} = -\frac{d\left(\Delta \bar{P}\right)}{d\bar{r}} + \frac{1}{\bar{R}e}\frac{\partial^2 \bar{V}_r}{\partial \bar{y}^2} \tag{2.14}$$

where $\bar{r} = 2r/d_{hs}$, $\bar{y} = y/\delta_{film}$, $\bar{V}_r = V_r/V_o$, $\Delta\bar{P} = \left(P(r) - P_o\right)/\left(\rho_{film}V_o^2\right)$, $\mathrm{Re} = V_o\delta_{film}/\left(2\nu_{film}\right)$, $\bar{R}e = \mathrm{Re}\cdot\xi$ and $\xi = \delta_{film}/d_{hs}$. V_o represents the inlet velocity, P_o is the inlet static pressure, ρ_{film} and ν_{film} are the density and kinematic viscosity, respectively, of the working fluid in the film region.

Solving for pressure drop in the film region requires numerical integration of the nonlinear differential equation (2.14) or by suitably approximating the nonlinear term to obtain a closed form analytical solution that closely matches the experimental observations and computational results. In particular, Vatistas [32, 33] derived a closed-form solution by approximating the nonlinear term with $\bar{V}_r\frac{\partial \bar{V}_r}{\partial \bar{r}} \cong \frac{-1}{\bar{r}}\frac{\partial \bar{V}_r}{\partial \bar{r}}$, resulting in the following equation for pressure drop between the inlet ($\bar{r} = 1$) and any $\bar{r} < 1$ as depicted in Figure 2.3:

$$\Delta \bar{P}_{film} = \frac{1}{2}\left(\frac{\bar{r}^2 - 1}{\bar{r}^2}\right)\left[\frac{\lambda}{\lambda - \tanh(\lambda)}\right] \tag{2.15}$$

where $\lambda = \sqrt{\frac{\bar{R}e\left(\bar{r}^2 - 1\right)}{2\bar{r}^2 \ln \bar{r}}}$. It should be noted that in this case, the magnitude of mean velocity changes as the fluid flows radially inwards towards the center. This change is due to reduction in the flow cross-sectional area and to continuous evaporation of the fluid along the flow path. In our analysis this fact has been taken into account numerically while evaluating the pressure drop.

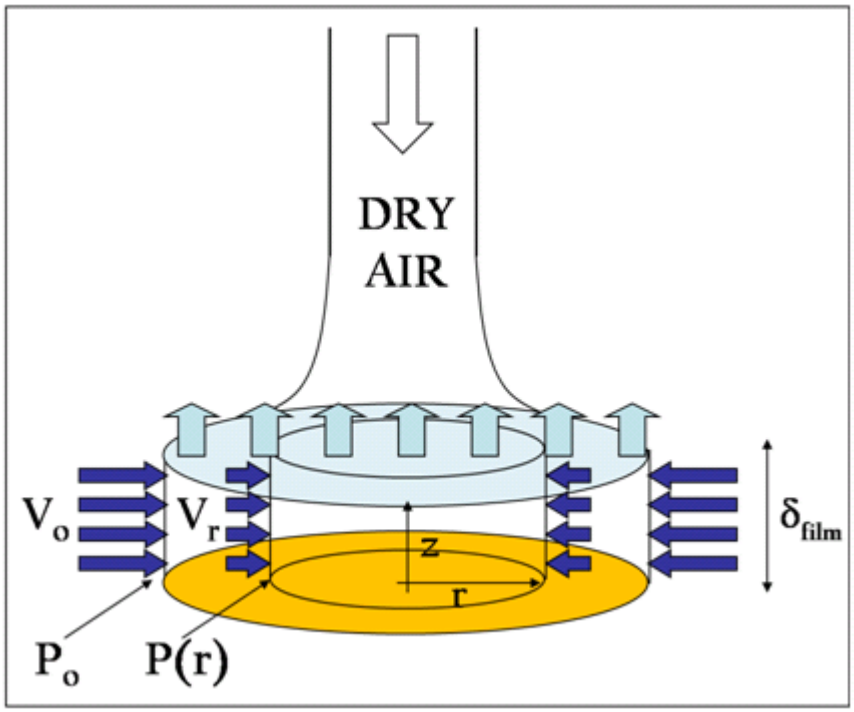

Figure 2.3 Pressure drop in the liquid flowing radially between two closely placed stationary parallel disks

In addition to the pressure drop taking place due to flow in the thin film region $\Delta \bar{P}_{film}$, the pressure drop due to flow across the membrane $\Delta \bar{P}_{memb}$, can also be evaluated. In the

case of a fully hydrophobic membrane, $\Delta\overline{P}_{memb} << \Delta\overline{P}_{film}$ since the flow of vapor phase in the membrane is not pressure driven but is driven by Knudsen diffusion only. On the other hand, for a hydrophilic membrane the pressure drop can be evaluated using the Darcy model as follows:

$$-\Delta P_{memb} = \frac{\mu_l}{K}\frac{4\dot{V}\delta_{memb}}{\pi d_{memb}^2} \tag{2.16}$$

where μ_l and $\dot{V}$ are the dynamic viscosity and volumetric flow rate of the coolant, respectively, and K and d_{memb} are the permeability and diameter of the membrane, respectively. Assuming one-dimensional, fully developed flow of liquid through straight cylindrical membrane pores, the permeability K is found to be $\varepsilon d_{pore}^2/32$ [34]. In evaluating the pressure drop across the membrane, $\Delta\overline{P}_{memb}$ was found to be much smaller than $\Delta\overline{P}_{film}$ even in the case of a hydrophilic membrane. For instance, with FC72 as coolant and $\delta_{memb} = 1\mu\text{m}$, $\delta_{film} = 5\mu\text{m}$, K, ΔP_{memb} can be evaluated using membrane properties, as given in Table 2.3. It is found that $\left|\Delta P_{memb}\right| \approx 7\,\text{kPa}$, whereas $\left|\Delta P_{film}\right| \approx 60\,\text{kPa}$. Since in this case the flow rates and the membrane thicknesses are much smaller in comparison to typical membrane applications, it is meaningful to put more emphasis on the pressure drop inside the film region, since a much higher contribution of pumping power is expected to circulate fluid in the film region.

The performance of the cooling system was analyzed parametrically for the system parameters listed in Table 2.3. The performance analysis was carried out computationally with water and dielectric fluid FC72 as working fluids, and their performance was critically compared. The coolant flow rate and the pressure drop required to circulate

FC72 were also determined and discussed. The performance was also analyzed experimentally using a meso-scale experimental setup with de-ionized water as coolant and commercially available porous alumina membrane. Apart from being a proof of concept, the experimental results are also used to validate the computational results which predict the ultimate performance limit of the evaporative cooling system. The details of the experimental study are described in detail in the next chapter.

Table 2.3 Input parameters for performance analysis. Values listed parenthetically are used for prediction of results for experimental conditions, as described in the next chapter.

Input Parameter	Value	Input Parameter	Value	Input Parameter	Value
Surface Temperature	90 ^{o}C (Measured)	Membrane Conductivity	20 W/mK (20 W/mK)	Mesh Conductivity	40 W/mK (400 W/mK)
Coolant Inlet Temperature	20 ^{o}C (Measured)	Membrane Porosity	0.9 (0.5)	Mesh Porosity	0.9 (0.3)
Air Inlet Temperature	20 ^{o}C (Measured)	Membrane Pore Size	200 nm (20 nm)	Mesh Diameter	1 mm (1.5 mm)
Hot Spot Diameter	1 mm (1.5 mm)	Membrane Diameter	1 mm (1.5 mm)	Position of LV-Interface	VFRAC = 1 (0 or 1)
Jet Nozzle Diameter	0.2 mm (1.067 mm)	Membrane Tortuosity	1.0 (1.0)	Film thickness	1 to 80 μm (200 μm)
Jet air flow rate	2.5×10^{-6} – 4.2×10^{-6} m^3/s (Measured)	Nozzle to Membrane Separation	2 mm (1 mm)	Membrane thickness	1 to 15 μm (60 μm)

2.3 Simulation Results and Discussion

The key factors that determine the dissipated heat flux are the choice of coolant, film and membrane thicknesses, air flow rate and the surface temperature. Since the application of any particular technique for electronic cooling is limited by the maximum

allowable junction temperature, it is more pertinent to analyze the influence of the remaining controlling factors. Table 2.3 lists the important input parameters used for performance evaluation. Values listed within parenthesis ( ), are parameters used for comparing experimental and computational results.

2.3.1 Performance using FC72 as the working fluid

The heat fluxes that can be dissipated using FC72 as the working fluid have been computed and shown in Figures 2.4 (a) and (b), for air flow rates between 2.5 to 4.17$\times$ 10^{-6} m^3/s (0.15 to 0.25 liters per minute (LPM)), which translates to jet velocities between 80 to 133 m/s. For the input parameters listed in Table 2.3, the effect of varying either the liquid film or the membrane thickness, keeping the other parameter invariant, is shown in Figures 2.4 (a) and (b), respectively.

The heat dissipated per unit area is higher for smaller thicknesses of both film and membrane. It is clear from the resistance diagram (Figure 2.1) that higher heat fluxes can indeed be expected, corresponding to smaller thermal resistance in the film and membrane region. A reduction in thermal resistance in the film or membrane region is a direct consequence of decreasing the film or membrane thickness, respectively. Hence, heat fluxes of the order of 700 W/cm^2 can be expected if sufficiently thin (~ 1 μm) film and membrane are utilized.

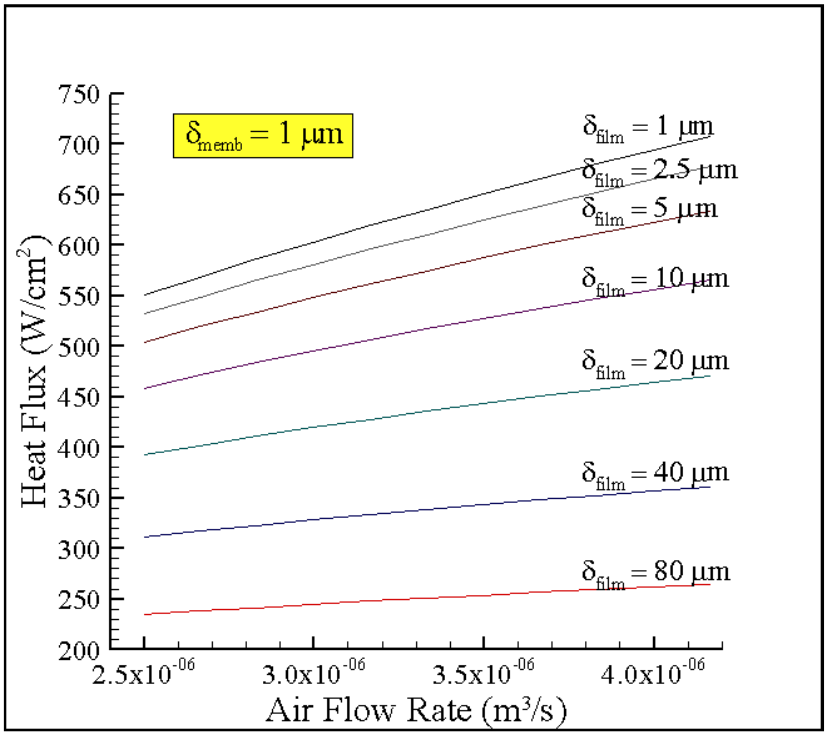

(a)

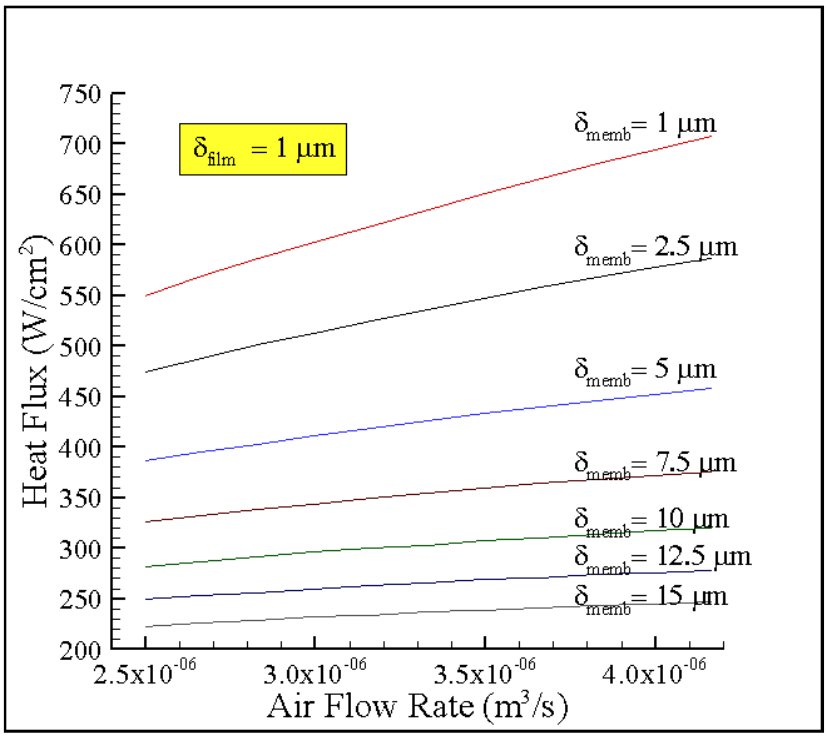

(b)

Figure 2.4 The device performance using FC72 for (a) A fixed membrane and varying film thickness, and (b) A fixed film and varying membrane thickness

A higher value of heat flux also results from a higher jet speed, as the resistance to convective heat and mass transfer at the membrane outlet is diminished, but this change, as can be seen, is not that prominent with flow rate varying between 2.5 to 4.17×10^{-6} m^3/s. More importantly, the results provide a clear indication that the heat fluxes are most sensitive to changes in membrane thickness in comparison to film thickness or air flow rate. The performance is vapor-advection limited only when film and membrane resistances are minimized, as clearly evident by results corresponding to film and membrane thicknesses of $1\ \mu m$.

2.3.2 Performance comparison of FC72 and Water as working fluids

The cooling performance (with parameters listed in Table 2.3) achieved by using FC72 and Water as coolants under similar conditions is illustrated by plotting the ratio of dissipated heat flux (FC72/H2O) for different combinations of the film and membrane thicknesses as well as air flow rates as shown in Figures 2.5 (a) and (b).

The heat fluxes obtained using FC72 are about two to three times higher than those for water for the same combination of input parameters. The plots also indicate that FC72 is more effective for thinner film and membrane thicknesses, while the relative performance improvement of FC72 decays for thicker films. For thinner film and membrane thicknesses, the advantage of higher thermal conductivity offered by water is greatly diminished. The use of a high conductivity mesh in the thin film region or a conductive membrane serves the same purpose. In such a scenario, a higher potential for mass transfer in the case of a more volatile coolant (like FC72) plays a bigger role in determining the resultant heat flux. The superiority of FC72 over water as an evaporative coolant is not that significant as film thickness increases, since the thermal conductivity

of water is higher compared to FC72. This leads to a higher interface temperature for water and thus also contributes to its enhanced volatility.

2.3.3 Pressure drop and flow rate of evaporating coolant

As established in the previous sections, maintaining a thin film of FC72 and using a thin membrane are beneficial for increasing heat fluxes. But the disadvantage of using thin films is that a larger pressure drop is required for circulating the coolant, essentially increasing pumping power. The key contribution to the overall pressure drop needed to circulate a working fluid occurs in the thin film region. To this end, the pressure drop is calculated for two different sets of conditions for pumping fluid into a circular cavity formed by two disks of 1 mm diameter (Figure 2.3). Figures 2.6 (a) and (b) show the pressure drop associated with different film and membrane thicknesses for air flow rates between 2.5 to 4.17×10^{-6} m^3/s.

The film thickness plays a significant role in determining the pressure drop in the fluid. The pressure drop associated with circulation of fluid for a film thickness of 5 μm is almost two orders of magnitude higher than that required in the case of a 20 μm thick film, while the coolant flow rates for the same conditions differ only by a factor of 0.75-0.8. On the other hand, the pressure drop is distinctly a weak function of air flow rate for a constant film and membrane thickness. The pressure drop corresponding to a constant film thickness of 1 μm and a membrane thickness varying between 1 and 15 μm is also plotted. Though the pressure drop corresponding to this film thickness is exceptionally high, making it impractical for implementation, this graph provides sufficient insight to deduce the effect of membrane thickness.

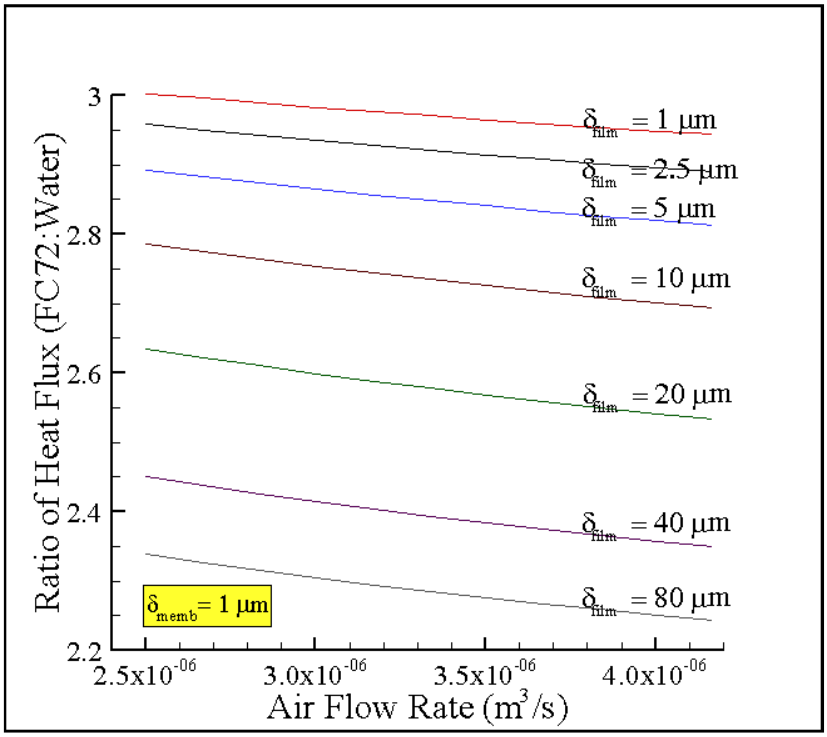

(a)

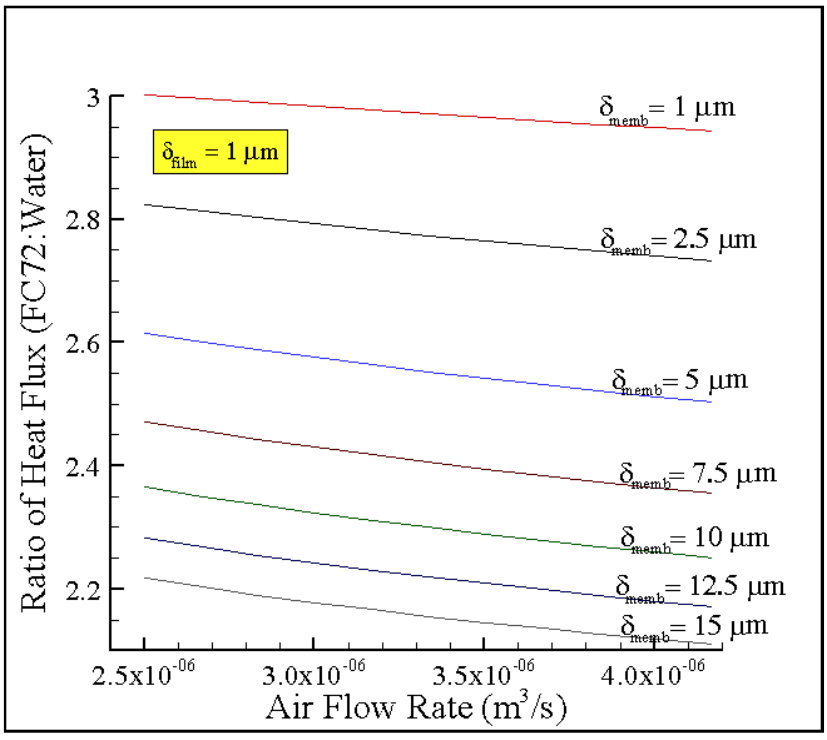

(b)

Figure 2.5 The device performance ratio for (a) A fixed membrane and varying film thickness, and (b) A constant film and varying membrane thickness

From the two graphs it can be concluded that the pressure drop is weakly dependent on membrane thickness and air flow rate, and that it is a strong function of film thickness. For efficient performance of the cooling device, the micro-fabricated cavity covering the hot spot should be continuously supplied with the working fluid. The coolant flow rate would depend on the rate of evaporation. For this device, the working fluid is pressurized at all times due to capillary confinement, thus making the volumetric flow rate of the fluid supply self-regulating, i.e., it automatically increases with enhancement in evaporation, producing greater pressure gradient driving the flow. Figures 2.6 (a) and (b) show the coolant flow rate associated with different film and membrane thicknesses for air flow rates between 2.5 to 4.17×10^{-6} m^3/s.

A decrease in the film thickness increases the volumetric flow rate, because of an increased rate of evaporation in the case of thinner films. The thermal resistance is lower across thinner films, increasing the rate of convective heat transfer, which results in increased rate of evaporation. Unlike the pressure drop, the volumetric flow rate of coolant is more sensitive to variation in membrane thickness than film thickness. While a change in membrane thickness from 1 μm to 15 μm reduces the coolant flow rate from 1.95 to 6.95×10^{-9} m^3/s (i.e., 70 to 25 milliliter per hour (MLPH)), it requires a much larger change of 1 μm to 80 μm in film thickness to cause an equivalent effect. It can also be seen that for the same film thickness, the volumetric flow rate increases with the air flow rate. The increase in air flow rate enhances the rate of mass transfer from the liquid-air interface, and hence increases heat flux as well as the flow rate of the working fluid required to sustain evaporation at higher rates.

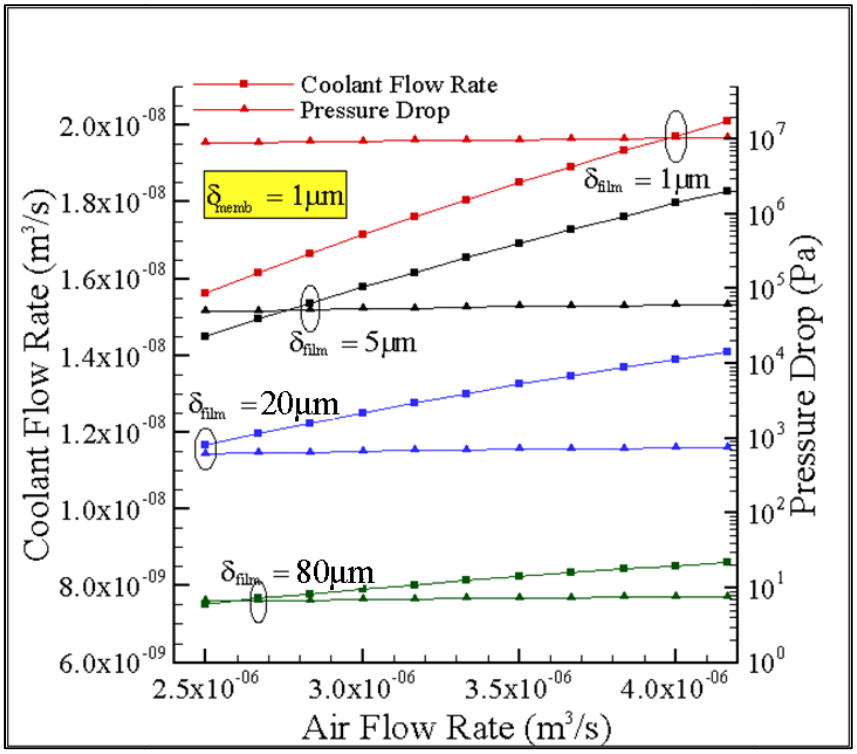

(a)

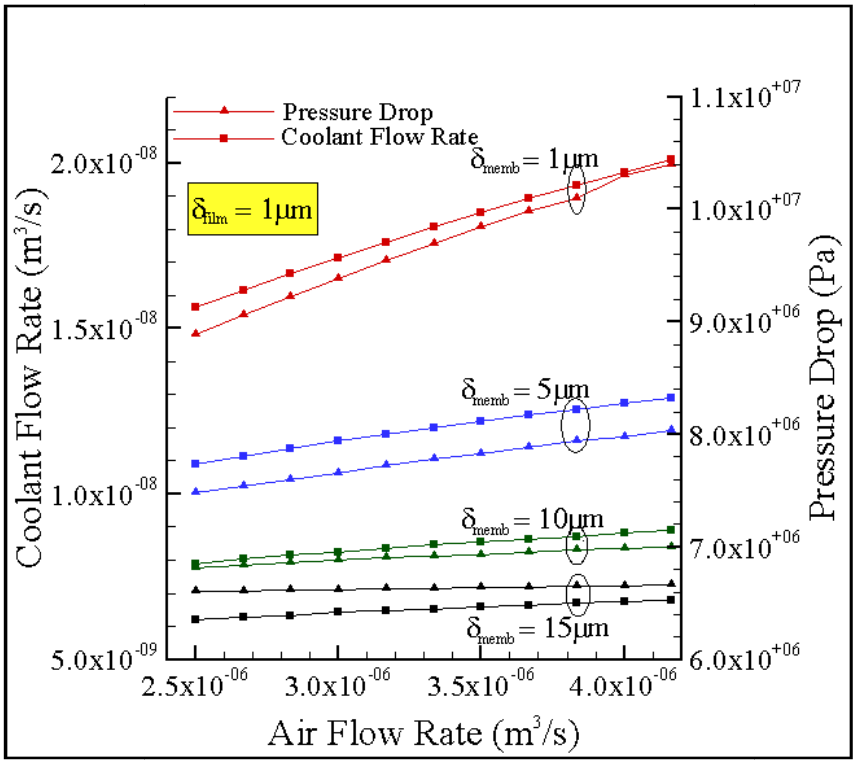

(b)

Figure 2.6 The pressure drop and flow rate vs. air flow rate for (a) A fixed membrane and varying film thickness, and (b) A constant film and varying membrane thickness

2.4 Summary and Conclusions

A new approach to evaporative cooling is described and analyzed for hot spot thermal management in microprocessors. It is demonstrated that the proposed approach could potentially dissipate heat fluxes in excess of 600 W/cm^2 by controlling the film thickness and enhancing evaporation by means of jet impingement of dry air. The specific system design, called "perspiration nanopatch", which exploits capillary confinement of the coolant using a highly porous membrane is illustrated as a route for implementation of this cooling concept.

Dielectric fluid FC72 is shown to result in superior heat transfer performance as an evaporative coolant, and is also desirable because its dielectric properties are suitable for direct on-chip application of the proposed cooling device. Using a thin porous membrane $(1-5\mu\text{m})$ and evaporating liquid film of FC72 $(5-10\mu\text{m})$, exposed to a normally impinging air jet of diameter $200\,\mu\text{m}$, it is possible to dissipate heat fluxes in excess of 300 W/cm^2, while maintaining the hotspot temperature below 90^{o}C. On comparing FC72's performance with that of water, in terms of net heat flux dissipated by evaporation at the same operating conditions, it is shown that FC72 can dissipate 2-3 times higher fluxes due to its higher volatility (saturation vapor pressure), making it more suitable as an evaporative coolant. The relative performance of FC72 in comparison to water decreases for thicker liquid films since water's high thermal conductivity plays a more significant role under these conditions.

Although high heat fluxes can be expected for coolant evaporation from thinning both the film and the membrane, the pressure drop essentially sets the limit on the thinnest possible film for practical implementation. The analysis indicates that film and

membrane thicknesses in the range of 5-10 μm and ~1-5 μm, respectively, are realistic to achieve. For these design parameters, a limiting pressure drop of ~ 20 kPa or lower can be expected, and heat fluxes of the order of 300 W/cm^2 are realizable. The volumetric flow rate of coolant ~ 50 ml/hr with 20 kPa pressure drop is achievable using commercially available, ready-to-use pumping hardware. In the following chapter, a preliminary experimental investigation of thin film evaporation is presented as a proof-of-concept demonstration. The experimental results obtained for different operating conditions using de-ionized water as coolant with air jet impingement as the sweeping gas is also compared with analytical results presented in this chapter.

CHAPTER 3

PRELIMINARY EXPERIMENTAL CHARCTERIZATION OF GAS-ASSISTED THIN FILM EVAPORATION

The preceding chapter introduced gas-assisted thin film evaporation and described its implementation to dissipate large heat fluxes from confined areas. The transfer mechanisms essential to enhance cooling performance were identified, and a parametric analysis established their relative significance. In this chapter, a preliminary experimental analysis of this cooling scheme is presented, with emphasis on the achievable cooling performance from a meso-scale experimental setup. A comparison of the device performance from the preliminary analysis and the experimental results from this meso-scale setup is also presented.

3.1 Experimental Test Setup and Data Analysis

The experimental test setup shown in Figure 3.1 consists of an insulated heater assembly, a leak-proof platform made from polycarbonate, holding a membrane and having inlet ports for coolant supply, and a height/angle adjustable nozzle holder for air jet impingement. A cartridge heater embedded into the base of a copper rod (9.5 mm diameter) supplies heat which is conducted through a smaller (1.5 mm) diameter rod, interfaced with the cooling system. The power input to the cartridge heater was provided by a DC power source (Agilent-6644A, 0 to 60V and 0 to 3.5A). Substantial silicone rubber insulation was provided to minimize loss of heat to the surroundings and to ensure one-dimensional heat conduction in the rod.

Four thermocouples (numbered TC-1 to TC-4) were attached along the copper rod with uniform spacing of $5 \pm 0.25\,\text{mm}\,(P = 0.95)$ to measure the axial temperature variation. Additional thermocouples were used to measure the temperature of the coolant close to the inlet port (TC-5), the temperature of the air used for jet impingement (TC-6) and ambient temperature (TC-7). Prior to use, all thermocouples were calibrated using a thermocouple calibration instrument (Omega-CL122) resulting in total uncertainty within $\pm 0.2\,^{\circ}C\,(P = 0.95)$.

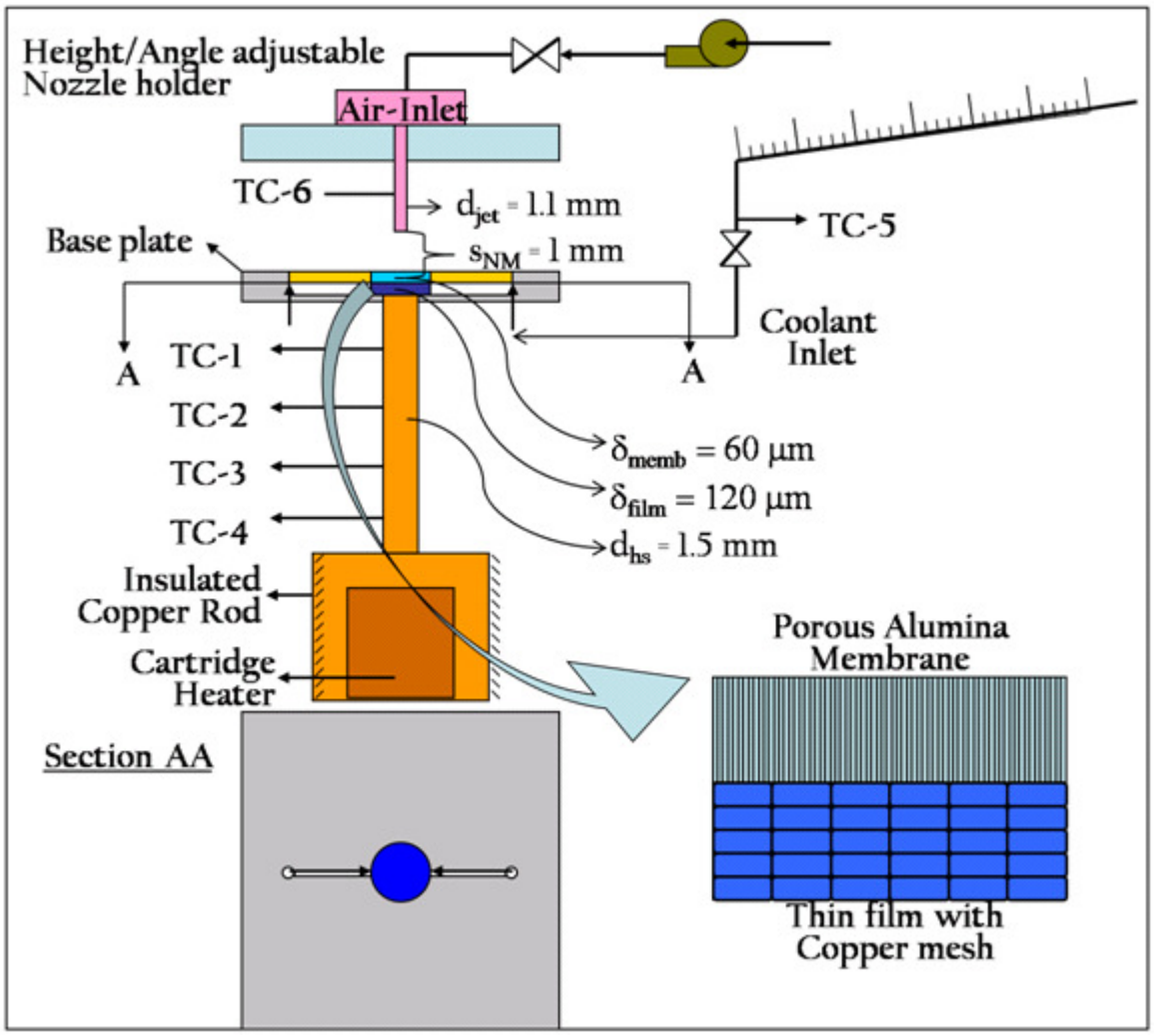

Figure 3.1 Schematic diagram of the experimental test setup

A polycarbonate base was fabricated and force-fitted onto the copper rod such that its surface was flush with the surface of the heater. Two coolant supply ports were drilled into the polycarbonate base and channels defined on the top surface to route the coolant from the inlet ports to the hot spot. The base provides a platform for holding a copper mesh saturated with the coolant as well as a membrane confining the coolant in the cavity (as indicated by the magnified view of film and membrane regions in Figure 3.1). The copper mesh used in the film region was made of 0.2 mm thick copper wires woven together and had a porosity of 30.25%.

Experiments were carried out using both single and dual layers of copper mesh in the film region. The membrane (ANOPORE - SPI supplies) made of porous alumina had an average thickness of 60 μm , pore size of 20 nm, pore density of $10^{11}/cm^2$, and a porosity of 50%. Dual sided Kapton-tape (200 μm thick) was used to seal and attach the mesh and the membrane to the base.

A nozzle holder was installed such that the membrane to nozzle separation as well as the angle of jet impingement could be varied. A miniature air-pump (Hargraves, BTC-Miniature Diaphragm Pump), powered by a DC power source (Instek PR-3060D) was used for delivery of impinging air jet. The air flow rate was metered using a needle valve and measured using an air flow meter (Aalborg GFM371S). The coolant was supplied at a constant inlet pressure by maintaining a constant hydrostatic pressure head using an inclined graduated tube (1.5875mm or 1/16 inch diameter) as schematically shown in Figure 3.1. Volumetric flow rate of the coolant was obtained by recording the drop in the position of liquid meniscus in the graduated tube. The time taken for the meniscus to drop

by 10 cm in the inclined tube was recorded using a stop watch and used for calculation of the volumetric flow rate.

The experimental demonstration was carried out using de-ionized water as coolant. A steady state was considered to be achieved when all the thermocouples recorded a change of less than 0.2 ^{o}C in a period of 5 minutes. The value of dissipated heat flux was obtained by the linear fit of temperature measurements by thermocouples TC-1 to TC-4 and the surface temperature was calculated by interpolation. The uncertainties in experimental measurements of the axial temperatures, axial positions of thermocouples and thermal conductivity of copper rod were used to estimate the uncertainty in reported heat flux and surface temperature. By following the procedure of propagation of uncertainty outlined by Kline and McClintock [35, 36], the uncertainty in the heat flux and the surface temperature were found to be less than 10% and 1%, respectively.

3.2 Effect of Location of LV Interface on Heat Flux Dissipated

The position of the LV interface within the membrane is critical in determination of the heat flux dissipated. As discussed in the previous section, the position of the LV interface was used as an input parameter, $\mathrm{VFRAC}\left(=\delta_2 / \delta_{memb}\right)$ to obtain computational results for conditions similar to the experiment. The value of VFRAC directly affects the effective transport and thermophysical properties in the membrane region, hence altering the value of thermal resistance in this region.

The variable VFRAC is assigned a value of zero for the interface coinciding with the outlet to the membrane, i.e., when the membrane is fully occupied by the liquid phase alone. On the other hand, a value of unity is assigned to VFRAC for LV interface coinciding with the inlet of the membrane, i.e., the membrane is fully dry. With LV

interface at the outlet of the membrane (VFRAC = 0), the vapor phase experiences the least possible resistance to mass transfer since the resistance to diffuse through the membrane is entirely absent. Therefore, the heat flux corresponding to VFRAC = 0 can be expected to reach the maximum for a given set of input parameters. On the other hand, when VFRAC = 1, the resistance to mass transfer is maximum due to significant resistance for coolant vapor transport across the porous membrane, and hence evaporative heat flux is expected to fall to its minimum. Since the position of the LV interface cannot be measured in the experiments, the theoretical results corresponding to VFRAC = 1 and VFRAC = 0 should establish the limits enveloping the heat fluxes that are achieved in experiments.

3.3 Experimental Results and Discussion

The first set of experiments was carried out using a single layer of copper mesh as a liquid-saturated spacer layer and an air flow rate of $5\times10^{-5}\ \mathrm{m^3/s}$ (3.0 LPM). The second set of experiments was carried out using dual (twice as thick) layer of copper mesh and varying air flow rates of $(5.8, 5.0, 4.2)\times10^{-5}\ \mathrm{m^3/s}$ (2.5, 3.0, 3.5 LPM, which yield air jet speeds of 47, 56, 65 m/s, respectively, for 1.07 mm ID nozzle) and angles of incidence for jet impingement (90^o, 45^o, 18^o) to investigate the effect of change in film thickness and characteristics of the air jet. A performance comparison of evaporative cooling relative to single phase air jet impingement cooling is also carried out.

3.3.1 Thin-film evaporation using a single layered copper mesh

Figures 3.2 (a) and (b) show the variation of measured heat flux and coolant volumetric flow rate with surface temperature, respectively. Results indicate a linear

increase in the heat flux and flow rate for surface temperatures below saturation temperature of water (100 ^{o}C at 1 atm). For a constant air flow rate, membrane and film thickness, there is no significant variation in the overall heat and mass transfer coefficient. Hence, for a uniform ambient temperature, the heat flux is expected to vary linearly with surface temperature. At 85 ^{o}C, the heat flux dissipated is close to 65 W/cm^2. As the surface temperatures approaches its saturation value of 100 ^{o}C, the rates of increase in heat flux and the coolant flow rate become higher due to much increased water vapor pressure at the film interface resulting in an increased rate of evaporation at the LV interface. At even higher surface temperatures, boiling likely takes place in the film region, with dissipated heat fluxes close to 120 W/cm^2 for the surface temperature of 115 ^{o}C at the hot spot.

Heat flux and coolant flow rate were also obtained computationally (corresponding to liquid film interface positions at the inlet (VFRAC = 1) and the outlet (VFRAC = 0) of the membrane) based on the experimentally measured air flow rate as well as temperatures of surface, coolant and air-inlet. Other input parameters required to generate computational results are listed parenthetically in Table 2.3.

Heat fluxes and coolant flow rates corresponding to different surface temperatures are plotted alongside experimental results in Figures 3.2 (a) and (b), respectively. The computational results envelop the measured values for the surface temperatures above 70^{o}C. The two outlying data points at lower temperatures are due to leakage of the pressurized coolant through the membrane making the model predictions not applicable.

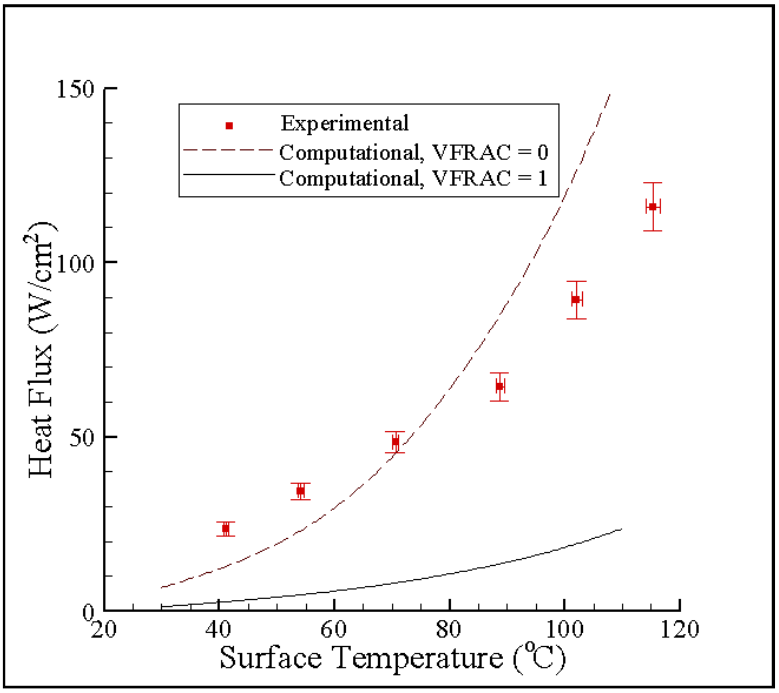

(a)

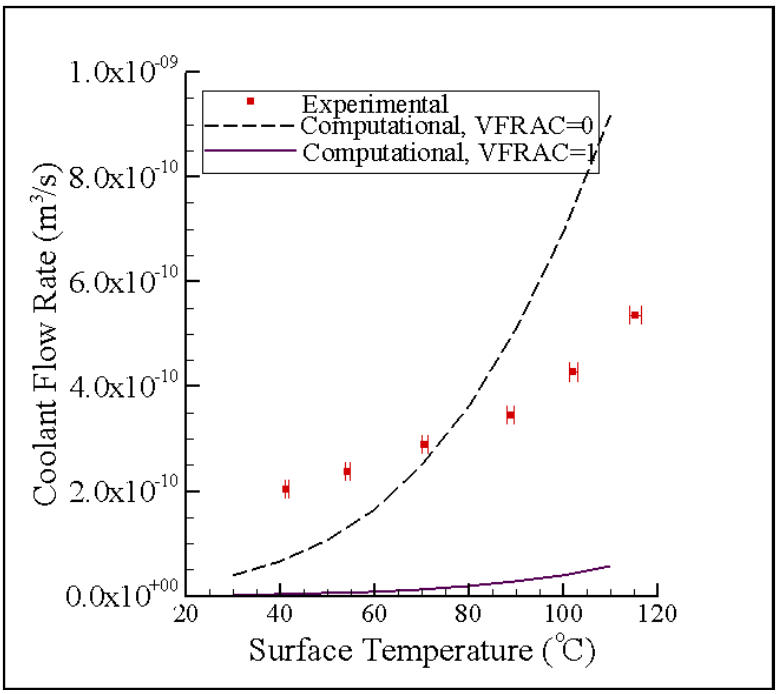

(b)

Figure 3.2 Computationally predicted vs. experimentally demonstrated results using a single layer of copper mesh and at an air flow rate of $5\times10^{-5}\,m^3/s$. (a) Dissipated heat flux, and (b) Coolant flow rate

Since the membrane used is hydrophilic, the pores are expected to be partially occupied by water with the interface closer to the membrane outlet. For the same fluid pressure at the membrane inlet and air flow rate, the rate of evaporation is lower for lower surface temperatures. The rate of evaporation in such a case could even be smaller compared to the rate of liquid supply, leading to a parasitic coolant 'leakage' through the membrane pores, which was visually observed in some experiments. Under these circumstances, the heat flux dissipated would be higher than the predicted value due to enhanced convective heat transfer through the film and membrane caused by leakage, a factor unaccounted for in the computational performance analysis. But at higher temperatures, since no leakage was observed, the experimental results are correctly bounded by the simulations for the limiting cases and the trends are in a good agreement.

3.3.2 Thin-film evaporation using a double layered copper mesh

The results from the second set of experiments carried out with dual layers of copper mesh are shown in Figures 3.3 (a), (b) and Figure 3.4. With single phase air jet impingement, the heat fluxes dissipated for air flow rates of $(5.8, 5.0, 4.2)\times10^{-5}$ m^3/s are modest and never exceed 35 W/cm^2 (Figure 3.3(a)). As expected, for the same surface temperature, a higher heat flux is dissipated with an increase in the air flow rate due to an increase in the heat transfer coefficient. Correspondingly, a steeper slope in heat flux vs. surface temperature is obtained as the air flow rate increases. With the largest air flow $(5.8\times10^{-5}$ $m^3/s)$, the maximum heat flux of 32 W/cm^2 is demonstrated for surface temperature of 74 ^{o}C.

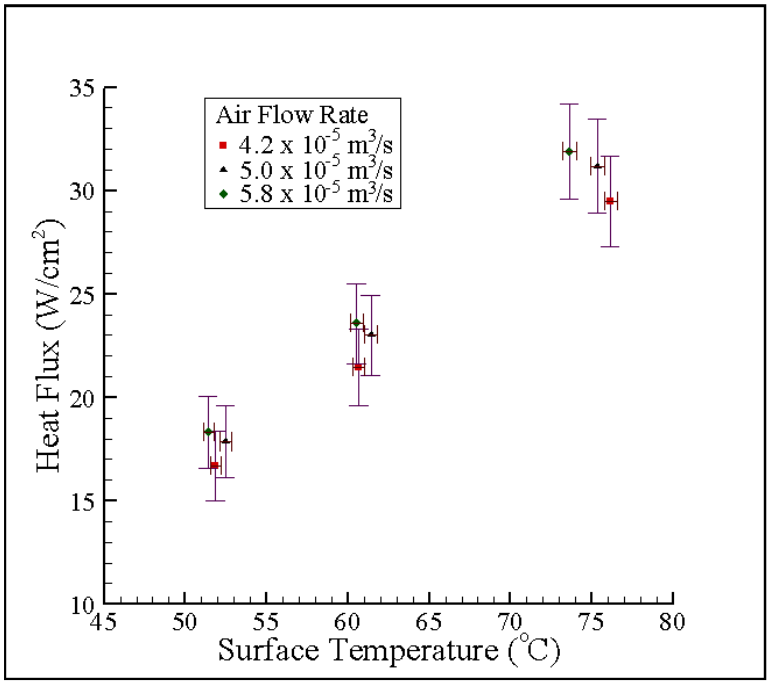

(a)

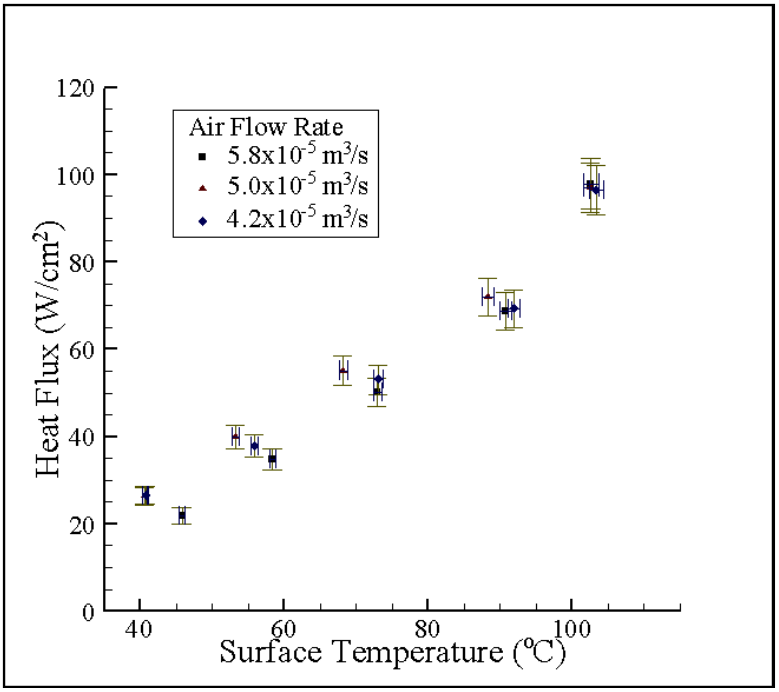

(b)

Figure 3.3 Experiments conducted using dual layers of copper mesh and varying air flow rates of $(4.2, 5.0, 5.8)\times10^{-5}$ m^3/s for (a) Single phase air jet impingement, and (b) Evaporative cooling

Figure 3.3(b) shows the heat flux dissipated using evaporative cooling for the same set of air flow rates. In comparison to single phase cooling (Figure 3.3(a)), evaporative cooling can dissipate twice the heat flux for the same surface temperature and air flow. At lower surface temperatures, the heat flux dissipated with evaporative cooling show modest spreading for different air flow rates considered. A higher air flow enhances both the heat and mass transfer coefficients at the membrane outlet for evaporative cooling. Yet, it may not necessarily yield higher heat dissipation, since a higher air flow rate corresponds to a larger stagnation pressure due to air impingement pushing the LV interface away from the membrane outlet, hence increasing the mass transfer resistance of the membrane. It is the interplay between enhanced heat and mass transfer coefficient outside the membrane and an increased resistance inside the membrane that dictates the overall performance of evaporative cooling. It is for this reason that results corresponding to $\left(5.8 \text{ and } 4.2\right)\times10^{-5}$ m^3/s both lie below that corresponding to 5.0×10^{-5} m^3/s . The heat flux dissipated using evaporative cooling with dual layers of copper mesh was close to 70 W/cm^2 corresponding to a surface temperature of 85 ^{o}C, while 100 W/cm^2 can be dissipated at 110 ^{o}C.

3.3.3 Evaporation using free surface oblique jet impingement

In order to investigate the effect of an oblique air jet impingement on the performance of evaporative cooling scheme, three different angles of jet impingement $\left(\theta = 18^{o}, 45^{o}, 90^{o}\right)$ with respect to the cooling surface were considered with an air flow ate of 5.0×10^{-5} m^3/s (Figure 3.4).

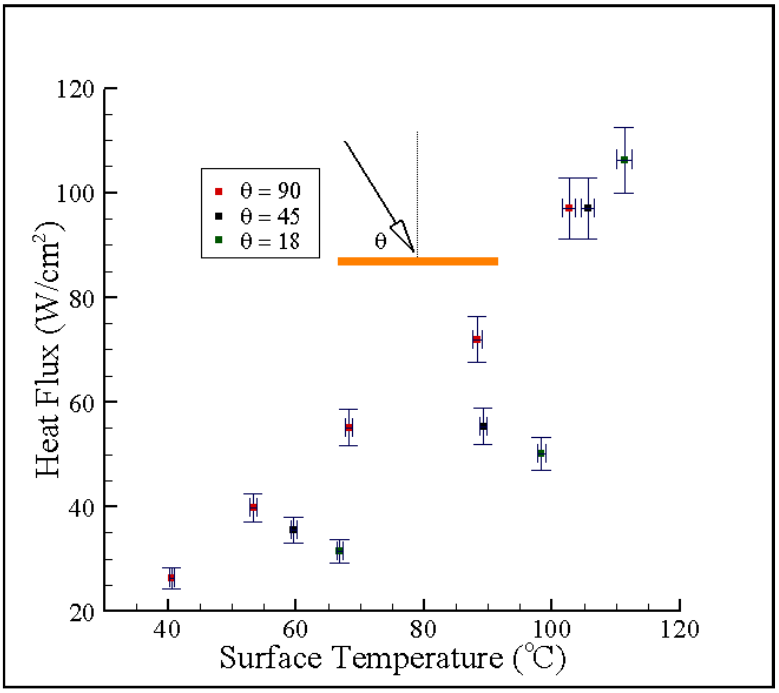

Figure 3.4 Effect of varying the angle of incidence of the jet on heat flux at 5.0×10^{-5} m^3/s air flow rate

Oblique incidence of jet was found to yield much lower heat and mass transfer coefficient at the membrane outlet, with the lowest heat flux corresponding to grazing angle of $\theta = 18^o$ and the highest heat flux in the case of normal incidence ($\theta = 90^o$). As a result of oblique jet impingement, the peak pressure location, which corresponds to the stagnation point shifts upstream from the geometric center of the jet [37]. Upon impingement, the jet thickens downstream while the thickness of the jet decreases upstream as a result of reduced fluid flow caused by the inclination. Furthermore, the heat transfer coefficient has been shown to be proportional to the spatial velocity gradient. A change in inclination will decrease the spatial velocity gradient, leading to a lower heat transfer [37]. Therefore, using oblique, free surface jet impingement, a change in the magnitude and location of the maximum Nusselt number at the surface of the membrane

is expected resulting in a decrease in the heat transfer coefficient at the geometric center of the air jet, which is also observed in Figure 3.4.

3.4 Summary and Conclusions

In this chapter a preliminary experimental investigation of thin film evaporation is presented. A meso-scale experimental test setup is built using a commercial ceramic membrane for capillary confinement of thin liquid films of de-ionized water. The experiments are carried out with de-ionized water under varying operating conditions and the net heat dissipated is compared with the performance analysis in Chapter 2.

With film and membrane thicknesses of 120 μm and 60 μm, respectively, heat dissipation in excess of 60 W/cm^2 at 90^{o}C was experimentally demonstrated from a hotspot of diameter 1.5 mm. In this case, water vapor is removed by a normally impinging air jet from a circular nozzle of diameter 1.1 mm, anchored 1 mm away from the membrane. Evaporative cooling with water was experimentally shown to provide heat dissipation twice as high as single-phase air jet impingement cooling, with heat fluxes greater than 100 W/cm^2 for surface temperatures approaching 110 ^{o}C. Furthermore, a reduction in heat dissipation from the hotspot was also demonstrated with increase in film thickness and by inclining the jet further away from surface normal impingement.

Using de-ionized water as coolant, the trends observed in computational predictions were shown to be in agreement with experimental results, with the position of liquid-vapor interface within the membrane being the key model parameter required to obtain quantitative agreement. While the reduced order model elucidates the effect of various design and operational parameters, a detailed analysis of evaporation is essential in order to determine the critical aspects of interfacial transport phenomenon. A detailed analysis

can also determine the position of the interface and provide a critical insight to establish the relative significance of interfacial resistance on overall performance.

In summary, it is clear from the preliminary computational and experimental analysis that application of evaporation to heat dissipation can be very effective if the thermal resistance in the liquid film is minimized and the rate of vapor transport is enhanced. Although absent in the meso-scale experimental device, these requirements can easily be implemented via micro-fabrication of a MEMS/NEMS device, that integrates hotspot simulation, temperature sensing as well as evaporative cooling. The design and fabrication process of such a monolithic device is described in the subsequent chapter.

CHAPTER 4

FABRICATION OF A MICRO-SCALE COOLING DEVICE FOR THIN-FILM EVAPORATION

It is well established that liquid coolants can offer the advantage of utilizing their latent heat of vaporization in addition to convective cooling, to provide large heat dissipation. Even though phase change has an appealing potential for enhancement of heat transfer, limitations do exist to implement it for applications with high power load. In particular, evaporation or phase change at the free surface of any liquid film is limited by the thermal resistance across the film (affecting heat conduction/convection) and the mass transfer resistance at the free surface of the film (affecting the rate of evaporation). In order to address these limitations, a cooling device based on gas assisted thin film evaporation was proposed. Specifically, the thermal resistance of liquid film was minimized by reducing the liquid film thickness, while the rate of evaporation at the liquid-vapor interface was maximized by jet impingement of a dry sweeping gas.

Building on the ideas outlined in the previous chapters, this chapter describes the process of fabricating a chip-mountable MEMS cooling device, as illustrated schematically in Figure 4.1. The heterogeneous fabrication process integrates micro and nanoscale components produced on different material substrates, which serve distinct functions, yielding a monolithic cooling device along with a microfabricated test structure in a single package.

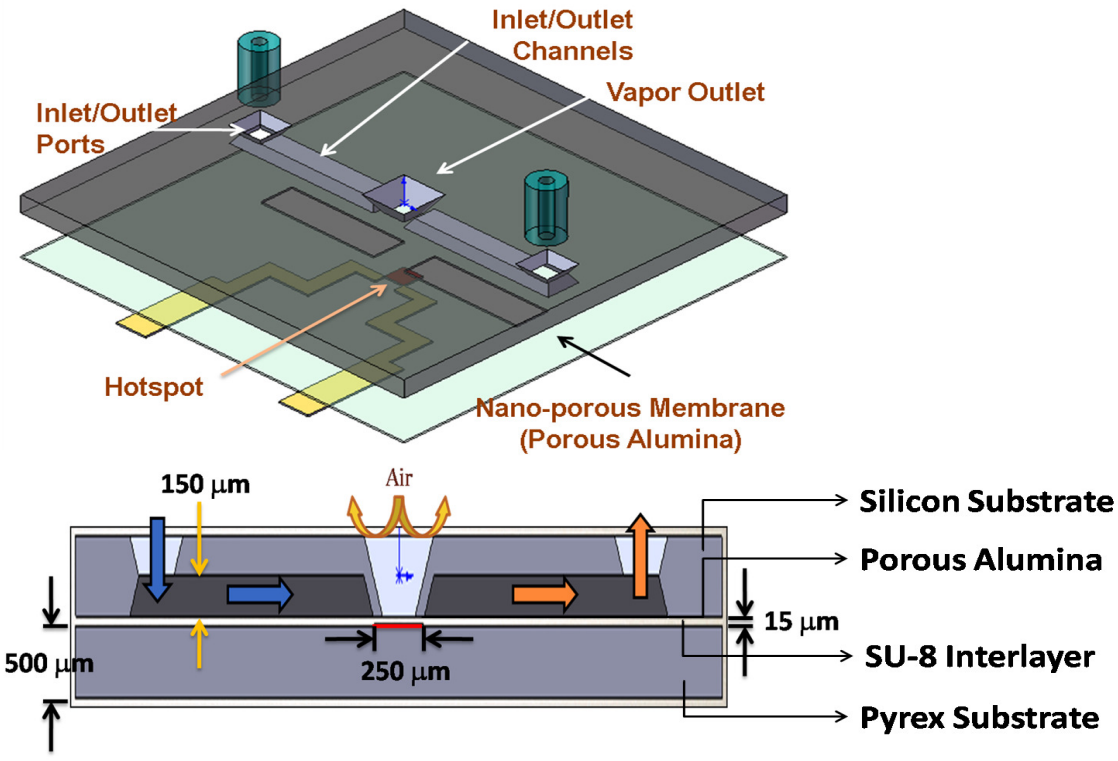

Figure 4.1 A schematic of cooling device, test structure layers and assembly.

4.1 Device Description

The cooling device and the test structure consist of three distinct layers, as shown in Figure 4.1, which are fabricated in a cleanroom environment. An array of resistance micro-sensors and heaters are fabricated on a pyrex substrate for temperature sensing and simulation of microprocessor hotspots. A second device layer facilitates fluid delivery to the hotspot with microchannels fabricated on a silicon substrate, including the inlet and outlet ports. This device layer also integrates a membrane made of porous anodic alumina (PAA), which confines a thin film of coolant within a cavity by capillary action and provides a passage only for vapor phase. A third intermediate adhesive layer bonds the pyrex and silicon substrates. This layer also provides the necessary spacing between the silicon and pyrex substrates, essentially defining the coolant film thickness between the

membrane and the hotspot. A detailed description of the fabrication process of these three layers is described in the following sections.

4.2 Fabrication of the Sensors and Hotspots on Pyrex Substrate

Fabrication of sensors on Pyrex substrate is carried out by deposition of multiple layers of metal (using electron beam evaporation, E-beam) followed by photo-resist liftoff process. The fabrication process starts with a polished 4-inch Pyrex wafer, which is first cleaned in Piranha (Hydrogen-peroxide and Sulphuric-acid, 1:4 v/v). This is followed by spinning a negative photo-resist (NR9-8000, Futurrex) at 3,000 RPM for 1 minute resulting in a resist-thickness of 8μm. After pre-exposure bake in a convective oven at 150 ^{o}C, the resist is UV-exposed providing 168 mJ/cm^2 dosage at a wavelength of 365 nm. It is then baked at 70 ^{o}C and developed using a resist-developer (RD6, Futurrex) at room temperature for approximately 1 minute. Given the use of a negative resist on a non-conductive substrate, resist baking in an oven instead of a hotplate yields more repeatable results.

It is worthwhile to note that photo-resist NR9-8000 is relatively more viscous, yielding a thick photo-resist layer (~8μm) upon spinning under the operating conditions mentioned above. With the absence of any adhesion promoter, and due to the presence of a thick resist on a non-conductive substrate, it was significantly difficult to obtain consistent results. Features in the patterned resist would either appear displaced after lithography or a very thin layer of resist would adhere to the surface even after a longer duration of development. In other words, the yield was quite sensitive to fabrication parameters such as bake time, exposure density and wettability of the substrate. In order to achieve consistent and higher yield, a thinner resist (NR7-3000P) with and adhesion

promoter was used for fabrication. After cleaning the substrate, an adhesion promoter called HMDS (Hexamethyldisilazane, Shipley Company) was spun at 3000 RPM for 45 seconds on the pyrex wafer. NR7 3000P, is then spun at 3000 RPM for 45 seconds, resulting in a resist which is 3±0.2μm thick. The resist on the substrate is subsequently cured in an oven maintained at 150^{o}C for 7 minutes. The substrate is then UV-exposed providing 65 mJ/cm^{2} dosage at a wavelength of 365 nm using a Mask aligner (MA 6, Karl Suss). It is then baked in an oven at 100^{o}C for 7 minutes and then developed using a resist-developer called RD6 (Futurrex) at room temperature for approximately 30 to 60 seconds. The use of a thinner resist (NR7 3000P) and an adhesion promoter (HMDS) resulted in a consistent fabrication yield.

Metallization on the patterned resist is carried out by depositing layers of Titanium (500 ^{o}A) and Platinum (3000^{o}A) using E-beam evaporation, where Titanium served to promote adhesion. In order to avoid charring the underlying photo-resist, the metal deposition by E-beam is carried out at slower rates (1.5–2.5 ^{o}A/s) and in intervals, allowing substrate to cool down. Subsequent lithography was performed following parameters mentioned above. After successfully patterning the resist, E-beam deposition of Titanium (500 ^{o}A), Copper (3000 ^{o}A) and Gold (2000 ^{o}A) was carried out followed by a lift-off process. The composite layer is formed by the metal lines connecting the sensor and hotspot to the device periphery. Use of a composite layer allows minimizing the electrical resistance of the metal lines, thus ensuring localized heating and temperature sensing. A thin layer of dielectric (silicon-oxide) is thermally deposited using plasma enhanced chemical vapor deposition (PECVD) to avoid direct contact of metal layer with the coolant during device testing. Lithography using a positive photoresist (SC-1827,

Microposit) defines square windows to expose underlying silicon-oxide. The details of lithography using SC-1827 are summarized in the subsequent section, which describes the fabrication of channels in silicon. Square windows (600 μm × 600 μm) are etched peripherally in deposited silicon-oxide to expose underneath metal for wire-bonding the devices to a printed circuit board (PCB) to interface with data acquisition and experimental control hardware. The process-flow diagram for fabrication of the RTDs on Pyrex substrate is shown in Figure 4.2.

With overall dimensions of 20 mm × 20 mm, the sensor substrate consists of a central heater (a hotspot) surrounded with thirty-five temperature sensors, as shown in Figure 4.3. The hotspots are fabricated as squares of different dimensions ranging from 250 to 750 μm sides, while all the surrounding sensors (thin-film platinum resistance thermal detectors or RTDs) are squares of 250μm sides. Design layout shown in Figure 4.3, illustrates centrally located hotspots surrounded by RTDs. The RTDs are densely spaced near the center (hot spot) to record maximum change in temperature and are spread more sparsely towards the periphery where the thermal gradients are modest. Figure 4.3 also shows a magnified view illustrating the detailed design of 250, 500 and 750 μm hotspot resistors. The long and thin (10 μm) serpentine lines of hotspot and RTDs provide relatively high resistance (~ 600 Ω), as compared to connecting metal lines (~ 5 Ω), within a very confined space of heating/sensing domain. Pyrex substrate is used as a sensing/heating layer for the following reasons: (1) being transparent, it provides optical access to monitor the fluid channel where evaporation is taking place, and (2) its low thermal conductivity (~1 W/mK) minimizes the heat spreading into the substrate, while the hotspot is activated.

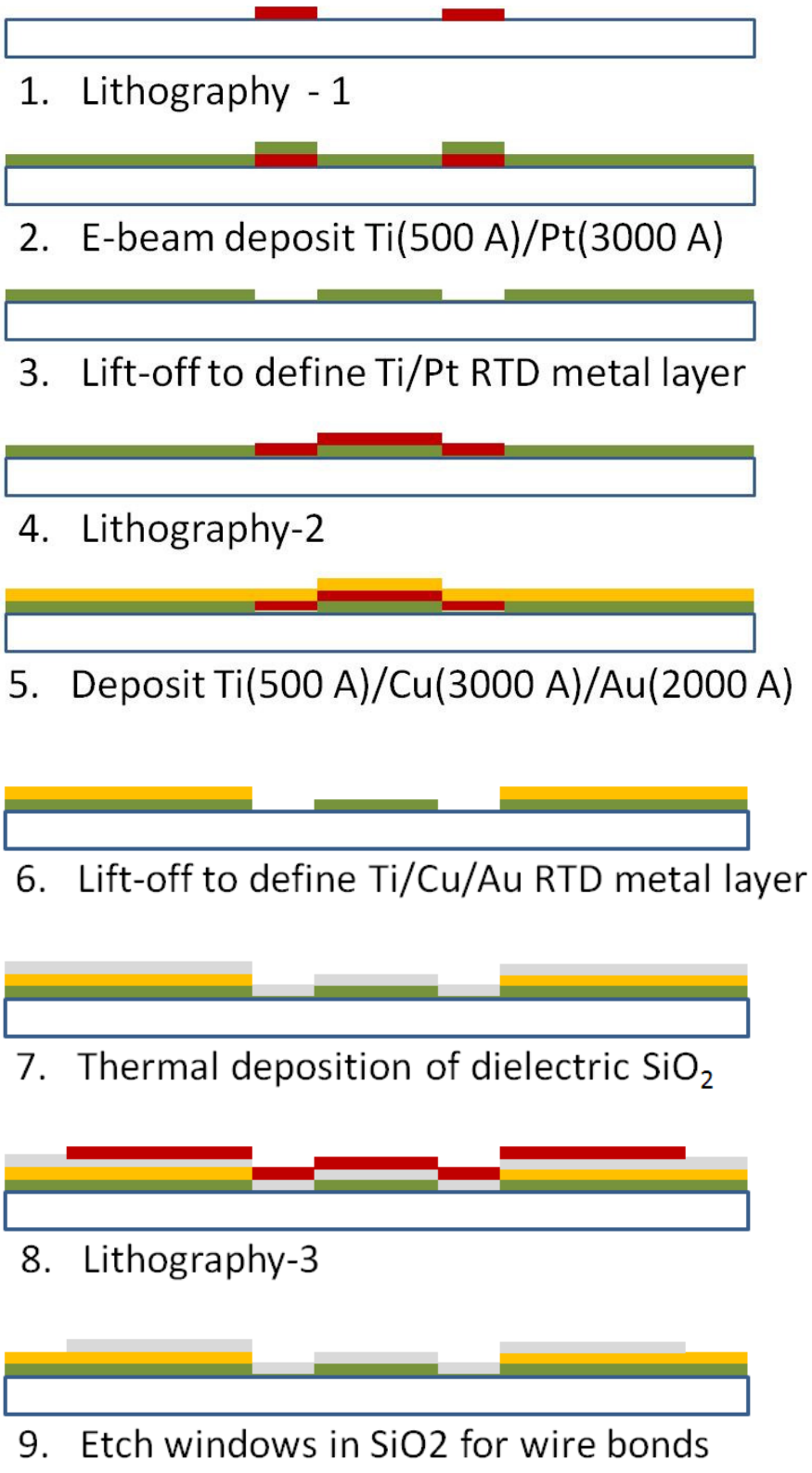

Figure 4.2 Process flow diagram for fabrication of RTDs on Pyrex wafers

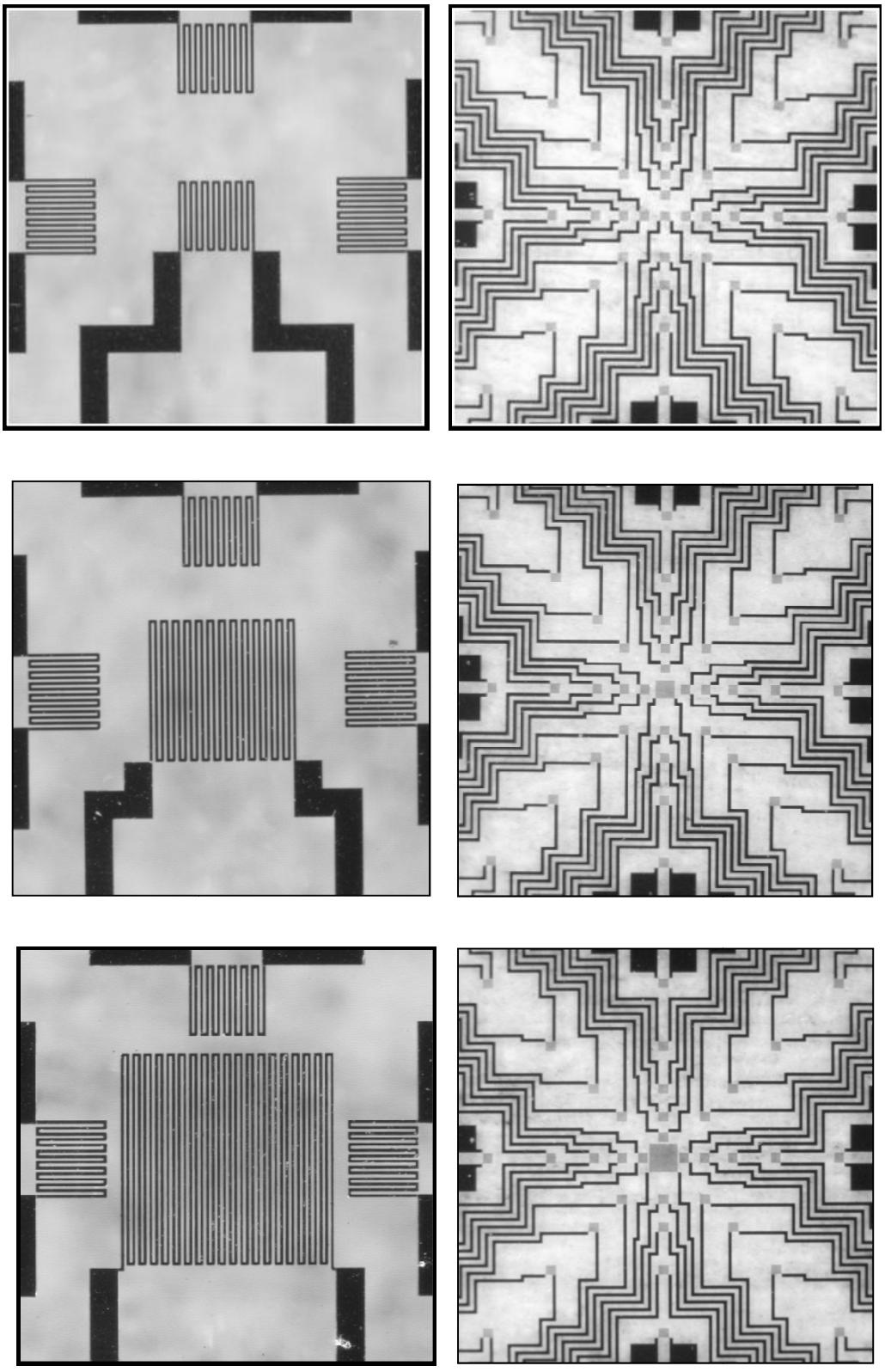

Figure 4.3 Layout of RTD array on the test-platform for sensing and hotspot simulation

4.3 Fabrication of Channels and Ports in Silicon Substrate

The fluidic channels and ports are fabricated on a 4-inch, N-type, both sides polished, silicon substrate (of 100 crystallographic orientation), as shown in Figure 4.4.

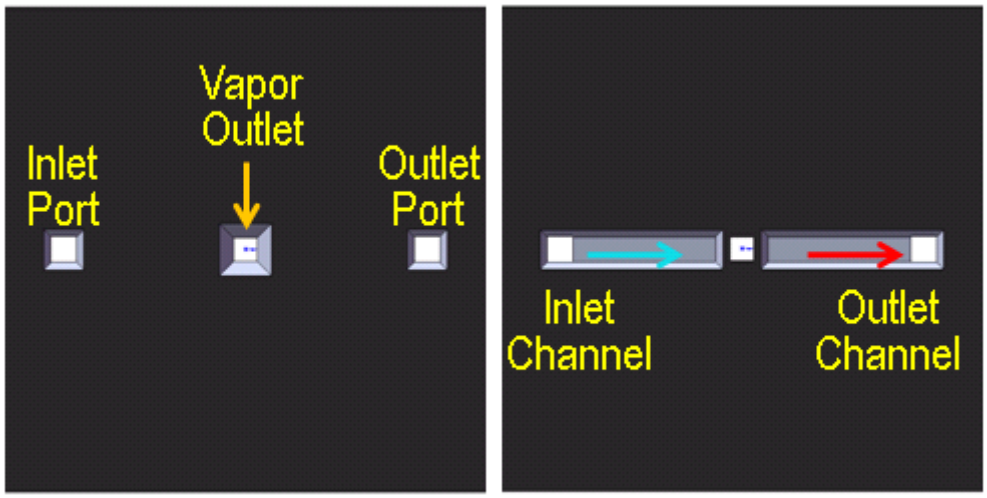

Figure 4.4 The top and bottom views of silicon substrate illustrating the design of inlet/outlet channels and ports for coolant delivery to hotspot.

The substrate is initially cleaned using Piranha as described in the previous section. The silicon substrates are then immersed in hydrogen-fluoride (HF) in order to etch the native oxide layer on the surface. Plasma enhanced chemical vapor deposition (PECVD) of silicon-nitride is subsequently carried out at a rate of 100^{o}A/minute to deposit 1µm thick silicon nitride film on both sides of the substrate.

Lithography on both sides of the wafer utilizes a positive tone photo-resist (SC1827, Shipley). An adhesion promoter (HMDS) is first coated at 3000 RPM and baked at 115^{o}C for 5 minutes on a hotplate. The photo-resist is then spun at 3000 RPM for 45 seconds resulting in a resist-thickness close to 3 µm. It is then baked on a hotplate at 115^{o}C for 5 minutes. The substrate is exposed to UV at 405 nm to provide a dosage of 300 mJ/cm^{2},

and then developed using a resist-developer (MF319, Shipley) at room temperature for 90 to 120 seconds. A patterned resist is obtained exposing underlying silicon nitride for a subsequent dry-etching process using Reactive Ion Etching (RIE, Vision). After the completion of etching silicon-nitride, the residual photo-resist on the surface is then stripped away using Acetone, followed by rinsing (in the order mentioned) with Methanol, Isopropanol and then de-ionized (DI) water. This provides a patterned nitride layer on the silicon substrate. It is essential that the ports on one side of the silicon substrate be in alignment with the channels on the other side. Therefore, in order to pattern the nitride on the other side of the substrate, the lithography, dry-etch and resist-stripping processes are carried out with the same parameters as mentioned above with the exception that the mask is now aligned using "back-side alignment" process before UV exposure. Patterned silicon-nitride layers were obtained on both sides of the substrate exposing underlying silicon for etching ports and channels.

In order to make micro-channels, silicon was anisotropically wet-etched in a Potassium Hydroxide (KOH) bath. For etch uniformity the KOH bath was magnetically stirred at 500 RPM and maintained at 75^{o}C. The etch rates of silicon as a function of temperature and concentration of KOH can be found in articles [15, 16]. The depth of etch was monitored and the process was stopped when a desired channel depth was fabricated. While the channels are etched on one side of the wafer, the other side is sealed from KOH by using a commercial wafer-holder designed specifically for silicon anisotropic wet etching. The wafer was then cleaned in Piranha, and de-hydrated in order to deposit a protective coating of silicon nitride. Using PECVD, a 2 μm thick silicon nitride layer was deposited on the channels etched in KOH. Protecting the channel-side of

the substrate from KOH using a wafer-holder, fluidic ports were then etched through the entire thickness of silicon. The wafer is then rinsed thoroughly in DI water and dehydrated. This concluded the procedure to prepare the substrate for electron beam deposition of Aluminum metal for the formation of free standing nano-porous membranes. Figure 4.5 illustrates the process flow diagram for fabrication channels and ports in the silicon substrate.

4.4 Fabrication of Free-standing Nanoporous Alumina Membranes

Fabrication of a nanoporous membrane (Porous Anodic Alumina, PAA) on the silicon substrate utilizes a two-step PAA fabrication process [38-45]. With channels and ports already fabricated, a uniform layer of titanium is deposited to promote adhesion. Pure aluminum (99.99% or higher, 10 μm thick) is then deposited using E-beam onto the silicon substrate. The wafer is then diced into smaller samples for membrane fabrication.

The PAA fabrication is initiated with anodization of the E-beam deposited aluminum in 0.3 M oxalic acid, stirred and maintained at 0^{o}C using a double-jacketed beaker and a chiller, as shown in Figure 4.6. An anodization voltage of 40 V is applied using a DC power supply (Agilent 6035A). The samples are then immersed in a solution of Chromic (1.5 wt%) and Phosphoric acid (6 wt%) stirred at 60 ^{o}C [46] to etch away the layer of aluminum oxide formed by the first anodization step. This leaves behind a nano-structured surface with indentations that act as pore-initiation sites for a second anodization step. The second anodization step is carried out with similar parameters as the first step, for a prolonged duration (exceeding 24 hours) to ensure anodization through the entire thickness of aluminum. The appearance of a transparent layer of dielectric (Alumina) marks the end of the second anodization step.

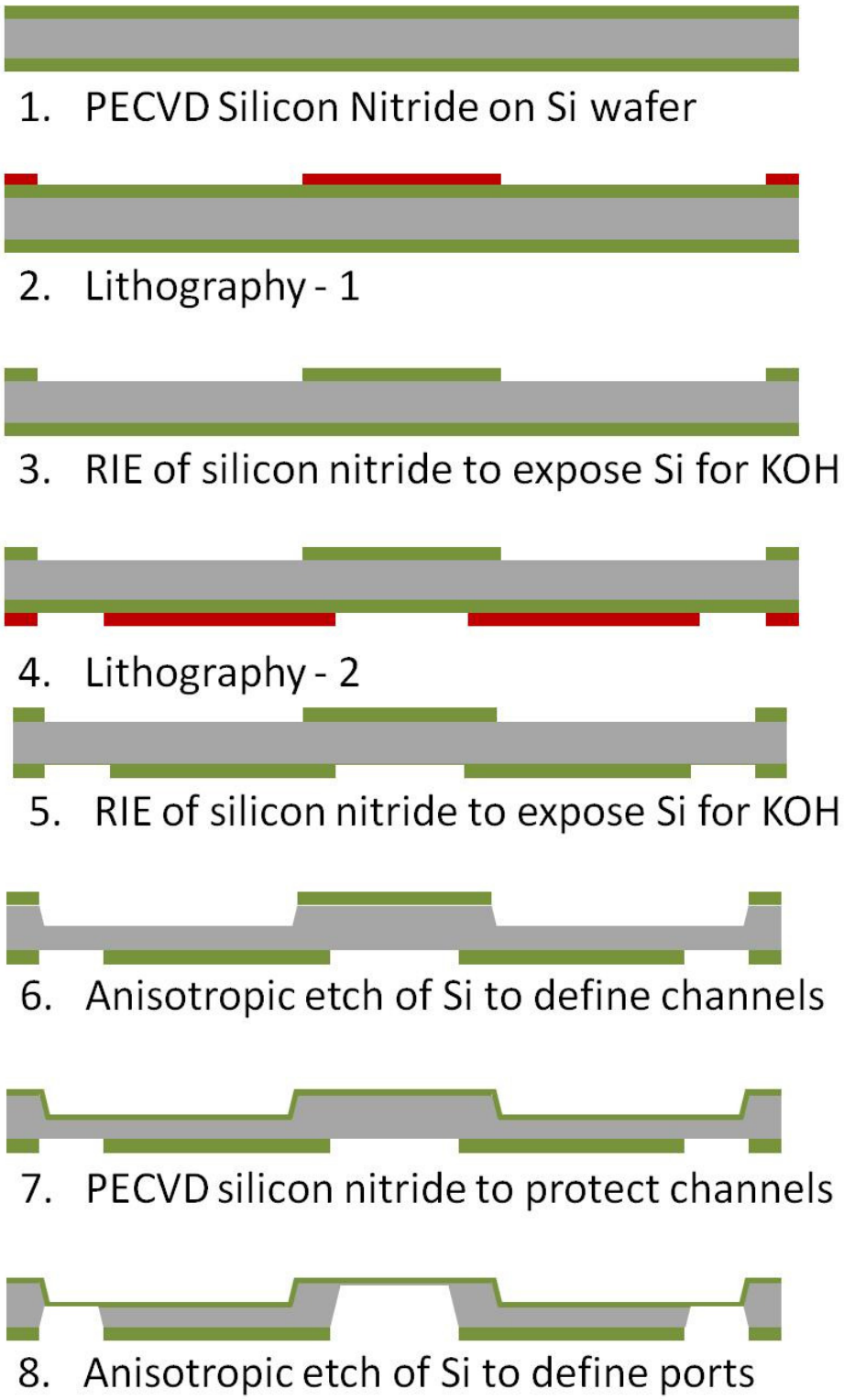

Figure 4.5 Process flow diagram for fabrication of channels and ports in Silicon wafers

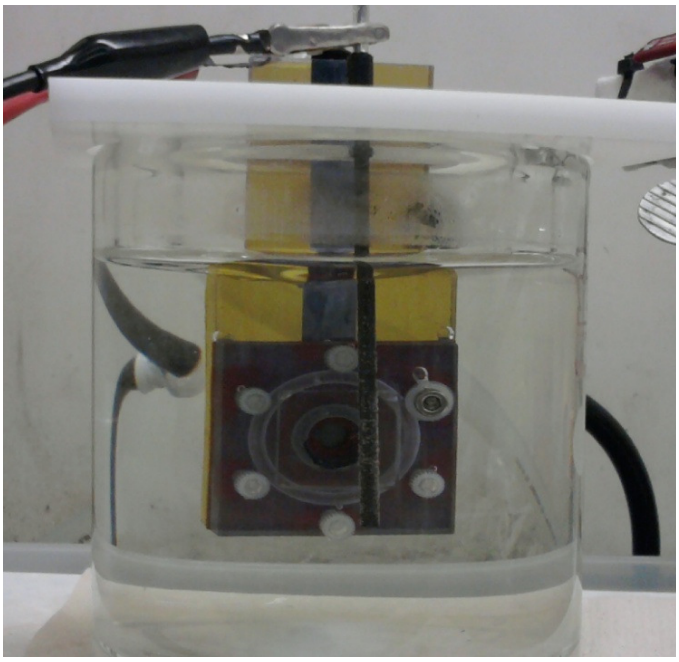

Figure 4.6 Anodization of electron-beam deposited aluminum in 0^{o}C, 0.3M Oxalic acid inside a double-jacketed beaker

The samples are then dipped in the buffered oxide etchant (BOE) at room temperature to etch away nitride layer supporting the alumina membrane layer from the back. While a photoresist can be used to protect alumina during BOE etch of silicon-nitride, exposed alumina is not found to be severely attacked as shown in the Figure 4.7 comparing porous alumina before and after BOE exposure.

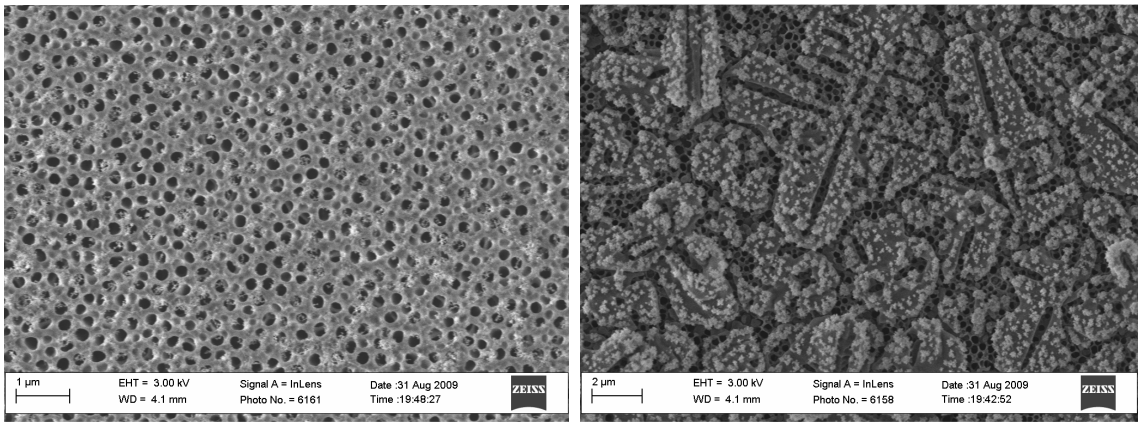

Figure 4.7 Porous alumina membranes before and after exposure to BOE

The membranes are then dipped in Phosphoric acid (5 wt%) at room temperature with mild stirring to carry out pore-widening. As illustrated in Figures 4.8 (a) and (b), a membrane with straight cylindrical pores of high aspect ratio (~ 1:75) is fabricated using two-step anodization process. The use of 0.3 M Oxalic-acid with anodizing voltage of 40V and pore widening at room temperature for about 60 minutes will result in pore diameters close to 80 nm with inter-pore spacing of ~ 110 nm.

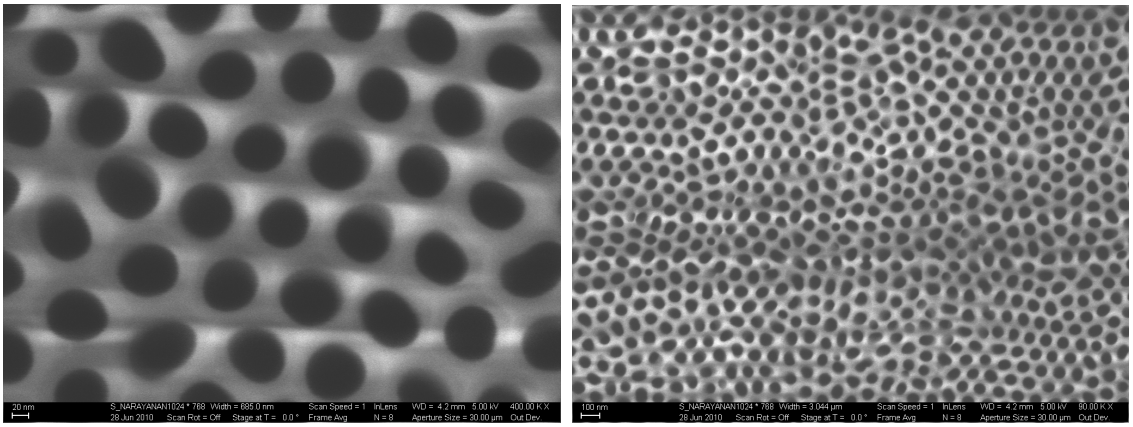

(a)

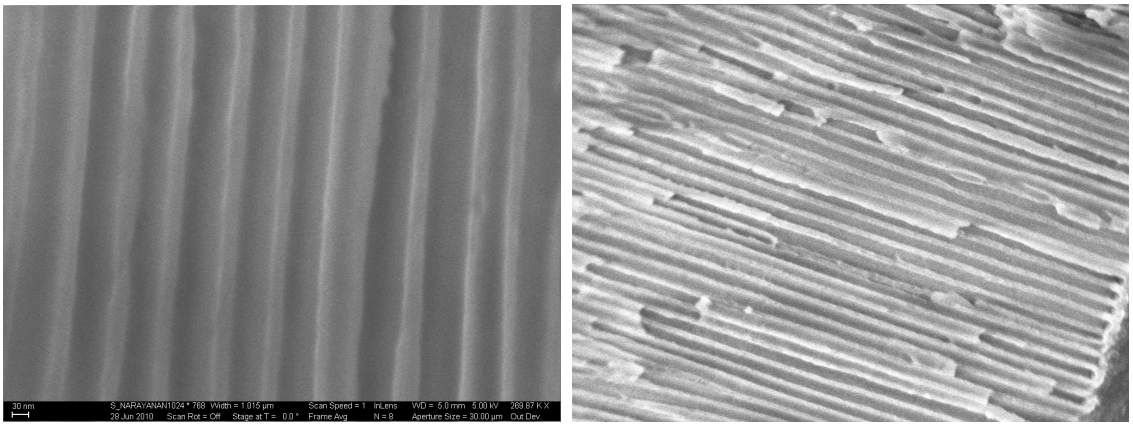

(b)

Figure 4.8 High and low magnification SEM micrographs of porous alumina membranes after two-step anodization followed by 60 minute pore widening at room temperature (a) Top views (b) Cross-sections

It is important to note that the fabrication of straight, cylindrical pores relies critically on the surface roughness, which can vary significantly with the operating conditions set for e-beam deposition of aluminum. For instance, in order to enhance the rate of aluminum deposition, the silicon wafer was placed at close proximity to the crucible inside the e-beam chamber. While the rate of deposition was greatly enhanced, it also resulted in a surface with significant roughness as shown in Figure 4.9. Anodization of surfaces with large roughness, as illustrated in Figure 4.9, resulted in self-intersecting pores, which are detrimental to the performance of evaporative cooling since the passage for vapor diffusion is blocked. A viable solution to address this issue is to carry out electro-polishing of the aluminum surface using Perchloric acid.

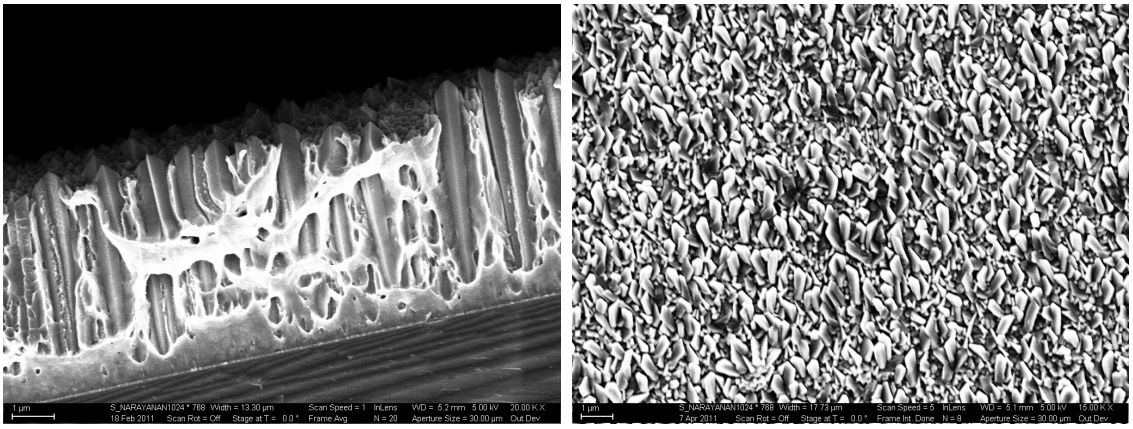

Figure 4.9 Large surface roughness resulting from high deposition rates of aluminum

While 'flat' surfaces with small roughness can significantly improve the quality and yield of fabricated porous membranes, it is indeed quite challenging to fabricate large membranes devoid of any defects as illustrated in Figure 4.10. Figure 4.11 shows the process flow diagram for fabrication of porous alumina membranes supported on a silicon substrate.

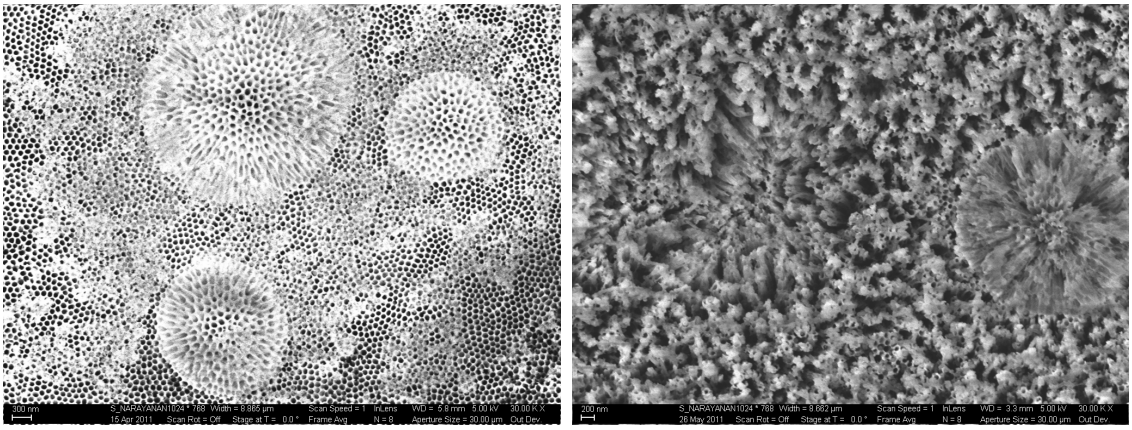

(a)

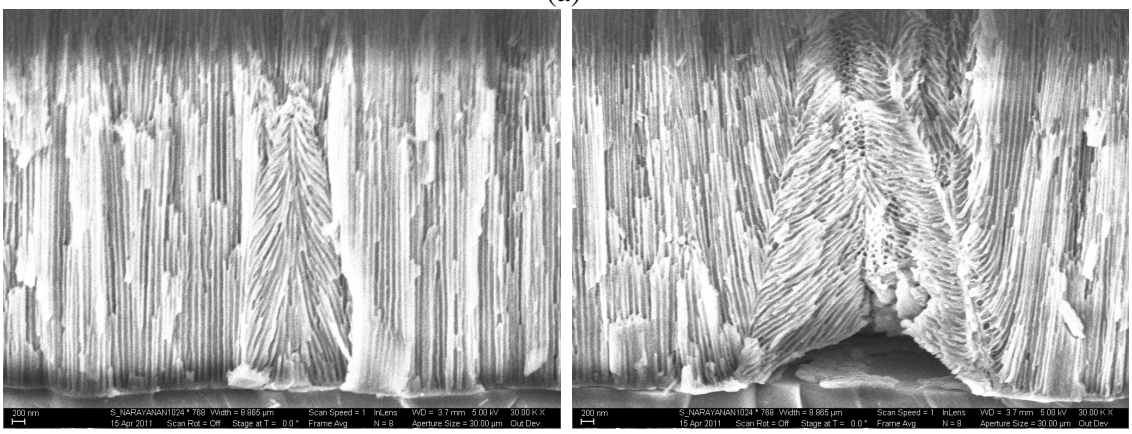

(b)

Figure 4.10 Defects in fabrication of large area, free standing, porous alumina membranes (a) Top views (b) Cross-sections

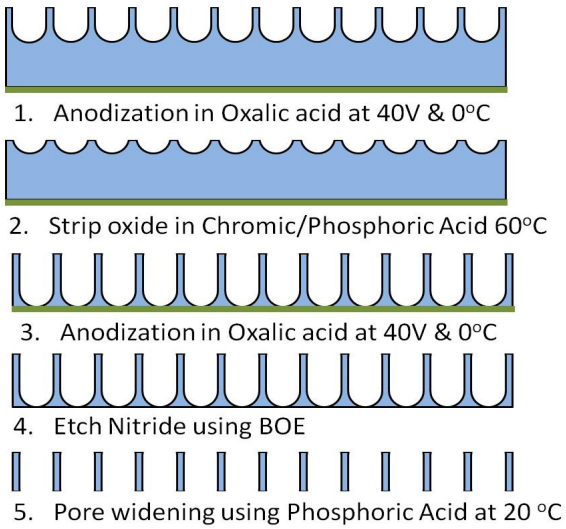

Figure 4.11 Process flow diagram for fabrication of porous alumina membranes

4.5 Adhesive Bonding of Pyrex and Silicon Substrates

Adhesive bonding allows joining non-planar substrates and is carried out at much lower temperatures compared to anodic or fusion bonding. It is often used for the dual purpose of fabricating interlayer features as well as bonding [47-55]. Bonding of sensor and membrane substrates is carried out using an SU-8 interlayer. SU-8 photoresist is first spun onto the sensor substrate at 3,000 RPM, followed by two-step pre-exposure bake at 65 ^{o}C (3 minutes) and 95 ^{o}C (7 minutes) on a hotplate. The substrate is then patterned under UV followed by a post-exposure bake at 95 ^{o}C (5 minutes). This is followed by developing the exposed substrate, resulting in a patterned substrate as shown in the figure below.

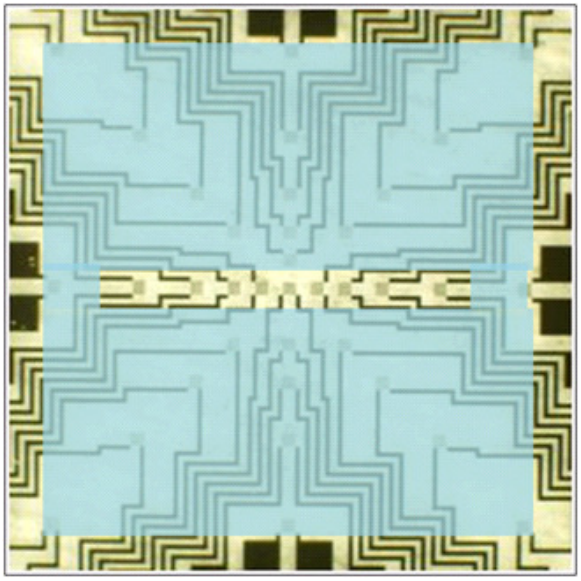

Figure 4.12 An illustration of patterned SU-8 on Pyrex substrate for adhesive bonding

Using a bonding jig built in-house, the two substrates are aligned for bonding such that the porous membrane is positioned centrally over the hotspot on the sensor substrate. The aligned substrates are then placed in an oven at 180 ^{o}C with application of pressure

creating an adhesive bond. After bonding, the device is tested for leaks by flowing de-ionized water through the fluidic channel. When no leaks are observed, the resulting bond strength is considered to be sufficient to withstand typical pressure drops (~ 15 kPa) associated with fluid flow in microchannels of this device. In order to interface with external hardware for data acquisition and experiment control, the device is wire-bonded to a printed circuit board (PCB) with board-to-wire connectors, as shown in the process flow diagram, Figure 4.13. Figure 4.14 shows a complete MEMS device after adhesive bonding and fluidic connections (Nanoports, Upchurch Scientific) are made to the inlet/outlet ports.

4.6 Summary and Conclusions

Device realization of evaporative cooling system for applications that require dissipation of large heat loads from small form-factor areas, such as hotspot thermal management, is fabricated. The chapter describes the design and fabrication process for an integrated MEMS-NEMS device, for gas-assisted evaporative cooling from confined domains.

The chip-mountable MEMS device takes advantage of highly efficient evaporation from a thin liquid film exposed to an impinging gas flow for dissipation of high heat fluxes while maintaining low junction temperatures. Design and fabrication of the device integrate various heterogeneous processes to create microfluidic and nano-scale features on different substrates to enhance the rate of heat transfer. The resulting device allows for integrated measurement/sensing of cooling performance under different heating conditions and for different cooling modes.

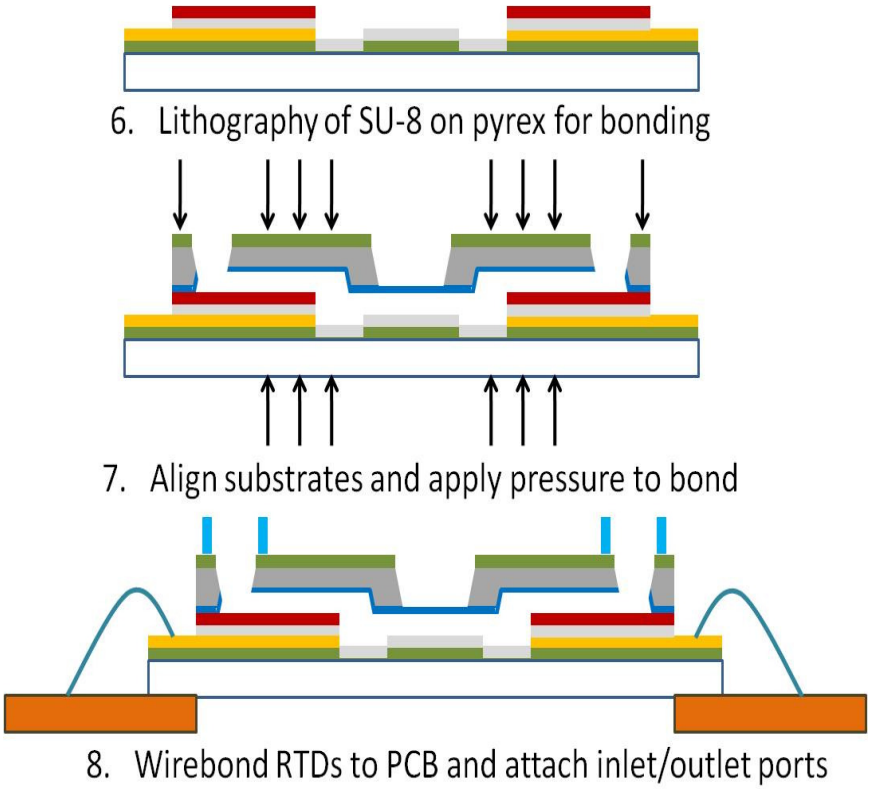

Figure 4.13 Adhesive bonding using SU-8 interlayer and interfacing of RTDs with PCB for data acquisition

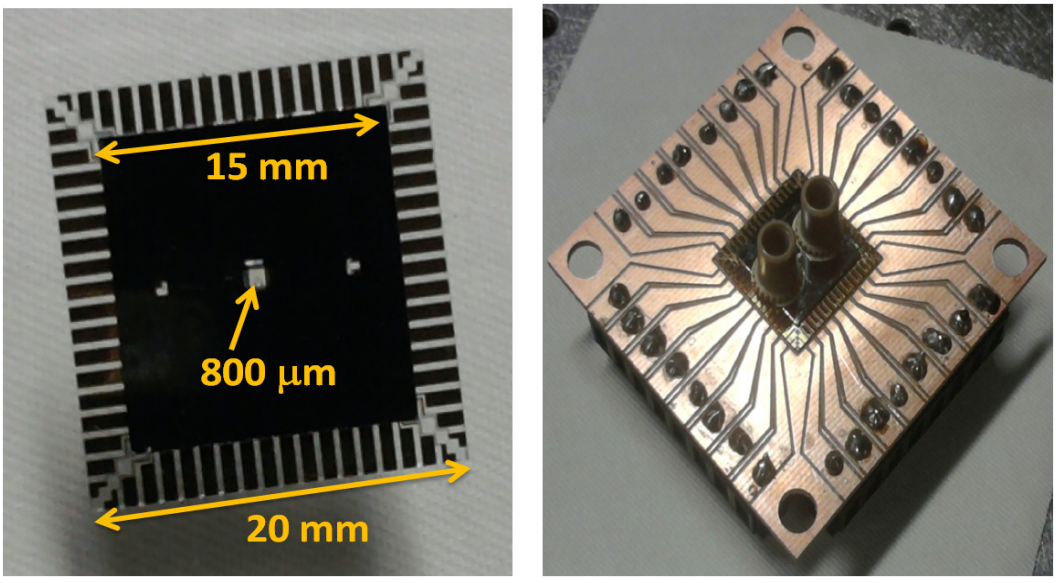

Figure 4.14 The device after SU-8 bonding and a wire-bonded device connected to the PCB with board-to-wire connectors

An array of 36 RTDs is fabricated on a Pyrex substrate, with overall dimensions of 20mm $\times$ 20mm. Pyrex is chosen as a suitable substrate since it allows optical access to monitor evaporation and minimizes heat spreading due to its low thermal conductivity. Square hotspots of sizes 250 μm , 500 μm and 750 μm are fabricated such that they are centrally located and surrounded by RTDs, which are densely packed at the center to record maximum temperature gradient when the hotspot is activated. The design of the hotspot and RTDs allow localized heating and sensing capability to provide an accurate thermal map during experimental testing. Furthermore, microchannels and inlet/outlet ports are fabricated on a silicon substrate for directing coolant to the hotspot location. Additionally, the fabrication of a nanoporous alumina membrane on the silicon device layer allows local confinement of liquid on the hotspot by capillary action. Adhesive bonding of silicon and Pyrex substrates with an intermediate SU-8 layer of pre-determined thickness allows good control over the film thickness. In summary, the compact design of the nanopatch allows integration with a suitable background cooling system, such as microchannels or pin-fin arrays etc. The subsequent chapter describes the performance of this micro-scale device under various operating conditions.

CHAPTER 5

EXPERIMENTAL CHARACTERIZATION OF EVAPORATIVE COOLING USING MICRO-FABRICATED DEVICE

The preceding chapter outlines the procedure to fabricate a MEMS-NEMS device to enable gas-assisted thin film evaporation from confined locations. Dissipation of large heat fluxes from small form-factor areas is made possible by minimizing the thermal resistance across the evaporating liquid film. This is achieved by maintaining a very thin film of coolant by capillary confinement using a nanoporous membrane. At the same time, evaporation is promoted by using jet impingement of dry air on the surface of the membrane. This chapter presents the performance of the micro-fabricated device under different operating conditions, wherein dissipation of heat fluxes in excess of 600 W/cm^2 is demonstrated with heat transfer coefficients approaching 0.1 MW/m^2K for hotspot temperatures well below the saturation temperature of the working fluid.

5.1 Experimental Procedure

5.1.1 Characterization of Resistance Temperature Detectors

The Resistance Temperature Detectors (RTDs) are first calibrated, prior to testing fabricated devices for cooling performance. The calibration process determines each sensor's electrical resistance as a function of temperature. During the process of calibration, thermal equilibrium is ensured by carrying it out in an insulated, forced

convection heating oven. The temperature at different locations inside the oven is monitored using calibrated T-type thermocouples (±0.1 ^{o}C resolution). Thermocouples are attached using thermally conductive adhesive tapes to both sides of the fabricated device, which is interfaced with a data acquisition system (Agilent – 34970A). The temperature measurements from these calibrated thermocouples are utilized for characterizing the RTDs. A typical response of a 500 μm hotspot and surrounding RTDs demonstrating their change in resistance with temperature is shown in Figure 5.1.

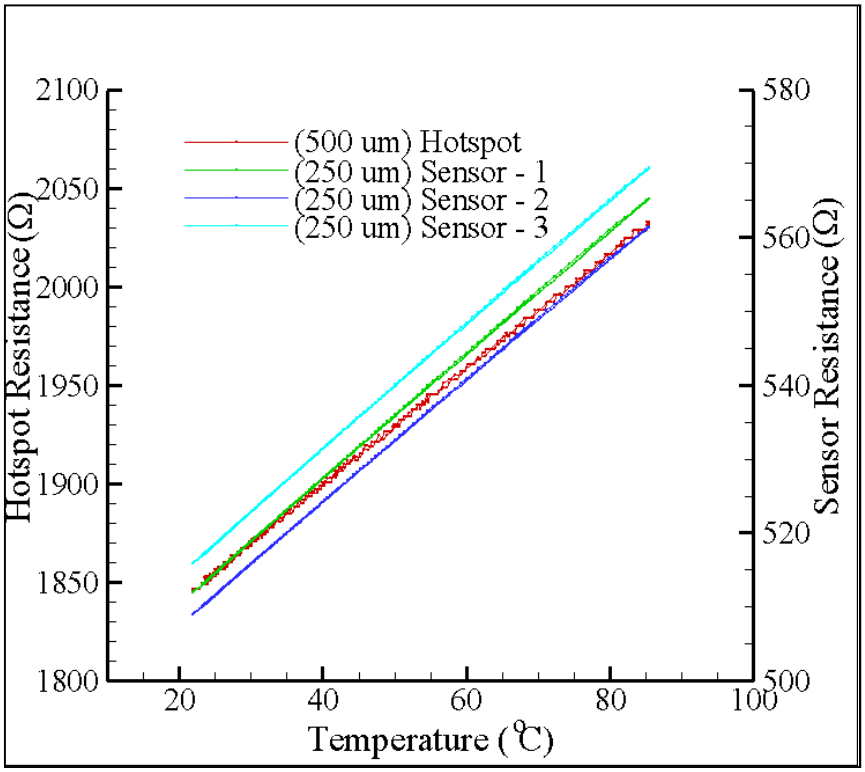

Figure 5.1 A typical (linear) resistance versus temperature calibration curve obtained for the central hotspot and three surrounding RTDs.

5.1.2 Experimental data analysis

Figure 5.2 illustrates the circuitry for an RTD (e.g., hot spot heater/sensor) consisting of the electrical resistances of heater/sensor itself (R_{HS}) and metal lines (R_L) connecting the sensor to the power source. The heater/sensors are designed such that $R_{HS} \gg R_L$ ($R_{HS} \sim 600\,\Omega$ in comparison to $R_L \sim 5\,\Omega$) to ensure localized heating (at hotspot) and temperature measurements (at different sensor locations).

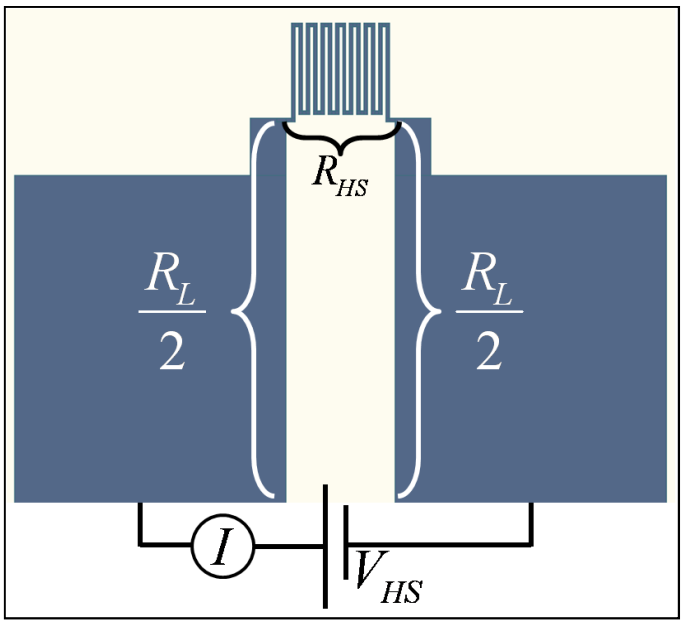

Figure 5.2 An illustration of the electrical circuit consisting of resistances of hotspot and metal line in series with a DC power supply.

Experiments are carried out by applying a bias of V_{HS} across the hotspot using a DC power supply (Agilent E3640A), while the current, I and RTD resistances are recorded using a data acquisition system (Agilent 34970A). At the hot spot, Joule heating is caused by the electric current flow, while the temperature and the heat flux dissipated are determined by measuring the resistance (V_{HS}/I) and the total power input ($V_{HS} \times I$), respectively. It is to be noted that the total power generated at the hotspot ($V_{HS} \times I$) is

dissipated either by active cooling from the top, or by heat spreading through the substrate,

$$\dot{q} = \dot{q}_c + \dot{q}_{sp} \tag{5.1}$$

where $\dot{q}_c$ and $\dot{q}_{sp}$ denote the power dissipated by the active cooling and heat spreading, respectively. The extent of heat dissipation to the substrate due to spreading can be evaluated as:

$$\dot{q}_{sp} \approx \frac{\left(T_{hs} - T_\infty\right)}{R_{sp} + R_{1\mathrm{D}} + R_{conv}} \tag{5.2}$$

where T_{hs} and T_∞ represent the hotspot and ambient temperature, respectively; R_{sp} represents the thermal resistance to heat spreading into the substrate from an infinitesimally thin, square-shaped heat source emanating a constant heat flux into a semi-infinite domain; and $R_{1\mathrm{D}}$ and R_{conv} represent thermal resistances corresponding to one-dimensional heat conduction through the substrate and free convection, respectively. These resistances are estimated as $R_{1\mathrm{D}} = \frac{\delta_{sub}}{k_{sub} A_{sub}}$ and $R_{conv} = \frac{1}{h_\infty A_{sub}}$, where δ_{sub}, k_{sub} A_{sub} denote the substrate thickness, thermal conductivity, and area, respectively, and h_∞ is heat transfer coefficient corresponding to free convection . The spreading resistance can be related to the substrate thermal conductivity and the heat source characteristic length using the following semi-empirical equation [56, 57]:

$$R_{sp} = \frac{0.4732}{k_{sub} \ell_{hs}} \tag{5.3}$$

With $k_{sub} = 1.1\,\text{W/mK}$, $\ell_{hs} = 2.5\times10^{-4}\,\text{m}$, $\delta_{sub} = 5.0\times10^{-4}\,\text{m}$, $A_{sub} = 4.0\times10^{-4}\,\text{m}^2$ and $h_{\infty} = 10\,\text{W/m}^2\text{K}$, the total thermal resistance is given by $R_{\text{total}} = R_{sp} + R_{1\text{D}} + R_{conv} = 1,972$ K/W. The heat flux dissipated by the active cooling is then calculated as:

$$\dot{q}_c'' = \frac{\dot{q} - \dot{q}_{sp}}{A_{hs}} \tag{5.4}$$

The overall heat transfer coefficient of the active cooling mechanism is defined as:

$$h_c = \frac{\dot{q}_c''}{\left(T_{hs} - T_{\infty}\right)} \tag{5.5}$$

where $\dot{q}_c''$ is the heat flux dissipated corresponding to a hotspot temperature of $T_{hs} = 85\,^{\circ}\text{C}$. Note that T_{∞} represents the ambient room temperature (=21.1+/-0.05 $^{\circ}$C) recorded during the experimental characterization of the device. Further details on data analysis are available in reference [58].

5.1.3 Device characterization procedure

To promote evaporation, air jet impingement from a nozzle (1mm in diameter) is implemented using a miniature diaphragm pump (Hargraves, BTC-Miniature Diaphragm Pump). The nozzle is held in place using a positioning tool that can control the angle of impingement and the nozzle-to-membrane separation (as shown in Figure 5.3). An air flow meter (GFM371S, Aalborg) and a pressure transducer (Omega) are used in series with the air pump to measure the volumetric air flow rate (AFR) and supply line pressure, respectively. These measurements are used to calculate the velocity of air exiting the nozzle. All experiments requiring jet impingement of air are carried out at normal incidence to the surface. The liquid coolant (De-ionized, (DI) water) is delivered at extremely low coolant flow rates (CFR ~ 10^{-10} to 10^{-8} m^3/s) using a syringe pump (SPI).

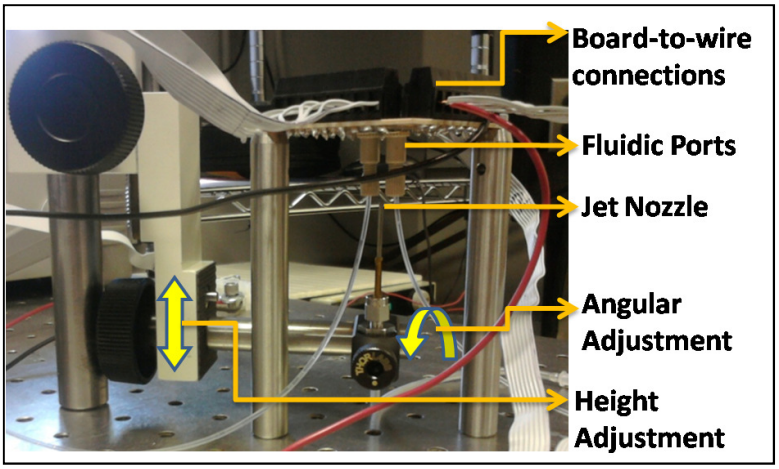

Figure 5.3 The device test rig complete with the fluidic and electrical connections and an air jet nozzle. The PCB is also shown, which is inverse-mounted for a clear view of the sensor substrate from the top. This allows for visual/optical monitoring the coolant flow in the channel during operation.

All experiments are performed on devices with hotspot dimensions of 250 μm × 250 μm. From our earlier theoretical analysis, the two operating parameters that can significantly affect the thermal and mass transfer resistances and therefore the rate of thin film evaporation are the coolant flow rate (CFR) and the air flow rate (AFR), respectively. Therefore, performance characterization of the cooling device is carried out to assess its response to different combinations of CFR and AFR. In order to estimate the extent of improvement achievable using this cooling mechanism, the following two relevant baseline tests are initially conducted to form a basis for comparison: (1) purely jet impingement of air (i.e., no liquid coolant) for varying the AFR and the nozzle-to-hotspot separation, and (2) single-phase micro-channel liquid cooling (i.e., no evaporation due to blocked membrane) for varying the CFR. During evaporation, the micro-fluidic device was monitored for dry-out conditions. Additionally, as the hotspot temperature was maintained below its saturation level, no drastic (run-away) increases in

the hostpot temperature due to formation of dry regions were observed in our experiments.

5.2 Results and Discussion

5.2.1 Air jet impingement cooling

Forced convection using air jet impingement is carried out by exposing the hotspot heater/sensor on the Pyrex substrate to the air jet at normal incidence. Moreover, to eliminate any additional thermal resistance due to the presence of a membrane and an intermediate SU-8 layer, the silicon substrate is not bonded with pyrex, as illustrated in Figure 5.4.

The experiments are carried out to analyze two important parameters that affect overall cooling: the mean jet velocity and the nozzle-to-hotspot separation. The air flow rate (AFR) is varied between 3.33×10^{-5} m^3/s and 6.67×10^{-5} m^3/s, which correspond to impingement velocities of 37–74 m/s, while the nozzle-to-hotspot separation is varied from 5.0×10^{-3} to 1.5×10^{-3} m. Under these operating conditions, heat from the hotspot is dissipated by turbulent forced convection of air flow within the stagnation zone of the jet. These experiments are conducted inside an enclosure to avoid interaction of stray air currents with the air jet and repeated to ensure consistency of measurements.

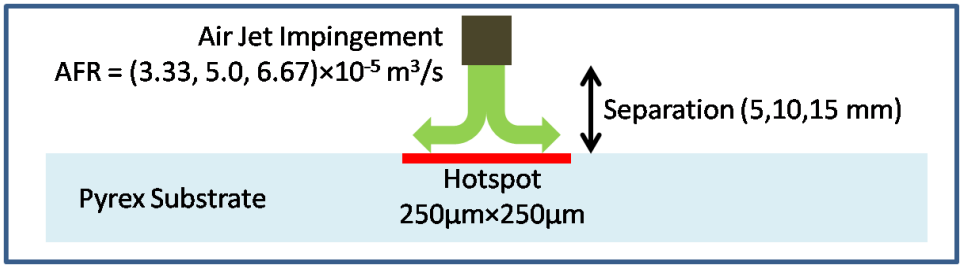

Figure 5.4 Schematic diagram showing experimental arrangement of the baseline experiments of jet impingement air cooling.

Figure 5.5 shows the linear variation of dissipated heat flux with the hotspot temperature at steady state. The average heat transfer coefficients, (HTC) defined by equation (5.5) for each set of operating conditions are summarized in Table 5.1. The HTC is found to increase with an increase in the mean jet velocity and with a decrease in nozzle-to-hotspot separation. A maximum HTC close to 5.5 kW/m^{2}K is demonstrated corresponding to the smallest nozzle separation of 5 mm and a mean velocity of 74 m/s.

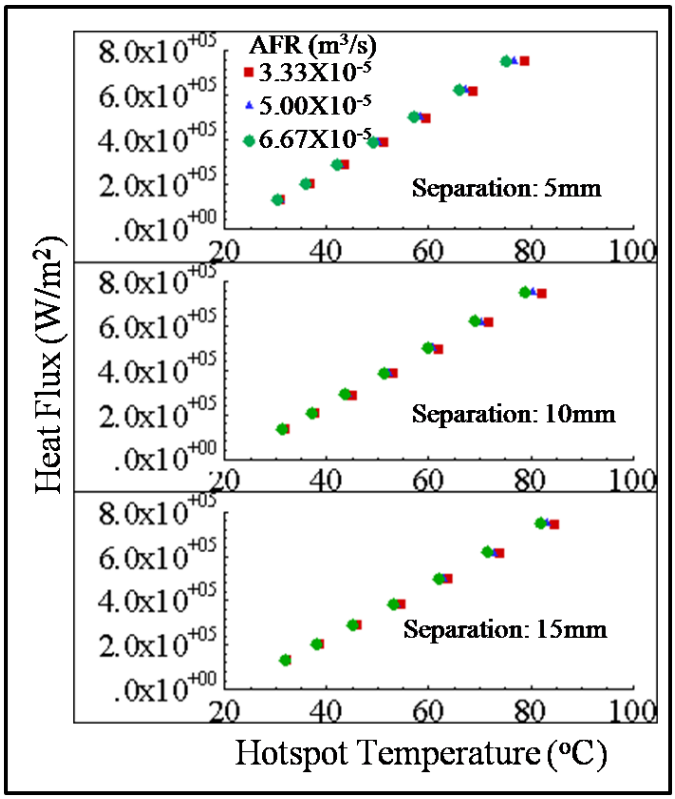

Figure 5.5 Heat flux dissipated by air jet impingement for different air flow rates and nozzle-to-hotspot separations

Table 5.1 The HTC (kW/m^{2}K) demonstrated by air jet impingement corresponding to different operating conditions

AFR/ Separation	3.33×10^{-5} m^3/s	5.0×10^{-5} m^3/s	6.67×10^{-5} m^3/s
5 mm	4.6±0.1	5.1±0.2	5.5±0.2
10 mm	3.8±0.1	4.2±0.1	4.5±0.3
15 mm	3.3±0.2	3.6±0.1	3.8±0.3

5.2.2 Single-phase microchannel liquid cooling

A simple modification is made to the fabricated cooling device to carry out single phase microchannel liquid cooling. The membrane outlet is blocked to eliminate evaporation in the membrane as schematically shown in Figure 5.6. With a blocked membrane and without air jet impingement, the cooling is only due to single phase flow of liquid coolant in the micro-constriction. The coolant flow rate is varied between 1.39×10^{-9} m^3/s and 3.47×10^{-9} m^3/s. The heat flux dissipated as a function of hotspot temperature is shown in Figure 5.7, and the heat transfer coefficients under these conditions are listed in Table 5.2. An increase in power dissipation with an increase in the coolant flow rate is due to a reduction in the bulk fluid temperature associated with lower sensible heating of the fluid, which in combination with an approximately constant heat transfer coefficient for fully-developed laminar flow in the micro-constriction results yields an improvement in observed heat fluxes.

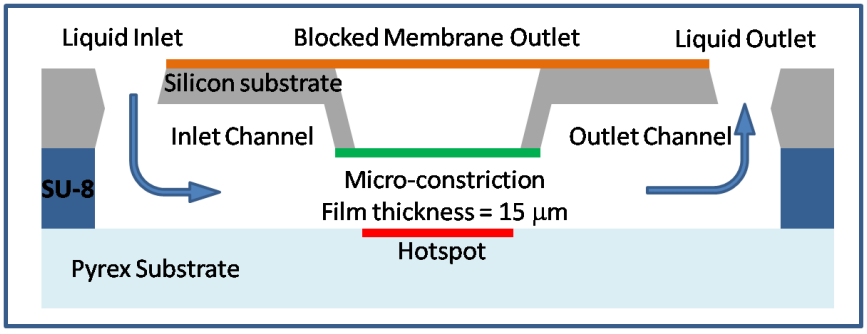

Figure 5.6 Hotspot thermal management using single-phase microchannel flow.

Table 5.2 The HTC (kW/m^2K) demonstrated by single-phase liquid cooling in microchannels corresponding to different flow rates at hotspot temperature of 85 oC

CFR (m^3/s)	1.39×10^{-9}	2.08×10^{-9}	2.78×10^{-9}	3.47×10^{-9}
HTC(kW/m^2K)	39 ± 0.4	56 ± 0.6	65 ± 0.7	76 ± 0.8

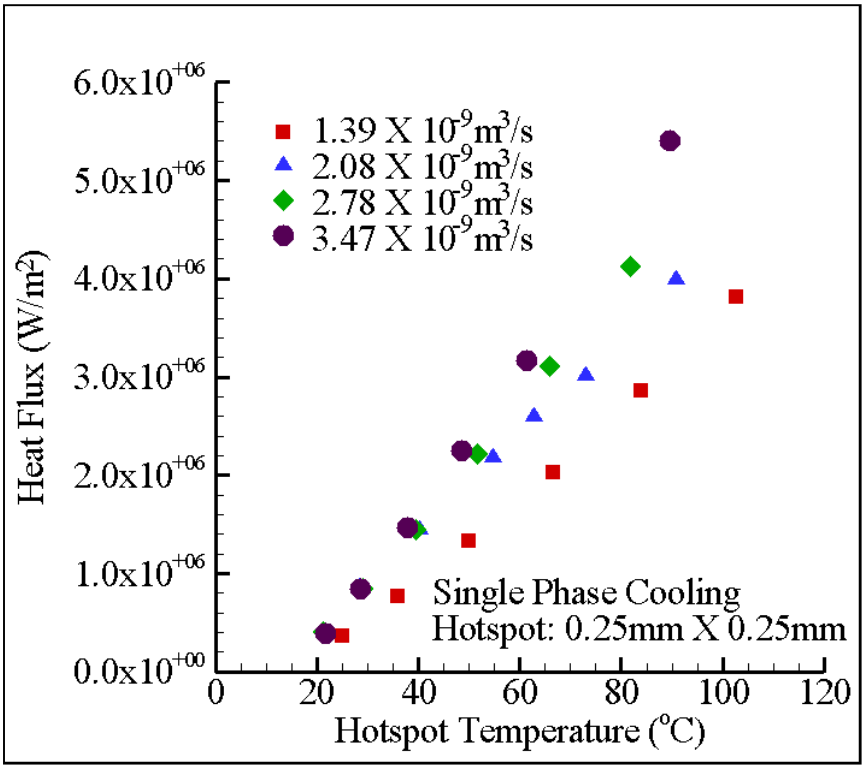

Figure 5.7 Heat flux dissipated by single-phase liquid flow for different CFRs.

5.2.3 Gas-assisted thin-film evaporative cooling

The coolant and air flow rates are varied to determine the change in overall heat transfer coefficient for gas-assisted liquid evaporation from membrane-confined thin films (as shown in Figure 5.8). Figures 5.9 and 5.10 show the net heat flux dissipated by the cooling mechanism as function of the hotspot temperature for different combinations of air and coolant flow rates for a nozzle to substrate separation of 1mm. These results clearly demonstrate the ability to dissipate heat fluxes in excess of 6 MW/m^2 while maintaining junction temperatures below 95 ^{o}C, which correspond to average heat transfer coefficients approaching 0.1 MW/m^{2}K. The average heat transfer coefficients evaluated at junction temperatures close to 85 ^{o}C under different operating conditions are listed in Table 5.3 and 5.4.

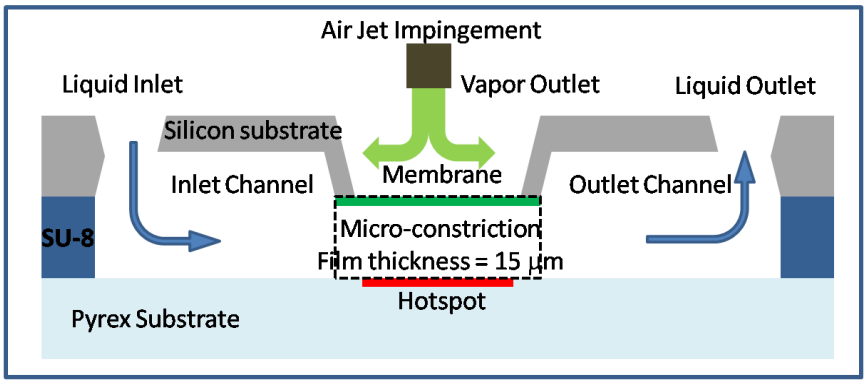

Figure 5.8 Hotspot thermal management using thin film evaporative cooling: air and coolant flow rates are varied to determine their effect on average heat transfer coefficient

Evaporative cooling clearly yields an improvement in performance compared to the baseline tests with purely air jet impingement and single-phase microchannel liquid cooling. By comparing the highest heat transfer coefficients demonstrated by different modes of heat dissipation, evaporative cooling yields a 17 times improvement over jet impingement and about 25% increase over single-phase microchannel cooling.

For a particular hotspot temperature, the dissipated heat flux can be enhanced either by increasing the air or coolant flow rate. In order to further enhance performance, the dominant resistance limiting the performance of the nanopatch can be identified from these experimental results. Figure 5.9 and Table 5.3 present heat fluxes dissipated for different AFRs (2.5 – 5×10^{-5} m^3/s), while maintaining a constant CFR of 2.78×10^{-9} m^3/s. The corresponding heat transfer coefficients are large, but vary relatively little 0.088 – 0.094 MW/m^2K with change in air flow rates. On the other hand, a relatively large change in a heat transfer coefficient is demonstrated varying the CFRs ($1.39–3.47\times10^{-9}$ m^3/s) with AFR maintained at 5×10^{-5} m^3/s, as shown in Figure 5.10 and Table 5.4. In this case, the heat transfer coefficient is almost doubled from 0.045 to 0.085 MW/m^2K for an increase in CFR from 1.39×10^{-9} to 3.47×10^{-9} m^3/s.

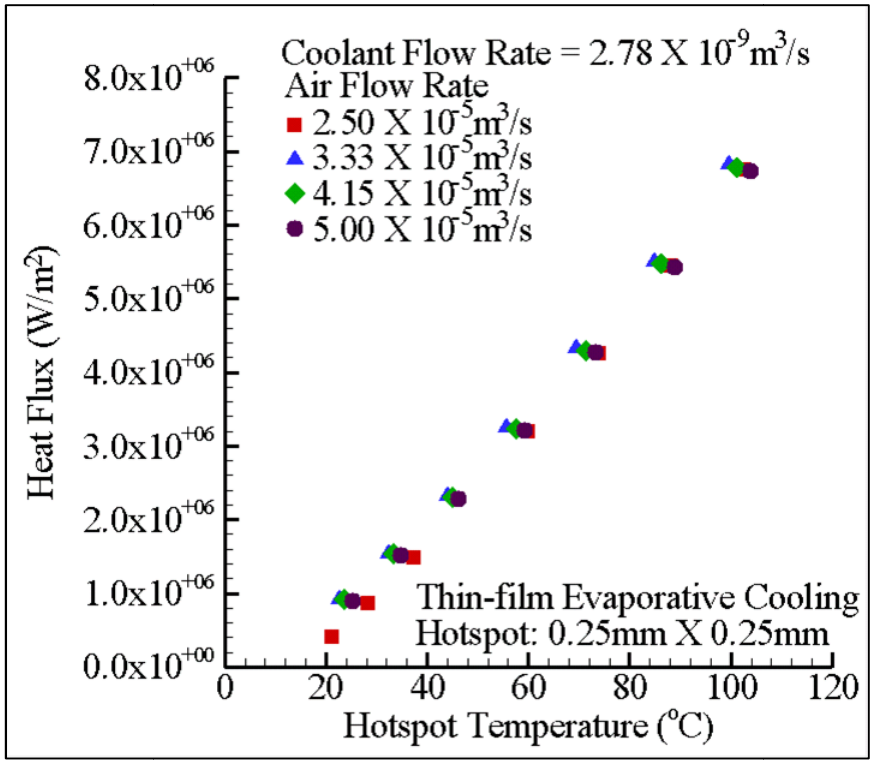

Figure 5.9 Device performance as a function of air flow rate

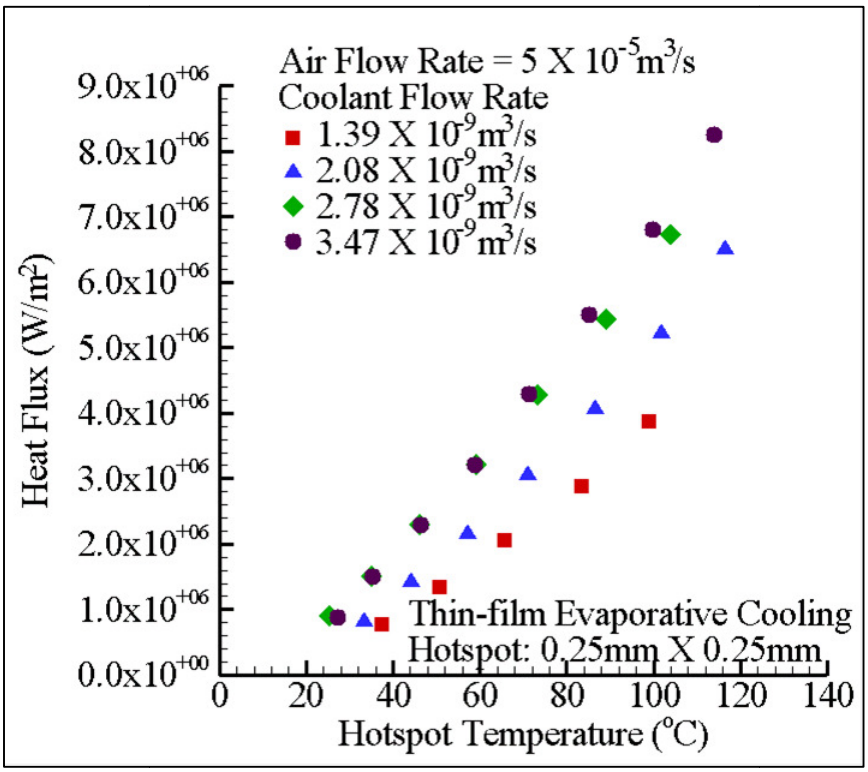

Figure 5.10 Device performance as a function of coolant flow rate.

Table 5.3 Heat transfer coefficients achieved by thin-film evaporation at hotspot temperatures approaching 85 ^{o}C and constant liquid coolant flow rate.

AFR (m^3/s)	2.50×10^{-5}	3.33×10^{-5}	4.17×10^{-5}	5.00×10^{-5}
CFR (m^3/s)	2.78×10^{-9}	2.78×10^{-9}	2.78×10^{-9}	2.78×10^{-9}
HTC (kW/m^2K)	89 ± 0.9	94 ± 0.9	92 ± 0.9	88 ± 0.9

Table 5.4 Heat transfer coefficients achieved by thin-film evaporation at hotspot temperatures approaching 85 ^{o}C and constant air flow rate.

AFR (m^3/s)	5.0×10^{-5}	5.0×10^{-5}	5.0×10^{-5}	5.0×10^{-5}
CFR (m^3/s)	1.39×10^{-9}	2.08×10^{-9}	2.78×10^{-9}	3.47×10^{-9}
HTC (kW/m^2K)	45 ± 0.5	61 ± 0.6	79 ± 0.8	85 ± 0.9

The variation in net heat flux with air (Figure 5.9) and coolant (Figure 5.10) flow rates indicate that the dominant resistance limiting the cooling performance is either conduction in thin film or vapor diffusion. However, it is also possible that resistance to advection is dominant in comparison to other factors. The variation in net heat dissipation with AFR and CFR can be explained as follows.

i. A large variation in heat transfer coefficient with CFR is likely due to the significant single phase cooling inside the thin film region. In this case, a large contribution of single phase convection to net heat dissipation can result in a prominent change in device performance with CFR.

ii. A relatively small variation in heat flux with AFR is observed due to:

   a. A large conduction or convective resistance in the thin film. This can be decreased by further thinning the film or incorporating a high conductivity porous structure within the thin film region.

b. Blockage membrane pores limiting the vapor transport via diffusion within the membrane. This can be addressed by suitably altering membrane fabrication process to avoid pore blockage.

c. Large diffusion resistance due to relatively smaller pores or thicker membranes. This can be addressed by enlarging the pore size and reducing the membrane thickness.

d. The decrease in advection resistance is significantly less in comparison to overall resistance, resulting only in a small deviation in device performance.

e. A large interfacial resistance to evaporation limiting the net heat flux dissipated.

A detailed analysis of heat and mass transfer including an interfacial transport study is therefore necessary to optimize the design of the nanopatch and improve the device performance. In the following section, the flow configuration of air jet is further explored to determine its effect on vapor advection and the net heat flux dissipated at the hotspot.

5.2.4 Effect of flow configuration of the sweeping gas

In order to determine the effect of flow configuration, jet impingement is carried out with varying two operating parameters, the nozzle to surface separation (Figure 5.11) and the inclination of jet relative to the surface normal (Figure 5.12). The net heat flux at different hotspot temperatures are obtained for a nozzle of diameter 1000μm impinging on a cavity of size $800\mu\text{m} \times 800\mu\text{m}$ .The nozzle-to-membrane separation was set at 4, 6 and 8 mm, while maintaining a constant AFR and CFR of 5×10^{-5} m^3/s and 4.2×10^{-9} m^3/s (Figure 5.11). The effect of jet impingement angle was studied for different inclinations (30^o, 45^o and 60^o) with respect to the surface normal (Figure 5.12).

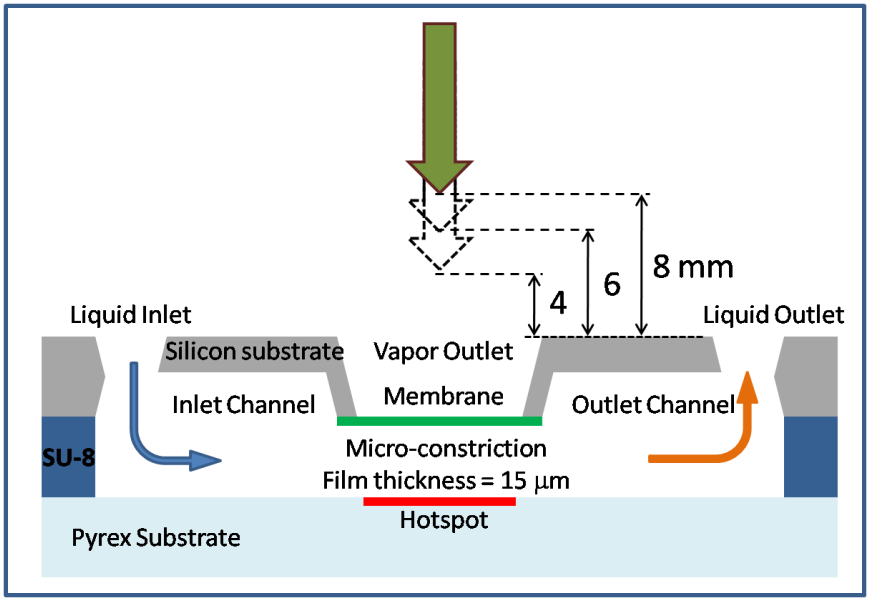

Figure 5.11 An experimental setup for studying effect of the nozzle-to-membrane separation

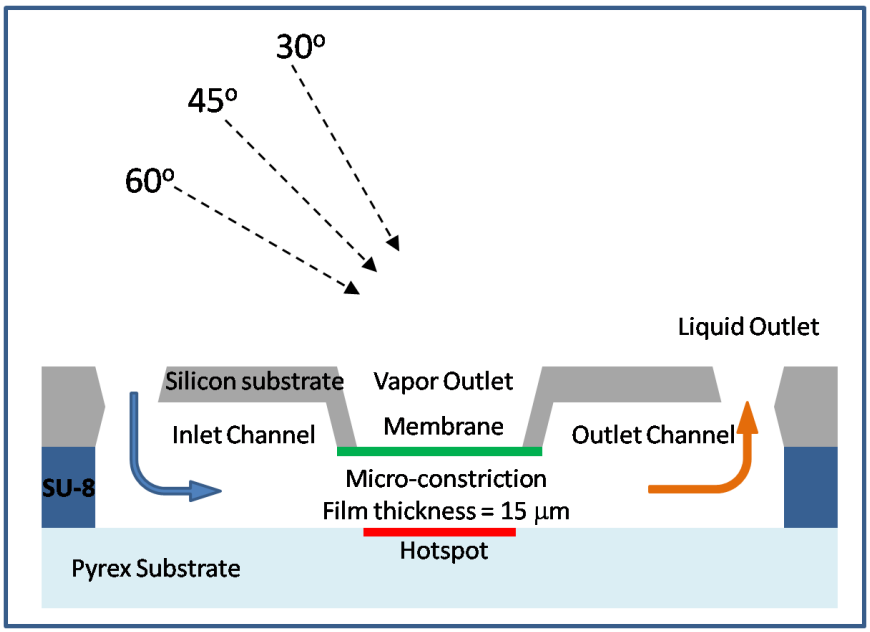

Figure 5.12 An experimental test setup for studying the effect of jet impingement angle

Figure 5.13 shows the variation of hotspot temperatures with respect to dissipated heat fluxes for perpendicular jet impingement. Heat fluxes in excess of 2.0 MW/m^2 can be dissipated from a $250\,\mu m$ hotspot while maintaining the coolant well below its saturation temperature (100 ^oC for de-ionized water at atmospheric pressure). As the nozzle-to-membrane separation was increased from 4mm to 8mm, only a small variation in heat flux was observed. Heat transfer coefficients (HTCs) obtained under these operating conditions is listed in Table 5.5. An increase of 25% in the overall heat transfer coefficient was observed when the nozzle separation was increased from 4 to 8mm.

Figure 5.14 on the other hand shows heat flux versus hotspot temperature, for a jet inclined at three different angles with respect to the normal. Dissipation of heat fluxes in excess of 2 MW/m^2 can still be demonstrated at close nozzle-to-membrane distance (0.2 cm) even using an oblique jet impingement, but as much as 70% increase in HTC is observed for jet impingement at 60^o as compared to 30^o with respect to the normal. A complete set of heat transfer coefficients at these operating conditions is listed in Table 5.6.

In this case, the change in net heat flux dissipated at the hotspot is due to two factors. The variation in nozzle-to-membrane separation and jet inclination can result in a change in both diffusion resistance as well as vapor advection. An increase in air flow rate or decrease in nozzle-to-membrane separation can result in a larger stagnation pressure that can change the resistance to vapor diffusion. This is due to the following factors:

i. A higher operating pressure inside the membrane pores can result in a decrease in mass-diffusivity since it is inversely proportional to pressure.

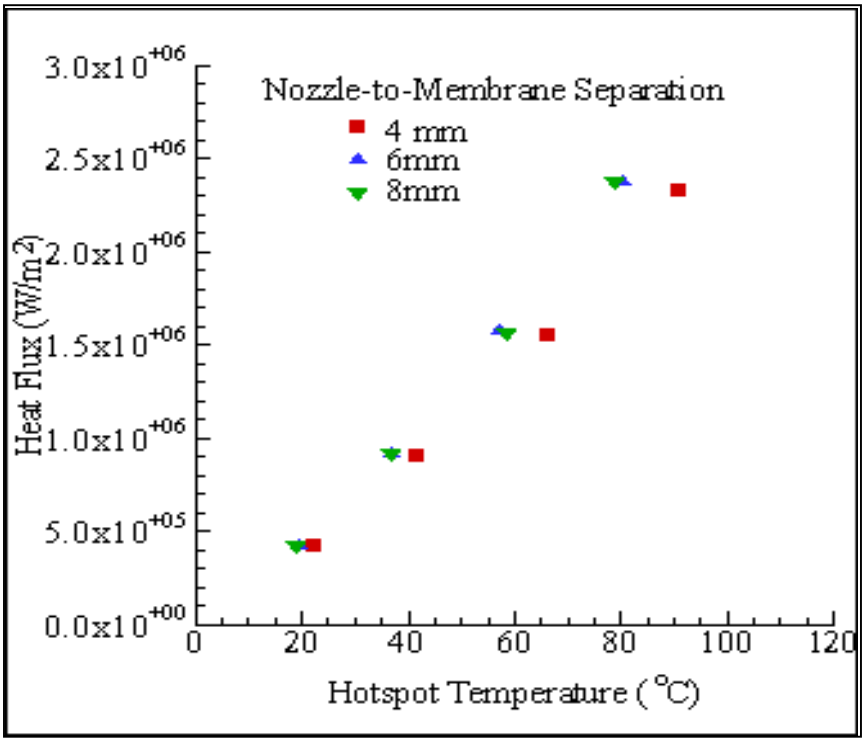

Figure 5.13 Device performance as a function of nozzle-to-membrane separation

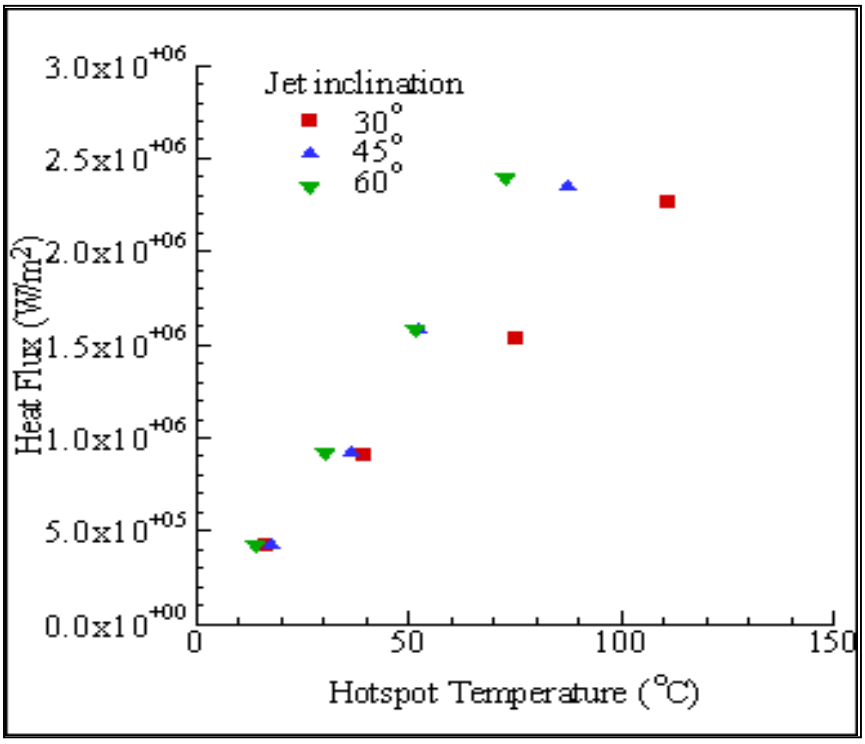

Figure 5.14 Device performance as a function of nozzle inclination with respect to the normal

Table 5.5 Heat transfer coefficients at a junction temperature of 90°C as a function of nozzle-to-membrane separation

Separation (m)	0.004	0.006	0.008
Jet Angle to the Normal	0	0	0
Air Flow Rate (m^3/s)	5×10^{-5}	5×10^{-5}	5×10^{-5}
Coolant Flow Rate (m^3/s)	4.2×10^{-9}	4.2×10^{-9}	4.2×10^{-9}
HTC (MW/m^2K)	0.032	0.038	0.04

Table 5.6 Heat transfer coefficients at a junction temperature of 90°C as a function of jet impingement angle

Separation (m)	0.002m	0.002 m	0.002 m
Jet Angle to the Normal	30	45	60
Air Flow Rate (m^3/s)	5×10^{-5}	5×10^{-5}	5×10^{-5}
Coolant Flow Rate (m^3/s)	4.2×10^{-9}	4.2×10^{-9}	4.2×10^{-9}
HTC (MW/m^2K)	0.025	0.033	0.043

ii. A higher stagnation pressure can force the liquid-vapor interface farther into the membrane, away from the outlet resulting in a longer diffusion path for the vapor molecules inside the membrane.

While the change in total diffusion resistance due to a varying stagnation pressure can moderately influence the net heat dissipation, the effect of flow configuration of the confined air jet can be more significant. Varying the operating characteristics for jet impingement of air affects both heat and mass transfer coefficients at the outlet of the membrane. The change in heat dissipation due to flow rate and nozzle separation of a

closely placed, perpendicular jet, impinging on a plain solid surface is well documented [26]. In this context, the performance of oblique free surface plane jet impingement is also crucial and has been studied [37]. While the change in heat and mass transfer by varying these factors is well characterized for a free surface jet, the overall performance of confined jet impingement can differ significantly for the same jet diameter, spacing and inclination. In other words, the net heat dissipated depends on the geometric configuration of the jet as well as the dimensions of the cavity confining the air jet. Therefore, in addition to the variation in vapor diffusion resistance, the change in the rate of vapor advection due to a varying nozzle-to-membrane separation or air-jet inclination can significantly affect the net heat flux dissipated at the hotspot. In this case, it is therefore postulated that the enhancement in heat flux observed is due to a more favorable flow configuration resulting from moving the nozzle away from the membrane and inclining farther away from surface normal.

In order to optimize the device performance, a detailed analysis of heat and mass transfer due to confined air jet impingement is necessary including an interfacial transport study, which will be presented in subsequent chapters.

5.3 Summary and Conclusions

Performance characterization of the device focused on assessing the effect of three key operating parameters, the coolant and air flow rates and air jet configuration, which directly affect thermal and mass transfer resistances. Comprehensive experiments conducted on a $250\,\mu$m-sized square hotspot allow estimation of the extent of improvement achievable over single-phase air jet and microchannel liquid cooling.

Device characterization by studying the net heat dissipation using only air jet impingement yields maximum heat flux close to 80 W/cm^2 at 80 ^{o}C for a thermal test die consisting of a centrally located 250 μm hotspot on a 2mm $\times$ 2mm Pyrex substrate. The hotspot-to-nozzle (diameter ~ 1,000 μm) separation and the average jet speed is varied between 5-15 mm and 35-75 m/s, respectively. The maximum overall heat transfer coefficient, defined as the ratio of heat flux to the difference in the hotspot and ambient temperatures was observed to lie between 3.3 - 5.5 kW/m^{2}K.

On a thermal test die with a 250 μm hotspot, the baseline tests of single phase convective heat transfer using de-ionized water flowing across a micro-constriction of 15 μm in height can dissipate heat fluxes close to 400 W/cm^2 at 80^{o}C, which is significantly larger in comparison to air jet impingement. The water flow rate varied between 1.39 and 3.47×10^{-9} m^3/s, resulting in an overall heat transfer coefficient between 39 - 76 kW/m^{2}K.

Gas assisted thin film evaporation was shown to dissipate heat fluxes close to 600 W/cm^2 at 90 ^{o}C, which is higher than both air jet and singe phase microchannel cooling on similar thermal test dies. The overall heat transfer coefficient demonstrated by thin film evaporation is found to lie between 88 to 94 kW/m^{2}K for a normally impinging jet with air speeds varying from 30 to 65 m/s and a fixed coolant flow rate of 2.78×10^{-9} m^3/s. For a fixed air jet speed of 65 m/s and coolant flow rates between 1.39 and 3.47×10^{-9} m^3/s, the heat transfer coefficients achieved lie in the range 45 to 85 kW/m^{2}K.

It is clearly demonstrated that evaporative cooling can outperform single phase convection using air jet or microchannel flow. Heat flux achieved by evaporative cooling demonstrates a 17 fold increase over air jet impingement and a 25% increase over single-phase microchannel cooling using water.

The effect of changing the flow configuration of the sweeping gas on the overall device performance is investigated. In particular, the device is tested for varying nozzle-to-membrane separation and angle of jet impingement. Heat flux in excess of 2 MW/m^2 is demonstrated for surface temperatures maintained below 90^oC. The heat transfer coefficient was found to increase from 0.032 to 0.04 MW/m^2K by increasing the nozzle-membrane separation from 4 mm to 8 mm. Likewise, the overall heat transfer coefficient was found to increase from 0.025 to 0.043 MW/m^2K by increasing the inclination with respect to the normal from 30^o to 60^o. The increase in performance is attributed to reduction overall resistance to mass transfer by diffusion and advection.

Heat fluxes in excess of 600 W/cm^2 are consistently demonstrated with hotspot temperatures approaching 95 ^oC. Clearly, a much higher heat flux can be dissipated by evaporation compared to critical heat fluxes (CHF) demonstrated by pool boiling, at surface temperatures well below saturation conditions. The results also indicate a possibility of further enhancement of heat dissipation through reduction of rate limiting resistances. Experimental observations suggest that to enhance overall performance the thermal resistance of liquid film and the mass transfer resistance of vapor transport through the membrane need to be further reduced by maintaining even thinner film and using a smaller thickness membrane, respectively.

In addition to suitably changing the device features for further enhancement in cooling, it is important to determine if the liquid-vapor interface offers relatively significant resistance to impede device performance. The next chapter is therefore dedicated to determine the interfacial characteristics during evaporation of water confined in nano-scale porous structures.

CHAPTER 6

INTERFACIAL TRANSPORT OF EVAPORATING WATER IN NANOPORES

6.1 Introduction

A detailed understanding of wetting characteristics of liquids on plain or structured solid surfaces and their effect on phase change are required for many applications. In order to analyze wetting and inter-phase transport, it is essential to identify all relevant factors affecting contact line dynamics. Capillarity alone has been extensively studied for interpreting the wetting phenomenon. Its relation to the chemical constitution of both solid and liquid was used to explain the extent of spreading and the equilibrium contact angle during partial wetting [59]. The role of capillary pressure and thermo-capillary effects during evaporation of liquid droplets on heated surfaces have also been investigated [60]. But, as the length scale decreases below $1\,\mu\text{m}$, long range interactions such as Van der Waals forces can also play an important role, in addition to surface tension, to define the interface shape and, in turn, the rates of mass and heat transfer due to phase change at the interface. The three forces due to dipole induction, molecular orientation and dispersion, which contribute towards the long range interaction between two molecules, are collectively known as the Van der Walls force. Among the constituent forces, dispersion is always present between molecules and is generally dominant, as compared to the dipole-dependent induction (Debye interactions) and orientation forces (Keesom interactions)[61].

An aspect of Van der Waals force which is less prominently addressed in the existing literature for analysis of interfacial transport is the retardation effect. The dispersion interactions between surfaces decay rapidly at longer separations due to attenuation of electromagnetic coupling. For very short and long distances, a well known asymptotic relation for disjoining pressure is given by $\Pi_d = -A_0 / 6\pi\delta^3$ and $\Pi_d = -B / \delta^4$, respectively, where A_0 is the non-retarded Hamaker's constant and B is the retarded dispersion constant [62], which is applicable beyond the crossover length. This length is roughly related to the characteristic ultraviolet radiation absorption wavelength of the medium and is generally of the order of 800 A^o [59]. While dispersion interactions are most significant in determining the disjoining pressure in the case of non-polar liquids, electrostatic interaction between molecules cannot be neglected when a polar solvent is utilized. The presence of both dispersion and electrostatic interaction between two interacting mediums is addressed by the DLVO (Derjaguin–Landau–Verwey–Overbeek) theory [63, 64] .

While DLVO can quantitatively describe electrostatic contribution towards surface forces in thin liquid films, it is now understood that additional interactions can exist which are "non-DLVO" in nature. From experimental observations, prior studies have estimated the effect of structural interactions in thin liquid films due to the forces other than Van der Waals and DLVO interactions [65-68]. The structural component of disjoining pressure arises when inter-phase boundary layers, whose structure is different from that of the bulk liquid, overlap. Supported by experimental measurements, the structural component of disjoining pressure was found to decay exponentially with distance [67]. However, with dissolved ions in water, these additional forces still fail to

explain the behavior of many colloidal systems. The concept of short range hydration forces was then introduced to relate theory to experiments based on interaction of mica surface with electrolyte solutions [69]. But this concept has been met with some skepticism [70], and is still amidst validation. Yet, there are more recent concepts based on additional interaction modes, such as image charge forces, steric interactions, and hydrophobic forces with an aim to fully explain experimental observations.

Given the uncertainty in establishing and estimating the universally applicable force interactions, a comprehensive investigation of interfacial transport in water films is not only challenging, but currently incomplete. Therefore, the objective of this analysis is to carry out a simplified analysis to identify the prominence of different interactions for sustaining flow, mass and energy transport in evaporating liquid film confined within a nanoscale capillary and to gain a mechanistic understanding of the process physics. Evaporation of simple, non-polar wetting liquids has been reported to elucidate effects arising due to Van-der Waals interactions, in addition to capillarity. In this regard it is noteworthy to acknowledge a contribution of Wayner and co-workers in both theoretical developments and experimental validation [71-73]. Additionally, experimental studies [74-77] and computational analysis [78, 79] of thermo-capillary convection and velocity slip in channels during phase-change [79] are of relevance to the problem analyzed in this work.

In the analysis of phase-change of fluids in confined spaces, the rate of evaporation at the free surface needs to be modified from the commonly used expression given by Schrage [80]. That is the change in equilibrium vapor pressure over a capillary meniscus, as compared to a “flat” interface, has to be accounted for using the Kelvin equation [81],

modified to include the effect of an adsorbed liquid film and presence of disjoining pressure [82-84]. Using interferometry, it has been shown that the predictions from the modified Kelvin equation match well with experimental measurements for capillary radii as small as few nanometers [83].

Interfacial transport of non-polar liquids is now well understood for evaporation in simple geometries like micro-channels and cylindrical tubes [71, 72, 74, 75, 78, 79, 85, 86]. However, the underlying solid-liquid-vapor interactions in previous studies were limited to dispersion and capillarity; the effect of electrostatic interactions, which are of much longer range, becomes important in the case of nano-confined liquids and is analyzed in the current study.

6.2 Analysis of Flow and Heat Transfer

The following mathematical model of fluid flow and heat transfer describes the interfacial transport of an evaporating meniscus inside a cylindrical pore. The cylindrical pore is assumed to be open-ended and exposed to atmospheric condition, which is a commonly encountered arrangement in practical applications of membrane-based phase-change processes. As a result, the interface is assumed to be surrounded by a gas phase comprising of air-vapor mixture at atmospheric pressure. The formulation presented herein includes the effects of capillary and disjoining pressures and also compares their importance relative to thermo-capillary stresses (Marangoni effect) at different operating conditions.

At steady state, the shape of an evaporating interface inside a channel or pore is often broadly divided into three regions, as shown in Figure 6.1: (1) a thin adsorbed film in equilibrium with gaseous phase forms the leading edge of the liquid-vapor interface; (2)

an adjacent thin-film region, which is significantly influenced by the disjoining pressure; and (3) the meniscus region where capillary pressure is a dominant force. Beyond the meniscus region, the flow can be considered fully-developed, laminar, and well described by the Hagen–Poiseuille equation. In this analysis, the origin of the cylindrical coordinate system is located at the junction of the evaporating thin-film region and the adsorbed film, as shown in Figure 6.1. Numerical integration of governing equations is carried out with respect to the axial coordinate, x, to compute other flow variables for $x \le 0$. The position of the interface is denoted by $r_i(x)$.

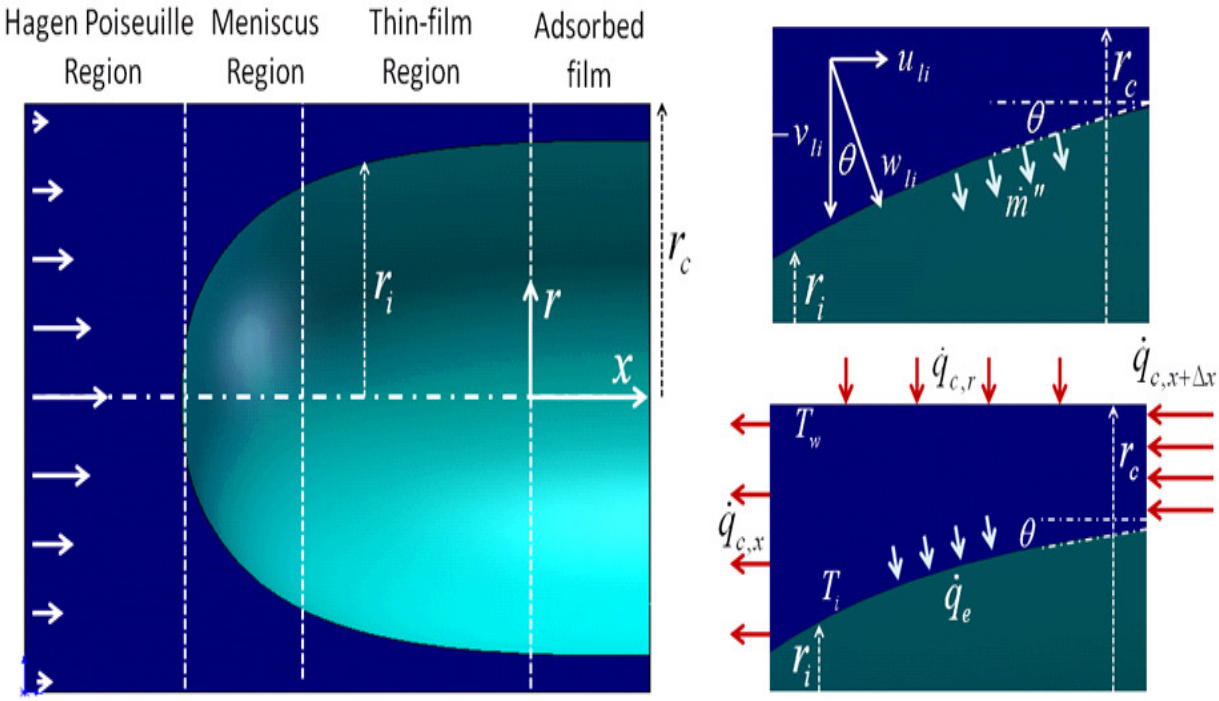

Figure 6.1 (a) Classification of the extended meniscus during evaporation (b) Schematic for evaluation of normal interfacial velocity and illustration of various boundary heat fluxes.

The model assumes a steady, axi-symmetric, incompressible flow. Furthermore, the hydrostatic pressure and radial pressure gradient is neglected as compared to the

dominant capillary, disjoining pressure and axial pressure gradients. With these assumptions, the axial component of momentum balance for liquid flow is given by:

$$-\frac{dp_{li}}{dx}+\frac{\mu_l}{r}\frac{\partial}{\partial r}\left(r\frac{\partial u_l}{\partial r}\right)=0 \tag{6.1}$$

The boundary conditions for fluid flow are the no-slip at the walls, $u=0$ at $r=r_c$ and thermo-capillary stress balance at the interface, $-\mu_l\frac{\partial u}{\partial r}=\frac{\partial \sigma}{\partial x}$ at $r=r_i$ [86]. The solution to the differential equation (6.1) with these boundary conditions is therefore given by:

$$u_l=\left(-\frac{1}{4\mu_l}\frac{dp_{li}}{dx}\right)\left(r_c^{\,2}-r^2+2r_i^2\ln\frac{r}{r_c}\right)-\frac{r_i}{\mu_l}\frac{\partial\sigma}{\partial x}\ln\frac{r}{r_c} \tag{6.2}$$

The mass flow rate at any axial position can be obtained by integration, $\int \rho_l u_l\left(2\pi r\right)dr$ between $r=r_i$ and $r=r_c$ to yield:

$$\begin{aligned}\dot{m}=&\frac{\pi\rho_l}{8\mu_l}\left(-\frac{dp_{li}}{dx}\right)\left[\left(r_c^{\,2}-r_i^2\right)\left(r_c^{\,2}-3r_i^2\right)-4r_i^4\ln\frac{r_i}{r_c}\right]\\&+\frac{\pi\rho_l}{8\mu_l}\left(\frac{d\sigma}{dT}\right)\left(\frac{dT_{li}}{dx}\right)\left[4r_i\left(r_c^{\,2}-r_i^2\right)+8r_i^3\ln\frac{r_i}{r_c}\right]\end{aligned} \tag{6.3}$$

The change in mass flow rate of the liquid along the axial position due to evaporation at the interface can be calculated in terms of the local mass flux. At any interfacial location the mass flux is given by evaporation kinetics [80],

$$\dot{m}''=\frac{2\hat{\sigma}}{2-\hat{\sigma}}\left(\frac{M}{2\pi R}\right)^{1/2}\left(\frac{p_{vi}}{T_{li}^{\,1/2}}-\frac{p_v}{T_v^{\,1/2}}\right) \tag{6.4}$$

where p_{vi} is the equilibrium vapor pressure, and p_v is the partial pressure of the vapor in the gas phase, which is a mixture of air and vapor at temperature T_v surrounding the

interface. In order to relate mass flux to the velocity of liquid phase, the mass continuity equation, $\partial u_l / \partial x + (1/r)\partial(r v_l)/\partial r = 0$ is integrated between $r = r_i$ and $r = r_c$.

$$r_i v_{li} = \frac{d}{dx}\int_{r_i}^{r_c} r\, u_l\, dr + r_i u_{li}\frac{dr_i}{dx} \tag{6.5}$$

Equation (6.5) assumes that $v_l = 0$ at $r = r_c$. Also, since the interface position r_i is a function of the axial variable, the Leibniz integral rule is used to obtain the expression at the right hand side of equation (6.5). This equation is transformed in terms of mass flow rate to obtain:

$$v_{li} = \frac{1}{2\pi\rho_l r_i}\frac{d\dot{m}}{dx} + u_{li}\frac{dr_i}{dx} \tag{6.6}$$

The interfacial velocity of liquid directed normal to the interface $w_{li} = \dot{m}'' / \rho_l$ can be evaluated in terms of the velocity components and the slope of the interface $\theta = \tan^{-1}(dr_i / dx)$ as illustrated in the Figure 6.1(b) and is given by the following equation:

$$w_{li} = u_{li}\sin\theta - v_{li}\cos\theta \tag{6.7}$$

Using equations (6.6) and (6.7), the mass flow rate at any axial location can be related to the rate of evaporation at the interface given by equation (6.4). The temperature discontinuity at the interface, $(T_{li} - T_v)$ using kinetic theory is given by $-0.45(T_v / 2R)^{1/2} u_v$ [87], where u_v represents the characteristic vapor speed during evaporation. Utilizing $\dot{m}'' / \rho_v$ as an appropriate scale for u_v, the temperature jump is ~5 ^{o}C for a conservatively large approximation for $\dot{m}''$ of ~5 kg/m^{2}s. In this case, the assumption of thermal equilibrium would then introduce an error less than ~5% even for

a high humidity $(95\%$ or $p_v / p_{vi} = 0.95)$ ambient environment. Therefore, to simplify the analysis, the discontinuity in temperature at the interface between the liquid and gas phase is neglected by assuming local thermal equilibrium or $T_v = T_{li}$ [86].

$$-\frac{\cos\theta}{2\pi r_i}\frac{d\dot{m}}{dx} = \frac{2\hat{\sigma}}{2-\hat{\sigma}}\left(\frac{M}{2\pi R T_{li}}\right)^{1/2}\left(p_{vi} - p_v\right) \tag{6.8}$$

Equation (6.3) relates mass flow rate to two unknown variables, namely the pressure and temperature gradient. The pressure distribution in the liquid phase can be obtained using balance of normal stress at the interface, while the interfacial temperature distribution is obtained using energy conservation.

Although the pressure in liquid phase varies along the interface, the total pressure of the gas phase consisting of air and evaporated vapor mixture can be assumed constant and equal to atmospheric pressure p_{atm}. This assumption is based on the evaluation of Knudsen number, $Kn = M\Big/\left(\sqrt{8}\pi d^2 \rho_v N_A r_c\right)$ for the transport of vapor molecules inside the cylindrical pore, which is estimated to be close to 10 for a pore radius of 25nm. Since the corresponding flow regime is Knudsen diffusion, the pressure drop in the gaseous phase is neglected. With this assumption, the balance of normal stress across the interface is given in terms of capillary and disjoining pressures by:

$$p_{atm} - p_{li} = 2\sigma\kappa + \Pi_d \tag{6.9}$$

where the local mean curvature of the interface [88] and the disjoining pressure [89, 90] are given by the following equations:

$$\kappa = \frac{1}{2}\left\{\frac{1}{r_i\left[1+\left(dr_i/dx\right)^2\right]^{1/2}} + \frac{d^2 r_i / dx^2}{\left[1+\left(dr_i/dx\right)^2\right]^{3/2}}\right\} \tag{6.10}$$

$$\Pi_d = \frac{-A}{6\pi\left(r_c - r_i\right)^3} + \frac{\varepsilon\varepsilon_o}{2\left(r_c - r_i\right)^2}\left(\frac{\pi k_B T_{li}}{Ze}\right)^2 \tag{6.11}$$

It is assumed that the value of surface tension remains close to bulk value even in the thin film region. Additionally the retardation of dispersion force is neglected in this analysis, and the Van der Walls component of disjoining pressure is evaluated using the non-retarded Hamaker's constant. The Hamaker's constant for two macroscopic phases 1 and 2 interacting across a medium 3 is calculated using the following equation [61],

$$A = \frac{3}{4}k_B T_{li}\left(\frac{\varepsilon_1 - \varepsilon_3}{\varepsilon_1 + \varepsilon_3}\right)\left(\frac{\varepsilon_2 - \varepsilon_3}{\varepsilon_2 + \varepsilon_3}\right) + \frac{3h\nu_e}{8\sqrt{2}}\frac{\left(n_1^2 - n_3^2\right)\left(n_2^2 - n_3^2\right)}{\sqrt{n_1^2 + n_3^2}\sqrt{n_2^2 + n_3^2}\left(\sqrt{n_1^2 + n_3^2} + \sqrt{n_2^2 + n_3^2}\right)} \tag{6.12}$$

where ε and n represent the dielectric constant and the refractive index of the interacting substances, respectively; k_B and h denote the Boltzmann's and Planck's constants, respectively; and ν_e denotes the absorption frequency, which is assumed to be $2.9\times10^{15}\,\mathrm{s}^{-1}$ [91]. According to equation (6.12), the Hamaker's constant varies slightly from -3.261×10^{-20} to -3.148×10^{-20} J corresponding to a temperature variation of 25 ^{o}C to 90 ^{o}C. In this analysis a constant value of -3.148×10^{-20} J is assumed for the non-retarded Hamaker's constant.

The electrostatic interactions arise due to charging of the pore wall when it is submerged in an electrolyte, due to either a chemical reaction inducing charge dissociation or due to adsorption of charged species from the electrolyte. For instance, surface carboxylic groups could dissociate by losing protons to the electrolyte to become negatively charged. On the other hand, calcium ions from electrolyte could get adsorbed onto previously uncharged surfaces of lipid bilayers to result in a positively charged surface. In both cases, the total charge on the pore wall is balanced by an equal number of

counter charges in the electrolyte. The disjoining pressure arising due to these electrostatic interactions is calculated using Langmuir's equation for thin films of dilute electrolyte on surfaces of high intrinsic electric potential. Langmuir's equation has been utilized to determine the electrostatic interactions between water and quartz surfaces. It is to be noted that Langmuir's equation offers simplicity and allows obtaining a critical insight to study the importance of electrostatic interaction. An alternative and more accurate analysis for a broader range of ionic strengths of electrolytes can be carried out by solving for charge and potential distribution in polar solvents. The electrostatic disjoining pressure can then be obtained from these distributions. Finally, the evaluation of disjoining pressure using equation (6.11) neglects the structural component due to lack of a well established and accepted relation to calculate structural forces as a function of film thickness.

The governing equation to determine the interfacial temperature gradient is derived from energy conservation applied to a differential volume as shown in Figure 6.1(b). In this case the net heat transferred to the control volume by conduction and advection causes evaporation of liquid at the interface. In order to simplify the energy conservation, the relative magnitudes of conduction and advection are assessed. The ratio of heat transferred by axial conduction $\left(\dot{q}_c \sim k_l A \Delta T / r_c\right)$ and advection $\left(\dot{q}_a \sim \dot{m} C_{pl} \Delta T\right)$ is estimated using the flow rate obtained from the dissipated heat flux from a single pore and the latent heat of evaporation, $\dot{m} \sim \dot{q}'' A / h_{fg}$. For a cylindrical pore of radius 25 nm and a reference heat flux of 1000 W/cm^2, the ratio of heat conduction to advection, $\dot{q}_c / \dot{q}_a \sim k_l h_{fg} / \left(\dot{q}'' C_{pl} r_c\right)$, is in excess of 10^3. A heat flux of ~1000 W/cm^2 is chosen because this analysis has been motivated by application of evaporative cooling for

thermal management of high performance electronic devices, which operate under high power dissipation loads. The analysis, however, is general enough and is applicable to other (lower and higher) heat fluxes supporting evaporation phase change within a nanopore. In this regard, the specific value of the heat flux is used only as a scaling parameter in the analysis. It will later be shown in the discussion of results that the heat flux used here for estimating the ratio is justified and therefore this approach is applicable even to pores of radius 500 nm. Neglecting advective heat transfer, the integral form of energy conservation is given by $\dot{q}_{c,r} - \dot{q}_{c,x} + \dot{q}_{c,x+\Delta x} = \dot{q}_e$. The net heat conducted along the axial direction, $\dot{q}_{c,x+\Delta x} - \dot{q}_{c,x} \simeq (\Delta x)\partial \dot{q}_{c,x} / \partial x$ is evaluated using the following equation, where Leibniz integral rule is again utilized.

$$\begin{aligned} \frac{\partial \dot{q}_{c,x}}{\partial x} &= \frac{\partial}{\partial x}\int_{r_i}^{r_c} -k_l (2\pi r)\frac{\partial T_l}{\partial x} dr \\ &= (-2\pi k_l)\int_{r_i}^{r_c} r\frac{\partial^2 T_l}{\partial x^2} dr + (2\pi k_l r_i)\left(\frac{\partial T_l}{\partial x}\right)_i \frac{dr_i}{dx} \end{aligned} \tag{6.13}$$

A further simplification introduced in this analysis is a linear temperature variation in the radial direction. This approximation has been used previously for study of interfacial transport in microscopic pores and channels [86], and should be equally applicable to nano-scale pores.

$$\frac{T_l - T_w}{T_{li} - T_w} = \frac{r - r_c}{r_i - r_c} \tag{6.14}$$

where T_{li} and T_w denote the temperature of the interface and the capillary wall, respectively. The governing equation for interfacial temperature distribution is obtained by using the linear temperature profile and the overall energy conservation. The derivation of this equation is included in Appendix A.

$$\left(2\pi k_l r_c\right)\frac{T_w - T_{li}}{r_c - r_i} + \frac{2\pi k_l}{3}\left(T_w - T_{li}\right)\left(\frac{dr_i}{dx}\right)^2 - \frac{2\pi k_l}{3}\left(r_c - r_i\right)\frac{dr_i}{dx}\frac{dT_{li}}{dx}$$
$$+\frac{\pi k_l}{3}\left(r_c + 2r_i\right)\left(T_w - T_{li}\right)\frac{d^2 r_i}{dx^2} - \frac{\pi k_l}{3}\left(r_c + 2r_i\right)\left(r_c - r_i\right)\frac{d^2 T_{li}}{dx^2} = -h_{fg}\frac{d\dot{m}}{dx} \tag{6.15}$$

Governing equations (6.3), (6.8), (6.9) and (6.15) are used to determine the shape of the interface, flow rate, pressure and temperature distribution. These equations are non-dimensionalized using the following scaling parameters. The axial and radial coordinates are scaled with capillary radius, r_c as $\bar{x} = x / r_c$ and $\bar{r} = r_i / r_c$, while pressure, flow rate and temperature are scaled as $\bar{p} = p_{li} / p_v$, $\bar{\dot{m}} = \dot{m} / \dot{m}_o$ and $\bar{T}_i = 2\pi r_c k_l \left(T_{li} - T_w\right) / \dot{m}_o h_{fg}$, respectively. The mass flow rate, $\dot{m}_o$ used for scaling other dependent variables is given by the following equation, where $p_{v,eq}\left(T_w\right)$ denotes the saturation pressure at temperature T_w.

$$\dot{m}_o = \frac{2\hat{\sigma}}{2 - \hat{\sigma}}\left(\frac{M}{2\pi R T_w}\right)^{1/2}\left(p_{v,eq}\left(T_w\right) - p_v\right)\left(2\pi {r_c}^2\right) \tag{6.16}$$

The non-dimensional form of governing equations is summarized below, where Π_i denote the non-dimensional parameters resulting from scaling flow variables. It is to be noted that in deriving the non-dimensional form of mass flux from evaporation kinetics (equation (6.8)), the Clausius–Clapeyron relation, $\left(dP / dT = \rho_v h_{fg} / T\right)$ has been used to determine the equilibrium vapor pressure as a function of temperature. A derivation of this equation is provided in Appendix A.

$$\bar{\dot{m}} = \frac{\pi}{8}\Pi_1\left(-\frac{d\bar{p}_{li}}{d\bar{x}}\right)\left[\left(1 - \bar{r}_i^2\right)\left(1 - 3\bar{r}_i^2\right) - 4\bar{r}_i^4 \ln \bar{r}_i\right]$$
$$+\frac{1}{16}\Pi_2\left(\frac{d\bar{T}_i}{d\bar{x}}\right)\left[4\bar{r}_i\left(1 - \bar{r}_i^2\right) + 8\bar{r}_i^3 \ln \bar{r}_i\right] \tag{6.17}$$

$$\left(1+\frac{1}{2\pi}\Pi_3\Pi_4\bar{T}\right)\left(1+\frac{1}{2\pi}\Pi_4\bar{T}\right)^{-1/2}=\frac{-1}{\bar{r}_i\left[1+\left(d\bar{r}_i/d\bar{x}\right)^2\right]^{1/2}}\frac{d\bar{\dot{m}}}{d\bar{x}} \tag{6.18}$$

$$\begin{aligned}\Pi_5-\bar{p}_{li}=\Pi_6&\left\{\frac{1}{\bar{r}_i\left[1+\left(d\bar{r}_i/d\bar{x}\right)^2\right]^{1/2}}+\frac{d^2\bar{r}_i/d\bar{x}^2}{\left[1+\left(d\bar{r}_i/d\bar{x}\right)^2\right]^{3/2}}\right\}\\&+\frac{\Pi_7}{6\pi\left(1-\bar{r}_i\right)^3}\;+\;\Pi_8\left(\frac{1+\Pi_4\bar{T}/2\pi}{1-\bar{r}_i}\right)^2\end{aligned} \tag{6.19}$$

$$\begin{aligned}&\frac{-\bar{T}_i}{1-\bar{r}_i}-\frac{\bar{T}_i}{3}\left(\frac{d\bar{r}_i}{d\bar{x}}\right)^2-\frac{\left(1-\bar{r}_i\right)}{3}\frac{d\bar{r}_i}{d\bar{x}}\frac{d\bar{T}_i}{d\bar{x}}\\&-\frac{\bar{T}_i}{6}\left(1+2\bar{r}_i\right)\frac{d^2\bar{r}_i}{d\bar{x}^2}-\frac{\left(1+2\bar{r}_i\right)\left(1-\bar{r}_i\right)}{6}\frac{d^2\bar{T}_i}{d\bar{x}^2}=-\frac{d\bar{\dot{m}}}{d\bar{x}}\end{aligned} \tag{6.20}$$

The non-dimensional parameters are defined as:

$$\Pi_1=\frac{\rho_l r_c^{\,3}p_v}{\mu_l\dot{m}_o},\ \Pi_2=\frac{\rho_l r_c h_{fg}}{\mu_l k_l}\left(\frac{d\sigma}{dT}\right),\ \Pi_3=\frac{\rho_v\left(T_w\right)h_{fg}}{p_{v,eq}\left(T_w\right)-p_v},\ \Pi_4=\frac{\dot{m}_o h_{fg}}{r_c k_l T_w},\ \Pi_5=\frac{p_{atm}}{p_v},\ \Pi_6=\frac{\sigma}{r_c p_v}$$

$$\Pi_7=\frac{-A}{r_c^{\,3}p_v},\ \Pi_8=\frac{\varepsilon\varepsilon_o}{2p_v}\left(\frac{\pi kT_w}{Zer_c}\right)^2$$

The ratio of non-dimensional parameters Π_2/Π_1, compares the pressure gradient arising from thermo-capillary effect to the total pressure gradient driving the flow in the meniscus. Π_4 represents a ratio of radial temperature drop across the extended meniscus to the wall temperature. The characteristic value of Π_4 is typically small (~10^{-3} - 10^{-2}) for evaporation inside nano-pores or channels. Π_6, Π_7 and Π_8 compare pressures arising due to capillary, Van der Waals and electrostatic interactions.

Equations (6.17) to (6.20) are numerically integrated using Runge-Kutta method to obtain the location of the interface, pressure and mass flow rate as function of the axial

variable. Due to the singularity $d\bar{r}_i / d\bar{x} \to \infty$ as $\bar{r}_i \to 0$, numerical convergence could not be achieved in the vicinity of $\bar{r}_i = 0$. In order to obtain the solution at $\bar{r}_i = 0$, the governing equations were transformed from $\bar{x}$ to $\bar{r}_i$ dependence to facilitate integration with respect to $\bar{r}_i$. By adopting this procedure, convergence was easily achieved since $d\bar{x} / d\bar{r}_i \to 0$ as $\bar{r}_i \to 0$. The transformed governing equations can also be found in Appendix A.

The boundary conditions at $\bar{x} = 0$ required to integrate equations (6.17) to (6.20) are $\bar{r}_i = \bar{r}_o$, $d\bar{r}_i / d\bar{x} = 0$, $\bar{\dot{m}} = 0$, $\bar{p} = \Pi_5 - \Pi_6 / \bar{r}_o - \Pi_7 / (1-\bar{r}_o)^3 - \Pi_8 / (1-\bar{r}_o)^2, \bar{T} = 0$ and $d\bar{T} / d\bar{x} = 0$ where $\bar{r}_o$ denotes the equilibrium radius, which is related to thickness of the adsorbed film as $\bar{r}_o = 1 - \bar{t}_o$. The following section describes the procedure used to calculate the adsorbed film thickness.

6.3 Equilibrium Thickness of an Adsorbed Film

The thickness of the adsorbed film on a pore or channel wall is determined by various factors that define equilibrium between the condensed and gas phase. Kelvin's relation was based on equilibrium between a capillary held liquid and its vapor phase. In the case of capillary rise, the equation takes the form $p_{v,eq} - p_{vi} = \sigma\kappa\rho_v / (\rho_l - \rho_v)$ where $p_{v,eq}$ and p_{vi} represent the vapor pressure in equilibrium with the liquid for a plane and curved interface, respectively [81]. A modification to Kelvin's equation proposed by Cohen incorporates gas adsorption on the walls of cylindrical pores. The resulting isothermal jump in equilibrium vapor pressure of a pure liquid-vapor system at

temperature T due to the presence of an adsorbed film of thickness t in a pore of radius r_c is given by the following equation [92].

$$\left(\rho_l RT / M\right) \ln\left(p_{vi} / p_{v,eq}\right) = -\sigma / \left(r_c - t\right) \tag{6.21}$$

Using equation (6.21) the change in the equilibrium vapor pressure due to a curved meniscus, with an effective capillary radius, $\left(r_c - t\right)$ of 25nm, at a temperature T ~ 90°C is estimated to be less than 2%. Therefore, in this analysis the equilibrium vapor pressure p_{vi} is calculated from saturation properties of water as a function of temperature.

A thermodynamic treatment of phase change in the cylindrical pore was later presented by de Boer [93], elucidating the hysteresis observed during capillary condensation and evaporation of simple dielectric fluids. The derivation of equilibrium film thickness presented herein is an extension of de Boer's study by incorporating the formulation of disjoining pressure by Derjaguin [89] and including electrostatic interactions in polar liquids as given by Langmuir [89, 90].

The thickness of an adsorbed layer in a liquid-vapor system confined inside a pore or channel is governed by the equilibrium established between the condensing (gas) and evaporating (liquid) phases. At a fixed pressure and temperature, the change in free energy of this thermodynamic system when dN moles of gas condense is given by $dG_{p,T} = \sum \left(\frac{\partial G}{\partial N}\right)_{p,T} dN$. The factors affecting the free energy of the system during capillary condensation or evaporation are the chemical potential of interacting phases, the surface tension and the disjoining pressure. These are mathematically expressed as $\hat{\mu} = \left(\partial G / \partial N\right)_{p,T}$, $\sigma = \left(\partial G / \partial S\right)_{p,T}$ and $\Pi_d = \left(-1/S\right)\left(\partial G / \partial t\right)_{p,T}$, where S represents the

surface area of the interface, t corresponds to the film thickness, and Π_d represents the disjoining pressure experienced by the condensed phase in contact with the pore. These factors affecting the net change in free energy are incorporated in the analysis as shown below:

$$dG_{p,T} = \left(\frac{\partial G}{\partial N}\right)_{p,T} + \left(\frac{\partial G}{\partial S}\right)_{p,T} \frac{dS}{dN} + \left(\frac{\partial G}{\partial t}\right)_{p,T} \frac{dt}{dN} \tag{6.22}$$

Using equations relating variables N, S and t, which are $dS/dN = -V_m/(r-t)$ and $dt/dN = V_m/A$ where V_m represents the molar volume of the condensed phase, the transformed equation (6.23) illustrates how both capillary and disjoining pressure can affect the free energy of the system during a phase-change process.

$$\frac{\partial G}{\partial N}_{p,T} = \hat{\mu}_c - \hat{\mu}_g - \frac{\sigma}{(r_c - t)} V_m - \Pi_d V_m \tag{6.23}$$

where the difference in the chemical potential $(\hat{\mu}_c - \hat{\mu}_g)$ in equation (6.23) can be represented in terms of pressure and temperature, $RT \ln(p_{v,eq}/p_v)$ for an ideal solution, where $p_{v,eq}$ is the saturation pressure at temperature T and p_v is the partial pressure of vapor in the air-vapor mixture surrounding the interface.

In order to establish equilibrium, the free energy should attain a minimum, which requires two conditions to be satisfied, namely $(\partial G/\partial N)_{p,T} = 0$ and $(\partial^2 G/\partial N^2)_{p,T} > 0$. Hence, the equilibrium film thickness is determined from the following two relations:

$$(\rho_l RT/M)\ln(p_{v,eq}/p_v) - \frac{\sigma}{(r_c - t_e)} - \Pi_d = 0 \tag{6.24}$$

$$-\frac{\sigma}{(r_c - t_e)^2} - \frac{d\Pi_d}{dt} \geq 0 \tag{6.25}$$

In deriving relation (6.25), the relation $dt/dN > 0$ has been used, which implies a growth in the film as vapor molecules are transferred from gas phase to the condensed layer. The values of film thickness for water at 90 ^{o}C confined inside a capillary of radius 30nm and satisfying equation (6.24) for different values of relative pressure $p_v / p_{v,eq}$ are shown in Figures 6.2 (a) and (b). Evidently there are multiple solutions of equation (6.24) as illustrated by circled data points in Figures 6.2 (a) and (b), but only those values satisfying inequality (6.25) can establish a stable equilibrium. These values are marked in Figure 6.2(a), which correspond to the conditions $\partial G/\partial N = 0$, as well as $\partial^2 G/\partial N^2 > 0$.

The equilibrium thickness of the adsorbed film is a function of three parameters, namely the temperature, the vapor-pressure ratio and the capillary radius. The adsorbed thickness as a function of capillary radius and vapor-pressure ratio is shown for water at a temperature of 90 ^{o}C in Figure 6.3a. The partial pressure of vapor, p_v in the gas phase surrounding the interface is governed by the rate of vapor transport away from interface. In other words, the ambient is relatively dry when vapor removal from the near interface zone via diffusion and/or advection is efficient and it is humid when gas phase mass transfer is poor and the process is mass transport limited. An increase in the vapor pressure of the ambient causes a decrease in the net driving potential for evaporation, resulting in a thicker adsorbed film in equilibrium with vapor.

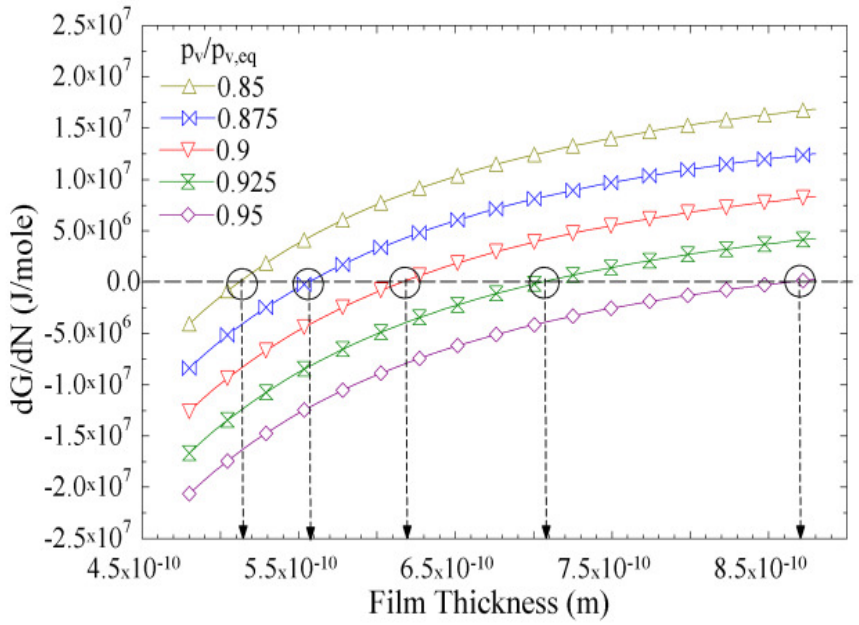

(a)

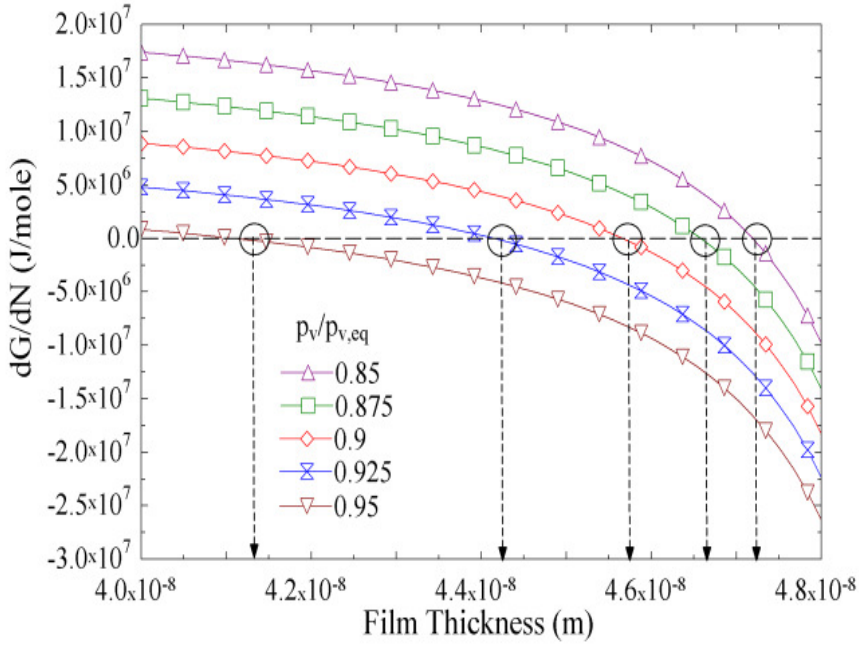

(b)

Figure 6.2. The adsorbed film thickness corresponding to $\partial G / \partial N = 0$ and (a) $\partial^2 G / \partial N^2 > 0$, (b) $\partial^2 G / \partial N^2 < 0$, calculated at different vapor pressures for $r_c = 30\text{nm}$ and $T_w = 90^\circ\text{C}$.

On the other hand, a decrease in the capillary radius also results in thicker adsorbed film for a given vapor pressure ratio. As the effective capillary radius decreases, the molecules at the free surface are more closely held by the neighboring surface molecules resulting in thicker equilibrium films. A constant decrease in capillary radii can potentially drive the system closer to equilibrium if the ambient is sufficiently saturated. This phenomenon is indeed observed during capillary condensation and evaporation and explains the hysteresis observed in the isotherms during adsorption and desorption [93]. It is to be noted that a fixed value of surface tension for water is assumed in this analysis to determine the equilibrium film thickness. Due to the interaction between ultra thin liquid film and the substrate, the thickness dependence of the surface tension is obtained by the integration of the corrected van der Waals pressure equation [94]. The deviation in the value of surface tension for very thin liquid films (~ 1nm) from its bulk value, at a fixed temperature was found to be within 3%. Therefore, while the temperature dependence of surface tension is included to account for the thermocapillary effect, the thickness effect is neglected due to its relatively minor contribution. The formulation presented in this study to calculate the equilibrium film thickness differs from that initially proposed by Wayner et al [71],

$$t_e = \left[\frac{-AV_m T_v}{6\pi M h_{fg} \left(T_{li} - T_v \right)} \right]^{1/3} \tag{6.26}$$

which was later adopted in many subsequent studies. The derivation of equation (6.26), applicable only to non-polar solvents is based entirely on evaporation kinetics and bears no information on the free energy of the liquid-vapor system. It is also evident that this formulation cannot be utilized in systems where the condensed phase is in thermal

equilibrium with its gas phase, while it is indeed possible for an unsaturated vapor phase to be in thermal equilibrium with its liquid phase, by establishing a non-evaporating adsorbed layer. The interfacial temperature jump, $(T_{li} - T_v)$ and vapor temperature, T_v, required for computing the adsorbed film thickness in equation (6.26) are commonly postulated as a-priori known parameters; however, for a self-consistent comparison of our approach (based on local thermal equilibrium between phases) to that of Wayner et al [71], the temperature jump and vapor temperature are scaled by $\dot{m}_o h_{fg} / (2\pi r_c k_l)$ and T_w, respectively, to calculate equilibrium film thickness, with evaporation rate $\dot{m}_o$ given by equation (6.16).

Figure 6.3(b) shows variation of adsorbed film thickness calculated using equation (6.26) for different capillary radii and vapor pressures, using $(T_{li} - T_v)$ and T_v, estimated as outlined above. Comparing results in Figures 6.3 (a) and (b) shows that an increase in the adsorbed film thickness with capillary radius and relative vapor pressure is observed in both cases, with difference in magnitude within a factor of 2. This mismatch is due to inclusion of electrostatic interactions, as well as the procedure used for estimating the temperature jump in terms of the evaporation rate.

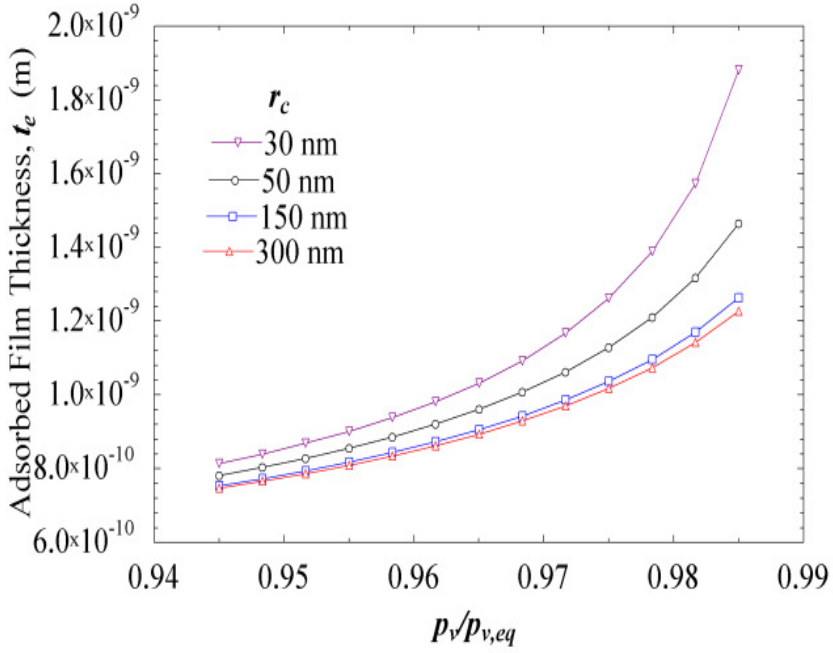

(a)

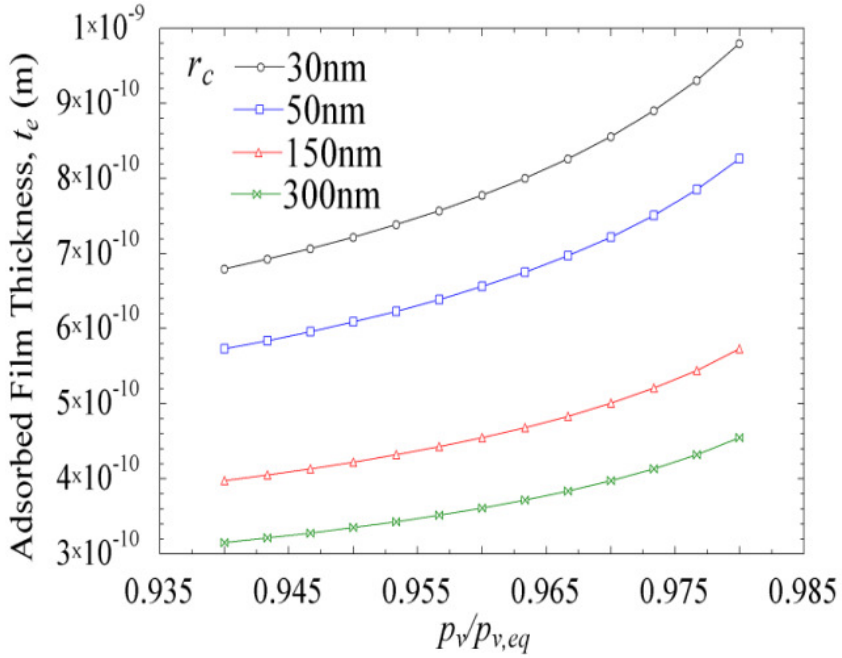

(b)

Figure 6.3. (a) The adsorbed film thickness calculated at $T_w = 90^{\circ}\mathrm{C}$ for different capillary radii and vapor pressures used in the model described in this work. (b) Adsorbed film thickness calculated using equation (6.26), which neglects electrostatic interactions.

6.4 Results and Discussion

The governing equations are solved to obtain the shape of the interface, mass flow rate, pressure and temperature distribution inside the capillary. The importance of including electrostatic disjoining pressure is discussed. The effects of thermo-capillary stresses are also presented for different operating conditions. The three operational parameters identified to be critical in the resulting flow characteristics are the radius of the capillary, r_c, the wall temperature, T_w, and the relative vapor-pressure, $p_v / p_{v,eq}$. The interface shown in all simulations is assumed to be pinned at $\bar{x} = 0$, which also marks the boundary of adsorbed film in equilibrium with the ambient vapor phase. The temperature dependent properties of water used for all calculations are listed in Appendix A. In order to build intuitive understanding of the problem in hand, the results are described in terms of physical (dimensional) parameters. A brief discussion of the results in terms of the relevant non-dimensional groups is also included where necessary to support the generality of our conclusions.

6.4.1 Capillary and disjoining pressures

The relative effects of capillary and disjoining pressures on the shape of the interface are compared in Figure 6.4, corresponding to $r_c = 30\text{nm}$, $T_w = 90^{\circ}\text{C}$ and $p_v / p_{v,eq} = 0.98$. During evaporation, the interface acquires a distinct shape to balance the viscous stresses and pressure forces. The total interface area of the meniscus inside a capillary tube is smallest when only capillary pressure is considered, while it is largest when capillary and disjoining pressures are both included in the analysis. Away from the pore-wall, where capillary forces are significantly larger than disjoining pressure, the meniscus

is highly curved, resulting in higher gradient in capillary pressure to balance the viscous pressure drop inside the liquid. On the other hand, the interface is less curved and the change in slope is more gradual when disjoining pressure is significant in addition to capillary pressure near the pore wall. The presence of electrostatic interaction in addition to Van der Waals forces enhances the disjoining pressure, causing a further reduction in the gradient in the curvature required to balance the viscous stress.

The relative magnitudes of various forces acting on the interface are shown in Figure 6.5 in terms of relative pressure along the axial position. The non-dimensional variables corresponding to $r_c = 30\text{nm}$, $T_w = 90^\circ\text{C}$ and $p_v / p_{v,eq} = 0.98$ are of the following orders of magnitude: $\Pi_6 = 3\times10^{1}, \Pi_7 = 9\times10^{-4}$, and $\Pi_8 = 6\times10^{-2}$, which indicate the relative strengths of capillary, Van der Waals and electrostatic interactions, respectively. It is clear that capillary pressure is a dominant force in nano-pores compared to disjoining pressure. The magnitudes of Van der Waals and electrostatic interactions are comparable to capillary pressure only at close proximities of $\overline{r_i} > 0.96$ and $\overline{r_i} > 0.95$ to the wall, respectively. Interestingly, the equilibrium radius of the adsorbed film for these conditions is $\overline{r_o}$=0.9373. This suggests that the capillary pressure is significant in a large portion of the extended meniscus; also, since even the adsorbed film inside a cylindrical pore has a non-zero curvature, the capillary forces are significant along the entire length of the meniscus in small pores (~ 30 nm).

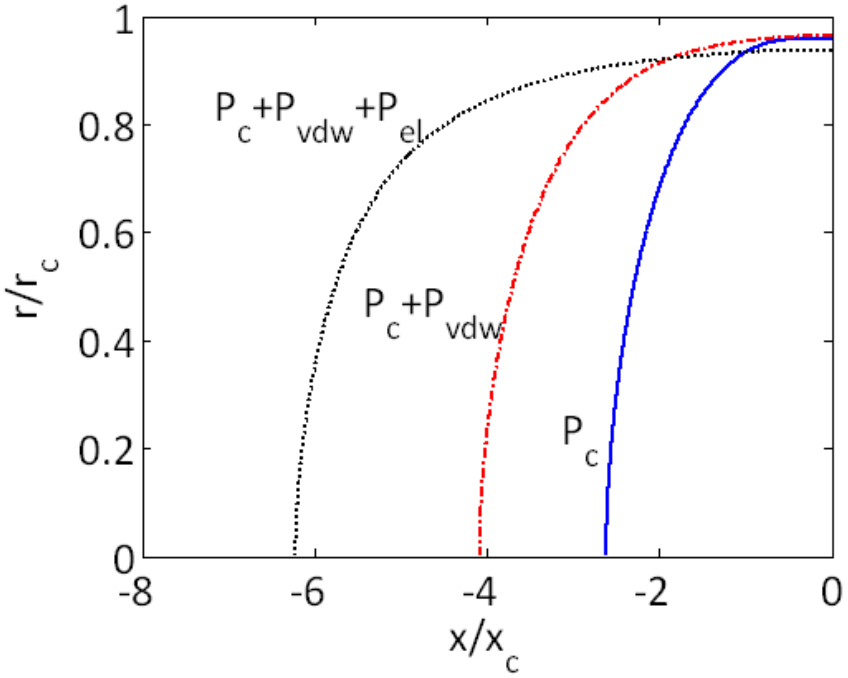

Figure 6.4. The effect of capillary and disjoining pressure on the shape of the interface is illustrated. The extension of meniscus due to electrostatic interaction is also shown. The interface is shown for the simulation conditions of $r_c = 30\text{nm}$, $T_w = 90^o\text{C}$ and $p_v / p_{v,eq} = 0.98$.

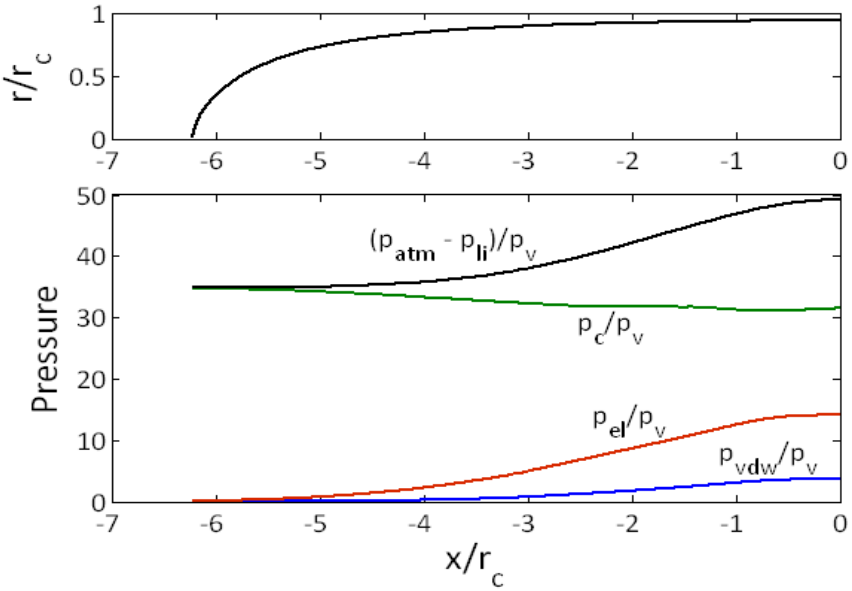

Figure 6.5. Axial variation of normalized capillary and disjoining pressures (electrostatic and van der Waals components) along a meniscus interface inside a cylindrical pore ($r_c = 30\text{nm}$, $T_w = 90^o\text{C}$ and $p_v / p_{v,eq} = 0.98$).

While the absolute pressure of the liquid phase is mainly determined by the capillary pressure, the disjoining pressure demonstrates a much larger gradient in the thin film region $(\bar{x} \to 0)$. Since it is the total pressure gradient that drives fluid flow, the contribution of electrostatic interaction is significant as shown in Figure 6.5, and is even greater than that due to capillary forces. Also, the capillary forces and disjoining (electrostatic together with van der Waals) pressure forces act in opposite directions, as reflected in different sign of pressure gradients.

While it is the pressure gradient (not an absolute value of pressure), which determines fluid flow in the extended meniscus inside the capillary, it is useful and relevant to the current analysis to describe the state of liquids confined in very small capillaries. It is known that liquids in tension can sustain extremely large negative pressures. In particular, it has been reported that water in hydrophilic nanochannels can exist under large negative pressures while being metastable [95, 96]. The derivation of an equilibrium film thickness shown previously in this study is in accordance with the general stability criteria for metastable liquids. A detailed description of a phenomenological approach to determine equilibrium conditions for metastable liquids and fluid mixtures is given in [97]. Additionally, the laws of hydrodynamics governing liquid flow are still applicable in this case since the approximation of a continuum phase is not violated.

6.4.2 Thermo-capillary stresses in cylindrical pores

In order to determine the effect of Marangoni stress on interfacial transport, the shape of the interface is calculated for two distinct operating conditions. At $T_w = 90^{\circ}\mathrm{C}$

and $p_v / p_{v,eq} = 0.98$, the interfaces corresponding to capillary radii of 50 nm and 500 nm are shown in Figure 6.6.

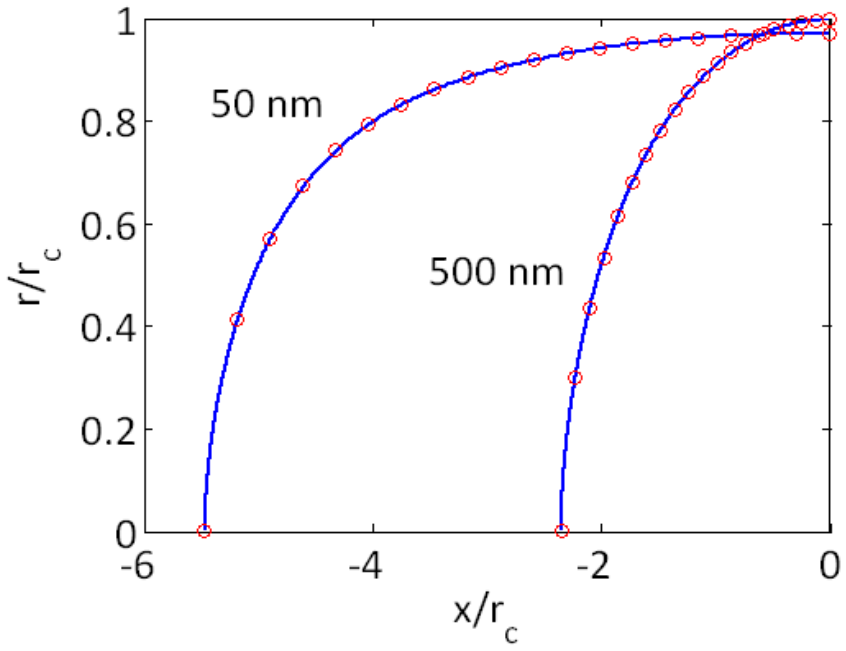

Figure 6.6. The effect of thermocapillary (Marangoni) stresses for water confined in nano-capillaries. The shape of interface in capillaries of different radii, as predicted with (solid lines) and without (circles) Marangoni stresses included in the analysis. The interfaces are shown for $T_w = 90^o\mathrm{C}$ and $p_v / p_{v,eq} = 0.98$.

For both radii, since $\Pi_1 / \Pi_2 > 40$, the ratio of viscous to thermocapillary stress is large, which indicates that Marangoni stresses are comparatively less significant in nano-capillaries. The shape outlined by open circles is for viscous-shear-only transport, and is qualitatively compared with the solid curves when Marangoni stresses are included. It is clear that the inclusion of thermocapillary stresses in the analysis results in a negligible change in the interface shape for both 50 and 500 nm pores. This is expected since Marangoni stresses are prominent only in much larger capillaries with large temperature gradient along the interface. In this analysis, with water as the evaporating liquid, the

temperature gradient is not substantial to affect the flow behavior even in 500 nm capillaries.

6.4.3 Effect of capillary radius

The interface corresponding to different capillary radii at a constant wall temperature and vapor pressure of $T_w = 90^o\mathrm{C}$ and $p_v / p_{v,eq} = 0.98$, respectively, is shown in Figure 6.7 in terms of non-dimensional radial and axial coordinates. As evident from equation (6.19), the non-dimensional parameters that control the interfacial shape and transport during evaporation are Π_6, Π_7, and Π_8, which compare the relative importance of capillary, Van der Waals and electrostatic interactions, respectively. Relative magnitude of these non-dimensional numbers for different capillary radii is indicative of the resulting interfacial shape.

In the case of a capillary pore of radius 500 nm, the non-dimensional numbers $\Pi_6 \sim 2$, $\Pi_7 \sim 2\times10^{-7}$, and $\Pi_8 \sim 2\times10^{-4}$ differ substantially from those for a capillary pore of radius 50nm, for which $\Pi_6 \sim 2\times10$, $\Pi_7 \sim 2\times10^{-4}$, and $\Pi_8 \sim 2\times10^{-2}$. While these values clearly indicate that capillary effect plays a key role in both cases, it is also evident that the relative importance of Van der Waals and electrostatic interactions are greater in smaller pores, which results in a further extension of the meniscus, as demonstrated in Figure 6.7.

The shape of interface during evaporation also depends on the pressure gradient driving the flow. For instance, the axial variation of capillary and disjoining pressures is shown in Figure 6.8 for cylindrical pores of radii 50 and 500 nm. The total pressure gradient is due to both capillary and disjoining pressures, as shown in Figure 6.8. In the

case of narrow pores, while capillary pressure is greater in magnitude, the disjoining pressure is significant over a larger portion of the interface. This observation is supported by the relative magnitudes of non-dimensional parameters Π_6, Π_7, and Π_8.

Also, Figure 6.8 demonstrates a substantial gradient in both capillary and disjoining pressures over a much larger portion of the interface for smaller pores. Consequently, fluid flow can be sustained over relatively long and significantly thinner film regions in smaller capillaries. It is the absence of a significant pressure gradient in large capillaries that results in a much smaller meniscus length relative to the capillary radius. Consequently, it can be established from Figure 6.7, which shows interfacial shape in non-dimensional units, that the total length of the interface does not increase proportionally with the capillary radius.

The ability of smaller pores to sustain fluid flow through relatively longer, thin film regions results in a larger rate of evaporation per unit pore cross-sectional area. This is shown in Figure 6.7 as an inset comparing average evaporation mass flux for different pore radii. It is noteworthy to mention that if the ambient gas phase can be maintained sufficiently dry to remove external mass transfer limitations, then large heat fluxes can be sustained through evaporation. For the mass fluxes given in the inset of Figure 6.7, the net evaporation corresponds to heat fluxes $\left(\dot{m}'' h_{fg}\right)$ in excess of 1000 W/cm^2.

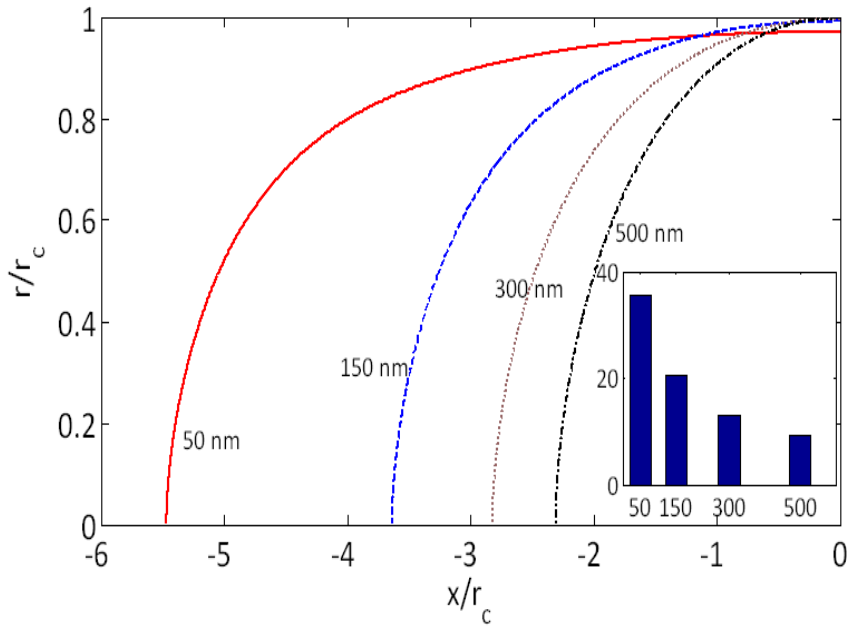

Figure 6.7. Interface shape corresponding to $T_w = 90^o\text{C}$, $p_v / p_{v,eq} = 0.98$ and $r_c = 50$ to 500nm. The inset compares the average evaporating mass flux (kg/m^{2}s) at different capillary radii (nm).

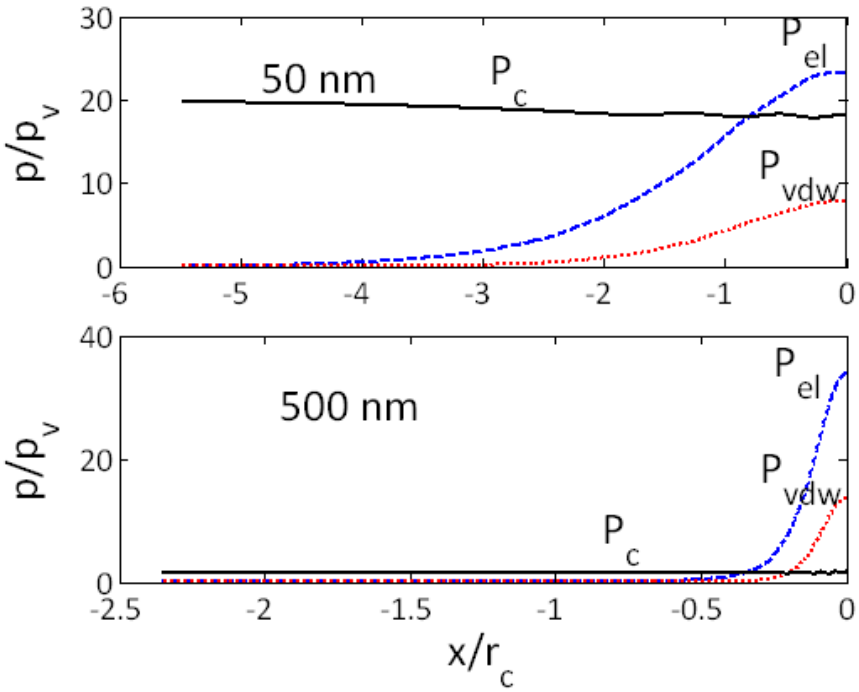

Figure 6.8. Comparison of capillary and disjoining pressures along the meniscus in capillaries at $T_w = 90^o\text{C}$, $p_v / p_{v,eq} = 0.98$ and $r_c = 50$ and 500nm.

6.4.4 Effect of wall temperature and vapor pressure

Figure 6.9 compares the shape of the interface corresponding to different wall temperatures. The total length of the interface is smaller at higher temperatures, but yields larger average evaporation rate in a pore, as shown in the inset in Figure 6.9. Since the temperature jump across the interface between the liquid and gas phase is neglected in this analysis, a higher evaporation rate for a fixed pore radius is mainly a result of higher equilibrium vapor pressure at higher temperatures. As a result, a larger gradient in the curvature of interface is expected in order to support a higher flow rate in the thin film region. The total length of the interface is therefore much smaller for evaporation at higher temperatures.

Figure 6.10 compares the shape of interface resulting from varying the vapor pressure of the ambient atmosphere surrounding the evaporating meniscus for a fixed wall temperature and capillary radius. The average mass flux per unit pore footprint area $\left(\pi r_c^2\right)$, is directly proportional to the difference of pressure at the interface, $(p_{vi} - p_v)$, as shown in equation (6.8). Therefore, analogous to the effect temperature, the length of the interface shrinks for smaller vapor pressure ratios, $p_v / p_{v,eq}$ due to higher flow rate in the thin film region.

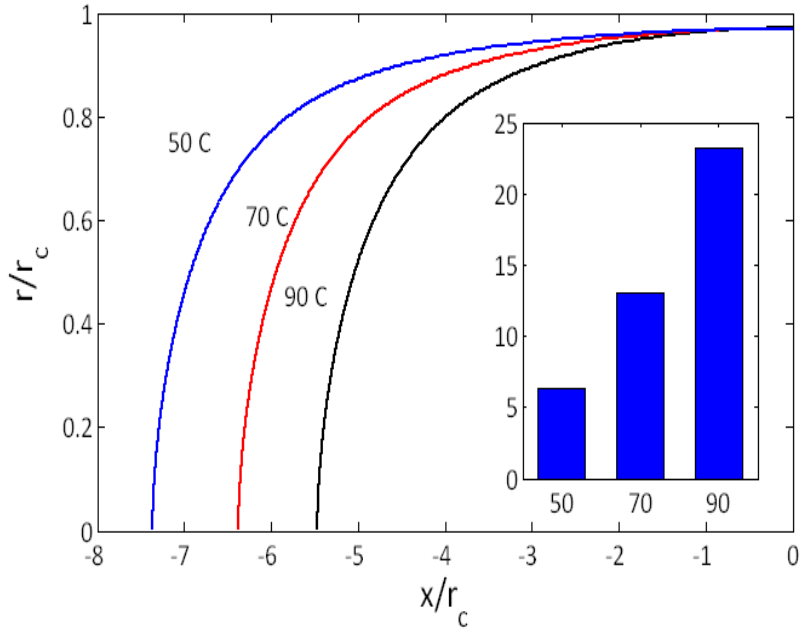

Figure 6.9. Interface corresponding to $p_v / p_{v,eq} = 0.98$, $r_c = 50\text{nm}$ and varying pore wall temperatures, $T_w = 50,\ 70$ and 90°C. The inset compares the average mass flux ($\text{kg/m}^2\text{s}$) at different wall temperatures ($^{\circ}\text{C}$).

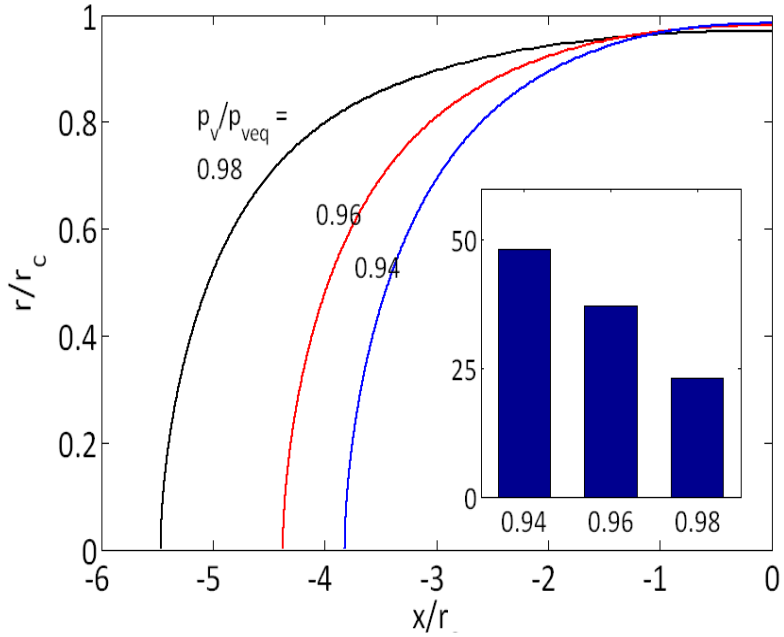

Figure 6.10. Interface corresponding to $r_c = 50\text{nm}$, $T_w = 90^{\circ}\text{C}$ and varying the relative pressure in the ambient environment surrounding the meniscus $p_v\ /\ p_{v,eq} = 0.98,\ 0.96$ and 0.94. The inset compares the average mass flux ($\text{kg/m}^2\text{s}$) at different vapor pressures.

6.4.5 Evaporation of a dielectric liquid versus water confined in nanopores

In the preliminary analysis of thin film evaporation presented in Chapter 2, the heat fluxes dissipated using FC72 under different operating conditions were found to be 2 to 3 times higher than water. This was attributed to the higher vapor pressure of FC72 compared to water at the same temperature. It is therefore of interest to compare the evaporation rates of water and FC72 at similar working conditions when they are confined within nanoscale pores. The following figure shows the interfacial shape of FC72 and water during evaporation in a capillary of radius 50nm and a wall temperature of 50 ^{o}C. The relative humidity of the gas phase surrounding the interface was maintained at 98% for both liquids.

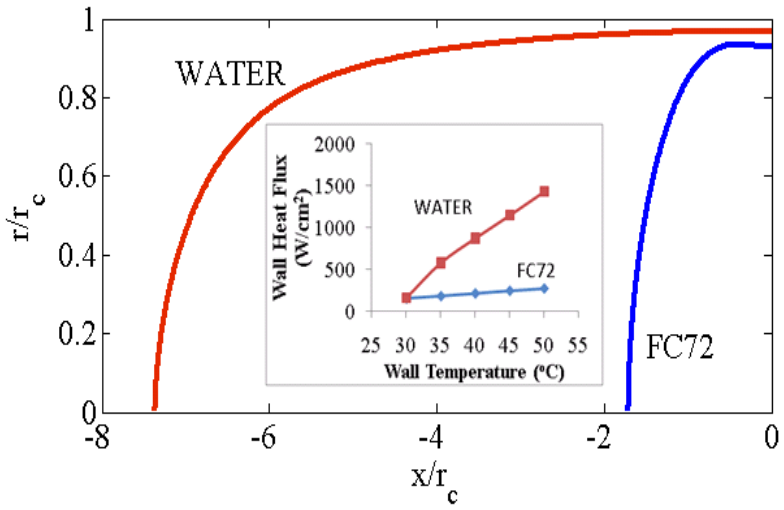

Figure 6.11 A comparison of interfacial shape of evaporating FC72 versus water confined in nanopores of radius 50nm, a wall-temperature of 50^{o}C and gas-phase relative humidity of 98%. The inset shows the total heat dissipated due to evaporation normalized by the pore cross-sectional area using FC72 and water at different wall temperatures.

It is clear from Figure 6.11 that the extension of liquid-vapor interface using water is more prominent than FC72 during evaporation inside nanopores. A comparatively longer interfacial shape in case of water is a result of the disjoining pressure, which also includes

the electrostatic interactions, which are absent in a dielectric fluid such as FC72. As a result, even though the vapor pressure of FC72 is higher, the use of water confined in nanopores supports a higher evaporation rate. Consequently, the heat flux dissipated per unit pore area is much higher in the case of water, as shown in the inset of Figure 6.11.

At higher temperatures, the vapor pressure of water increases more rapidly in comparison to FC72. Additionally, the latent heat of evaporation of water is much larger than FC72. Consequently, the relative increase in total heat dissipated per unit pore cross-sectional area is significantly large for water at higher wall temperatures, as shown in the inset of Figure 6.11.

6.5 Summary and Conclusions

Analysis of interfacial transport is carried out for water evaporating in the confines of a cylindrical nano-pore. The governing equations for fluid flow and heat transfer are derived in the limit of continuum transport. In addition to capillarity and dispersion forces, the analysis incorporates the electrostatic interaction in a solid-liquid-vapor system using the Langmuir equation and demonstrates its effect on the interfacial characteristics. A thermodynamic approach to the calculation of equilibrium film thickness is presented, which differs from the conventional formulation [71] that relies only on evaporation kinetics. The governing, non-linear differential equations are solved numerically to determine the axial variation of flow variables and the shape of the interface under various operating conditions.

At a constant wall temperature the equilibrium thickness of adsorbed film is found to increase with the relative vapor pressure, $p_v / p_{v,eq}$, while it decreases with increase in pore radius, r_c. An increase in the vapor pressure of the ambient environment causes a

reduction in the external driving potential for evaporation, resulting in a thicker adsorbed film in equilibrium with its vapor phase. On the other hand, as the capillary radius decreases, the molecules at the free surface are more strongly held by the neighboring surface molecules resulting in thicker equilibrium films.

This study also demonstrates a significant change in the shape of the interface when electrostatic interactions are included, in addition to Van der Waals and capillary forces. In particular, the interface is found to extend further due to electrostatic forces. Therefore, the net rate of evaporation is promoted due to an increase in the total free surface area, as well as owing to an enlarged thin film region in the meniscus.

The inclusion of thermocapillary stress does not yield measurable variation in interfacial characteristics for nanoscale capillaries, due to insufficient temperature gradient to induce stresses comparable to other driving forces.

The analysis identifies three important parameters that significantly affect the overall performance of the system, namely the capillary radius, wall temperature and the degree of saturation of vapor phase. In smaller capillaries the viscous pressure drop is supported by significant gradient in both disjoining and capillary pressures over a large fraction of the meniscus. In larger capillaries, the pressure gradient is significant only at the leading edge of the entire meniscus, where the contribution of the disjoining pressure is important. As a result, the extension of meniscus is prominent for smaller nanoscale capillaries, in turn, yielding a greater net rate of evaporation per unit pore area.

The effects of temperature and ambient vapor pressure on net rate of evaporation are shown to be analogous. An increase in wall temperature, which enhances saturation pressure, or a decrease in the ambient vapor pressure, both result in an overall increase in

the net potential for evaporation from the interface. Also, since a higher rate of evaporation requires larger pressure gradient inside the meniscus, the length of the meniscus shrinks for higher evaporation fluxes to accommodate higher pressure gradients. The results of this analysis are important not only from a fundamental prospective, but also for advancing numerous applications, from water distillation [22-25] to thermal management of high power sources [98, 99], which take advantage of highly efficient phase change in nanoporous systems.

CHAPTER 7

COMBINED HEAT AND MASS TRANSFER IN EVAPORATING THIN FILM CONFINED BY NANOPOROUS MEMBRANE

The initial performance analysis [99] and experimental study [98, 100] of the micro-scale evaporative cooling device presented in Chapters 2, 3 and 5 demonstrate that a reduction in the film and membrane thicknesses along with enhanced vapor transport can improve the overall heat dissipation. Subsequently, a detailed analysis of interfacial transport during evaporation of water confined in nanoscale pores was presented in Chapter 6. This analysis established that the interfacial resistance to evaporation was insignificant in comparison to the overall resistance to vapor transport from the interface by diffusion and advection [101].

In this section the contribution of evaporation and convection to overall heat dissipation from the hotspot is identified during the operation of this microfluidic device. In order to enhance evaporative cooling, microfluidic devices with thin membranes and film thicknesses (~5 μm) were fabricated for experimental demonstration of device performance. A detailed computational model identifying the relative contributions of evaporation, convection and spreading is also presented here, along with the experimental study that supports numerical predictions.

7.1 Description of Physical Model and Device Operation

The device's performance is predicted by a detailed computational analysis of heat and mass transfer for a physical model shown in Figure 7.1, where characteristic dimensions of the device are shown in micro-meters (10^{-6} m). A coolant is supplied through a narrow channel bounded by the hotspot and a nanoporous membrane made from alumina. The membrane, being inherently hydrophilic, can self-propel the liquid by capillary action. On the other hand, viscous drag inside the membrane pores resists liquid flow. When the viscous shear exceeds the pressure differential driving liquid across the membrane, a complete saturation of the membrane is prevented and the liquid is confined within the membrane. Consequently, the location of the liquid-vapor interface lies within the membrane. In this case, the film thickness is controlled by the separation of the membrane and the hotspot, a parameter which is controlled during micro-fabrication of the cooling device.

Evaporation at the liquid-vapor interface is illustrated in the magnified view of the porous membrane, which is partially saturated with the liquid as shown in Figure 7.1. Due to variable pinning of the liquid-vapor interface between the inlet and outlet of the membrane pores, the liquid penetration into the membrane is non-uniform across the membrane area. For pores completely void of liquid, the vapor resulting from evaporation diffuses through the entire length of the pore. On the other hand, vapor diffusion in pores is eliminated when the membrane is fully saturated with liquid. For thick porous membranes, the diffusion resistance can be substantial, resulting in significantly different performance for a membrane which is fully dry as opposed to one that is fully saturated with liquid [99]. In either case, the vapor generated by evaporation is eventually carried

away from the membrane by advection using jet impingement of dry air, as illustrated in Figure 7.1.

During device operation, the liquid infiltrating the pores of the hydrophilic membrane evaporates due to the heat generated at the hotspot. When the flow rate of coolant in the "liquid film" (Figure 7.1) region exceeds the overall rate of evaporation, the net heat dissipation at the hotspot is due to evaporation as well as to sensible heating of the coolant flowing across the hotspot. For coolant flow rates much larger than the overall rate of evaporation, sensible heating of the liquid between the membrane and the hotspot can provide significant heat dissipation due to the small hydraulic diameter (~10 μm) of the thin liquid film. Heat spreading from the hotspot into the substrates can also be significant, especially when liquid cooling is ineffective. Therefore, for a given coolant flow rate and heat generation at the hotspot, this analysis predicts the rate of heat dissipation due to evaporation, single-phase cooling and the extent of spreading into the substrate.

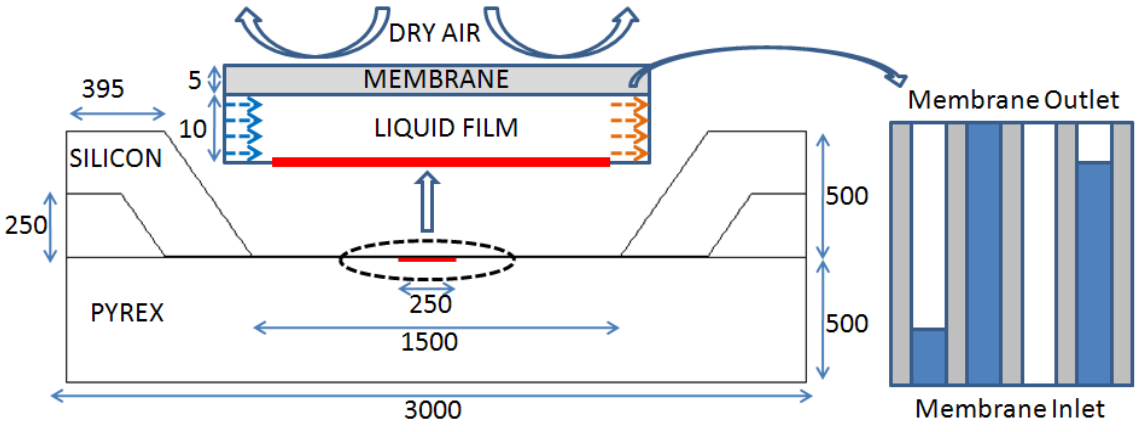

Figure 7.1. The physical model used for analysis of heat and mass transfer with characteristic lengths given in units of 10^{-6} m. The magnified views of the thin liquid film and the membrane illustrate device operation with both convective and evaporative modes of heat transfer.

7.2 Analysis of Fluid Flow and Heat Transfer in Thin-film Region

A two-dimensional analysis of fluid flow and heat transfer is carried out to predict the device performance under different operating conditions. Assuming a Newtonian fluid with constant density, ρ_l and viscosity, μ_l, the steady flow of a liquid film confined inside the microchannel is governed by the following equations:

$$\frac{\partial u_{lx}}{\partial x}+\frac{\partial u_{ly}}{\partial y}=0 \tag{7.1}$$

$$u_{lx}\frac{\partial u_{lx}}{\partial x}+u_{ly}\frac{\partial u_{lx}}{\partial y}=-\frac{1}{\rho_l}\frac{\partial p_l}{\partial x}+\frac{\mu_l}{\rho_l}\left(\frac{\partial^2 u_{lx}}{\partial x^2}+\frac{\partial^2 u_{lx}}{\partial y^2}\right) \tag{7.2}$$

$$u_{lx}\frac{\partial u_{ly}}{\partial x}+u_{ly}\frac{\partial u_{ly}}{\partial y}=-\frac{1}{\rho_l}\frac{\partial p_l}{\partial y}+\frac{\mu_l}{\rho_l}\left(\frac{\partial^2 u_{ly}}{\partial x^2}+\frac{\partial^2 u_{ly}}{\partial y^2}\right) \tag{7.3}$$

where u_l and p_l represent the velocity and pressure of the liquid. The temperature distribution in the liquid is governed by the following equation, which assumes constant thermal conductivity, k_l, no internal heat generation and negligible compressibility effects. Viscous dissipation can also be neglected, since the Brinkman number, $\mathrm{Br}=u_l^2\,\mathrm{Pr}\big/\left(c_{pl}\Delta T\right)$, under typical operating conditions is found to be close to 10^{-9}. Furthermore, the viscous number [102], $\mathrm{Vi}=\mu_l u_l L\big/\left(\rho_l c_{pl} T_{ref} d_h{}^2\right)$ for typical operating conditions is 2×10^{-9}, which clearly satisfies the relation $\mathrm{Vi}\,\mathrm{Pr}^{-0.1}\le 0.056$ for neglecting viscous dissipation. In this relation Pr represents the Prandtl's number for water.

$$u_{lx}\frac{\partial T_l}{\partial x}+u_{ly}\frac{\partial T_l}{\partial y}=\frac{k_l}{\rho_l c_{pl}}\left(\frac{\partial^2 T_l}{\partial x^2}+\frac{\partial^2 T_l}{\partial y^2}\right) \tag{7.4}$$

where c_{pl} and T_l is the specific heat and temperature of the liquid phase.

In order to include heat dissipation by evaporation of liquid inside the membrane pores, the rate of vapor generated at the interface and transported through the membrane by diffusion and advection is determined. The rate of evaporation per unit surface area, $\dot{m}''$ at the liquid-vapor interface, surrounded by an air-vapor mixture is given by:

$$\dot{m}'' = \frac{2\hat{\sigma}}{2-\hat{\sigma}}\left(\frac{M_l}{2\pi R}\right)^{1/2} p_{atm}\left(\frac{X_{v,eq}}{T_{li}^{1/2}} - \frac{X_{vi}}{T_{vi}^{1/2}}\right) \tag{7.5}$$

$X_{v,eq}$ and X_{vi} are the equilibrium and interfacial mole fractions of vapor phase, given by the ratios $p_{v,eq}/p_{atm}$ and $p_{v,i}/p_{atm}$, respectively, where $p_{v,eq}$ and p_{vi} denote the saturated vapor pressure at temperature T_{li} and the partial pressure of vapor in the air-vapor mixture in the immediate vicinity of the interface. T_{li} and T_{vi} represent the liquid and vapor temperatures at the interface, respectively. M_l is the molecular weight of the evaporating coolant. The rate of vapor transport by mass diffusion inside the membrane and convection by air jet at the membrane outlet are given by equations (7.6) and (7.7), respectively.

$$\dot{m}'' = \frac{D_k M_l p_{atm}}{\delta_v R}\left(\frac{X_{vi}}{T_{vi}} - \frac{X_{vo}}{T_{vo}}\right) \tag{7.6}$$

$$\dot{m}'' = \frac{h_m M_l p_{atm}}{R}\left(\frac{X_{vo}}{T_{vo}} - \frac{X_{v\infty}}{T_{\infty}}\right) \tag{7.7}$$

where X_{vo} and T_{vo} represent the mole fraction and temperature of the vapor phase at the membrane outlet, respectively. D_k represents the coefficient of combined Knudsen-Molecular diffusion [99] across the length δ_v inside the pore. h_m is the mass transfer coefficient for transport of the vapor phase by the sweeping gas of mole fraction X_{vo} and

temperature T_{vo}. Based on the location of the interface inside the membrane, the permissible values of δ_v are given by $0 \le \delta_v \le \delta_m$, where δ_m represents the membrane thickness.

For a thin ceramic membrane (~10^{-6} m) with thermal conductivity ~10 W/mK, the temperature difference across the membrane is estimated to be close to 0.1 K, corresponding to a heat flux of 10^6 W/m^2. Assuming the vapor and membrane to be in thermal equilibrium, the analysis can be simplified by neglecting the temperature difference $T_{vi} - T_{vo}$. Furthermore, the liquid and vapor at the interface are assumed to be in thermal equilibrium as well, so that $T_{li} \sim T_{vi}$ [101]. In other words, $T_{vi} - T_{vo}$ and $T_{li} - T_{vi}$ are neglected in comparison to differences in mole-fractions $X_{vi} - X_{vo}$ and $X_{v,eq} - X_{vi}$, respectively. This simplification is justified because the temperature discontinuities are diminished by efficient thermal transport, whereas the differences in mole fractions are finite due to relatively inefficient vapor transport. Using dry air $\left(X_{v\infty} = 0\right)$, the overall rate of evaporation per unit area, after inclusion of the above stated simplifications, is given by the following equation, which takes into account the available area for evaporation (or the porosity of the membrane, ε):

$$\dot{m}'' = \frac{p_{atm} M_l X_{v,eq} \varepsilon}{R T_{vi}} \left(\frac{1}{\left(2-\hat{\sigma}\right)/\left(2\hat{\sigma}\right)\left(2\pi M_l / \left(R T_{vi}\right)\right)^{1/2} + \delta_v / D_k + 1/h_m} \right) \tag{7.8}$$

In this analysis, the heat dissipation by evaporation of liquid confined within the thin porous membrane is accounted approximately by a uniform volumetric heat sink $\dot{q}'''_m$, as shown in equation (7.9). It is to be noted that the use of a volumetric heat sink, as opposed to the use of a heat flux as a boundary condition is appropriate in order to

account for the ambiguity of defining a location of the liquid-vapor interface inside the membrane. The volumetric heat sink is derived from the overall rate of evaporation inside the membrane as $\dot{q}_m''' = \dot{m}'' / \delta_m$. Due to extremely small evaporation rates inside the membrane, convective heat transfer due to liquid and vapor flow in membrane pores is neglected in comparison to the latent heat of phase change and conduction across the solid structure of the membrane. The temperature distribution in the membrane is therefore given by:

$$k_m \left(\frac{\partial^2 T_m}{\partial x^2} + \frac{\partial^2 T_m}{\partial y^2} \right) + \dot{q}_m''' = 0 \tag{7.9}$$

where k_m is the effective thermal conductivity of the membrane, approximated by $(1-\varepsilon)k_{al} + \varepsilon k_l$ for a wet membrane and by $(1-\varepsilon)k_{al} + \varepsilon k_v$ for a dry membrane. k_{al}, k_l and k_v are the thermal conductivities of alumina and water in liquid and vapor phases, respectively. The hotspot is represented as a heat generating (via resistive electric energy dissipation) platinum layer (10^{-6} m) embedded in Pyrex substrate, and its temperature is governed by the following equation.

$$k_s \left(\frac{\partial^2 T_s}{\partial x^2} + \frac{\partial^2 T_s}{\partial y^2} \right) + \dot{q}_s''' = 0 \tag{7.10}$$

The boundary conditions on faces 1 – 14, as marked in Figure 7.2, are listed in Table 7.1. A no-slip condition and continuity in heat flux and temperature is assigned at the interface of silicon and water. These hydrodynamic and thermal boundary conditions are not listed in Table 7.1. It is clear from equation (7.8) and Table 7.1 that accurate evaluation of heat and mass transfer coefficients, h_{mem}, h_{si} and h_m is essential to predict the system performance. This is done by a separate analysis of air jet impingement, which

is used as the sweep gas for convective transport of vapor away from the surface of the membrane into the ambient.

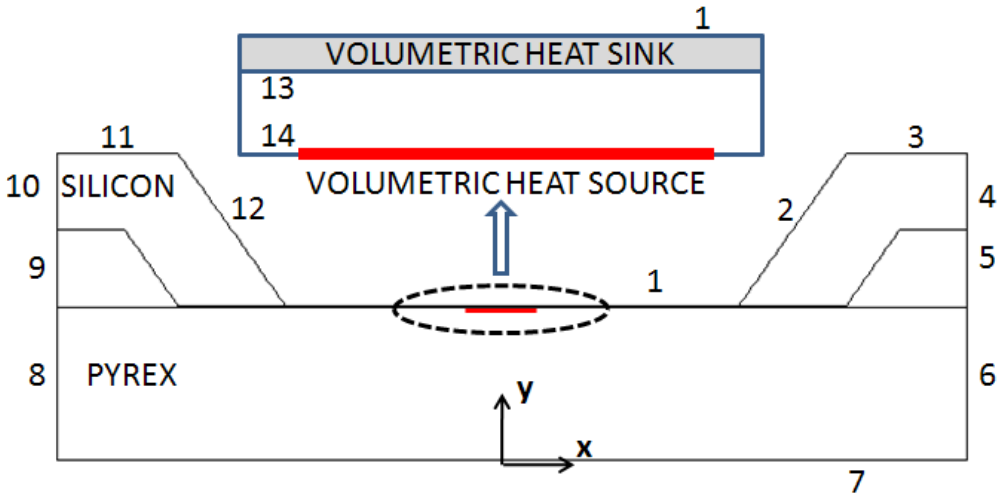

Figure 7.2. Schematic diagram identifying the boundary conditions required to numerically integrate the governing equations. The boundary conditions numbered 1-14 are listed in Table 7.1

Table 7.1 Boundary conditions for faces 1 – 14 in Figure 7.2

Face	Boundary type	Value
1	Forced Convection	$\dot{q}'' = h_{mem}\left(T_m - T_\infty\right),\ T_\infty = 295\ \mathrm{K}$
2,12	Forced Convection	$\dot{q}'' = h_{si}\left(T_s - T_\infty\right),\ T_\infty = 295\ \mathrm{K}$
3,7,11	Natural Convection	$\dot{q}'' = h_\infty\left(T_s - T_\infty\right), h_\infty = 10\ \mathrm{W/m^2K},$ $T_\infty = 295\ \mathrm{K}$
4,6,8,10	Adiabatic wall	$\dot{q}'' = 0$
5	Outlet Pressure	Gage pressure, $p_{gage} = 0$
9	Inlet Velocity and Temperature	$u_y = 0, u_x = u_o, T_l = 295$
13	Velocity profile	$u_y = \dot{m}'' / \rho_l, u_x = 0$
14	No slip; Temperature and heat flux continuity	$u_y = 0, u_x = 0, T_l = T_s, \dot{q}_l'' = \dot{q}_s''$

7.3 Analysis of Air-Jet Impingement in a Confined Volume

Fluid flow and heat transfer resulting from a confined air jet, incident normally on the porous membrane, is computationally analyzed for a physical model illustrated in

Figure 7.3. In this axisymmetric analysis, the effects of confining the air jet and the extent of heat spreading in the substrates are studied on the overall rate heat and mass transfer. Assuming constant density, ρ_a, and viscosity, μ_a, for air, a steady, laminar flow, and neglecting body force due to gravity, the analysis numerically computes the solution of mass continuity and momentum conservation equations governing the flow of the air jet, wherein the velocity and pressure is denoted by u_a and p_a, respectively.

$$\frac{\partial u_{ax}}{\partial x}+\frac{\partial u_{ar}}{\partial r}+\frac{u_{ar}}{r}=0 \tag{7.11}$$

$$u_{ar}\frac{\partial u_{ar}}{\partial r}+u_{ax}\frac{\partial u_{ar}}{\partial x}=-\frac{1}{\rho_a}\frac{\partial p_a}{\partial r}+\frac{\mu_a}{\rho_a}\left[\frac{1}{r}\frac{\partial}{\partial r}\left(r\frac{\partial u_{ar}}{\partial r}\right)+\frac{\partial^2 u_{ar}}{\partial x^2}-\frac{u_{ar}}{r^2}\right] \tag{7.12}$$

$$u_{ar}\frac{\partial u_{ax}}{\partial r}+u_{ax}\frac{\partial u_{ax}}{\partial x}=-\frac{1}{\rho_a}\frac{\partial p_a}{\partial x}+\frac{\mu_a}{\rho_a}\left[\frac{1}{r}\frac{\partial}{\partial r}\left(r\frac{\partial u_{ax}}{\partial r}\right)+\frac{\partial^2 u_{ax}}{\partial x^2}\right] \tag{7.13}$$

Assuming constant thermal conductivities, k_a and k_s, with no internal heat generation, and neglecting viscous dissipation and compressibility effects, the temperature distributions in air, T_a and the substrate, T_s are governed by the following equations:

$$u_{ar}\frac{\partial T_a}{\partial r}+u_{ax}\frac{\partial T_a}{\partial x}=\frac{k_a}{\rho_a c_{pa}}\left[\frac{1}{r}\frac{\partial}{\partial r}\left(r\frac{\partial T_a}{\partial r}\right)+\frac{\partial^2 T_a}{\partial x^2}\right] \tag{7.14}$$

$$\frac{1}{r}\frac{\partial}{\partial r}\left(r\frac{\partial T_s}{\partial r}\right)+\frac{\partial^2 T_s}{\partial x^2}=0 \tag{7.15}$$

The partial differential equations (7.11) to (7.15) are numerically solved using FLUENT, a computational fluid dynamics software, with the boundary conditions denoted by numbers 1 – 7 in Figure 7.3, and listed in Table 7.2 to determine the pressure, velocity and temperature distributions. The hydrodynamic and thermal boundary conditions at the interface of air and silicon are no-slip condition and continuity in heat

flux and temperature, respectively, which are not listed in Table 7.3. Numerical convergence is checked by monitoring the total rate of heat transfer from all surfaces to achieve energy conservation and ensuring all residuals are less than 10^{-9}. The thermophysical properties of the porous membrane saturated with liquid water and for dry conditions are listed in

Table 7.3 along with the properties of air, Silicon and Pyrex used in this analysis.

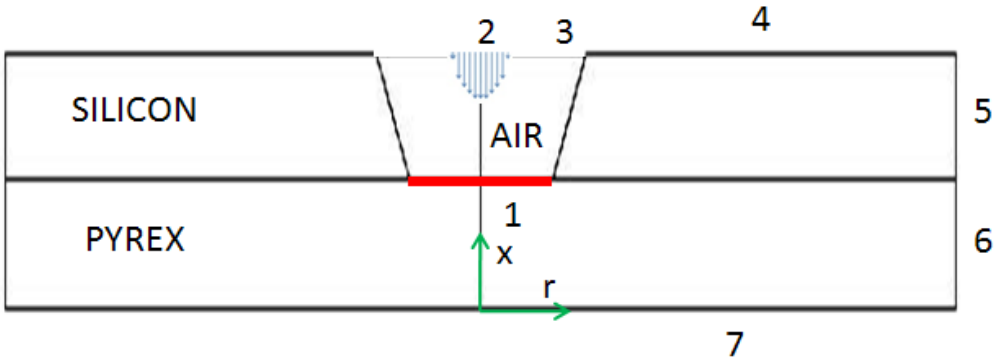

Figure 7.3. A normally incident air jet of diameter and a nozzle-to-hotspot separation of $5\text{x}10^{-4}$ m. Faces denoted by numbers 1 – 7 represent the boundary conditions described in Table 7.2.

Table 7.2 Boundary Conditions for Air Jet Impingement as shown in Figure 7.3

Face	Boundary Conditions	Value
1	Constant temperature and no-slip condition	$T = 363.15\ \text{K}, \bar{u} = 0$
2	Prescribed inlet velocity and temperature	$T = 295.15\ \text{K}, u_r = 0, u_x = 2u_o\left(1 - r^2 / r_{jet}^2\right)$ $u_o = 10 - 40\ \text{m/s}, r_{jet} = 250\,\mu\text{m}$
3	Pressure outlet	Gage Pressure, $p_{gage} = 0$
4	Heat Transfer by natural convection	$h = 10\ \text{W/m}^2\text{K}$
5	Adiabatic wall	$q'' = 0$
6	Adiabatic wall	$q'' = 0$
7	Heat Transfer by natural convection	$h = 10\ \text{W/m}^2\text{K}$

Table 7.3 Thermo-physical properties of different materials used in the analysis

Property	Air	Water	Wet Memb.	Dry Memb.	Silicon	Pyrex
Density (kg/m^3)	1.225	998	2029	1415	2324	2230
Specific Heat (J/kg.K)	1006.43	4182	2996	1600	857	750
Thermal Cond. (W/mK)	0.0242	0.66	13.15	12.75	66	1.1
Viscosity (kg/ms)	1.7894x10^{-5}	3.145x10^{-4}	---	---	---	---

Figure 7.4 shows the grid sensitivity study carried out to determine the effect of grid size on the computed values of heat transfer coefficient using air jet impingement. It is clear from Figure 7.4 that the profile of heat transfer coefficient becomes invariant to mesh refinement from 69,933 to 126,390 cells, which translates to a minimum discretized length of 4 μm and 2 μm, respectively.

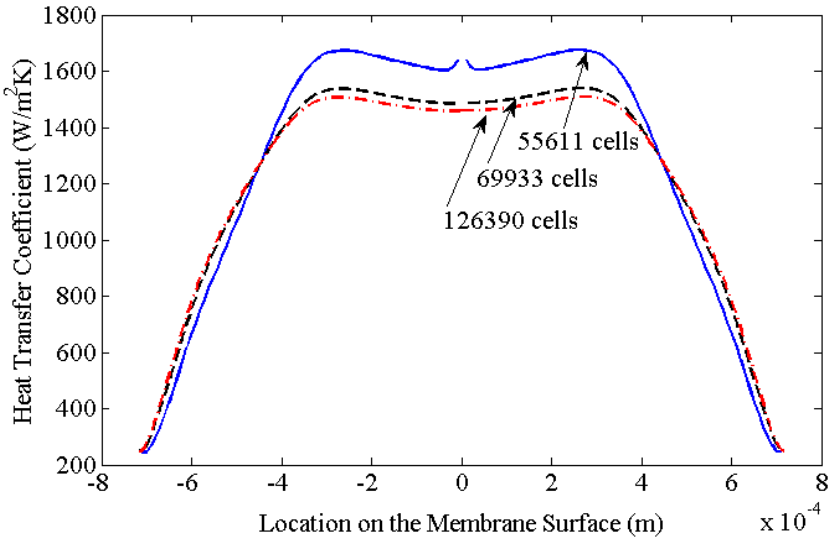

Figure 7.4. Grid dependence study for air jet impingement illustrating the effect of grid size on the calculated magnitude of local heat transfer coefficient

7.4 Results and Discussion

7.4.1 Significance of flow configuration

In order to improve the overall performance of thin film evaporation, it is essential to maximize advection of vapor using jet impingement of dry air. The flow characteristics

can be significantly altered with different nozzle diameters and separation from the impinging surface, especially when the jet is operated within a confined space, as illustrated in Figure 7.3.

The streamlines, velocity and pressure distribution characterizing the flow resulting from jet impingement in a confined space is shown in Figures 7.5 (a), (b) and (c), respectively. In this case, a nozzle of diameter 500 μm is used for jet impingement of air with a mean velocity of 30 m/s, on the horizontal surface of the cavity of diameter 1,500 μm at a distance of 500 μm (see Figures 7.1 and 7.3). Figure 7.5 can qualitatively illustrate the significance of utilizing a nozzle of relatively smaller size in comparison to the size of the cavity that confines the jet. A smaller nozzle in close proximity ensures that both the stagnation zone and the radial outflow region contribute significantly to heat and mass transfer. The stagnation zone, representing the region of highest pressure, accelerates the air jet outwards in the radial direction. A steeper radial pressure gradient, as shown in Figure 7.5(c) will result in fluid acceleration, a thinner boundary layer and therefore better heat and mass transfer. Furthermore, use of a smaller nozzle diameter ensures no re-circulation of moisture on the surface of the membrane, since water vapor from the membrane will be efficiently swept away by the accelerating air jet.

In contrast, an air jet from a nozzle of much larger diameter and separation distance impinging on a relatively small confined volume can result in significantly different flow characteristics. For instance, the streamlines, velocity vectors and isobaric contours for such a representative scenario are shown in Figure 7.6. In this case, the nozzle and surface diameters are 1,000 μm and 800 μm, respectively, placed 1,500 μm apart. The streamlines shown in Figure 7.6(a) clearly indicate that a large fraction of the air jet is

diverted away from the cavity at its entrance without contributing towards overall heat and mass transfer inside the confined volume. The velocity distribution of air inside the cavity suggests minimal advection and the absence of any radial acceleration of air on the bottom surface. This is caused by the characteristic pressure distribution, which indicates that the entire cavity is at a constant pressure and opposes flow inside the cavity. A significant favorable pressure gradient exists only at the inlet to the cavity, which diverts the flow away from the cavity entrance. For this configuration moisture accumulation within the cavity can clearly exacerbate vapor transport, resulting in a very inefficient heat and mass transfer.

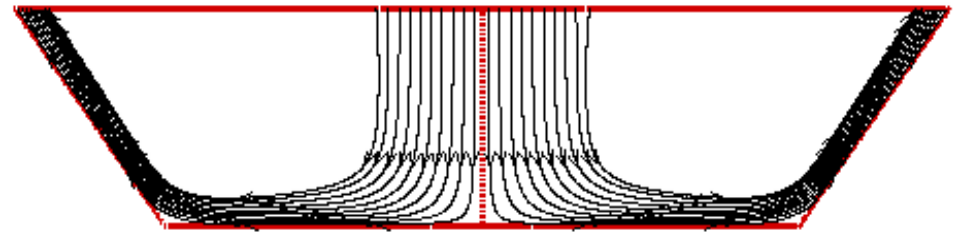

(a)

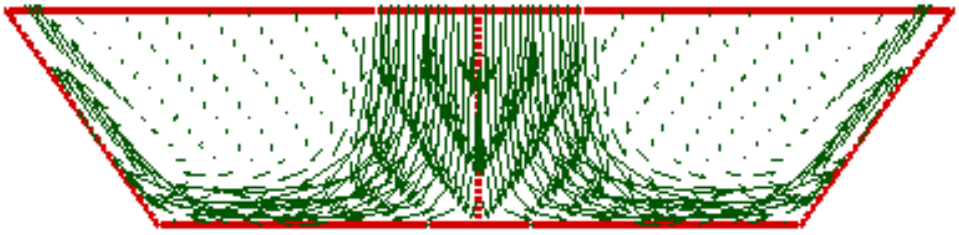

(b)

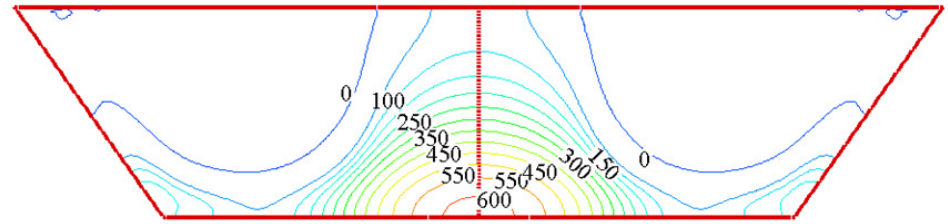

(c)

Figure 7.5. The flow configuration for air jet from a nozzle of diameter 500 μm impinging normally on a cavity-confined surface of diameter 1,500 μm at a distance of 500 μm : (a) Flow streamlines (b) Velocity distribution, and (c) Pressure contours.

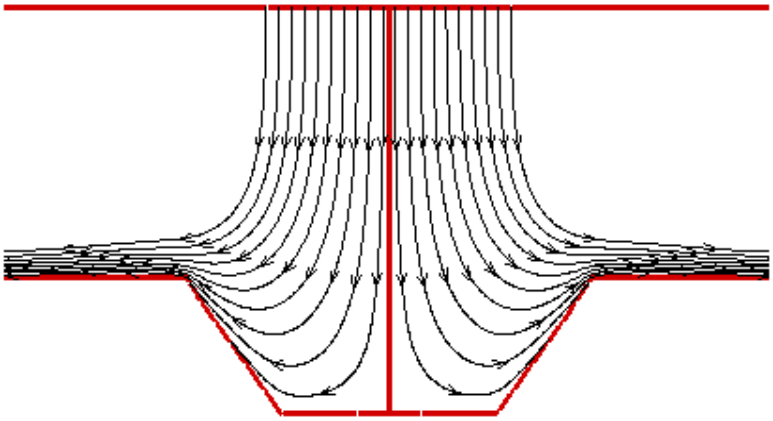

(a)

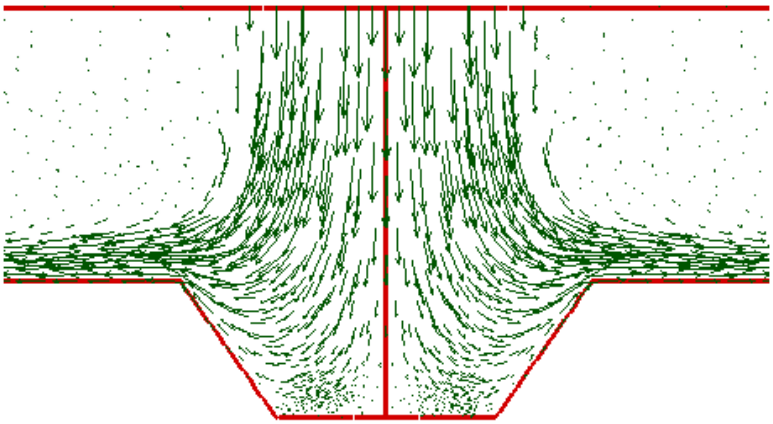

(b)

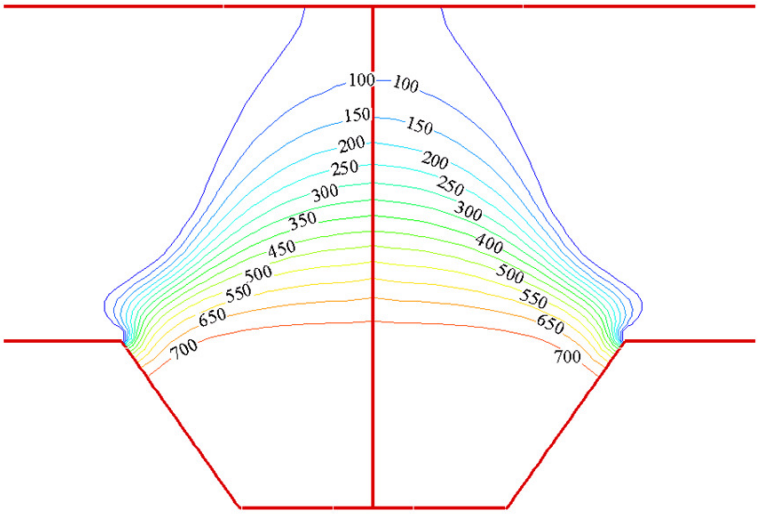

(c)

Figure 7.6. The flow configuration for air jet from a nozzle of diameter 1000 μm impinging normally on a cavity-confined surface of diameter 800 μm at a distance of 1,500 μm : (a) Flow streamlines (b) Velocity distribution, and (c) Pressure contours.

7.4.2 Heat and mass transfer using confined jet

The net rate of heat and mass transfer is determined for a normally incident air jet from a nozzle of fixed diameter of $500\,\mu$m and nozzle-to-surface separation of $500\,\mu$m. The average velocity of air from the nozzle is varied from 10 to 50 m/s, which corresponds to jet Reynolds number, Re_j, of 20 to 200, relative to the nozzle diameter, evaluated at 25°C. The local heat transfer coefficient, h_{mem}, on the cavity surface represented by Face 1 in Figures 7.1 and 7.3, is evaluated from the local surface heat flux dissipated by air, $\dot{q}_a''$ as $h_{mem} = \dot{q}_a'' / (T_s - T_\infty)$, where T_s and T_∞ are the surface and ambient temperatures, respectively. The local heat flux is given by $\dot{q}_a'' = -k_a \nabla T \cdot \hat{n}$, where the temperature gradient is obtained along the surface normal, $\hat{n}$. Figure 7.7 shows the profiles for h_{mem} for air jet velocities varying from 10 to 50 m/s, which indicates an increase in the average heat transfer coefficient from 1,129 to 2,761 W/m^{2}K in the stagnation zone.

Following the procedure outlined above, the heat transfer coefficient on the inclined silicon surfaces represented by Faces 2 and 12 in Figure 7.1 is also evaluated. An average value of the heat transfer coefficient over the inclined surface, h_{si} is given by Figure 7.8 as a function of the average velocity of the jet. The local mass transfer coefficient, h_m, along the cavity surface represented by Face 1 in Figures 7.1 and 7.3, is evaluated from the heat transfer coefficient, h_{mem} using the analogy between heat and mass transfer. Figure 7.9 shows the profile for the local mass transfer coefficient, h_m as a function of average jet velocity. The computed surface profiles of heat and mass transfer coefficients are then utilized in predicting the overall device performance.

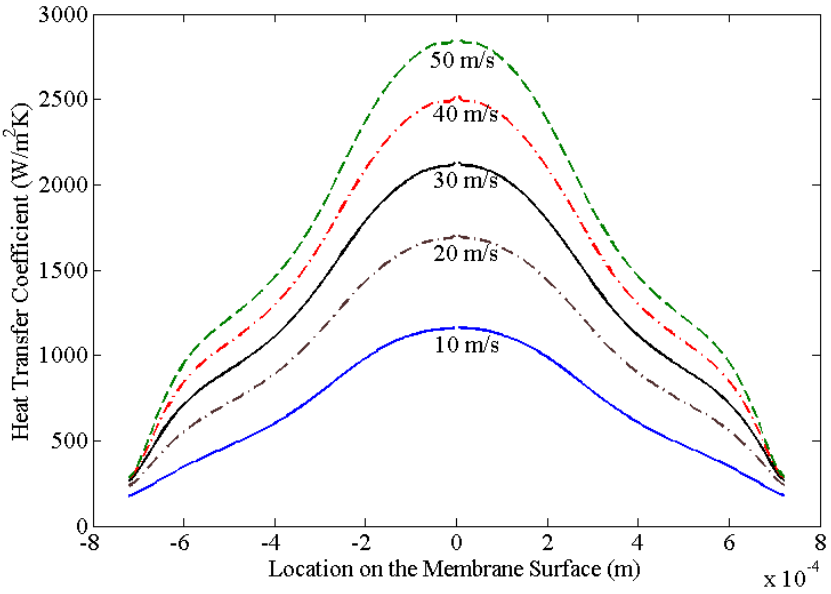

Figure 7.7. Local heat transfer coefficient, h_{mem} on the membrane surface, denoted by face-1 in Figures 7.1 and 7.3

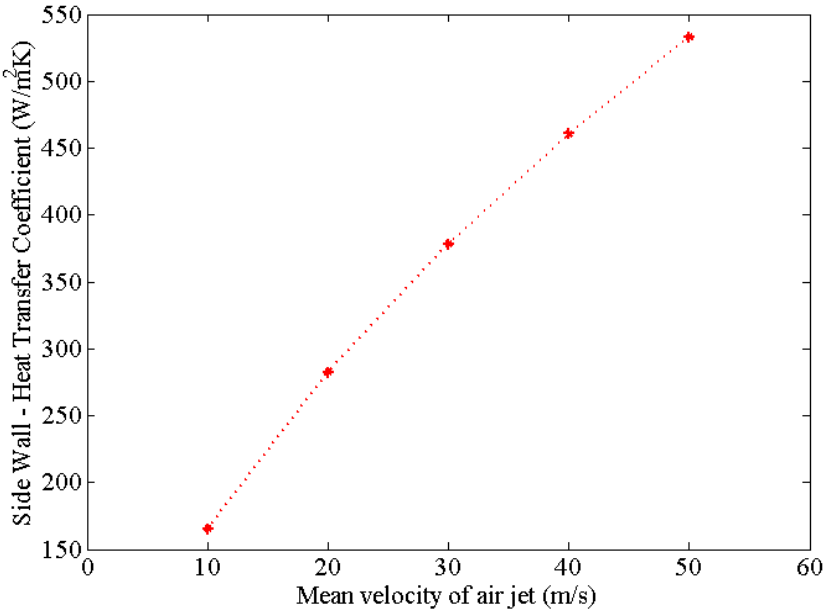

Figure 7.8. The average heat transfer coefficient on the side walls of silicon substrate, denoted by face-2 & 12 in Figure 7.1, as a function of average air velocity

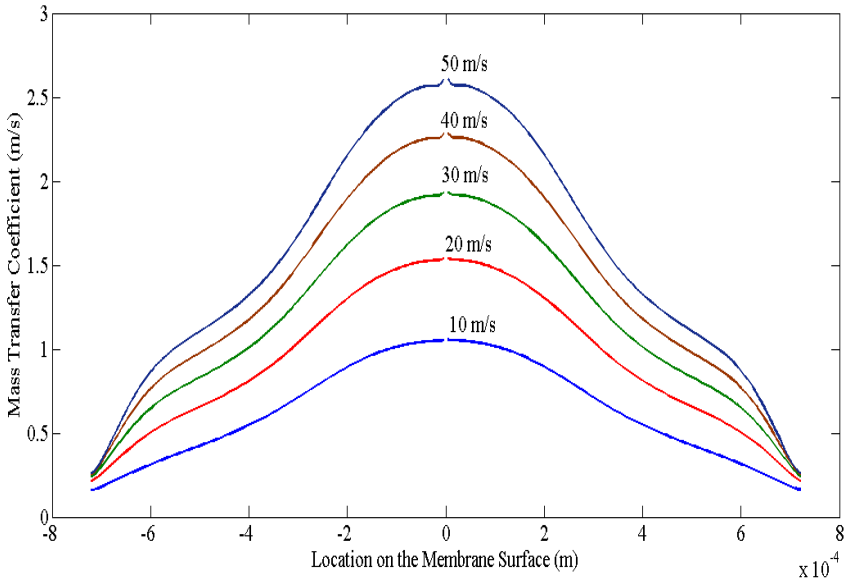

Figure 7.9. Local mass transfer coefficient, h_m on the membrane surface, denoted by face-1 in Figures 7.1 and 7.3

7.4.3 Evaporative cooling as a function of liquid and air flow rate

The net heat flux dissipated at the hotspot at different coolant and air flow rates is presented in Figures 7.10 and 7.11, respectively. In order to determine the performance sensitivity to varying liquid and air flow rates, the resistance to vapor diffusion inside the membrane is made minimal by fixing the liquid vapor interface at the membrane outlet. Mathematically this constraint is enforced by setting $\delta_v = 0$ in equation (7.8).

The enhancement in heat flux achieved by increasing the coolant flow rate for a fixed air jet velocity of 30 m/s is shown in Figure 7.10. The effect of coolant flow is studied by changing the inlet velocity of the coolant from 0.001 to 0.004 m/s, which corresponds to liquid Reynolds numbers, Re_l, varying from 0.25 to 1, where the Reynolds number is calculated as $Re_l = \rho_l u_l d_h / \mu_l$, with the hydraulic diameter of the thin film region given by $d_h \sim 10\mu$m .

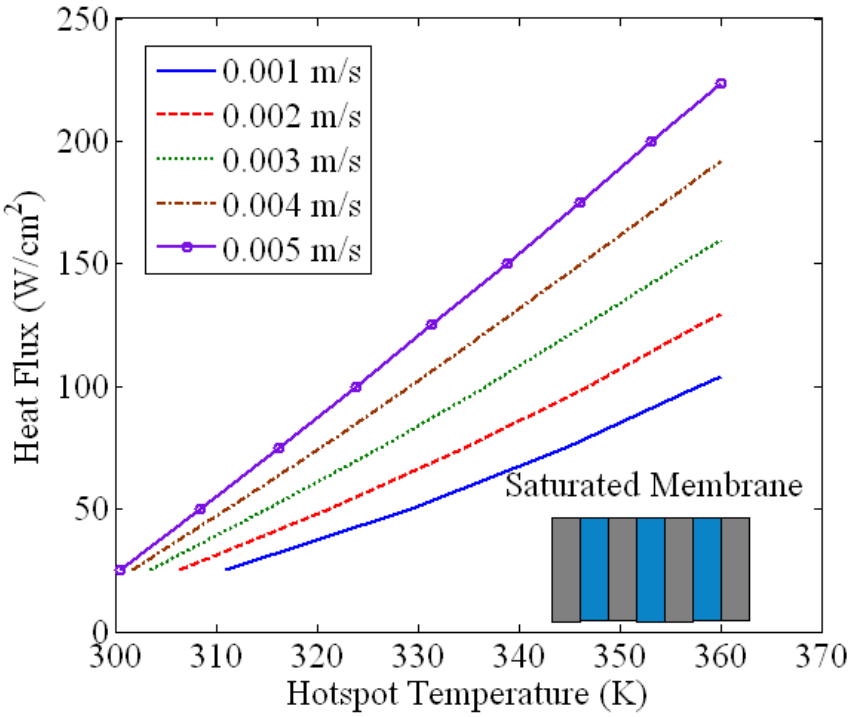

Figure 7.10. Net heat flux dissipated vs. hotspot temperature as a function of coolant average velocity.

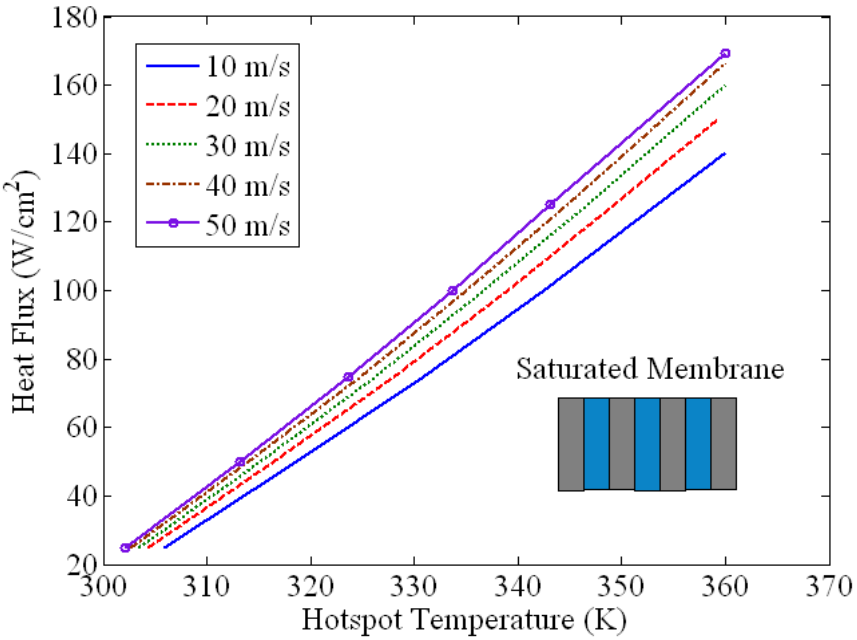

Figure 7.11. The net heat flux dissipated versus hotspot temperature as a function of air average velocity.

For extremely small flow rates, heat diffusion and convection are equally important, and the net heat dissipation is due primarily to evaporation. In this case the net heat flux dissipated from the hotspot at 360 K is 90–100 W/cm^2 for an inlet velocity of 0.001 m/s, which is improved two-fold to 175–185 W/cm^2 with a quadruple increase in coolant flow rate. The pressure drop to pump liquid across the thin film region for inlet velocities of 0.001 m/s and 0.004 m/s is 6.1 kPa and 24.7 kPa, respectively, which translates to a sixteen-fold increase in pumping power for a quadruple increase in liquid flow rate. In summary, though higher flow rates can enhance single phase convection, and therefore the net heat flux dissipated, a significantly larger pumping power is necessary for coolant circulation.

The variation in the net heat flux dissipated with air jet velocity is shown in Figure 7.11 for a fixed coolant velocity of 0.003 m/s. Contrary to the performance sensitivity observed with variation in coolant velocity, a five-fold increase in air flow rate enhances the net heat dissipation only by 20%. In this case, the contribution of evaporation to total dissipated heat flux increases from 47.6% to 65.7%, an increase of only 38% due to a change in air velocity from 10 to 50 m/s. It is important to note that the heat transfer coefficient at the stagnation zone, as shown earlier in Figure 7.7, is enhanced 2.5 times for a five-fold increase in air velocity. A similar trend in the mass transfer coefficient is also illustrated in Figure 7.9. At a first glance, one might therefore expect a corresponding 2.5 times increase in evaporative cooling, and yet the increase is only 38% in net evaporation heat flux. This is explained based on the variation of mass transfer coefficient, vapor pressure and interfacial temperature as result of enhanced air flow on the membrane surface.

In a membrane fully saturated with liquid water, the interfacial resistance to evaporation per unit area, $(2-\hat{\sigma})/(2\hat{\sigma})\cdot(2\pi RT_{vi}/M_l)^{1/2}/(p_{atm}\varepsilon)$ is negligible in comparison to the vapor advection resistance, $RT_{vi}/(M_l p_{atm}\varepsilon h_m)$. For instance, assuming an accommodation coefficient, $\hat{\sigma}=1$ and porosity, $\varepsilon=0.4$, the interfacial resistance to evaporation for water at $T_{vi}=300\text{K}$ is only 0.012 $\text{m}^2\text{s/kg}$. On the other hand, the resistance to vapor transport at the stagnation zone corresponding to an air jet velocity of 50m/s is $1.5\text{m}^2\text{s/kg}$. Therefore, from equation (7.8) it is clear that the rate of evaporation varies with $h_m\left(p_{atm}X_{v,eq}\right)/T_{vi}$, wherein the expression within the parenthesis denotes saturation pressure $p_{v,eq}$ at temperature T_{vi}. The variation of $h_m p_{v,eq}/T_{vi}$ over the surface of the membrane for different mean velocities of air jet is shown in Figure 7.12.

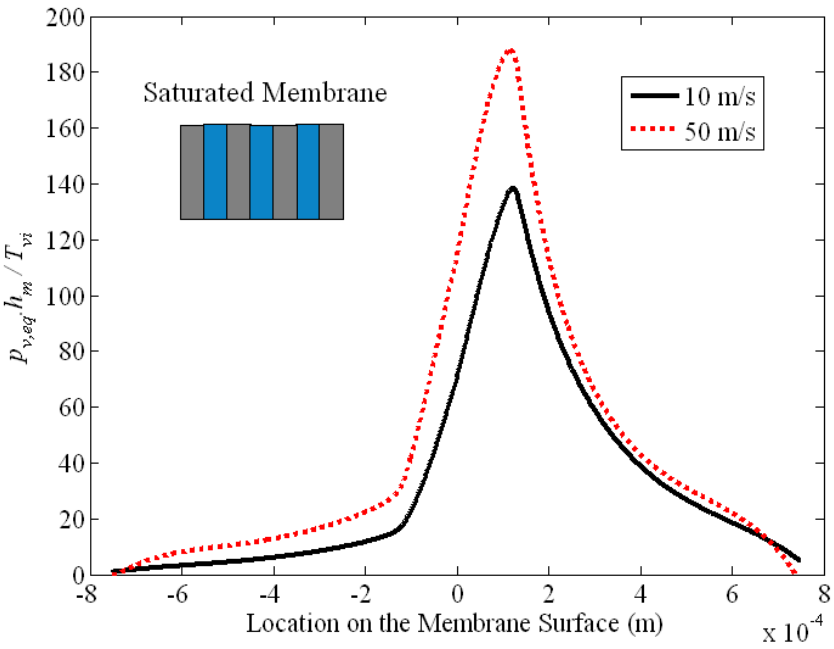

Figure 7.12 The variation of $h_m p_{v,eq}/T_{vi}$ on the surface of the membrane corresponding to mean air jet velocities of 10 and 50 m/s.

While h_m increases by 150%, the increase in the average value of $h_m p_{v,eq} / T_{vi}$ over the surface of the membrane is only 37%, which matches the increase in the net evaporative heat flux. Therefore, while enhanced mass transport can improve advection, a consequent decrease in the interfacial temperature and vapor pressure can depreciate the rate of evaporation. It is the combination of these two factors that determines the net rate of evaporation from the interface.

7.4.4 Effect of resistance to vapor diffusion on device performance

The addition of vapor diffusion resistance within the membrane increases the net mass transfer resistance for vapor transport, reducing the overall performance of the device. The reduction in performance is less severe when the coolant flow rate is progressively enhanced. For a sufficiently large coolant flow rate, since sensible heating provides significant heat dissipation, the reduction in evaporative cooling is less perceptible in the net heat flux. This is illustrated by Figure 7.13, which shows a relatively small decrease in performance for a coolant velocity of 0.005 m/s, in comparison to a larger drop in performance for a coolant velocity of 0.001 m/s, when the resistance to vapor diffusion is included in the analysis. As shown in Figure 7.13, for a dry membrane, the net heat flux dissipated at 360 K is close to 100 W/cm^2 and 200 W/cm^2 for an average coolant velocity of 0.001 m/s and 0.005 m/s, respectively.

If the coolant velocity is fixed at 0.003 m/s, significant performance reduction is observed by including diffusion resistance at a higher air velocity, as shown in Figure 7.14. The relative contribution of evaporation to net heat dissipation increases with air jet velocity. As a result, at an average jet velocity of 50 m/s, the addition of diffusion resistance can alter performance by a relatively higher margin.

In both cases discussed above, evaporation was limited by the rate of vapor diffusion as well as advection. The implementation of a more effective vapor transport mechanism can therefore result in dissipation of higher heat fluxes from the hotspot. Figure 7.13 and 7.14 also show heat flux dissipated when vapor transport is limited only by vapor diffusion and interfacial resistance. It is clear that the resulting enhancement in heat flux is not significantly larger in either case. From Figures 7.13 and 7.14, it can be inferred that vapor advection and diffusion are equally limiting the overall performance. Therefore, by replacing one of the vapor transport resistances with the other does not yield an appreciable increase in net heat flux dissipated at the hotspot as illustrated in these figures.

As an extension of the foregoing discussion, Figure 7.15 shows the net heat flux dissipated for different membrane and film thicknesses. By neglecting the resistance to vapor advection at the membrane outlet, a higher heat flux can be dissipated by minimizing the resistance to vapor and thermal diffusion across the membrane and thin film. For a thin membrane ($\sim 2\mu$m) and liquid film ($\sim 3\mu$m), heat fluxes in excess of 270 W/cm^2 can be dissipated by evaporation at the hotspot. For small membrane and film thicknesses, the resistance to vapor transport can still be significant. It is therefore desirable to eliminate both advection and diffusion resistance to vapor transport, such that the heat flux is limited only by conduction across the thin liquid film and membrane. The heat flux is then obtained by solving the equations $q''_{hs} = \frac{(2\hat{\sigma})}{(2-\hat{\sigma})} p_{atm} X_{v,eq} \varepsilon h_{fg} \left(\frac{M}{2\pi R T_{vi}} \right)^{1/2}$ and $q''_{hs} = \frac{T_{hs} - T_{vi}}{\delta_m / k_m + \delta_f / k_f}$. Implementation of the device under these ideal operating conditions can result in significantly large heat fluxes, as illustrated in Figure 7.16.

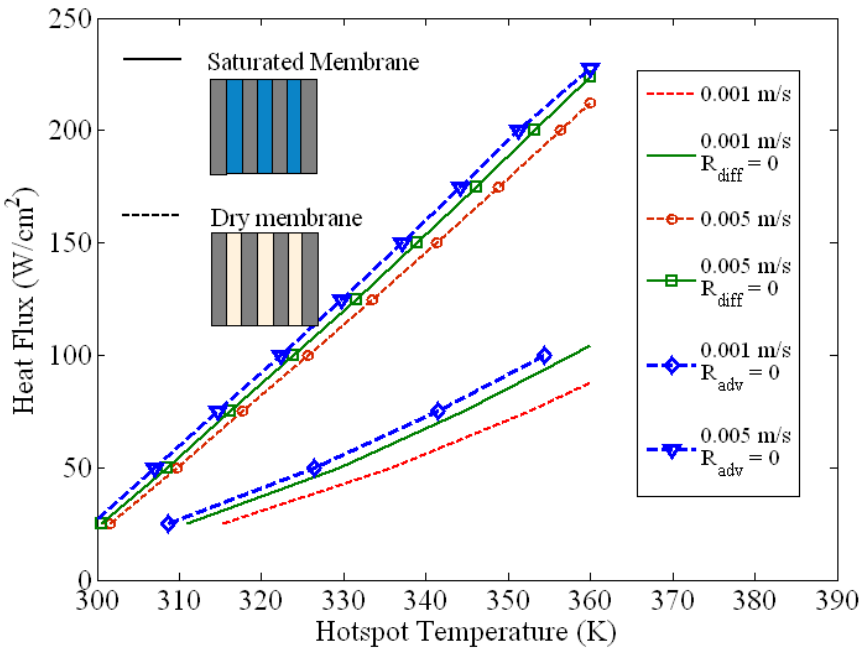

Figure 7.13. The net heat flux dissipated versus hotspot temperature when the interface is assumed to be pinned at the membrane inlet and outlet. The average inlet coolant velocities are 0.001 and 0.005 m/s for a fixed air jet velocity of 30 m/s.

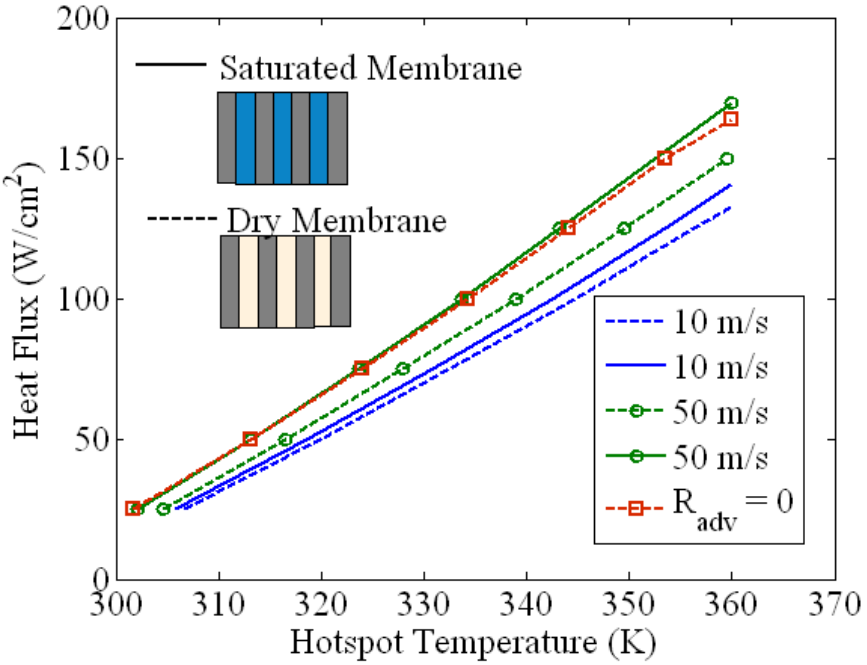

Figure 7.14. The net heat flux dissipated versus hotspot temperature when the interface is assumed to be pinned at the membrane inlet and outlet. The average air jet velocities considered are 10 and 50 m/s for a fixed coolant inlet velocity of 0.003 m/s.

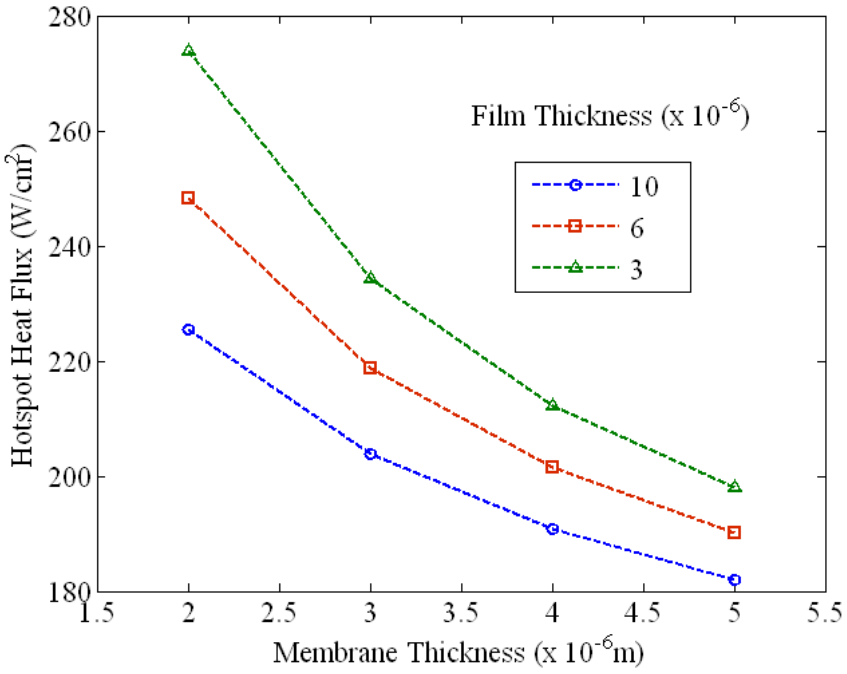

Figure 7.15 Heat flux dissipated at an average coolant velocity of 0.005m/s, due only to evaporation for different membrane and film thicknesses. Resistance to advection is eliminated by assuming a large value of mass transfer coefficient at the membrane outlet, while the heat transfer coefficient is assumed to be 0 W/m^{2}K.

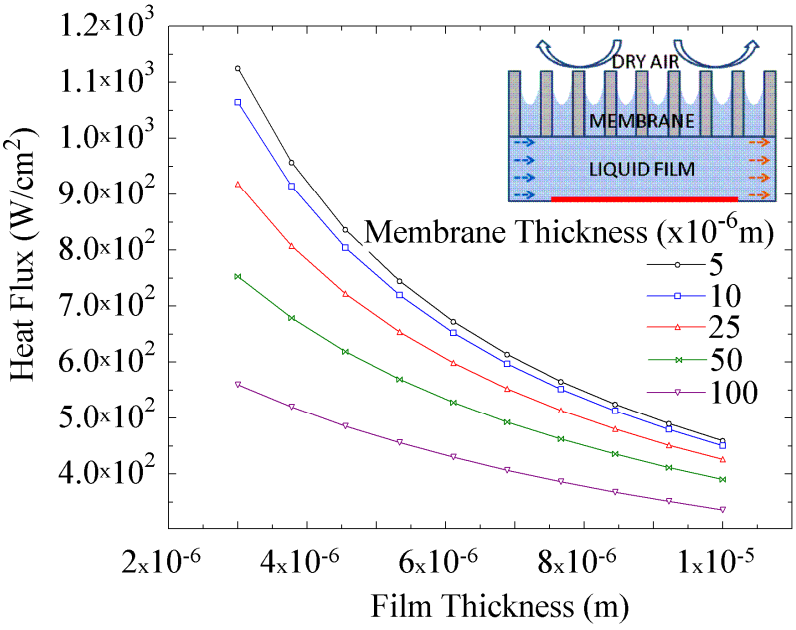

Figure 7.16 Heat flux dissipated under ideal conditions, wherein the overall performance of the device is only heat transfer limited, since resistances to both vapor diffusion and advection are eliminated.

7.4.5 Contribution of evaporation, single phase cooling and spreading

The relative contributions of evaporation, convection and spreading to net heat dissipation from the hotspot are illustrated in Figure 7.17 for different coolant flow rates and a fixed air jet velocity of 30m/s. Figure 7.17(a) illustrates that at a low coolant flow rate, evaporation and sensible cooling contribute about 90 % and 7% of heat dissipation, respectively, and the remaining 3% is spread out in the substrate. For an increased coolant velocity of 0.004m/s, the relative contribution of evaporation, though still higher than sensible cooling, is now more equally matched (64 and 34%, respectively), as illustrated in Figure 7.17(b). But at higher coolant velocities, sensible cooling supersedes evaporative cooling, as illustrated for a velocity of 0.01m/s shown in Figure 7.17(c). For completeness, the net heat flux dissipated at the hotspot by elimination of resistance to vapor advection and inclusion of diffusion resistance is also shown by dotted lines.

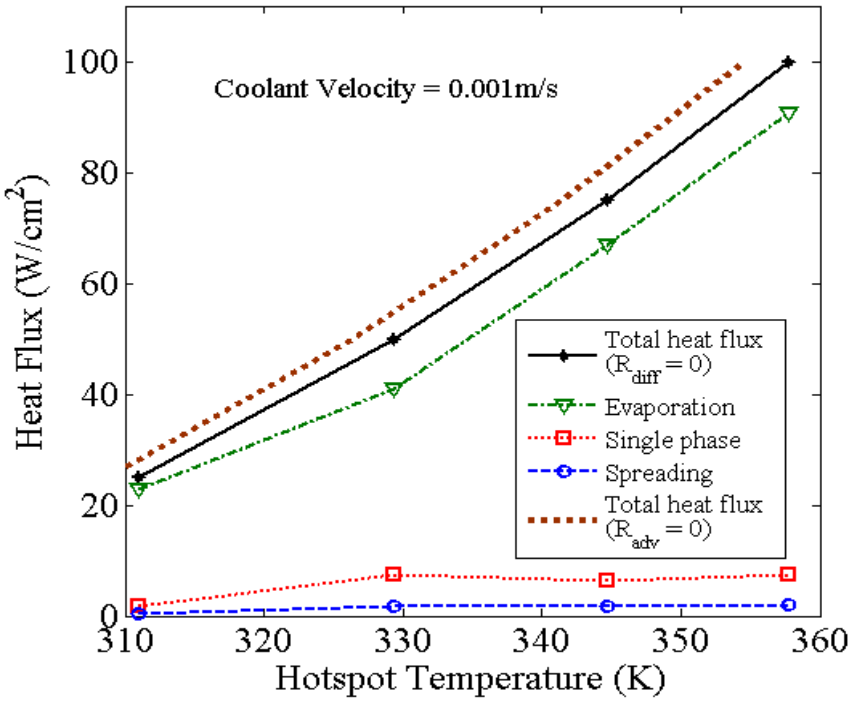

(a)

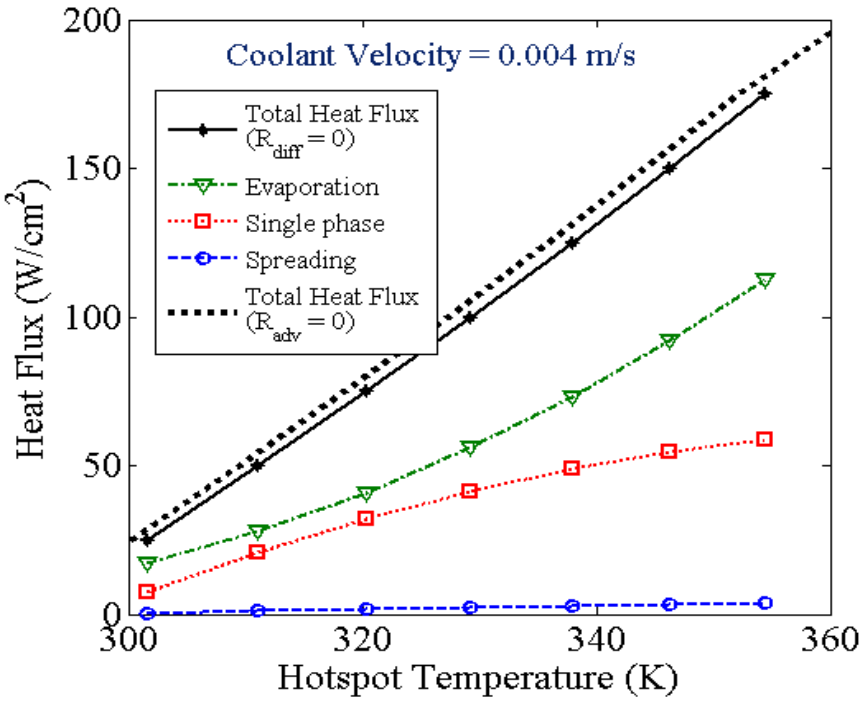

(b)

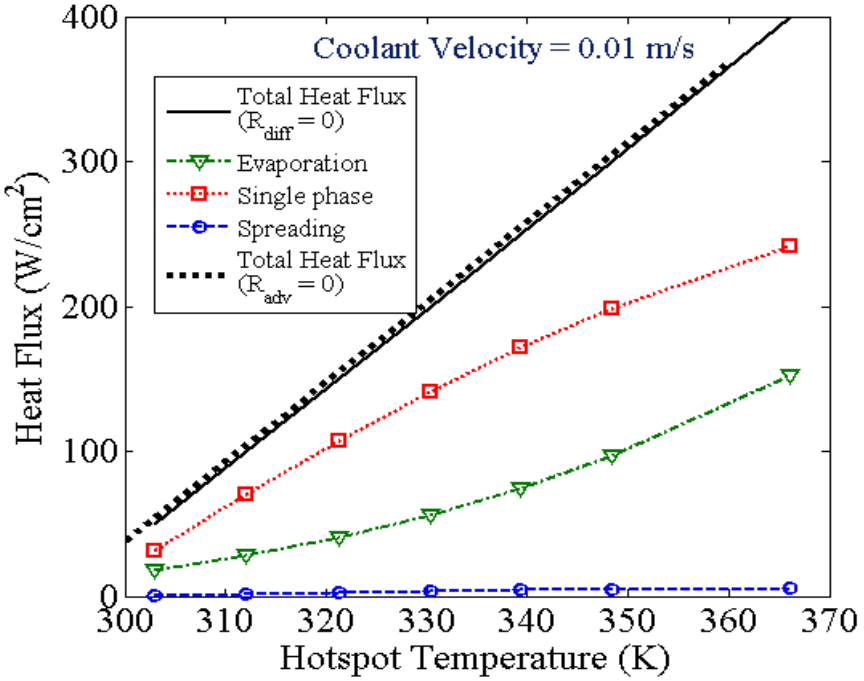

(c)

Figure 7.17. A comparison of heat dissipated by evaporation, convection and spreading with a fixed air velocity of 30m/s and for different average coolant velocities of (a) 0.001 m/s, (b) 0.004 m/s and (c) 0.01 m/s

7.5 Experimental Study of Evaporation

7.5.1 Device description

A MEMS/NEMS device built using micro-fabrication process [98, 100] is described in detail in Chapter 4. The device is made from two distinct substrates, silicon and Pyrex, bonded together by a polymer interlayer (SU-8). The Pyrex substrate consists of an array of resistance temperature detectors (RTDs) that function to simulate hotspots as well as measure the temperature of the surface (Figure 4.3). The silicon substrate consists of microchannels and fluidic ports (Figure 4.1) for delivery and circulation of coolant to the hotspot. More importantly, this substrate also houses a porous ceramic membrane, which confines the liquid to a thin film over the hotspot and provides a passage for the vapor phase to diffuse into the ambient upon evaporation. The diameters of the pores in the membrane made of porous anodic alumina were measured to be 60-80 nm (Figure 4.8).

7.5.2 Experimental procedure

The performance of gas assisted evaporative cooling at very low coolant flow rates is observed on devices with film and membrane thicknesses of 10 μm and 5.5 μm, respectively. The planar dimensions of the membrane being used in this case are $1,500\mu\text{m}\times1,500\mu\text{m}$. In another set of experiments, the contribution of sensible cooling relative to evaporation is measured using higher coolant flow rates. In these experiments, relatively larger film and membranes thicknesses are utilized (15 μm and 10 μm, respectively) to manage higher coolant pressure in the thin film region, while the planar dimensions of the membrane used are $800\mu\text{m}\times800\mu\text{m}$. The dimensions of the hotspot in both cases are $250\mu\text{m}\times250\mu\text{m}$.

RTD calibration prior to experimental testing is carried out following the procedure outlined in Chapter 4 to obtain the linear correlation of each RTD's resistance response to temperature. The hotspot is activated using a DC power supply, causing Joule heating at the location of the hotspot where the resistance is highest. Jet impingement of air is implemented using nozzles with inner diameters of 500 μm and 1000 μm connected to compressed air supply. The gas line is connected in series with a flow meter to measure volumetric flow rate and with a pressure transducer to measure gage pressure in the supply line. The nozzle is held in place using a positioning tool such that its separation from the hotspot and the angle of impingement can be precisely controlled. The results presented herein correspond to normal incidence of an air jet at different flow rates.

The coolant used for thin film evaporation was de-ionized and de-aerated water which was circulated using a syringe pump capable of precisely delivering low flow rates (~ 10^{-10} to 10^{-8} m^3/s). The temperature of the coolant at the inlet was measured using a calibrated thermocouple. The experiments were carried out using different coolant and air flow rates to determine their effects on the overall heat transfer achievable through evaporation and sensible cooling.

7.5.3 Uncertainty in temperature and heat flux

The temperature at the hotspot RTD was calculated based on the resistance values derived from the voltage and current measurements, as shown in the circuit diagram below:

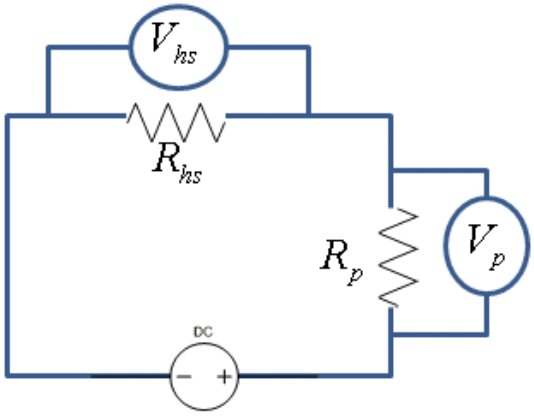

Figure 7.18 Circuit diagram illustrating the use of precision and hotspot resistance to calculate the temperature

The resistance at the hotspot, R_{hs} is given by $V_{hs}R_p / V_p$ where V_{hs}, V_p, represent the voltage measured across the hotspot and the precision resistor, respectively and R_p is the precision resistance $(3 \pm 0.03\Omega)$. The uncertainty in calculation of the hotspot resistance due to the voltage measurements and to the precision resistance is given by the following equation:

$$\left(\delta R_{hs} / R_{hs}\right) = \left(\left(\delta V_{hs} / V_{hs}\right)^2 + \left(\delta V_p / V_p\right)^2 + \left(\delta R_p / R_p\right)^2\right)^{1/2} \tag{7.16}$$

The maximum uncertainty in determining the resistance was therefore found to be less than 1%. The temperature and heat flux at the hotspot are calculated as shown below,

$$T_{hs} = mR_{hs} + c \tag{7.17}$$

$$\dot{q}'' = \frac{V_{hs}V_p}{R_p A_{hs}} \tag{7.18}$$

where A_{hs} represents the area of the hotspot. The slope, m and intercept, c are obtained from RTD calibration, wherein a linear regression model correlates hotspot temperature with resistance. The representative values of the standard error in calculation of the slope and the intercept are 0.04% and 0.05%, respectively. The uncertainty in measurement of the temperature and the heat flux at the hotspot are given by the following equations:

$$\left(\frac{\delta T_{hs}}{T_{hs}}\right)^2 = \left(\frac{m\delta R_{hs}}{T_{hs}}\right)^2 + \left(\frac{R_{hs}\delta m}{T_{hs}}\right)^2 + \left(\frac{\delta c}{T_{hs}}\right)^2 \quad (7.19)$$

$$\left(\frac{\delta \dot{q}''}{\dot{q}''}\right)^2 = \left(\frac{\delta V_p}{V_p}\right)^2 + \left(\frac{\delta V_{hs}}{V_{hs}}\right)^2 + \left(\frac{\delta R_p}{R_p}\right)^2 + \left(\frac{\delta A_{hs}}{A_{hs}}\right)^2 \quad (7.20)$$

In summary, the uncertainty in the measurement of hotspot temperature and heat flux are found to be less than 2% and 1%, respectively.

7.5.4 Cooling performance at low flow rates

The inlet velocity for the coolant was set at 0.004 m/s, while the device performance was studied for an air jet velocity of 30 m/s and 50 m/s using a nozzle of diameter 500 μm, using normally incident air jet, and anchored at a distance of 500 μm from the membrane surface. The net heat flux dissipated at the hotspot is plotted as a function of hotspot temperature in Figures 7.19 and 7.20. Corresponding to the operating conditions and device features matching the experiments, the performance was also predicted using the detailed computational analysis described in the previous section. Computational simulations of device performance were carried out for two distinct positions of the interface inside the membrane. The positions of the interface at the membrane inlet and outlet are represented by solid and dotted lines, respectively as shown in Figures 7.19 and 7.20, signifying a dry and a saturated membrane, respectively.

In both cases, with the air velocities corresponding to 30 and 50m/s, the net heat flux dissipated at 360 K was found to be in excess of 180 W/cm^2. With the aid of computational simulations, the net contributions of evaporation were observed to be about 65 % and 35% due to sensible cooling, with spreading in the substrate being negligibly small. The simulations indicate that the performance limiting resistance in this

case is vapor transport from the interface to the ambient. The thermal resistance calculated as the ratio of heat dissipated by evaporation to the corresponding temperature drop indicates that the air side resistance is about 5 times higher than the resistance of the thin film.

A comparison of experimental results with computational predictions demonstrates an interesting observation that elucidates a characteristic feature of device performance. When the coolant flow rate is held constant, the rate of evaporation is smaller for lower heat fluxes and is expected to increase as the hotspot temperature rises with higher heat dissipation. At lower fluxes, the liquid-vapor interface is pushed further into the membrane, close to the membrane outlet, with direct exposure to air jet impingement. But at higher fluxes, the rate of evaporation is significant in comparison to the rate of coolant supply, and therefore the interface recedes into the membrane, close to the membrane inlet. The overall resistance to vapor transport in this case is a sum of resistance due to diffusion inside the membrane and advection at the membrane outlet. Figures 7.19 and 7.20 support this line of reasoning, since the experimental results match with the computational predictions corresponding to a liquid saturated membrane at lower fluxes, and a dry membrane for higher heat fluxes at the hotspot.

7.5.5 Cooling performance at high flow rates

A device with film and membrane thicknesses of 15 μm and 10 μm, respectively, is tested at higher liquid flow rates, corresponding to inlet velocities between 0.01m/s and 0.03 m/s of the coolant. The air velocity is fixed at 65 m/s, for normally impinging dry air from a nozzle 1,000 μm in diameter placed 1,500 μm from the membrane surface $(800\mu\text{m}\times800\mu\text{m})$. The net heat flux recorded during the experiments is plotted as a

function of the hotspot temperatures, along with analytical results for different coolant flow rates, in Figure 7.21. At higher coolant velocities, the inclusion of vapor diffusion resistance in the analysis introduces an insignificant variation in the predicted values of device performance due to the dominance of sensible cooling. Therefore the computational results have been evaluated assuming a membrane saturated with liquid.

Combining evaporation and sensible cooling modes, the net heat dissipation can be significantly enhanced while maintaining a low temperature at the hotspot. Heat dissipation in excess of 500 W/cm^2 is realizable with hotspot temperatures under 360 K. In this case, the contribution of sensible cooling is larger than 65% for inlet velocities exceeding 0.01 m/s.

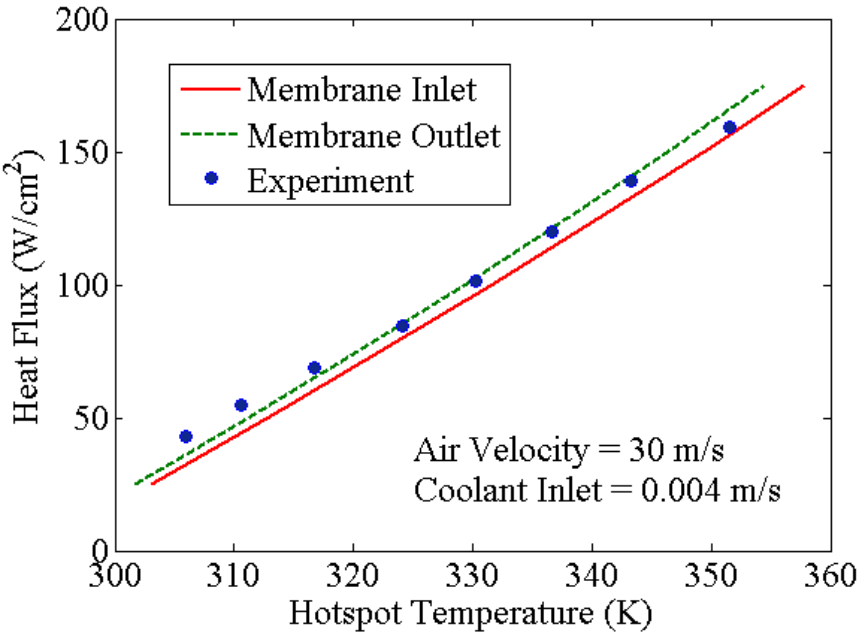

Figure 7.19. The net heat flux dissipated versus temperature at the hotspot. The average coolant and air jet velocity are held fixed at 0.004 m/s and 30 m/s, respectively.

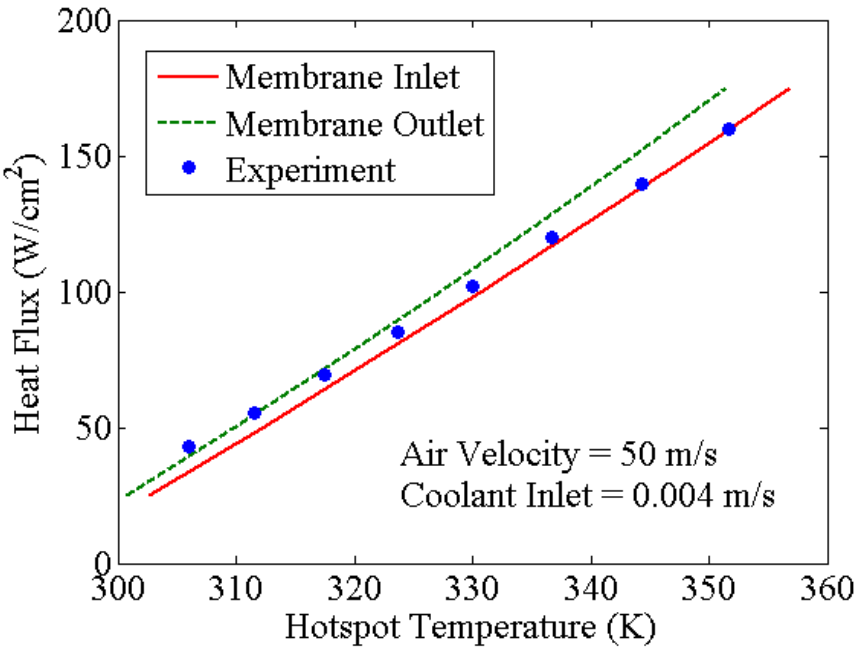

Figure 7.20. The net heat flux dissipated versus temperature at the hotspot. The average coolant and air jet velocity are held fixed at 0.004 m/s and 50 m/s, respectively.

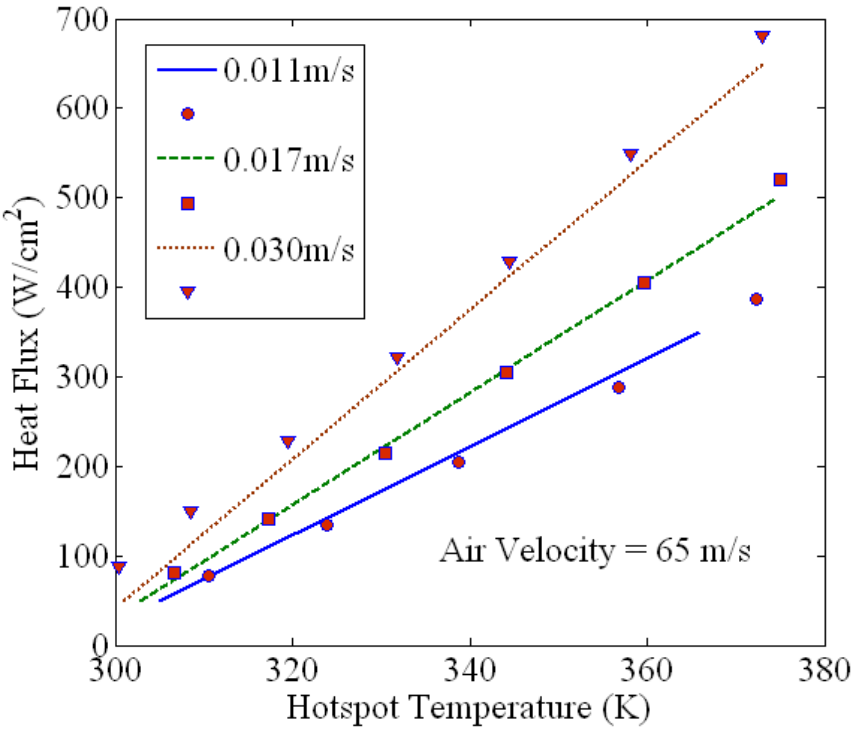

Figure 7.21. Net heat flux disspated at the hotspot for coolant flow rates much larger than the rate of evaporation

7.6 Influence of Coolant Properties on Dissipated Heat Flux

The effect of liquid thermal conductivity and the vapor pressure is determined for different mass transfer coefficients at the membrane outlet using a simple resistance analysis of 1D heat and mass transfer. This study is carried out to determine if the thermophysical properties of an evaporating liquid can be suitably modified such that the performance of the cooling device can be enhanced to dissipate heat fluxes in excess of 1000 W/cm^2. The interface in both cases is assumed to be located at the membrane outlet, so that the resistance to vapor diffusion is negligible.

Figure 7.22 shows the effect of the liquid thermal conductivity, varying between 0.5 and 25 W/mK on the net heat flux dissipated by thin film evaporation using a membrane and liquid film of thickness 5 μm. The vapor pressure at the interface for this case is calculated using the thermophysical properties of water as a function of temperature. The figure shows that in order to dissipate the same heat flux by evaporation, a liquid with higher thermal conductivity will require a smaller mass transfer coefficient. On the other hand, Figure 7.23 shows the effect of vapor pressure on net heat flux for a fixed membrane and film thickness of 5 μm. The thermal conductivity of the liquid is fixed at 0.66 W/mK and the location of the interface is assumed to be at the membrane outlet. It is clear from Figure 7.23 that higher heat fluxes can be dissipated using a liquid with higher vapor pressure, which allows the use of a sweeping gas with much smaller mass transfer coefficient.

It is to be noted that in estimating these results, the interfacial characteristics of capillary confined liquids has been excluded for simplicity. As presented in Chapter 6, the interface can be highly extended in the case of a polar liquid, like water due to

electrostatic interactions. On the other hand, the interfacial area using a dielectric liquid, like FC72, can be relatively small in comparison to water. Additionally, the magnitudes of latent heat of evaporation can significantly affect the net heat flux dissipated.

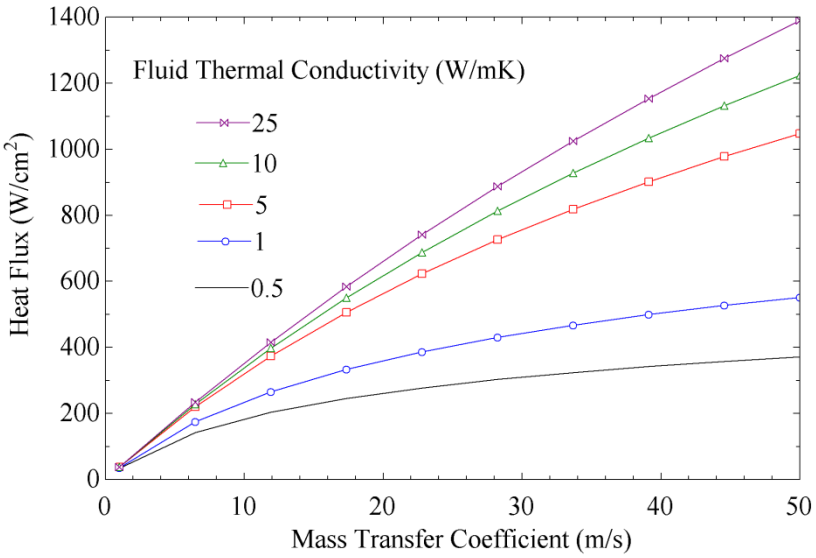

Figure 7.22 Heat flux dissipated as a function of mass transfer coefficient for different liquid thermal conductivities.

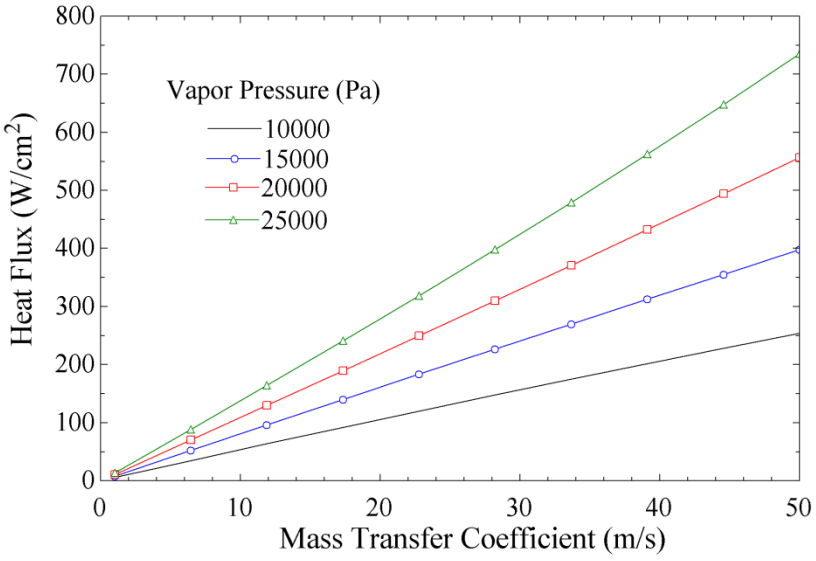

Figure 7.23 Heat flux dissipated as a function of mass transfer coefficient for different vapor pressures.

7.7 Summary and Conclusions

A comprehensive computational analysis of heat and mass transfer is carried out to estimate the performance of a microfluidic device that utilizes evaporation of a microscopically thin liquid film to dissipate heat generated at the hotspot. The thickness of the liquid film in this device is controlled by capillary confinement using a highly porous, thin ceramic membrane. The vapor generated by evaporation at the liquid-vapor interface, located within the membrane, diffuses through the membrane pores into the immediate ambient, and is eventually transported away by advection using jet impingement of dry air (Figure 7.1).

The computational analysis determines the contributions of simultaneously occurring modes of heat dissipation, namely evaporation, convection and spreading. A detailed analysis of air jet impingement is also presented which calculates the rate of heat and mass transfer achievable within a confined volume of the device (Figures 7.7 and 7.9). The results from the analysis of air jet impingement are then used to predict device performance for thin film evaporation. The net rate of heat dissipation is presented as a function of hotspot temperature for different operating conditions. Complementary to the computational predictions, the results from experimental demonstration of thin film evaporation are also presented and compared to simulations.

A significant change in the flow characteristics of a confined air jet is demonstrated with different combinations of nozzle diameters and cavity size. It is shown that a smaller nozzle in close proximity to the membrane ensures that both the stagnation zone and the radial outflow region contribute significantly to heat and mass transfer. The pressure distribution inside the cavity is favorable to promote radial acceleration of flow, resulting

in a thin boundary layer and consequently, efficient heat and mass transfer. On the other hand, an air jet from a nozzle of much larger diameter and separation (as compared to the dimensions of the cavity confining the jet) impinging on a relatively small confined space can result in significantly poor flow characteristics. In this case, due to an unfavorable pressure distribution in the cavity, the advection of heat and vapor due to air jet impingement is an inefficient process.

The performance of the evaporative cooling device was analyzed using both computational and experimental tools. The net heat flux dissipated at the hotspot was computed for different coolant and air jet velocities. A significant enhancement in performance is shown with an increase in the coolant flow rate, but no significant increase was observed with variation in the air jet impingement velocity. The performance was doubled from 90 to 185 W/cm^2 for an increase in the coolant velocity from 0.001 to 0.004 m/s. On the other hand, the cooling was enhanced only by 20% when the air jet velocity was increased five-fold from 10 to 50 m/s.

The resistance to vapor diffusion in the membrane was not found to affect the net heat dissipation significantly at higher flow rates, since cooling was achieved mostly by convective heat transfer. On the other hand at smaller coolant flow rates, when evaporation contributes significantly to net heat dissipation, the position of the interface has a more prominent effect on the overall performance. In this case the design of the membrane can play an important role for dissipation of large heat fluxes from the hotspot. In studying the relative contribution of evaporation and convection to net heat dissipation, it was demonstrated that evaporation contributes significantly at low coolant flow rates while convection is prominent at higher flow rates. At an average coolant

velocity of 0.001 m/s and air jet velocity of 30 m/s, the net heat flux dissipated at the hotspot is 100 W/cm^2 at 358 K, wherein evaporation and sensible cooling contribute about 90 and 7% of net heat dissipation, respectively. On the other hand, for a coolant velocity of 0.01m/s, evaporation contributes only about 38% to a net heat flux of 400 W/cm^2, at a hotspot temperature of 365 K. Hence, although larger coolant flow rates can provide relatively higher heat fluxes, they require more pumping power for coolant circulation. On the other hand, smaller coolant flow rates may allow the device to be operated passively, but the net heat flux dissipated is smaller.

In the experimental study of evaporative cooling, the net heat flux dissipated at the hotspot is determined for different air and coolant velocities. In the experiments carried out at a coolant velocity of 0.004 m/s, the change observed in net heat dissipation at different air jet velocities was not significant, as also predicted by the computational analysis. In this case the decrease in the air side resistance to vapor advection was not sufficiently large to exhibit a significant change in net heat dissipation. At higher coolant velocities, with enhanced contribution of convective heat transfer, the net heat fluxes are much higher. With a coolant velocity of 0.03m/s and an average air jet velocity of 65 m/s, heat fluxes in excess of 600 W/cm^2 were demonstrated at 365 K.The current design of this microfluidic device allows one to make use of both evaporation and convection for heat dissipation at relatively high flow rates. In order to dissipate heat fluxes in excess of 1000 W/cm^2 at significantly smaller coolant flow rates, it is essential to maximize the rate of evaporation. This requires maintaining a very thin liquid film using a hydrophilic membrane and minimizing the significantly higher vapor advection resistance observed in the current design of the microfluidic device.

CHAPTER 8

CONCLUSIONS AND RECOMMENDATION FOR FUTURE WORK

8.1 Conclusions and Recommendations

In this thesis, a new approach to evaporative cooling using microscopically thin liquid films is presented to address the emerging thermal challenges in current and next generation electronics. As opposed to relying on flow hydrodynamics to maintain a thin liquid film, the specific system design uses capillary confinement of the coolant using a nanoporous membrane. The membrane also provides a pathway for the vapor resulting from evaporation to be continuously removed using a dry sweeping gas, hence enabling sustained heat dissipation. The thesis describes the design, fabrication and characterization of a MEMS/NEMS device, called "perspiration nanopatch", for gas-assisted evaporative cooling from confined domains. Such a cooling technology would find application where large power loads need to be dissipated from small form-factor areas, such as microprocessor hotspots. With its compact design it can be integrated with a suitable background cooling method, e.g., microchannels or pin-fin arrays, to meet the cooling demand from devices featuring spatially non-uniform power dissipation.

A detailed theoretical analysis of interfacial transport during evaporation of water confined within nanopores is also presented, highlighting the advantage of using thin film evaporation over single phase cooling. Furthermore, a detailed computational analysis determines the contribution of single phase convection and evaporative cooling to net

heat dissipation during the operation of a prototypical device, and identifies the rate limiting thermal resistance to enable further enhancement in device performance.

In Chapter 2, a performance analysis of gas assisted thin film evaporation is presented, wherein the effects of various operating conditions and device characteristics are discussed. The thermal resistance modeling presented in this chapter incorporates temperature dependence of thermophysical properties of water and FC72, which are both examined as potential coolants. This chapter evaluates the performance of a device for various membrane and film thicknesses, with varying flow rates of air jet impingement for vapor advection from the membrane surface. It also determines if the flow rates and pressure drops encountered in circulating the coolant are practically feasible under these operating conditions. In this chapter it is demonstrated that using a thin $(1-5\mu\text{m})$ evaporating film of FC72 and a nanoporous membrane of thickness $1-5\mu\text{m}$:

i. Heat dissipation in excess of 300 W/cm^2 is achievable while maintaining the hotspot temperature under 90^{o}C.
ii. A volumetric flow rate of ~50 ml/hr with 20 kPa pressure drop is expected for circulating FC72.
iii. The cooling performance (neglecting the interfacial resistance to evaporation) obtained using FC72 is 2 – 3 times larger than that found for water. For thin film evaporation, a higher vapor pressure of the evaporating liquid is found to be more beneficial than a superior thermal conductivity.
iv. Higher heat fluxes can be dissipated with a thinner liquid film and membrane. The pressure drop for coolant circulation and the mechanical strength of the membrane essentially set the limit on practically achievable heat fluxes.

In Chapter 3, a preliminary experimental investigation of thin film evaporation is presented. A meso-scale experimental test setup is built using a commercial ceramic membrane for capillary confinement of thin liquid films of de-ionized water. The experiments are carried out with de-ionized water under varying operating conditions and the net heat dissipated is compared with the performance analysis presented in Chapter 2. In a meso-scale experimental test setup, with film and membrane thicknesses of 120 and 60 μm, respectively, heat dissipation in excess of 60 W/cm^2 at 90^{o}C was experimentally demonstrated. The variation of net heat flux dissipated with hotspot temperature was shown to be in agreement with the analytical predictions calculated using the thermal resistance network analysis. Furthermore, a reduction in heat dissipation from the hotspot was also demonstrated with increase in film thickness and by inclining the nozzle further away from normally incident free surface jet impingement.

An essential feature of "Perspiration Nanopatch" is its operation in a closed loop. In order to assess the feasibility of coolant circulation, the following recommendation is made.

A. Exploration of different configurations for separation of air-vapor mixture and vapor condensation is essential. A feasibility analysis should be carried out for different vapor condensation alternatives, including condensers with extended surfaces, adsorption based condensation and use of solid state cooling devices such as thermoelectric and super-lattice coolers. Additionally, a preliminary investigation of heat and mass transfer during condensation of vapors is essential to determine the practicality of a chosen condensation scheme; this investigation should include volume, power and materials requirements.

In Chapter 4, the design and fabrication of a micro-fluidic device is presented. The device enables thin film evaporation by incorporating a nanoporous ceramic membrane with characteristic dimensions chosen in accordance with the results of the performance analysis presented in Chapter 2. The fabricated device integrates micro and nanoscale features in a monolithic structure that combines multiple functionalities of hotspot simulation, temperature sensing as well as evaporative cooling. The following conclusions are derived from the experimental testing of the micro-scale device presented in Chapter 5:

i. The fabrication of a monolithic test device incorporating multiple functionalities of heating, sensing and cooling minimizing interfaces with parasitic contact resistances is essential for demonstrating and characterizing cooling mechanisms for the next generation of electronic devices, especially when heat dissipation strongly relies on micro and nano-structured features.

ii. With the latest micro-fabrication tools, precise control over the film thickness can be achieved, in addition to in-situ fabrication of nanoporous membranes of desired dimensions. The use of an RTD array and hotspots on Pyrex is instrumental for providing localized heating with minimal spreading and optical access to monitor the microchannel during device operation.

iii. Gas assisted thin film evaporation was shown to dissipate heat fluxes close to 600 W/cm^2 at 90 ^oC, which is higher than both air jet and singe phase microchannel cooling on similar thermal test dies. Heat flux achieved by evaporative cooling demonstrates a seventeen-fold increase over air jet impingement and a 25% increase over single-phase microchannel cooling using water. The overall heat transfer

coefficient demonstrated by thin film evaporation is found to lie between 88 - 94 kW/m^2K.

iv. A much higher heat flux is demonstrated by evaporation at surface temperatures well below saturation conditions compared to the critical heat flux achieved in pool boiling of water (CHF ~ $120W/cm^2$) at atmospheric conditions. High performance at the low junctions temperatures enabled by thin film evaporation is a critical advantage for electronic cooling applications, which have a strict limit on maximum die temperature.

v. The effect of the flow configuration of the sweep gas on vapor transport from the membrane surface inside a confined volume was found to be critical to enhance performance. The change in overall heat transfer coefficient using evaporation by varying the nozzle-to-membrane separation and air jet inclination was experimentally characterized.

Based on the experimental study of the micro-scale device for gas assisted thin film evaporation, the following recommendations are made for future work:

A. Having demonstrated the performance and advantages of thin film evaporation in this study, the implementation of this cooling mechanism in microprocessors should include the following design change. The fabrication of sensors and hotspot should be carried out in the same silicon die, which includes microchannels as opposed to the use of a separate Pyrex wafer. This will eliminate the thermal resistance arising due to the presence of interfaces between bonded substrates.

B. The design of the heater and sensor array should incorporate background heating along with hotspots. This can be done following the same fabrication procedure

outlined in this study. The design of microchannels on the reverse side should incorporate "nanopatches" for thin film evaporation for hotspot cooling and microchannels or pin-fin array for background heat dissipation.

C. The current study utilizes capillary confined water for demonstrating thin film evaporation to dissipate heat fluxes over 600W/cm^2. The performance analysis in Chapter 2 shows that use of FC72 can support heat fluxes 2 to 3 times larger in comparison to water. FC72, being less viscous, was found to easily flood the membrane with 60-80 nm diameter pores. Furthermore, it was difficult to contain FC72 leakage through contact interfaces across the fluid channels. In order to implement cooling with FC72, it is essential that the pores be made narrower, such that viscous stress can contain the liquid film within the membrane. On the other hand, narrow pores will also increase resistance to vapor diffusion. Therefore, optimal dimensions have to be determined to maximize the dissipated heat flux. Additionally, a more suitable procedure to bond device components is essential to avoid leakage of FC72.

D. Alumina is inherently weakly hydrophilic, which results in capillary pressure driving fluid into the nanopores of the alumina membrane. Performance enhancement using thinner membranes can eventually result in the pores getting completely flooded with water. In order to avoid this, hydrophobization of membrane pores will be essential for coolant confinement.

E. The use of thin membranes is structurally unfavorable, although it is desired for enhancing thermal performance. Fabrication of membranes with modulated pore diameters is therefore a viable solution for addressing both concerns. Using current

techniques, a hydrophobized membrane can be fabricated with pores of large diameter and capped with smaller sections of relatively small diameters at the membrane inlet and outlet (Figure 8.1). It is indeed possible to fabricate axially aligned cylindrical pores of different diameters using mild and hard (high-field) anodization [40]. In addition to electrochemical fabrication, nano-imprint lithography and electron beam lithography can also be used for making axially aligned pores of different dimensions.

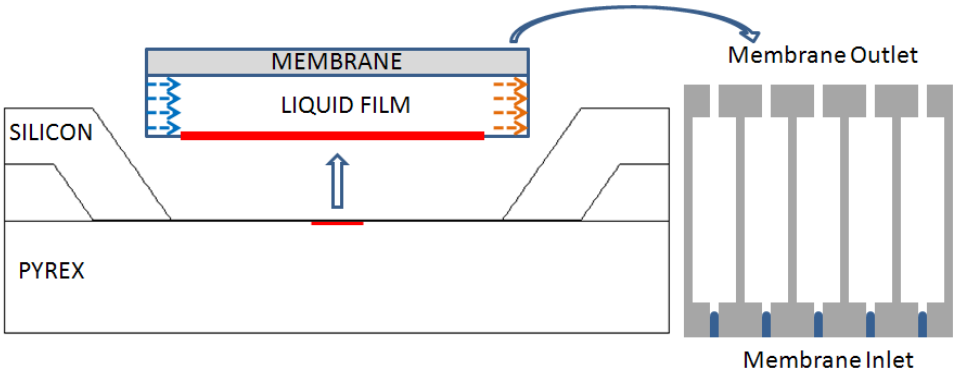

Figure 8.1 The use of modulated pore diameters in the membrane to enhance vapor diffusion

Chapter 6 describes a detailed analysis of water evaporation confined by nanoscale pores of alumina membrane. A theoretical study of interfacial transport process is presented, which accounts for dispersion and electrostatic interactions in addition to capillary forces. In this study, the effect of temperature, pore radius and relative humidity of surrounding vapor on the shape of the interface and net evaporation rate from a pore is presented. The following conclusions are derived from this study:

i. The interfacial transport characteristics depend on the adsorbed film thickness in equilibrium with the surrounding vapor phase in a nanopore. The equilibrium film thickness is evaluated including electrostatic interactions and differs from the analysis

proposed by Wayner [71], which accounts only for evaporation kinetics and dispersion forces. In this study, for a constant wall temperature, the equilibrium thickness of the adsorbed film is found to increase with the relative vapor pressure, and to decrease with an increase in pore radius.

ii. A significant variation in the shape of the interface is observed when electrostatic interactions are included, in addition to Van der Waals and capillary forces. The interface is found to extend further due to the presence of electrostatic forces, and as a result, the net rate of evaporation from a single pore is enhanced.

iii. The inclusion of thermocapillary stresses does not yield measurable variation in interfacial characteristics for nanoscale capillaries, due to a temperature gradient that is insufficient to induce stresses comparable to other driving forces such as capillary and disjoining pressures.

iv. It is shown that the extension of the liquid-vapor interface is more prominent for smaller nanoscale capillaries, therefore, yielding a larger net rate of evaporation per unit pore area. An increase in capillary wall temperature, which enhances saturation pressure, or a decrease in the ambient vapor pressure, both result in an overall increase in the net rate of evaporation from the interface. In order to support a higher flow rate inside the pore, the length of the interface decreases to provide the necessary pressure gradient to support flow.

The current understanding of interfacial transport inside nano-capillaries will be significantly enhanced if the following factors can be elucidated:

A. In this study, the disjoining pressure arising due to the electrostatic interactions is calculated using Langmuir's equation for thin films of a dilute electrolyte on a surface

of high intrinsic electric potential. In order to include electrostatic interactions between various surface-liquid pairs, an alternative and more accurate analysis for a broader range of ionic strengths of electrolytes needs to be carried out by solving for free charge and electric potential distribution in polar solvents. The electrostatic disjoining pressure can then be obtained from these distributions and incorporated into the analysis.

B. The current study demonstrates interfacial characteristics and transport when water wets the surface of the membrane pores. Since hydrophobization of the membrane is an essential alternative for implementing this cooling mechanism, a theoretical analysis of interfacial transport of water confined by non-wetting pores is essential, and is yet to be reported in the literature.

Chapter 7 determines the contribution of single phase convection and evaporation to net heat dissipation at the hotspot by carrying out a detailed, device-level computational analysis of heat and mass transfer. The computational analysis is supported by experimental characterization of device performance. This study identifies the rate limiting transport mechanism and identifies different modes of device operation wherein either evaporation or single phase convection contributes significantly towards net heat dissipation. The following conclusions are drawn from this study:

i. A significant change in the flow characteristics of a confined air jet is demonstrated with different combinations of nozzle diameters and cavity size. It is shown that a smaller nozzle in close proximity ensures that both the stagnation zone and the radial outflow region contribute significantly to heat and mass transfer. On the other hand, an air jet from a nozzle of much larger diameter and separation impinging on a

relatively small confined space from a large distance results in significantly poorer flow characteristics due to an unfavorable pressure distribution inside the cavity.

ii. In studying the relative contribution of evaporation and convection to net heat dissipation, it is demonstrated that evaporation contributes significantly at low coolant flow rates while convection is dominant at higher flow rates. For example,at an average coolant velocity of 0.001 m/s and air jet velocity of 30 m/s, the net heat flux dissipated at the hotspot is 100 W/cm^2 at 85 ^{o}C, wherein evaporation and sensible cooling contribute about 90% and 7% of net heat dissipation, respectively and the remaining 3% are lost to spreading. On the other hand, for a coolant velocity of 0.01m/s, evaporation contributes only about 38% to net heat flux, which is 400 W/cm^2 at a hotspot temperature of 93 ^{o}C. Higher coolant flow rates can result in dissipating heat fluxes in excess of 600 W/cm^2, with enhanced contributions from convective heat transfer in addition to evaporation.

iii. In order to improve the heat dissipation per unit pumping power in a multi-processor architecture, it would be beneficial to eliminate the use of the pump at lower heat fluxes by relying on capillary transport for coolant delivery, while selective, on-demand activation of the pump can provide much higher cooling depending on the computational demand in any particular processor.

In order to enhance heat dissipation by thin film evaporative cooling, the following recommendations for future work are suggested:

A. In this study, vapor advection using a sweep gas has been explored with different flow configurations. In order to further enhance vapor transport from the liquid-vapor interface, evaporation into a low pressure environment is a viable option. Under ideal

conditions at extremely low pressures, the rate of evaporation will be limited only by Knudsen diffusion inside the membrane pores since vapor transport into vacuum will essentially be ballistic. It was found that heat fluxes in excess of 270 W/cm^2 can be dissipated if a thin liquid film and membrane of thickness 3 μm and 2 μm, respectively is utilized. Elimination of both advection and diffusion resistance can be quite beneficial to enhance device performance. In this case, the performance is just heat transfer limited and the net heat fluxes are in excess of 1000 W/cm^2 for a liquid film and membrane of thickness 3 μm and 10 μm, respectively.

B. Chapters 6 and 7 demonstrate that capillary pressure can be significant in driving the flow inside the nanopores of alumina membrane. This represents an opportunity to operate the device passively and therefore minimize pumping power, volume as well as audible noise, all of which are major concerns for electronics. It is therefore useful, in exploring capillary pressure-driven coolant delivery and incorporating a micro-scale condenser, to allow operation of the device in a closed loop using only a pure liquid-vapor system, similar to the functioning of a heat pipe.

C. It has been demonstrated that net heat dissipation can be enhanced if the resistance to vapor transport is minimized. It is also well established that the net heat and mass transfer using air is fundamentally limited in comparison to liquids such as FC72 or water. Therefore, a vapor transport mechanism using a sweeping liquid in contrast to a dry gas could provide an intriguing opportunity, since it would eliminate the use of a condenser and a dedicated air-vapor separation unit. This would require a re-design of the membrane, such as the use of hydrophobized membranes with modulated pore

diameters [40] to separate the vapor and liquid phases, as shown in Figure 8.1, and it would require study of condensation and absorption of vapor by the sweeping liquid.

8.2 Application Space for Nanopatch Cooling

Heat generation from the integrated circuits can be highly non-uniform with very large heat fluxes at few locations on the die, resulting in hotspots. The presence of such intense heat sources in many electronic applications therefore demand a localized cooling solution, such as thin film evaporative cooling using the "Perspiration Nanopatch". The applications that can potentially take advantage of this low-temperature, compact, localized phase-change cooling scheme includes:

1. *Hotspot mitigation in multi-core processors for desktops and data center servers.*

   The presence of hotspots highly exacerbates the complexity of cooling, which become more challenging in stacked ICs to route heat from within the stack to the periphery while maintaining the junction temperature under 85 ^{o}C. Interlayer hybrid cooling can incorporate a nanopatch for hotspot mitigation and microchannels for background cooling with a characteristic volume under $10\times10\times0.25$ mm^3 between two layers of a 3D stack. The hybrid cooling can potentially dissipate 500 W/cm^2 from hotspots and 100 W/cm^2 average heat flux over the entire chip surface.

2. *High power light emitting diodes (LEDs).*

   The typical classification of LEDs based on their power rating include, low power LEDs (<0.1W), medium-power LEDs (0.1–0.5 W) and high-power LEDs (>0.5W). The thermal management incorporated into the packaging of high power LEDs must address significantly high power densities, which correspond to heat fluxes in excess of 500

W/cm^2 from a 1 mm^2 die. For most applications of LEDs, thermal management is a key requirement to maintain junction temperatures to maximize their operational life and optical performance. The maximum allowable LED power dissipation and junction temperature is currently 7 W and 109 ^oC, respectively, and will correspond to 10 W and 86 ^oC, respectively by year 2022 [103].

3. *Radio-frequency (RF) and millimeter wave packaging.*

   Radio-frequency (RF) and millimeter wave packaging include RF CMOS based technologies. The applications of RF technology in automotive radar typically require packaging that can support high operational frequencies and thermal management exceeding 300 W/cm^2. Static radar equipment, especially high power transmitters can potentially generate high power, which must be dissipated to prevent equipment damage. Inclusion of thermal management with RF packaging is essential to improve reliability and increase RF power density.

4. *Automotive packaging*

   Automotive packaging incorporates electronic systems that operate in a typically high ambient temperatures that from range from 85 ^oC to 175 ^oC. The drivers for automobile packaging are therefore high operational temperature, large heat dissipation and reliability. In order to integrate power and power controls to reduce size and enhance efficiency, on-board electronics can potentially create hotspots. Moreover, dissipation of large heat fluxes is required for high operational frequency and enhanced performance of existing on-board RF devices. This can be addressed by the use of a localized cooling scheme such as gas assisted thin film evaporation using a Nanopatch.

8.3 Integration of the Hotspot and Background Cooling

In order to provide localized cooling for hotspot thermal management and dissipate average heat fluxes over the entire area of the chip, the integration of thin-film evaporation with a suitable background cooling mechanism is necessary. A combination of thin film evaporation with microchannel cooling is shown in Figure 8.2. Shallow microchannels of a smaller depth (~ 10 μm) can be fabricated on the backside of the IC chip (Substrate-1). Complimentary, but higher aspect ratio microchannels for the background liquid coolant and a porous membrane are fabricated using reactive ion-etching on the same side of Substrate-2, while the opposite side is etched to define the air channel as shown in Figure 8.2. A cover plate is then fabricated with inlet and outlet ports for fluid and air delivery to Substrates 1 and 2.

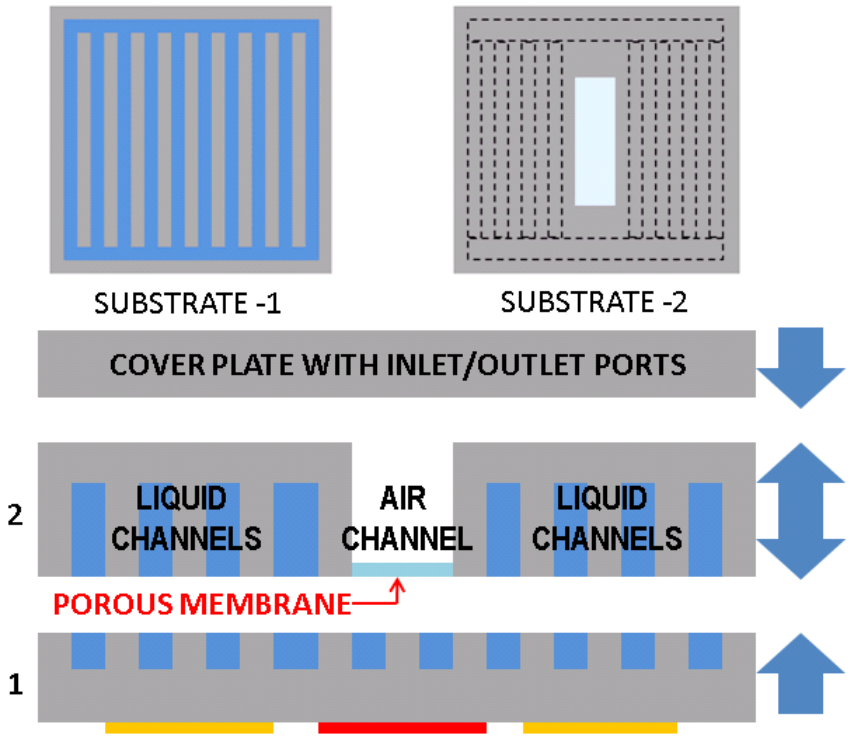

Figure 8.2 An illustration of an implemention scheme for thin-film evaporation cooling of hotspots with microchannels for dissipation of background heat fluxes.

These substrates are bonded together to create a leak-free monolithic structure to provide a comprehensive cooling mechanism for hotspot thermal management, as well as background cooling. In this case wafer the substrate assembly can be carried out using either adhesive or fusion bonding, since smooth silicon surfaces are available for contact. For compatibility with CMOS fabrication process, the use of SU-8 or any other adhesive bonding technique is more applicable since they can be carried out at much lower temperatures. In the case of adhesive bonding, the use of SU-8 will not affect the thermal performance significantly if its thickness is minimized (~ 5 μm) during wafer bonding. On the other hand, while fusion bonding takes place at much higher temperatures (300 to 700^{o}C) followed by annealing at 1100 to 1400^{o}C, it ensures minimal interfacial resistance between bonded substrates.

The application of hotspot cooling integrated with background thermal management can be extended to 3D stacked IC configuration for the next generation of electronic devices. As an extension of the design shown in Figure 8.2, Figure 8.3 illustrates the application of combined hotspot and background cooling. The figure illustrates how inter-die through-silicon vias can actually be more beneficial for overall performance of thin film evaporation. If a membrane is supported by the through-silicon vias on either side, the effective thermal resistance on the evaporating liquid film can be further reduced due to the presence of in-channel microstructures with higher thermal conductivity. Additionally, vapor advection is also promoted by inducing turbulence at higher flow rates or better mixing due to vortices generated by air flow around the vias.

The implementation of thin film evaporation was shown to dissipate heat fluxes in excess of 600 W/cm^2 at 90 ^{o}C. This cooling mechanism is therefore applicable for

hotspots that demand aggressive cooling techniques. On the other hand, for applications that require a compact and liquid-free cooling mechanism, the use of solid state cooling can be utilized. It has to be noted that the total heat fluxes dissipated at the hotspot in this case will be much less (~ 150 W/cm^2) in comparison to thin film evaporation. The use of solid phase change cooling mechanism in addition to solid state cooling are suitable for applications demanding a compact technique to address time varying cooling loads but lower heat fluxes.

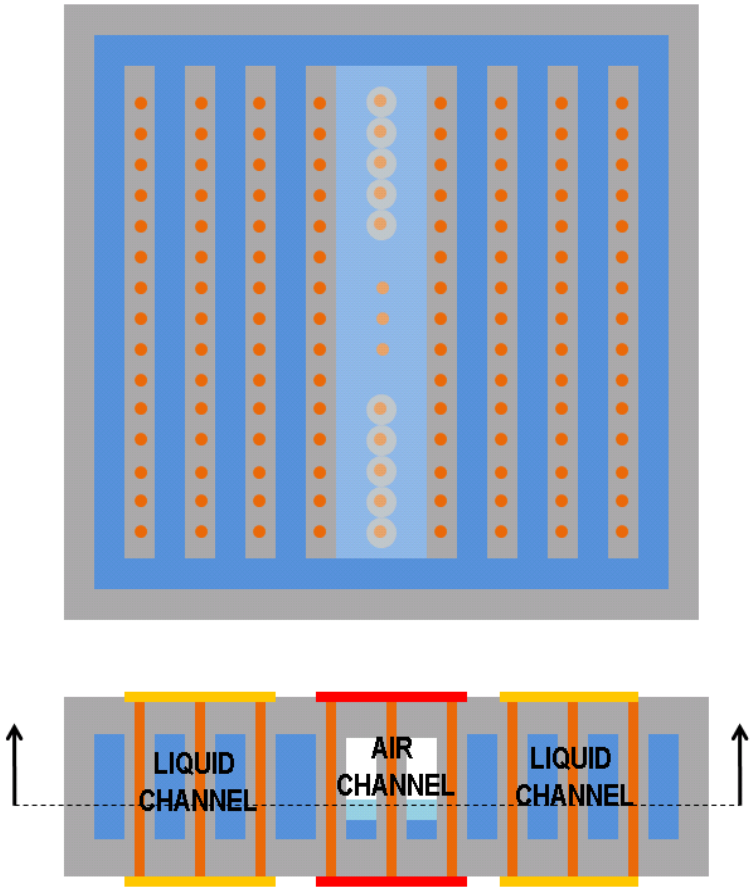

Figure 8.3 The application of thin-evaporation for hotspot mitigation with microchannel background cooling for a 3D stack of ICs.

An alternate configuration of microchannels wherein the thin film evaporation can be integrated to operate in a closed loop configuration is shown in Figure 8.4. The stacked

microchannel configuration illustrates the idea of utilizing a flowing liquid to provide in-situ condensation of the vapor diffusing across a hydrophobic membrane. As shown in Figure 8.4, the evaporator and condenser are separated by a hydrophobic membrane with a pore structure that maximizes the rate of vapor diffusion. In this simple implementation, the excess liquid that does not vaporize in the evaporator flows across the condenser to collect the vapor at the membrane outlet. The heated liquid which leaves the microchannel heat sunk outlet can be cooled back to room temperature using a remotely located heat sink.

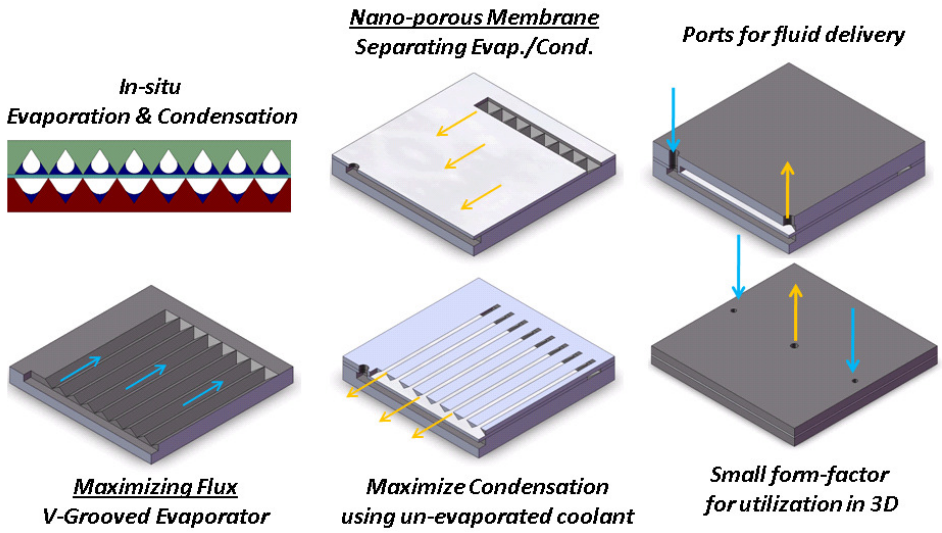

Figure 8.4 A schematic diagram illustrating the use of a sweeping liquid for in-situ vapor condensation and operation of the cooling system in a closed loop configuration.

APPENDIX A

1. Derivation of governing equation for interfacial temperature:

$$\dot{q}_{c,r} - \dot{q}_{c,x} + \dot{q}_{c,x+\Delta x} = \dot{q}_e \tag{A.21}$$

$$\dot{q}_{c,x+\Delta x} - \dot{q}_{c,x} \simeq (\Delta x)\partial \dot{q}_{c,x} / \partial x \tag{A.22}$$

$$\dot{q}_{c,r} = -k_l (2\pi r_c \Delta x)\left(\frac{\partial T}{\partial r}\right)_w \tag{A.23}$$

$$\dot{q}_{c,x+\Delta x} - \dot{q}_{c,x} = (-2\pi k \Delta x)\left[\int_{r_i}^{r_c} r \frac{\partial^2 T}{\partial x^2} dr - r_i \frac{dr_i}{dx}\left(\frac{\partial T}{\partial x}\right)_i\right] \tag{A.24}$$

Using equation (6.14),

$$\frac{\partial T}{\partial x} = -\frac{(r - r_c)(T_i - T_w)}{(r_i - r_c)^2}\frac{dr_i}{dx} + \frac{(r - r_c)}{(r_i - r_c)}\frac{dT_i}{dx} \tag{A.25}$$

$$\left(\frac{\partial T}{\partial x}\right)_i = -\frac{(T_i - T_w)}{(r_i - r_c)}\frac{dr_i}{dx} + \frac{dT_i}{dx} \tag{A.26}$$

$$\begin{aligned}\frac{\partial^2 T}{\partial x^2} = {} & \frac{2(r - r_c)(T_i - T_w)}{(r_i - r_c)^3}\left(\frac{dr_i}{dx}\right)^2 - \frac{2(r - r_c)}{(r_i - r_c)^2}\left(\frac{dr_i}{dx}\right)\left(\frac{dT_i}{dx}\right) \\ & - \frac{(r - r_c)(T_i - T_w)}{(r_i - r_c)^2}\left(\frac{d^2 r_i}{dx^2}\right) + \frac{(r - r_c)}{(r_i - r_c)}\frac{d^2 T_i}{dx^2}\end{aligned} \tag{A.27}$$

$$\begin{aligned}\left(\dot{q}_{c,r} - \dot{q}_{c,x} + \dot{q}_{c,x+\Delta x}\right)/\Delta x = {} & (2\pi k_l r_c)\frac{T_w - T_i}{r_c - r_i} + \frac{2\pi k_l}{3}(T_w - T_i)\left(\frac{dr_i}{dx}\right)^2 - \\ & \frac{2\pi k_l}{3}(r_c - r_i)\frac{dr_i}{dx}\frac{dT_i}{dx} + \frac{\pi k_l}{3}(r_c + 2r_i)(T_w - T_i)\frac{d^2 r_i}{dx^2} - \frac{\pi k_l}{3}(r_c + 2r_i)(r_c - r_i)\frac{d^2 T_i}{dx^2}\end{aligned} \tag{A.28}$$

$$\dot{q}_e / \Delta x = -h_{fg}\frac{d\dot{m}}{dx} \tag{A.29}$$

2. Derivation of mass flux as a function of interfacial temperature

$$\dot{m}'' = \frac{2\hat{\sigma}}{2-\hat{\sigma}}\left(\frac{M}{2\pi R T_{li}}\right)^{1/2}\left(p_{vi} - p_v\right) \tag{A.30}$$

$$\dot{m}_o'' = \frac{2\hat{\sigma}}{2-\hat{\sigma}}\left(\frac{M}{2\pi R T_{w}}\right)^{1/2}\left(p_{v,eq}\left(T_w\right) - p_v\right) \tag{A.31}$$

$$\frac{\dot{m}''}{\dot{m}_o''} = \left(\frac{T_w}{T_{li}}\right)^{1/2}\frac{p_{vi}\left(T_i\right) - p_v}{p_{v,eq}\left(T_w\right) - p_v} \tag{A.32}$$

Note that p_{vi} used in the equations above is strictly the equilibrium vapor pressure of a curved meniscus which can be different from the saturation vapor pressure at the same temperature. But it has been shown in Chapter 6 that this deviation is less than 2%. Therefore, p_{vi} is calculated as the saturation vapor pressure at local temperature T_i of the interface.

Using Clausius Clapeyron relation:

$$p_{vi}\left(T_i\right) = p_{v,eq}\left(T_w\right) + \frac{\rho_v\left(T_w\right)h_{fg}}{T_w}\left(T_{li} - T_w\right) \tag{A.33}$$

$$\frac{\dot{m}''}{\dot{m}_o''} = \left(\frac{T_w}{T_{li}}\right)^{1/2}\left[1 + \frac{\rho_v\left(T_w\right)h_{fg}}{p_{v,eq}\left(T_w\right) - p_v}\left(\frac{T_{li} - T_w}{T_w}\right)\right] \tag{A.34}$$

Using equation (6.8), which relates mass flux to the total mass flow rate, equation (A.34) is transformed as shown below:

$$-\frac{1}{\dot{m}_o''}\frac{\cos\theta}{2\pi r_i}\frac{d\dot{m}}{dx} = \left(1 + \frac{\Delta T}{T_w}\overline{T}\right)^{-1/2}\left[1 + \frac{\rho_v\left(T_w\right)h_{fg}}{p_{v,eq}\left(T_w\right) - p_v}\left(\frac{\Delta T}{T_w}\overline{T}\right)\right] \tag{A.35}$$

where $\Delta T = \dfrac{\dot{m}_o'' h_{fg} r_c}{k_l}$.

The non-dimensional form of equation (A.35) becomes:

$$\frac{-1}{\bar{r}_i\left[1+\left(d\bar{r}_i/d\bar{x}\right)^2\right]^{1/2}}\frac{d\bar{\dot{m}}}{d\bar{x}}=\left(1+\Pi_4\bar{T}\right)^{-1/2}\left(1+\Pi_3\Pi_4\bar{T}\right) \tag{A.36}$$

3. Governing equations transformed to facilitate numerical integration with respect to $\bar{r}_i$

$$\bar{\dot{m}}\frac{d\bar{x}}{d\bar{r}_i}=\Pi_1\left(-\frac{d\bar{p}_{li}}{d\bar{r}_i}\right)\left[\left(1-\bar{r}_i^2\right)\left(1-3\bar{r}_i^2\right)-4\bar{r}_i^4\ln\bar{r}_i\right]+\Pi_2\left(\frac{d\bar{T}_i}{d\bar{r}_i}\right)\left[4\bar{r}_i\left(1-\bar{r}_i^2\right)+8\bar{r}_i^3\ln\bar{r}_i\right] \tag{A.37}$$

$$\left(1+\Pi_3\Pi_4\bar{T}\right)\left(1+\Pi_4\bar{T}\right)^{-1/2}=\frac{-1}{\bar{r}_i\left[1+\left(d\bar{x}/d\bar{r}_i\right)^2\right]^{1/2}}\frac{d\bar{\dot{m}}}{d\bar{r}_i} \tag{A.38}$$

$$\Pi_5-\bar{p}_{li}=\Pi_6\left\{\frac{d\bar{x}/d\bar{r}_i}{\bar{r}_i\left[1+\left(d\bar{x}/d\bar{r}_i\right)^2\right]^{1/2}}-\frac{d^2\bar{x}/d\bar{r}_i^2}{\left[1+\left(d\bar{x}/d\bar{r}_i\right)^2\right]^{3/2}}\right\}+\frac{\Pi_7}{\left(1-\bar{r}_i\right)^3}+\frac{\Pi_8}{\left(1-\bar{r}_i\right)^2} \tag{A.39}$$

$$\begin{aligned}&\frac{-\bar{T}_i}{1-\bar{r}_i}\left(\frac{d\bar{x}}{d\bar{r}_i}\right)^3-\frac{\bar{T}_i}{3}\frac{d\bar{x}}{d\bar{r}_i}-\frac{\left(1-\bar{r}_i\right)}{3}\frac{d\bar{x}}{d\bar{r}_i}\frac{d\bar{T}_i}{d\bar{r}_i}+\frac{\bar{T}_i}{6}\left(1+2\bar{r}_i\right)\frac{d^2\bar{x}}{d\bar{r}_i^2}\\&-\frac{\left(1+2\bar{r}_i\right)\left(1-\bar{r}_i\right)}{6}\left(\frac{d^2\bar{T}_i}{d\bar{r}_i^2}\frac{d\bar{x}}{d\bar{r}_i}-\frac{d^2\bar{x}}{d\bar{r}_i^2}\frac{d\bar{T}_i}{d\bar{r}_i}\right)=-\frac{d\bar{\dot{m}}}{d\bar{r}_i}\left(\frac{d\bar{x}}{d\bar{r}_i}\right)^2\end{aligned} \tag{A.40}$$

Table A.1 Thermophysical properties of water used in the analysis

Property	Temperature function (T_w expressed in K)
A (J)	-3.148×10^{-20}
M (kg/kmol)	18
k (W/mK)	$-0.761419614 + 0.00744487347T_w - 0.000009712152T_w^2$
μ (Ns/m^2)	$0.0152155435 - 0.0000803832959T_w + 1.08362632\times10^{-07}T_w^2$
σ (N/m)	$0.123633 - 0.000172708T_w$
ρ_v (kg/m^3)	$9.93175603 - 0.0654668119T_w + 0.00010819298T_w^2$
h_{fg} (J/kgK)	$3.17254303\times10^{06} - 2448.68302T_w$
ρ_l (kg/m^3)	998
ε	80
Z	1

REFERENCES

1. I.T.R.S, 2007, Executive Summary 2007 Edition. *The International Technology Roadmap for Semiconductors*. **Online: www.itrs.net**.

2. Hamann, H.F., A. Weger, J.A. Lacey, et al., 2007, Hotspot-Limited Microprocessors: Direct Temperature and Power Distribution Measurements. *Solid-State Circuits, IEEE Journal of*. **42**(1): p. 56-65.

3. Mudawar, I., 2001, Assessment of high-heat-flux thermal management schemes. *IEEE Transactions on Components and Packaging Technologies*. **24**(2): p. 122-141.

4. Bar-Cohen, A., M. Arik and M. Ohadi, 2006, Direct liquid cooling of high flux micro and nano electronic components. *Proceedings of the IEEE*. **94**(8): p. 1549-1570.

5. Agostini, B., M. Fabbri, J.E. Park, et al., 2007, State of the Art of High Heat Flux Cooling Technologies. *Heat Transfer Engineering*. **28**(4): p. 258 - 281.

6. Amon, C.H., S.C. Yao, C.F. Wu, et al., 2005, Microelectromechanical System-Based Evaporative Thermal Management of High Heat Flux Electronics. *Journal of Heat Transfer*. **127**: p. 66.

7. Pijnenburg, R.H.W., R. Dekker, C.C.S. Nicole, et al. Integrated micro-channel cooling in silicon. in Solid-State Device Research conference, 2004. ESSDERC 2004. Proceeding of the 34th European. 2004.129-132

8. Hetsroni, G., M. Gurevich and R. Rozenblit, 2006, Sintered porous medium heat sink for cooling of high-power mini-devices. *International Journal of Heat and Fluid Flow*. **27**(2): p. 259-266.

9. Overholt, M.R., A. McCandless, K.W. Kelly, et al. Micro-jet arrays for cooling of electronic equipment. in 3rd International Conference on Microchannels and Minichannels. 2005. Toronto, ON, Canada: American Society of Mechanical Engineers.PART B.249-252

10. Faulkner, D., M. Khotan and R. Shekarriz. Practical design of a 1000 W/cm2 cooling system. 2003. San Jose, CA, United states: Institute of Electrical and Electronics Engineers Inc.223-230

11. Kosar, A., C.J. Kuo and Y. Peles, 2005, Boiling heat transfer in rectangular microchannels with reentrant cavities. *International Journal of Heat and Mass Transfer*. **48**(23-24): p. 4867-4886.

12. Chen, Z.Q., P. Cheng and T.S. Zhao, 2000, An experimental study of two phase flow and boiling heat transfer in bi-dispersed porous channels. *International Communications in Heat and Mass Transfer*. **27**(3): p. 293-302.

13. Kim, J.H., S.M. You and S.U.S. Choi, 2004, Evaporative spray cooling of plain and microporous coated surfaces. *International Journal of Heat and Mass Transfer*. **47**(14-16): p. 3307-3315.

14. Li, C. and G.P. Peterson, 2006, Evaporation/Boiling in Thin Capillary Wicks (II)—Effects of Volumetric Porosity and Mesh Size. *Journal of Heat Transfer*. **128**: p. 1320.

15. Li, C., G.P. Peterson, Y. Wang, et al., 2006, Evaporation/Boiling in Thin Capillary Wicks (l)—Wick Thickness Effects. *Journal of Heat Transfer*. **128**: p. 1312.

16. Ho Song, C., D.Y. Lee and S. Tack Ro, 2003, Cooling enhancement in an air-cooled finned heat exchanger by thin water film evaporation. *International Journal of Heat and Mass Transfer*. **46**(7): p. 1241-1249.

17. Hasan, A. and K. Sirén, 2003, Performance investigation of plain and finned tube evaporatively cooled heat exchangers. *Applied Thermal Engineering*. **23**(3): p. 325-340.

18. Bar-Cohen, A., G. Sherwood, M. Hodes, et al., 1995, Gas-assisted evaporative cooling of high density electronic modules. *Components, Packaging, and Manufacturing Technology, Part A, IEEE Transactions on [see also Components, Hybrids, and Manufacturing Technology, IEEE Transactions on]*. **18**(3): p. 502-509.

19. Fedorov, A.G., *"Nano-Patch Thermal Management Devices, Methods, and Systems", U.S. Patent No. 7,545,644 (2009).* 2007: USA.

20. Findley, M.E., V.V. Tanna, Y.B. Rao, et al., 1969, Mass and heat transfer relations in evaporation through porous membranes. *AIChE Journal*. **15**(4): p. 483-489.

21. Johnson, D.W., C. Yavuzturk and J. Pruis, 2003, Analysis of heat and mass transfer phenomena in hollow fiber membranes used for evaporative cooling. *Journal of Membrane Science*. **227**(1-2): p. 159-171.

22. Lawson, K.W. and D.R. Lloyd, 1997, Membrane distillation: review. *Journal of Membrane Science*. **124**(1): p. 1–25.

23. Schofield, R.W., A.G. Fane and C.J.D. Fell, 1987, Heat and mass transfer in membrane distillation. *Journal of Membrane Science*. **33**(3): p. 299-313.

24. Schofield, R.W., A.G. Fane and C.J.D. Fell, 1990, Gas and vapour transport through microporous membranes. II. Membrane distillation. *Journal of Membrane Science*. **53**(1-2): p. 173–185.

25. Schofield, R.W., A.G. Fane and C.J.D. Fell, 1990, Gas and vapour transport through microporous membranes. I. Knudsen-Poiseuille transition. *Journal of Membrane Science*. **53**(1-2): p. 159–171.

26. Martin, H., 1977, Heat and mass transfer between impinging gas jets and solid surfaces. *Advances in heat transfer*.

27. E. U. Schlünder, V.G., 1967, Wärme- und Stoffübertragung zwischen Gut und aufprallendem Düsenstrahl. *Chemie Ingenieur Technik - CIT*. **39**(9-10): p. 578-584.

28. Colburn, A.P., 1933, A Method of Correlating Forced Convection Heat Transfer Data and a Comparison with Fluid Friction. *Transactions of the American Institute of Chemical Engineers*.

29. Chilton, T.H. and A.P. Colburn, 1934, Mass Transfer (Absorption) Coefficients Prediction from Data on Heat Transfer and Fluid Friction. *Industrial & Engineering Chemistry*. **26**(11): p. 1183-1187.

30. Miranda, J.M. and J.B.L.M. Campos, 2002, Mass transfer in the vicinity of a separation membrane--the applicability of the stagnant film theory. *Journal of Membrane Science*. **202**(1-2): p. 137-150.

31. 3MProducts, 3M™ Fluorinert™ Electronic Liquid FC-72. www.3m.com.

32. Vatistas, G.H., 1988, Radial flow between two closely placed flat disks. *AIAA Journal*. **26**: p. 887-889.

33. Vatistas, G.H., 1990, Radial inflow within two flat disks. *AIAA Journal*. **28**(7): p. 1308-1309.

34. Kaviany, M., *Principles of Heat Transfer in Porous Media*. 1995: Springer.

35. Kline, S.J., 1985, The Purposes of Uncertainty Analysis. *Journal of Fluids Engineering-Transactions of the ASME*. **107**(2): p. 153-160.

36. Kline, S.J. and F.A. McClintock, 1953, Describing Uncertainties in Single-Sample Experiments. *Mechanical Engineering*. **75**(1): p. 3-8.

37. Tong, A.Y., 2003, On the impingement heat transfer of an oblique free surface plane jet. *International Journal of Heat and Mass Transfer*. **46**(11): p. 2077-2085.

38. Crouse, D., Y. Lo, A. Miller, et al., 2000, Self-ordered pore structure of anodized aluminum on silicon and pattern transfer. *Applied Physics Letters*. **76**: p. 49.

39. Jessensky, O., F. Müller and U. Gösele, 1998, Self-organized formation of hexagonal pore arrays in anodic alumina. *Applied Physics Letters*. **72**: p. 1173.

40. Lee, W., R. Ji, U. Gösele, et al., 2006, Fast fabrication of long-range ordered porous alumina membranes by hard anodization. *Nature materials*. **5**(9): p. 741-747.

41. Li, A., F. Müller, A. Birner, et al., 1998, Hexagonal pore arrays with a 50–420 nm interpore distance formed by self-organization in anodic alumina. *Journal of Applied Physics*. **84**: p. 6023.

42. Masuda, H. and K. Fukuda, 1995, Ordered metal nanohole arrays made by a two-step replication of honeycomb structures of anodic alumina. *Science*. **268**(5216): p. 1466.

43. Masuda, H., H. Yamada, M. Satoh, et al., 1997, Highly ordered nanochannel-array architecture in anodic alumina. *Applied Physics Letters*. **71**: p. 2770.

44. Rabin, O., P. Herz, Y. Lin, et al., 2003, Formation of thick porous anodic alumina films and nanowire arrays on silicon wafers and glass. *Advanced Functional Materials*. **13**(8): p. 631-638.

45. Wu, Z., C. Richter and L. Menon, 2007, A study of anodization process during pore formation in nanoporous alumina templates. *Journal of the Electrochemical Society*. **154**: p. E8.

46. Li, Y., G.W. Meng, L.D. Zhang, et al., 2000, Ordered semiconductor ZnO nanowire arrays and their photoluminescence properties. *Applied Physics Letters*. **76**: p. 2011.

47. Agirregabiria, M., F. Blanco, J. Berganzo, et al., 2005, Fabrication of SU-8 multilayer microstructures based on successive CMOS compatible adhesive bonding and releasing steps. *Lab on a Chip*. **5**(5): p. 545-552.

48. Blanco, F., M. Agirregabiria, J. Garcia, et al., 2004, Novel three-dimensional embedded SU-8 microchannels fabricated using a low temperature full wafer adhesive bonding. *Journal of Micromechanics and Microengineering*. **14**: p. 1047-1056.

49. Francisco, J.B., A. Maria, T. Maria, et al. Novel low-temperature CMOS-compatible full-wafer-bonding process for the fabrication of 3D embedded microchannels using SU-8. 2004. C. Jung-Chih, et al.: SPIE.5276.131-142

50. Carlier, J., S. Arscott, V. Thomy, et al., 2004, Integrated microfluidics based on multi-layered SU-8 for mass spectrometry analysis. *Journal of Micromechanics and Microengineering*. **14**: p. 619-624.

51. Chen, Y. and D. Lee, 2007, A bonding technique using hydrophilic SU-8. *Journal of Micromechanics and Microengineering*. **17**: p. 1978-1984.

52. Li, S., C. Freidhoff, R. Young, et al., 2003, Fabrication of micronozzles using low-temperature wafer-level bonding with SU-8. *Journal of Micromechanics and Microengineering*. **13**: p. 732-738.

53. Svasek, P., E. Svasek, B. Lendl, et al., 2004, Fabrication of miniaturized fluidic devices using SU-8 based lithography and low temperature wafer bonding. *Sensors & Actuators: A. Physical*. **115**(2-3): p. 591-599.

54. Tuomikoski, S. and S. Franssila, 2004, Wafer-Level Bonding of MEMS Structures with SU-8 Epoxy Photoresist. *Physica Scripta*. **114**: p. 223-226.

55. Tuomikoski, S. and S. Franssila, 2005, Free-standing SU-8 microfluidic chips by adhesive bonding and release etching. *Sensors & Actuators: A. Physical*. **120**(2): p. 408-415.

56. Yovanovich, M., J. Culham and P. Teertstra, 1998, Analytical modeling of spreading resistance in flux tubes, half spaces, and compound disks. *IEEE Transactions on Components Packaging and Manufacturing Technology Part A*. **21**: p. 168-176.

57. Yovanovich, M., Y. Muzychka and J. Culham, 1999, Spreading Resistance of Iso ux Rectangles and Strips on Compound Flux Channels. *Journal of Thermophysics and Heat Transfer*. **13**(4).

58. Narayanan, S., A.G. Fedorov and Y.K. Joshi, *Experimental characterization of a micro-scale thin-film evaporative cooling device*, in *ITHERM*. 2010: Las Vegas, accepted.

59. de Gennes, P.G., 1985, Wetting: statics and dynamics. *Reviews of Modern Physics*. **57**(3): p. 827.

60. Orlando, E.R. and Z.B. William, 2002, Evaporation of Water Droplets Placed on a Heated Horizontal Surface. *Journal of Heat Transfer*. **124**(5): p. 854-863.

61. Israelachvili, J.N., *Intermolecular and surface forces*. 3 ed. 1992, London: Academic Press.

62. Rabinovich, Y.I., B.V. Derjaguin and N.V. Churaev, 1982, Direct measurements of long-range surface forces in gas and liquid media. *Advances in Colloid and Interface Science*. **16**(1): p. 63-78.

63. Derjaguin, B.V., 1941, Theory of the stability of strongly charged lyophobic sols and the adhesion of strongly charged particles in solutions of electrolytes. *Acta Physicochim. USSR*. **14**: p. 633-662.

64. Verwey, E.J.W., 1947, Theory of the Stability of Lyophobic Colloids. *The Journal of Physical Chemistry*. **51**(3): p. 631-636.

65. Pashley, R.M. and J.A. Kitchener, 1979, Surface forces in adsorbed multilayers of water on quartz. *Journal of Colloid and Interface Science*. **71**(3): p. 491-500.

66. Deryagin, B.V. and N.V. Churaev, 1987, Structure of water in thin layers. *Langmuir*. **3**(5): p. 607-612.

67. Deryagin, B.V., Y.M. Popovskii and A.A. Goryuk, 1987, Structural component of disjoining pressure in wetting films of nitrobenzene formed on the lyophilic surface of quartz. *Langmuir*. **3**(5): p. 628-631.

68. Gee, M.L., T.W. Healy and L.R. White, 1990, Hydrophobicity effects in the condensation of water films on quartz. *Journal of Colloid and Interface Science*. **140**(2): p. 450-465.

69. Pashley, R.M., 1982, Hydration forces between mica surfaces in electrolyte solutions. *Advances in Colloid and Interface Science*. **16**(1): p. 57-62.

70. Ninham, B.W., 1999, On progress in forces since the DLVO theory. *Advances in Colloid and Interface Science*. **83**(1-3): p. 1-17.

71. Wayner, P.C., Y.K. Kao and L.V. LaCroix, 1976, The interline heat transfer coefficient of an evaporating wetting film. *Int. J. Heat Mass Transfer*. **19**(2): p. 487–492.

72. Wayner Jr, P.C., 1979, Effect of thin film heat transfer on meniscus profile and capillary pressure. *AIAA Journal*. **17**: p. 772-776.

73. DasGupta, S., J.A. Schonberg and P.C. Wayner Jr, 1993, Investigation of an evaporating extended meniscus based on the augmented Young-Laplace equation. *ASME Transactions Journal of Heat Transfer*. **115**: p. 201-208.

74. Buffone, C. and K. Sefiane, 2004, Investigation Thermocapillary Convection in Pores and Its Role in Heat and Mass Transfer Enhancement. *Int. J. Multiphase Flow*. **30**: p. 1071–1091.

75. Buffone, C., K. Sefiane and J.R.E. Christy, 2004, Experimental investigation of the hydrodynamics and stability of an evaporating wetting film placed in a temperature gradient. *Applied Thermal Engineering*. **24**(8-9): p. 1157-1170.

76. Buffone, C., K. Sefiane and J.R.E. Christy, 2005, Experimental investigation of self-induced thermocapillary convection for an evaporating meniscus in capillary tubes using micro–particle image velocimetry. *Physics of Fluids*. **17**: p. 052104.

77. Dhavaleswarapu, H.K., P. Chamarthy, S.V. Garimella, et al., 2007, Experimental investigation of steady buoyant-thermocapillary convection near an evaporating meniscus. *Physics of Fluids*. **19**: p. 082103.

78. Wang, H., J.Y. Murthy and S.V. Garimella, 2008, Transport from a volatile meniscus inside an open microtube. *International Journal of Heat and Mass Transfer*. **51**(11-12): p. 3007-3017.

79. Wee, S.K., K.D. Kihm and K.P. Hallinan, 2005, Effects of the liquid polarity and the wall slip on the heat and mass transport characteristics of the micro-scale evaporating transition film. *International Journal of Heat and Mass Transfer*. **48**(2): p. 265-278.

80. Schrage, R.W., *A theoretical study of interphase mass transfer*. 1953: Columbia University Press.

81. Skinner, L.M. and J.R. Sambles, 1972, The Kelvin equation--a review. *Journal of Aerosol Science*. **3**(3): p. 199-210.

82. Fisher, L.R., 1982, Forces due to capillary-condensed liquids: Limits of calculations from thermodynamics. *Advances in Colloid and Interface Science*. **16**(1): p. 117-125.

83. Fisher, L.R., R.A. Gamble and J. Middlehurst, 1981, The Kelvin equation and the capillary condensation of water. *Nature*. **290**(5807): p. 575-576.

84. Fisher, L.R. and J.N. Israelachvili, 1981, Experimental studies on the applicability of the Kelvin equation to highly curved concave menisci. *Journal of Colloid and Interface Science*. **80**(2): p. 528-541.

85. DasGupta, S., J.A. Schonberg and P.C. Wayner Jr, 1993, Investigation of an Evaporating Extended Meniscus Based on the Augmented Young-Laplace Equation. *ASME, Transactions, Journal of Heat Transfer (ISSN 0022-1481)*. **115**(1).

86. Swanson, L.W. and G.C. Herdt, 1992, Model of the evaporating meniscus in a capillary tube. *Journal of Heat Transfer (Transactions of the ASME (American Society of Mechanical Engineers), Series C);(United States)*. **114**(2).

87. Aoki, K. and C. Cercignani, 1983, Evaporation and condensation on two parallel plates at finite Reynolds numbers. *Physics of Fluids*. **26**(5): p. 1163-1164.

88. Philip, J.R., 1977, Unitary approach to capillary condensation and adsorption. *The Journal of Chemical Physics*. **66**: p. 5069.

89. Derjaguin, B.V. and N.V. Churaev, 1974, Structural component of disjoining pressure. *Journal of Colloid and Interface Science*. **49**(2): p. 249-255.

90. Langmuir, I., 1938, Repulsive forces between charged surfaces in water and the casue of the Jones-Ray effect. *Science*. **88**(2288): p. 430-432.

91. Kumar, D. and S.K. Biswas, Contribution of different physical forces to the disjoining pressure of a thin water film being pressed by an oil droplet. *Journal of Colloid and Interface Science*. **348**(1): p. 255-264.

92. Cohan, L.H., 1938, Sorption Hysteresis and the Vapor Pressure of Concave Surfaces. *Journal of the American Chemical Society*. **60**(2): p. 433-435.

93. Broekhoff, J.C.P. and J.H. de Boer, 1967, Studies on pore systems in catalysts : IX. Calculation of pore distributions from the adsorption branch of nitrogen sorption isotherms in the case of open cylindrical pores A. Fundamental equations. *Journal of Catalysis*. **9**(1): p. 8-14.

94. Matsuoka, H., K. Oka, Y. Yamashita, et al., Deformation characteristics of ultra-thin liquid film considering temperature and film thickness dependence of surface tension. *Microsystem Technologies*. **17**(5): p. 983-990.

95. Niels, R., P. Mela, T. Kramer, et al., 2003, Capillarity induced negative pressure of water plugs in nanochannels. *Nano Letters*. **3**(11): p. 1537-1540.

96. Briggs, L.J., 1955, Maximum superheating of water as a measure of negative pressure. *Journal of Applied Physics*. **26**(8): p. 1001-1003.

97. Debenedetti, P.G., *Metastable liquids*. 1996: Princeton Univ. Press.

98. Narayanan, S., A.G. Fedorov and Y.K. Joshi, 2010, On-chip thermal management of hotspots using a perspiration nanopatch. *Journal of Micromechanics and Microengineering*. **20**(7): p. 10.

99. Narayanan, S., A.G. Fedorov and Y.K. Joshi, 2009, Gas-Assisted Thin-Film Evaporation from Confined Spaces for Dissipation of High Heat Fluxes. *Nanoscale and Microscale Thermophysical Engineering*. **13**(1): p. 30 - 53.

100. Narayanan, S., A.G. Fedorov and Y.K. Joshi. Experimental characterization of a micro-scale thin film evaporative cooling device. in Thermal and Thermomechanical Phenomena in Electronic Systems (ITherm), 2010 12th IEEE Intersociety Conference on.1-10

101. Narayanan, S., A.G. Fedorov and Y. Joshi, Interfacial Transport of Evaporating Water Confined in Nanopores. *Langmuir*. **http://dx.doi.org/10.1021/la201807a**.

102. Xu, B., K.T. Ooi, C. Mavriplis, et al., 2003, Evaluation of viscous dissipation in liquid flow in microchannels. *Journal of Micromechanics and Microengineering*. **13**: p. 53.

103. ITRS, 2010, The next Step in Assembly and Packaging: System Level Integration in the package (SiP). *Online at http://www.itrs.net*.